

FUNCTIONAL GRAPHENE-BASED
MATERIALS AND THEIR APPLICATIONS IN
ENVIRONMENTAL REMEDIATION AND
WEARABLE ELECTRONICS

A thesis submitted to the University of Manchester for the degree of

Doctor of Philosophy

in the Faculty of Science and Engineering

2022

Heng Zhai

School of Natural Sciences

List of Contents

List of Contents	2
List of Figures	6
List of Tables	8
List of Abbreviations	9
List of Publications	10
Abstract	11
Declaration	12
Copyright Statement	13
Acknowledgements	14
Chapter 1 Introduction	
1.1 Research background.....	15
1.2 Research challenges.....	17
1.3 Research objectives	18
1.4 Research methodologies	18
1.5 Thesis outline	21
Chapter 2 Literature Review	
2.1 Introduction	24
2.2 Functional graphene-based materials	25
2.2.1 Fabrication of graphene oxide	25
2.2.2 Fabrication of graphene fibres.....	31
2.2.3 Fabrication of graphene-TiO ₂ composites	38
2.2.4 Summary	44
2.3 Functionalised graphene-based textiles fabrication.....	44
2.3.1 Deposition-based techniques	44
2.3.2 Textile-based techniques	49
2.3.3 Summary	53
2.4 Applications in environmental remediation and wearable electronics	54
2.4.1 Waste textiles management	54
2.4.2 Wastewater treatment	57
2.4.3 Humidity sensor.....	59
2.4.4 Strain sensor	63

2.4.5 Summary	69
2.5 Summary and research gaps	69
Chapter 3 Waste textile reutilisation via a scalable dyeing technology: A strategy to enhance dyestuffs degradation efficiency	
Abstract	72
3.1 Introduction	73
3.2 Experimental section	75
3.2.1 Preparation of GO dispersion and TiO ₂ /GO composite dispersion	75
3.2.2 Pad dyeing of wool fabric.....	75
3.2.3 Dark adsorption Test	76
3.2.4 Photocatalytic degradation measurements.....	76
3.2.5 Characterisation of the TiO ₂ /rGO coated wool fabric	77
3.3 Results and discussions	77
3.3.1 Preparation of functionalised fabrics.....	77
3.3.2 Characterisations	80
3.3.3 Adsorbing capacity of FF-rGO.....	83
3.3.4 Enhanced photocatalytic performance of FF-rGO	85
3.3.5 Integration of night-time adsorption and day-time photodegradation.....	89
3.3.6 Sustainability of FF-rGO.....	91
3.3.7 Applications in degradation of large-amount dyestuffs contaminations	92
3.4 Conclusions	94
3.5 Supplementary information.....	94
Chapter 4 Coolmax/Graphene-Oxide Functionalised Textile Humidity Sensor with Ultrafast Response for Human Activities Monitoring	
Abstract	101
4.1 Introduction	102
4.2 Experimental section	105
4.2.1 Preparation of the graphene dispersion	105
4.2.2 Preparation of GO-fibres and sensors.....	105
4.2.3 Characterisation of the GO-fibres and sensors	106
4.3 Results and discussions	108
4.3.1 Analysis of GO functionalisation	108
4.3.2 Analysis and comparison of GO-Fibres as humidity sensors.....	110

4.3.3 GO-Coolmax performance characterisation.....	113
4.3.4 Applications.....	117
4.4 Conclusions	121
4.5 Supplementary information.....	122
Chapter 5 Twisted graphene fibre based breathable, wettable and washable anti-jamming strain sensor for underwater motion sensing	
Abstract	129
5.1 Introduction	130
5.2 Experimental section	132
5.2.1 Preparation of GO dispersion.....	132
5.2.2 Wet spinning of continuous TGOFs and chemical reduction.....	132
5.2.3 Fabrication of BWWAJ strain sensor via hand weaving loom.....	133
5.2.4 Washability Test.....	133
5.2.5 Characterisations	133
5.3 Results and discussions	134
5.3.1 Fabrication and characterisations of TGFs.....	134
5.3.2 Fabrication, calibration and mechanism of BWWAJ sensor.....	137
5.3.3 Electromechanical properties of the BWWAJ sensor	140
5.3.4 Washability, breathability and wettability of the BWWAJ sensor.....	142
5.3.5 Underwater motion monitoring	145
5.4 Conclusions	147
5.5 Supplementary information.....	148
Chapter 6 A highly sensing-reliable fabric strain sensor with tunable sensitivity for motion sensing and identification	
Abstract	160
6.1 Introduction	161
6.2 Experimental section	163
6.2.1 GO/TiO ₂ dispersion preparation.....	163
6.2.2 Wet-spinning and wet-fusing assembly of TGTF	163
6.2.3 Hand weaving of strain sensor.....	164
6.2.4 Washability test and self-cleaning test	164
6.2.5 Characterisation.....	164
6.3 Results and discussions	165

6.3.1 Wet-fusing assembly of flexible TGTFs	165
6.3.2 Characterisation of TGTF.....	166
6.3.3 Sensor fabrication, calibration and tunable sensitivity	168
6.3.4 Sensing reliability and self-cleaning properties.....	172
6.3.5 Applications in motion detection and respiration identification.....	175
6.4 Conclusions	176
6.5 Supplementary information	177
Chapter 7 Conclusions and Future work	
7.1 Conclusions	183
7.2 Novelties and contributions	185
7.3 Limitations.....	186
7.4 Future work	186
Reference.....	188

Word counts: 36119

List of Figures

Figure 1-1. Outline of thesis.	23
Figure 2-1. Outline of literature review.	25
Figure 2-2. Procedure scheme for modified Hummers' method to synthesize GO.	27
Figure 2-3. The structural models of GO.	28
Figure 2-4. Dispersibility of GO in various solvents.	29
Figure 2-5. Mechanism for the chemical reduction of GO.	30
Figure 2-6. Development of graphene fibres.	32
Figure 2-7. Wet-spinning fabrication of GF.	33
Figure 2-8. Dry-spinning fabrication of GOF.	35
Figure 2-9. Sheet axial orientation and radial alignment of GF.	36
Figure 2-10. Schematic diagram of the tunable penetration screen-printing fabrication.	46
Figure 2-11. Schematic diagram of the all inkjet-printed graphene e-textile manufacturing process.	47
Figure 2-12. Schematic diagram of the fabrication of pad-dyed graphene-based strain sensor.	48
Figure 2-13. Fabrication of graphene-metallic textiles by ELD.	49
Figure 2-14. An embroidery-fabricated strain sensor.	50
Figure 2-15. A plain-woven magnetic fabric for energy harvesting.	52
Figure 2-16. Fabrication of ultraelastic yarns via wrapping conductive filaments on the elastic core.	53
Figure 2-17. Chemical recycling of waste textile by separation of natural polymers from blended fabrics.	56
Figure 2-18. Applications of flexible humidity sensors.	63
Figure 2-19. Applications of flexible strain sensors.	69
Figure 3-1. Concept of waste textiles reutilisation and wastewater treatment.	78
Figure 3-2. Schematic illustration of the fabrication of FF-rGO.	79
Figure 3-3. Characterisations of FF-rGO.	81
Figure 3-4. Schematic diagram of interactions between MB molecular and rGO sheets.	84
Figure 3-5. The photocatalytic degradation of MB over different fabrics.	87
Figure 3-6. The integration of dark adsorption and photodegradation (PD) of MB over different fabrics.	90
Figure 3-7. Sustainability of FF-rGO.	92
Figure 3-8. Wasted socks reutilisation in degradation of large-amount dyestuffs contaminations.	93
Figure 4-1. The process of GO-functionalisation on fibres.	107

Figure 4-2. Characterisation of GO-functionalised fibres.	109
Figure 4-3. Morphological structures (SEM and schematic images) and chemical components of three fibres.	110
Figure 4-4. Water transportation, evaporation and wicking properties of three GO-functionalised sensors.	112
Figure 4-5. Characterisation of humidity sensing performance.	116
Figure 4-6. Applications of GO-Coolmax sensor for vapour and liquid water sensing.	121
Figure 5-1. Fabrication of TGOF.	136
Figure 5-2. Fabrication of BWWAJ sensors and their electrical responses to external interferences.	138
Figure 5-3. Electromechanical properties of the BWWAJ sensors.	141
Figure 5-4. The washability, breathability and wettability of BWWAJ sensors.	143
Figure 5-5. Underwater wireless motion monitoring system.	146
Figure 6-1. Schematic illustration of fabrication of TGOTF.	166
Figure 6-2. Characterisations of the TGTF.	167
Figure 6-3. Fabrication, tunable sensitivity and sensing mechanism of strain sensor.	170
Figure 6-4. Sensing reliability and self-cleaning properties of SRTSS sensor. ..	173
Figure 6-5. The application of SRTSS strain sensors in motion detection and identification.	176

List of Tables

Table 2-1. The performance of GFs associated with their preparation methods. .	38
Table 2-2. Photocatalytic performance of graphene-based TiO ₂ composite materials	43
Table 2-3. Adsorption capacities of MB by various GO-based adsorbents.	57
Table 2-4. Comparisons of degradation intensity for TiO ₂ -based composites.....	58
Table 2-5. Properties of wearable humidity sensors	61
Table 2-6. Performances of reported encapsulation-free fabric strain sensors	66
Table S3-1. Grain size and FWHM of FF-rGO	98
Table S3-2. Adsorption capacities of various adsorbents to MB	98
Table S3-3. Analysis of adsorption activity based on Langmuir and Freundlich model.....	99
Table S3-4. Comparisons of degradation intensity for TiO ₂ -based composites ...	99
Table S4-1. Water transport results of MMT	127
Table S4-2. High resolution of XPS analysis of three main types of carbon bonds	127
Table S4-3. Special surface area of fibres.....	128
Table S4-4. The performance comparison from our work to others.....	128
Table S5-1. Comparisons of reported twisted graphene fibres	157
Table S5-2. Taxonomy of encapsulation-free strain sensor	158
Table S5-3. Comparisons of air permeability and water vapor permeability	159

List of Abbreviations

CA	Contact Angle
CNT	Carbone Nanotubes
CB	Conduction Band
EDX	Energy-dispersive X-ray Spectrometer
FTIR	Fourier Transform Infrared
GO	Graphene Oxide
GOF	Graphene Oxide Fibres
GF	Graphene Fibres
HI	Hydroiodic Acid
L-AA	L-ascorbic Acid
MB	Methylene Blue
PDMS	Polydimethylsiloxane
PL	Photoluminescence
TEM	Transmission Electron Microscope
rGO	Reduced Graphene Oxide
RhB	Rhodamine B
SEM	Scanning Electron Microscope
TGF	Twisted Graphene Fibres
TGTF	Twisted Graphene/TiO ₂ Fibres
TGOF	Twisted Graphene Oxide Fibres
VB	Valence Band
VC	Ascorbic Acid
XRD	X-ray Diffraction
XPS	X-ray Photoelectron Spectroscopy

List of Publications

Journal Papers

H.Z, L.X, Z.L, L.J, Y.Y, J.Z, Y.F, D.C, J.L, X.L, Y.L ‘Twisted graphene fibre based breathable, wettable and washable anti-jamming strain sensor for underwater motion sensing’. Chemical Engineering Journal, 2022, 128639

L.X, **H.Z**, X.C, Y.L, M.W, Z.L, M.U, C.J, L.J, Z.L, T.T, Y.L ‘Coolmax/Graphene-Oxide functionalized textile humidity sensor with ultrafast response for human activities monitoring’. Chemical Engineering Journal, 2021, 128639 (L.X and **H.Z** contributed equally)

L.X, Z.L, **H.Z**, X.C, R.S, S.L, Y.F, Y.Y, Z.C, L.J, J.Z, T.T, Y.L ‘Moisture-resilient graphene-dyed wool fabric for strain sensing’. ACS Applied Materials & Interfaces, 2020, 12(11), Pp. 13265-13274 (L.X, Z.L and **H.Z** contributed equally)

H.Z, Y.F, Y.L ‘The effect of graphene oxide sheets on the mechanical properties of graphene fibres’. Journal of Fibre Bioengineering and Informatics, Vol. 11, Issue 1, 2018, Pp. 49-63

H.Z, Z.L, L.X, T.L, Y.F, L.J, Y.L ‘Waste textile reutilization via a scalable dyeing technology: A strategy to enhance dyestuffs degradation efficiency’. Advanced Fibre Materials, 2022, 1-14

Conference Papers

H.Z & Y.L ‘A review of photocatalytic activity of graphene based TiO₂ composites materials’. Textile Bioengineering and Informatics Symposium Proceedings, 2018, 3, Pp. 158-168

H.Z & Y.L ‘A review on fabricating graphene fibre via wet spinning’. Textile Bioengineering and Informatics Symposium Proceedings, 2017, 3, Pp. 1243-1248

Abstract

The rapid expansion of fast fashion industry brings out environmental concerns such as dyestuffs-related water pollutions and waste textiles. Conventional wastewater-disposal strategies emphasize the optimisation of photocatalytic activity to improve pollutant degradation efficiency, while the adsorptivity, recyclability and sustainability of photocatalysts are largely ignored. The overproduced textiles are still in urgent of being recycled and reutilised in eco-friendly approaches. In this thesis, a scalable dyeing technology is employed to achieve green and sustainable reutilisation of waste textiles. The functionalised TiO₂/reduced graphene oxide wool fabrics show excellent sustainability, remarkable adsorbing capacity and enhanced photocatalytic performance. By taking advantages of these properties, we develop an integrated strategy of night-time adsorption and day-time photodegradation which could significantly optimize the dyestuffs degradation efficiency. The concept of waste textiles reutilisation and wastewater treatment in this work provides practical potentials in the efficient and sustainable environmental remediation.

On the other hand, graphene-based materials have been widely used in wearable electronics for their superior properties in electron and heat transport. However, recent wearable devices are mostly assembled by coating graphene into flexible substrates and stretchable encapsulations. Such fabrication technologies sacrifice the physical comfort, wettability and washability which are the essential elements to wearables. In this thesis, we report a continuous twisted graphene fibre with high tensile strength (369 MPa) and outstanding breaking strain (48.5%) by wet-fusing assembling method, which could be directly woven into fabric-based breathable, wettable and washable strain sensors with anti-jamming properties to bend, pressure, temperature and humidity. The strain sensor displays undifferentiated performance of sensitivity, stability and durability both in air and underwater. We also optimize the mechanical properties of twisted graphene fibre by integrating TiO₂ nanoparticles into the fibre. The as-prepared twisted graphene/TiO₂ fibre has improved tensile strength (515 MPa) and novel photocatalytic performance, which can be assembled into highly sensitive (gauge factor of 350) and self-cleaning stain sensor with extra reliable sensing properties in harsh environment. Moreover, we discover a graphene oxide functionalised Coolmax humidity sensor with ultrafast response/recovery time (0.6 s) after studying textile-based humidity sensors constructed from various natural and synthetic fibres (i.e., cotton, wool and Coolmax). The humidity sensor exhibits wide applications in respiration sensing, diaper wetness alert and woven fabric touchpad.

Declaration

No portion of the work referred to in this thesis has been submitted in support of an application for another degree or qualification of this or any other university or other institute of learning.

Copyright Statement

- i. The author of this thesis (including any appendices and/or schedules to this thesis) owns certain copyright or related rights in it (the “Copyright”) and s/he has given The University of Manchester certain rights to use such Copyright, including for administrative purposes.
- ii. Copies of this thesis, either in full or in extracts and whether in hard or electronic copy, may be made only in accordance with the Copyright, Designs and Patents Act 1988 (as amended) and regulations issued under it or, where appropriate, in accordance with licensing agreements which the University has from time to time. This page must form part of any such copies made.
- iii. The ownership of certain Copyright, patents, designs, trademarks and other intellectual property (the “Intellectual Property”) and any reproductions of copyright works in the thesis, for example graphs and tables (“Reproductions”), which may be described in this thesis, may not be owned by the author and may be owned by third parties. Such Intellectual Property and Reproductions cannot and must not be made available for use without the prior written permission of the owner(s) of relevant Intellectual Property and/or Reproductions.
- iv. Further information on the conditions under which disclosure, publication and commercialisation of this thesis, the Copyright and any Intellectual Property and/or Reproduction described in it may take place is available in the University IP Policy (<http://www.campus.manchester.ac.uk/medialibrary/poolicies/intellectual-property.pdf>), in any relevant Thesis restriction declarations deposited in the University Library, The University Library’s regulations (<http://www.manchester.ac.uk/library/aboutus/regulations>) and in The University’s policy on presentation of Theses.

Acknowledgements

I would like to express my sincere gratitude to my main supervisor Prof Yi Li for his patient and creative guidance on this research. He taught me to critically analyse scientific problems and carry out experiments in an effective way. His devotion and passion to scientific exploration have deeply impressed me. Moreover, the positive modes of living and working he showed to me will be precious treasure in my future.

Meanwhile, I would like to thank Dr. Xuqing Liu and Dr. Jiashen Li who gave me essential supports in my PhD studies. Their valuable comments, continuous supervision and constructive guidance during the last four years have led me in the right direction. My PhD study would be less productive without them.

I would like to acknowledge the supports from the administrative and technician staffs in the University of Manchester. Special thanks to Mrs Olwen Richert who assisted me in tackling the routine problems. My appreciation also extends to Mrs Damindi Jones, Mrs Elizabeth Carlton, Mrs Hannah Rampley, Mr Stuart Morse, and Dr Teruo Hashimoto who gave technical supports in experiment preparation and characterisation.

I would like to thank my group member Dr Lulu Xu, Mr Zekun Liu, Mr Yangyang Fan, Dr Lu Jin, Mr Yangpeiqi Yi, Mr Zhangchi Liu, Miss Yan Zheng, Miss Sirui Yao and Mr Zhongda Chen. I enjoy and cherish the days with them, and those moments will always be remembered.

My greatest appreciation is given to my beloved family, including my wife Mrs Han Wang, my parents Mr Hanmin Zhai and Mrs Yalin Cheng, my sister Mrs Wei Zhai and my nephews Xiaoxiao and Lele. Their unconditional support and love have always been the motivation behind my success.

Chapter 1 Introduction

1.1 Research background

Wearable electronics are attracting increasing research interests in recent years on account of their flexibility, biocompatibility, lightweight properties in contrast to conventional rigid electronics,¹⁻³ which have been widely applied into energy harvesting and storage, motion detection, respiration monitoring, internet of things and human-machine interfaces.⁴⁻⁶ Textile-based wearable electronics are even more favorable due to their natural homologies to commercial garments, such as their breathable, washable, wettable and conformable features.⁷ These essential wearing elements in textile-based wearable electronics make them authentic smart wearables by realizing the electrical functions without any sacrifices of wearing comfortability and durability.

To develop textile-based wearable electronics, the fabrications of conductive fibres and yarns are the significant prerequisites. Noncoated conductive fibres, intrinsically conductive fibres and hybrid conductive fibres are the most frequently used functional fibres for textile-based wearable electronics constructions.⁸ The nanocoated conductive fibres are fabricated by depositing conductive nanomaterials (i.e. metals and carbonaceous materials) onto the fibre substrates. The producing process is simple and easy-handled, however, the conductivity and durability performance of as-prepared conductive fibres are moderate due to the insecure and vulnerable bonding between conductive materials and substrates.^{5,9} Additional Layers of elastomers (i.e. Ecoflex or PDMS) are always employed to encapsulate the nanocoated textiles to protect the structure and increase the flexibility, while worsening the breathability and wearing comfortability. On the contrary, intrinsically conductive fibres and hybrid conductive fibres based on metal wires are extremely conductive while their stiffness and rigidity restrict their practical applications in wearable electronics.¹⁰ By contrast, carbonaceous fibres such as carbon nanotube (CNT) fibres and graphene fibres (GF) shows

advantages in both flexibility and conductivity, which are the desirable fibres for the assembly of wearable electronics.^{11, 12}

On the other hand, environmental crisis, especially water pollution has caused wide concerns due to the shortages of water resources. The textile industry, typically the developed fast fashion market is estimated to be responsible for approximately 20% of global clean water contamination arising from dyeing and finishing production.¹³ Moreover, the overproduced textiles from the fast fashion market are still in urgent of being recycled and reutilised in eco-friendly and sustainable approaches.¹⁴ To address the water pollution concerns caused by organic dyestuffs, the most efficient and effective solution is to employ photocatalytic technology to convert solar energy to degrade pollutants. Conventional photocatalysts such as TiO₂ nanoparticles have limitations in fast recombination rate of photogenerated electron-hole (e^-/h^+) pairs and weak adsorbing affinity of nanoparticles towards target contaminants.¹⁵⁻¹⁷ Various doping strategies have been put forward to optimize the photocatalytic performance of TiO₂, such as metallic doping, non-metallic doping and noble-metal loading. Among these materials, carbonaceous materials such as carbon nanotube and graphene are more favourable owing to their superior properties in transporting electrons, good optical transmittance, large specific surface and strong adsorption capacity.^{18, 19}

Graphene, as the elementary component of all the graphene-based materials, is a flat two-dimensional (2D) monolayer of sp²-hybridised carbon atoms tightly piled into a honeycomb lattice.²⁰ It is a rapidly rising star in the field of material science and condensed-matter physics due to its extraordinary electrical, mechanical and thermal properties.²¹ The promising applications for graphene and graphene-based materials (i.e. graphene-doped composites and fibres) in electronic devices, sensors and composites have led to an explosion in interests.^{17, 22, 23} Among all these applications, the outstanding properties of graphene are optimised in macroscopic aspects by one-dimensional (1D) graphene fibres. Compared with 2D and 3D graphene materials, a 1D graphene fibre is believed to show potential high electrical conduction, ultrahigh

mechanical strength after stretching, unique flexibility and weavability.²⁴

1.2 Research challenges

The fabrications and properties of graphene-based materials, as well as their applications in environmental remediation and wearable electronics are summarised in literature review in Chapter 2.5. According to the summary, the research challenges of this thesis are as follows:

1. Graphene has been widely used as a co-catalyst to improve the photocatalytic performance of TiO₂ nanoparticles. Recent strategies for dyestuff degradation in wastewater are frequently accomplished by graphene modified TiO₂ composites. However, there are insufficient systematic studies on the enhancement of adsorbing capacities of graphene/TiO₂ composites to optimize the contamination degradation efficiency.
2. Most of the waste textiles end up by the way of disposal, such as landfilling or incineration. However, the process of incineration will bring about other environmental risks such as carbon dioxide emissions. There is a lack of sustainable approach to reutilise waste textiles.
3. Currently, pure fabric-based humidity sensors have rarely been investigated due to their low response speed. Textile materials will retain water molecules inside the fibre/fabric even humidity is removed, resulting in longer recovery time for the humidity sensing. There is a vacancy to design and fabricate fabric-based humidity sensor with rapid response and recovery (less than 1 seconds).
4. Recent reported wearable sensing techniques are implemented mainly by either encapsulated packaging approaches or deposition of conductive nanomaterials onto flexible textiles. However, such fabrication technologies sacrifice the physical comfort, washability and wettability which are the essential elements to wearables. It is desirable to fabricate fibres with intrinsic flexibility and conductivity, along with the feasibility in the fabrication of fabric-based strain sensors, to develop a

breathable, wettable and washable anti-jamming strain sensor.

5. The recent reported encapsulation-free strain sensors have limitations in sensitivity and sensing reliability. The ideal strain sensor should overcome the challenges in eliminating various interferences and detecting tensile strain solely in harsh environment. The strain sensor should be insensitive to various physical deformations (e.g., bend and pressure), fickle environmental interferences (e.g., temperature, humidity) and even surface contaminations.

1.3 Research objectives

To address the above research challenges identified from literature review in Chapter 2.5, the following research objectives are developed:

1. To optimize the dyestuff degradation efficiency in wastewater by improving the adsorbing capacity and enhancing photocatalytic activity of graphene/TiO₂ functionalised textiles.
2. To develop a sustainable and green approach for the textile reutilisation.
3. To design and construct a pure fabric-based humidity sensor with high performance (rapid response and insensitive to external pressure and temperature changes) by using graphene-based materials for human humidity-related activity monitoring.
4. To synthesize ultra-flexible and robust graphene fibre for the assembly of breathable, wettable and washable strain sensors.
5. To design and fabricate a strain sensor with high sensitivity (Gauge factor is larger than 300), and excellent sensing reliability against various physical deformations and fickle environmental interferences and self-cleaning properties.

1.4 Research methodologies

The following methodologies have been developed to achieve the listed research objectives in Chapter 1.3. Specifically, to achieve the first and second objectives, I

introduced the pad-dyeing technology to firmly deposit GO/TiO₂ composites onto the surface of waste wool fabrics. The GO dispersion was synthesised *via* a modified hummers method, while we used microwave to heat expandable graphite to gain GO with large-size sheets. The large GO sheets can wrap TiO₂ nanoparticles on the fabric surface which can be confirmed by Scanning Electron Microscope (SEM) and Transmission Electron Microscope (TEM). Raman spectra was exhibited to indicate the reduced level of GO and X-ray Photoelectron Spectroscopy (XPS) spectra was used to investigate the chemical nature of graphene/TiO₂ functionalised wool fabric. Photoluminescence (PL) Spectra was widely employed to investigate the behaviours of photoinduced e⁻/h⁺ pairs, including trapping, immigration and transfer of charge carries. We used Langmuir model and Freundlich model to describe the equilibrium of adsorption and calculate the maximum adsorbing capacity of graphene/TiO₂ functionalised wool fabric. The photocatalytic experiments were carried out under a 150 W Xenon lamp. The concentration of MB was recorded at equal interval time and analysed by using M550 UV/Visible Spectrophotometer (see details in Chapter 3.2).

To achieve the third objective, different kinds of fibres (wool, cotton and Coolmax) were dyed into functionalised fibres in GO bath, followed by weaving into interdigital structures to assemble humidity sensors. To validate the effectiveness of GO coating and fibres morphologies, oxygen/carbon content and graphene peaks were analysed by SEM, Raman spectrum and XPS spectra. Meanwhile, the sensor's water contact angle and water evaporation rate were evaluated to address the humidity sensing mechanism of three sensors. Besides, the humidity response time of three sensors via resistance-humidity changes were compared, where humidity sensor constructed by GO-Coolmax performed the best with the rapidest response and recovery time. To investigate the pressure and temperature effects on sensor performance, the sensor's resistance was measured under the Instron mechanical tester and the environmental chamber respectively. Finally, to demonstrate the potential applications for monitoring human activities, the sensor was integrated into a facemask, sports clothing, baby diaper and fabric keypad for the detection of human breathing activities, sport activities, wet-alert

and finger touching respectively (see details in Chapter 4.2).

To achieve the fourth objective, we fabricated the twisted graphene fibre (TGF) by using the wet-assembly of two wet graphene oxide fibres (GOFs) coming from wet spinning coagulation bath. The surface morphology and twisting angles of TGF were observed by SEM. The parallelised and condensed states of GO sheet in TGF were confirmed by XRD and Raman spectra. The mechanical properties of TGF were measured under Instron mechanical tester. To construct the woven-structure fabric strain sensor, the TGF was served as weft yarn and elastic Lycra yarn was served as warp yarn under hand weaving loom. Mechanical tests and electrical calibration of the sensor were performed using a universal testing machine (Instron 3344) and a multimeter (Keithley 2000) respectively. The air and water vapour permeability were tested by commercialised instruments (SDL, M021A, M216). The temperature and humidity tests were carried out in a conditioning cabinet (Datacolor CONDITINER). The underwater wireless motion monitoring system was built by a wireless multichannel signal transmission module (LinkZill, LZ-01ARC). The complete methodology could be found in Chapter 5.2.

To achieve the fifth objective, we added TiO_2 nanoparticles in graphene oxide dispersion and fabricated twisted graphene/ TiO_2 fibres (TGTF) with self-cleaning properties. The strain sensors were constructed under hand weaving loom in the same way, with TGTF served as weft yarn and Lycra yarn served as warp yarn. However, we designed the strain sensor with various working width (6, 10, or 14 mm) and analysed their corresponding sensitivity. The washability measurement was carried out under standard: ISO 105 CO9 C1&C2. The self-cleaning property of strain sensor was tested by the photodegradation of 10 mg/L methylene blue (MB), Rhodamine B (RhB) and urea respectively under a 150W Xenon lamp. The photodegradation efficiency was measured by analysing the residual dyestuffs using the M550 UV/Visible spectrophotometer (see details in Chapter 6.2)

1.5 Thesis outline

This research is carried out in the logic as shown in Figure 1-1. It focuses on the fabrication of functional graphene-based materials and their applications in environmental remediation and wearable electronics. Chapter 1 presents a brief research background of textile-based wearable electronics and environmental degradation, followed by research challenges, objectives, methodologies of this thesis. Chapter 2 reports a comprehensive literature review with recent progress in graphene-based materials, especially for the wet-spinning fabrication of GF. Various construction technologies for functionalised graphene-based textiles have also been introduced in detail. The performances, as well as potential challenges of functionalised graphene-based textiles in wearable electronics and wearable remediation have been summarised. Moreover, we made a comprehensive summary of literature review and identified the research gaps towards this thesis in the end of Chapter 2.

Chapter 3 and Chapter 4 both put emphasis in the functional GO-coated fabrics. Chapter 3 proposes a scalable dyeing technology to synchronously realize the sustainable reutilisation of waste textiles and efficient degradation of dyestuffs in wastewater, which provides practical potentials in the efficient and sustainable environmental remediation. The TiO_2/rGO functionalised fabrics exhibit decent sustainability, improved adsorbing and photocatalytic performance, displaying great potentials to solve the concerns of overproduced textiles and water contaminations arising from fast fashion industry. In Chapter 4, we explore different fibre materials (cotton, wool and Coolmax) coated by GO and compare their response and recovery times on humidity changes and study their morphologies, micro-structure, as well as water adsorption, transportation and evaporation properties. The humidity sensors integrated with GO-Coolmax functionalised fibres show ultrafast response/recovery time (less than 0.6 s), insensitive to external pressure and temperature change, as well as various wearable applications (e.g., respiration sensing, diaper wetness alert and woven fabric touchpad).

Chapter 5 and Chapter 6 are described in the context of functional graphene fibres. In Chapter 5, we have proposed a wet-fusing assembling methodology to fabricate continuous twisted graphene fibres with high tensile strength (369 MPa) and superior breaking strain (48.5%), as well as stable electrical and mechanical performances under cyclic washing and chronic wetting. The as-prepared TGF shows remarkable weavability and could be woven into strain sensor with outstanding sensitivity (gauge factor ~ 63) to strain while negligible sensitivity upon bend, pressure, temperature and humidity. The fabric strain sensor also exhibits decent breathability, washability and wettability. Owing to its remarkable properties, we establish an underwater wireless motion monitoring system, which could provide information about vital motion signal characters of swimmers underwater to supervise swimming movements, train swimming learners and evaluate risks of drowning. In Chapter 6, we integrate TiO_2 nanoparticles into TGF for fabrication of TGTF with improved tensile strength (515 MPa), which is woven to a fabric strain sensor. The fabric sensor shows outstanding sensitivity to strain (Gauge factor ~ 350) and highly reliable sensing performance. By taking advantages of the hydrophobic and photocatalytic properties of TGTF, the sensor is possessed of a novel self-cleaning capability in photodegrading surface contaminations. The conclusions and future work are stated in Chapter 7.

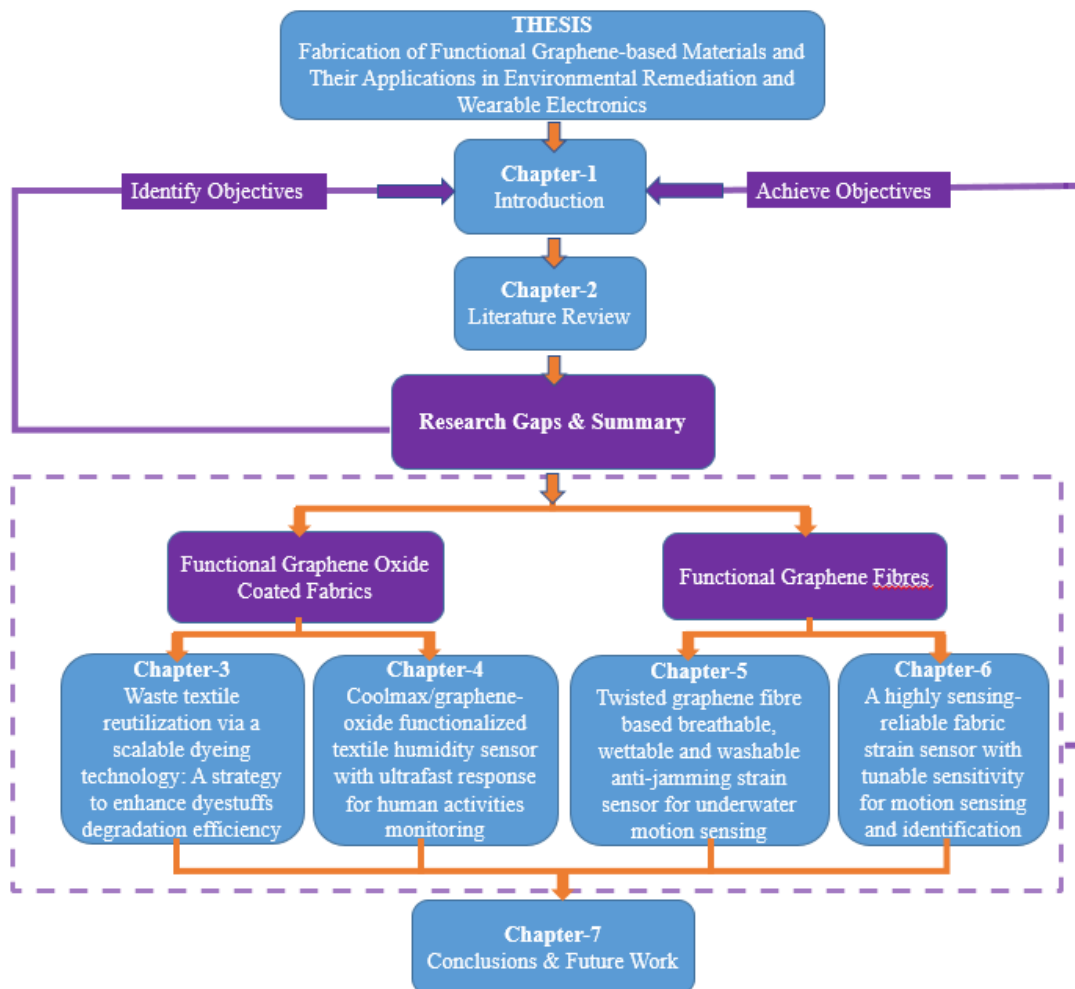


Figure 1-1. Outline of thesis.

Chapter 2 Literature Review

2.1 Introduction

Graphene and its derivatives have become hotspots in sustainable environmental remediation and wearable electronics due to their superior properties in adsorption, light transmission, electron transporting, mechanical strength and modulus.^{17, 25, 26} In order to get insight into the up-to-date developments of graphene-based materials and their typical applications in environmental management and flexible electronics, we investigate literature review *via* a bottom-up approach by starting from the fabrications and properties of raw graphene-based materials, to the assemblies and applications of the functionalised textiles. Finally, we determined the existing gaps and challenges in this research summarised from the literature review (see outline in Figure 2-1).

In the beginning of this Chapter, we gave detailed introductions about the preparations and essential properties of graphene-based materials, including GO, GF and graphene/TiO₂ composites. The chemical reduction of GO, dominating parameters in wet-spinning of GF and mechanical enhancement of GF were highlighted. In Chapter 2.3, we summarised techniques (e.g., depositions and textile constructions) to integrate graphene-based materials into functionalised textiles. The applications of smart textiles in environmental remediation and wearable electronics were exhibited in Chapter 2.4. We made brief summaries by the end of each section of this chapter and an overall summary in Chapter 2.5 to illustrate the research gaps and challenges in fabrications of high-performance graphene-based materials to satisfy their applications in environmental remediation and wearable electronics.

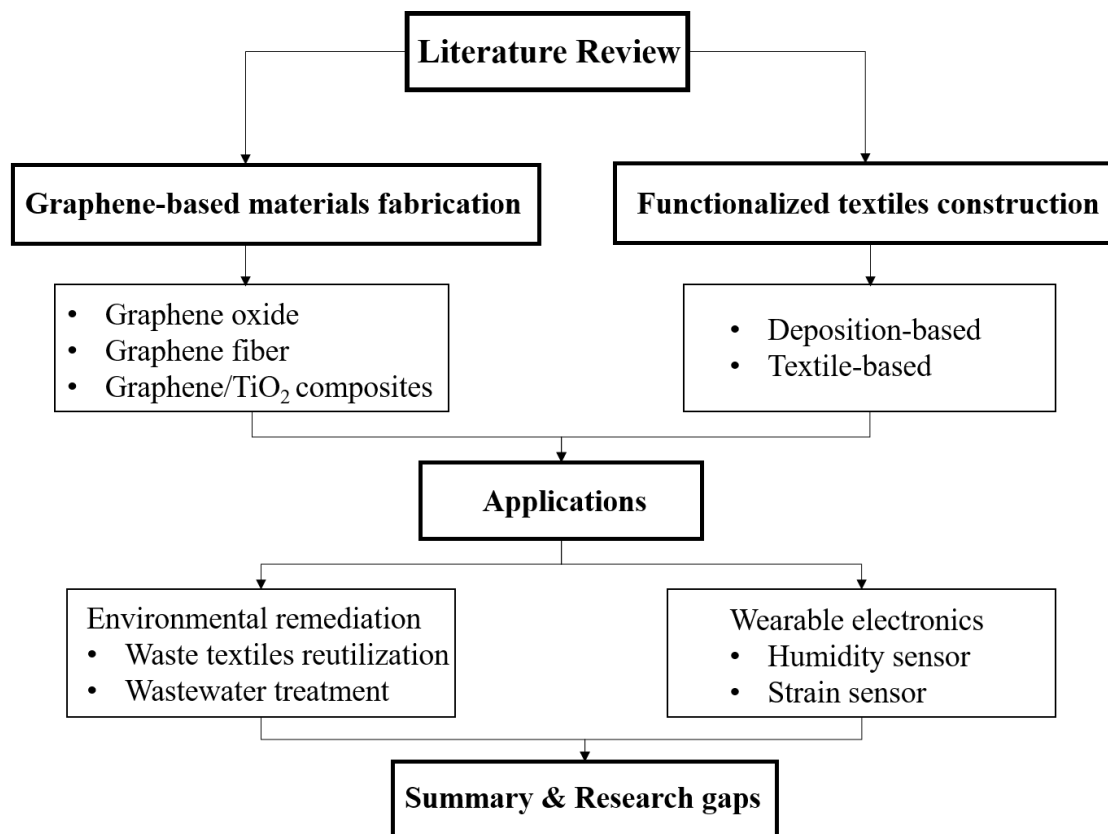


Figure 2-1. Outline of literature review.

2.2 Functional graphene-based materials

2.2.1 Fabrication of graphene oxide

Over the last decades, graphene oxide (GO) as a substrate and intermedia for various chemical transformations such as its reduction to single and multilayer graphene-like materials, has been studied in the applications of composites, sensors, biomedical and energy-related materials.²⁷ The fabrication methods for GO have been developed and modified since it was firstly introduced. In this section, we will introduce abundant knowledge about the chemical synthesizing methodologies, properties and reduction of GO.

2.2.1.1 Synthesis methods of GO

The theory of chemical synthesis of GO is originated from the addition of strong

oxidant to the graphite such as potassium perchlorate and potassium permanganate. The strong oxidizing agents destroy the conjugated structure and surficial oxygen functional groups of graphite oxide in the strong acid environment, which reduces the Van de Waal interactions among the graphene sheets and results in an improvement in dispersibility in solution. The well-dispersed graphite oxides dissolve into the single-layer graphite oxide sheets, forming the graphene oxide. Various methodologies were applied to synthesize GO, including Brodie's method, Staudenmaier's method and Hummers' method.

Brodie's method

Brodie was the forerunner to discover the abundant chemical properties of graphite and graphene, who carried out vast repetitive oxidative processes to obtain the highly oxidised GO. He adopted the potassium chlorate and nitrosonitric acid as the oxidizing agent and reactive solvent respectively and confirmed the molecular formula of graphite oxide was $C_{2.19}H_{0.8}O_{1.00}$. However, higher temperature of exfoliation and phase transition, together with more different degrees of oxidation after each oxidation step were exhibited in Brodie's method, which resulted in the mixed products of soluble graphite oxide and graphene oxide.²⁸

Staudenmaier's method

Forty years after the graphite oxide were synthesised firstly by Brodie, L. Staudenmaier overcame the disadvantage of repetitive oxidation in Brodie's method. The addition of potassium perchlorate in Staudenmaier's synthesis was divided into several steps instead of one-step addition, which led to a more oxidised graphic material. Despite that, the synthesis of GO in Brodie and Staudenmaier method generates toxic gas such as ClO_2 and has the potential risks of explosions.²⁹

Hummers' method

To avoid the exhaustion of toxic gases, Hummers and offeman employed an oxidative system of potassium permanganate and concentrated sulfuric acid for the production of

highly oxygenated graphite oxides.³⁰ In this system, Mn_2O_7 as an intermediate that enables the effective and efficient oxidation of graphite, which reduces the oxidative process to 2 days (10 days required in Brodie and Staudenmaier method) and improves the safe operational conditions.³¹ To eliminate the manganese from dispersion and achieve the higher oxidation degree, hydrogen peroxide (H_2O_2) was added in the dispersion. A following time-consuming filtration and wash treatments were carried out to purify the GO dispersions, which are the largest weakness of this method. Based on the Hummers' method, various modified methodologies had been come up to improve the synthesizing efficiency and quality of GO. For instance, Figure 2-2 shows the post treatment of GO to achieve ultra-large GO sheets by adopting phosphoric sulfuric acid compound system.³²

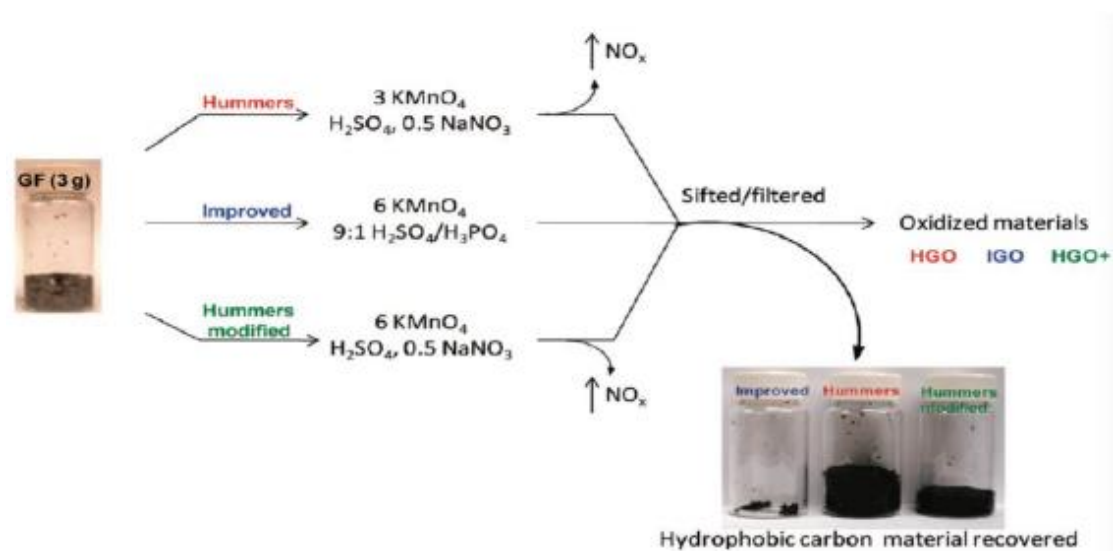


Figure 2-2. Procedure scheme for modified Hummers' method to synthesize GO.³²

2.2.1.2 The properties of GO

The interests in the structure of GO have increased due to the intriguing properties of GO. Although there is comprehensive acceptance that epoxy and hydroxyl groups are the main chemical functional groups, the accurate structure of GO has remained elusive. In the early period, the Hofmann Model only considered C-O structure while the Ruess Model contained both C-O and O-H structure. The Scholz-Boehm and Nakajima-Matsuo Model confirmed the regular periodic structure of GO.³³ However, the most

acceptable structural model was given by the Leaf-Klinowski Model and Decany Model, which differed according to the chemical oxidation process (Figure 2-3). In the Leaf-Klinowski Model, the structures of five- and six-membered-ring lactols and an occasional 2-hydroxynaphthalic anhydride or 1,3-dihydroxyx-anthone have been confirmed by experimental support.³⁴

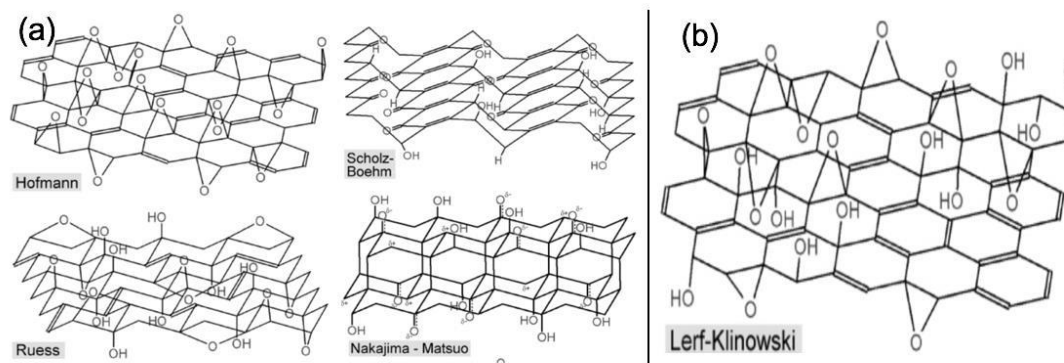


Figure 2-3. The structural models of GO. a) The four models in the early period. b) The improved Leaf model.³⁴

Mechanical properties

The original Young's Modulus and breaking strength of graphene are 1.0 TPa and 130 GPa relatively according to the tip-induced deformation experiment. By the same testing method, Gomez-Navarro found the single reduced GO sheets exhibit an unexceptionable stiffness ($E=0.25$ TPa) and a high flexibility despite their defect contents.³⁵ Schniepp tested the folding and bending properties of reduced GO through atomic force microscope (AFM). He observed that the single sheets can be reversibly folded and unfolded several times without breakage, and the folding almost appeared in the same location.³⁶

Dispersibility

After oxidation of graphene, the surface of GO contains abundant functional groups which weaken the interactions of Van der Waals force between conjugated structures of graphene. Meanwhile, there are strong solvation functions between the small solvent molecules, which makes GO well-dispersed in water and many other organic solvents.

In the experiment of Paredes, GO dispersions produced by Hummers methods has been tested in different organic solvents as shown in Figure 2-4, which shows GO has long-term stability in water, DMF, NMP and THF, and short-term stability in acetone, ethanol, DMSO and pyridine while nearly no dispersibility in dichloromethane and n-hexane.³⁷

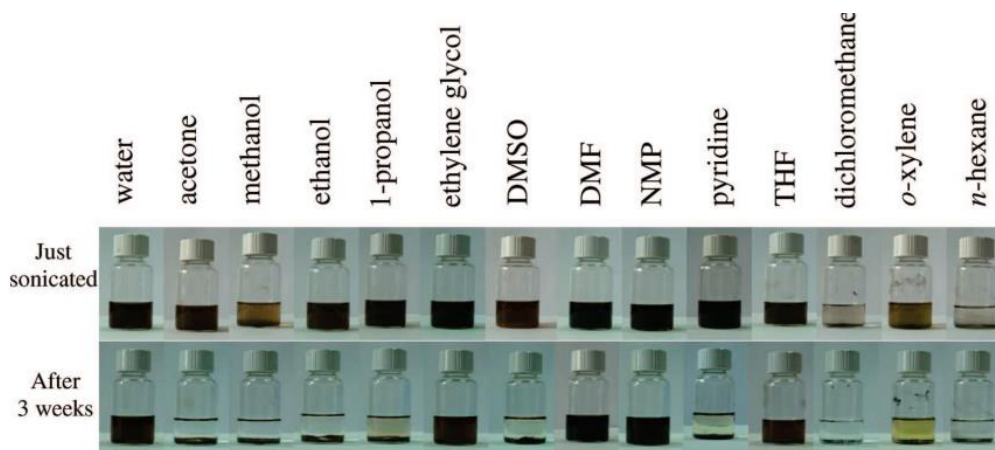


Figure 2-4. Dispersibility of GO in various solvents.³⁷

2.2.1.3 The reduction of GO

Chemical reduction

The reduction of GO by various chemical reagents is principled on their chemical reactions with GO. However, most of strong reductants have more or less reactivity with water, which creates side reactions and productions. Hydrazine monohydrate as one of the first reported reagent to reduce GO, is an attractive option for reducing GO in aqueous without reacting with solvents. The mechanism is to release a water molecule towards the formation of an aminoaziridine and go through a thermal elimination of diimide to achieve the formation of a double bond, which is *via* a direct nucleophilic attack of hydrazine on the epoxide group as shown in Figure 2-5a³⁸. Despite being widely applied in the industry as the reduction agent of GO, hydrazine has disadvantages of being highly toxic and hazardous.

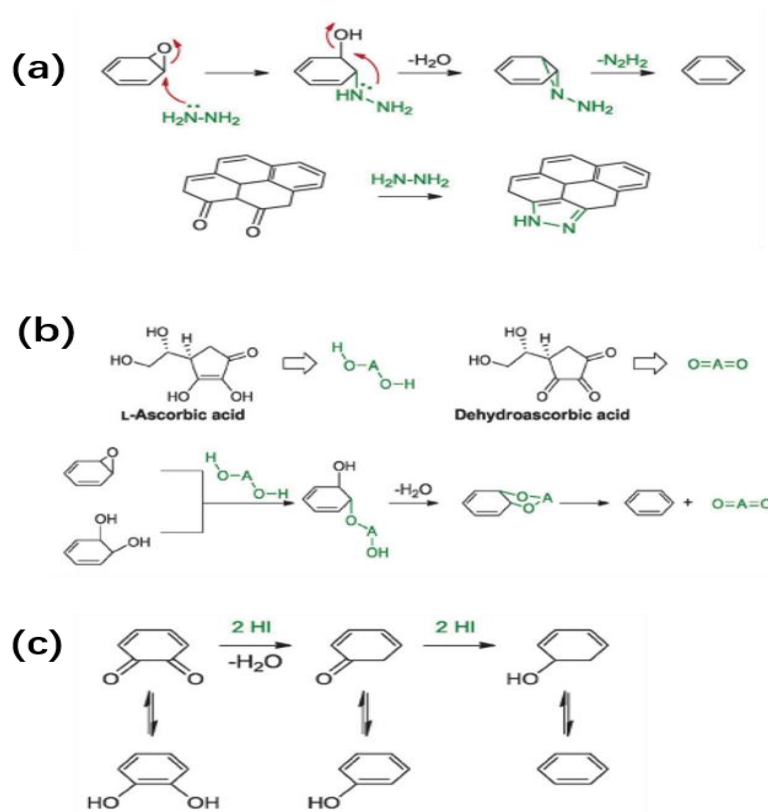


Figure 2-5. Mechanism for the chemical reduction of GO. a) Reduction of the epoxide group with hydrazine. b) Reduction of epoxide and di-hydroxyl groups with L-ascorbic acid. c) Reduction of hydroxyl and diketone groups with HI.³⁸

Ascorbic acid (Vitamin C: VC) is a nontoxic reductant which is considered to be an ideal substitute for hydrazine.³⁹ Figure 2-5b exhibits the proposed mechanism for the reduction of epoxide and di-hydroxyl groups with L-ascorbic, where L-ascorbic acid functions as a reducing agent while L-tryptophan acts as the stabilizer by adsorbing onto the resulting graphene sheet with π - π interaction.⁴⁰ Hydroiodic acid (HI) is a strong reducing reagent which was reported for the reduction of GO in the recent years, which has the advantages of reducing GO in various forms including colloid, powder and film in the gas, solution or even room-temperature environment.⁴¹ The reduction mechanism in Figure 2-5c includes the iodination of alcohols, cleavage of ether and reduction of aromatic iodides.⁴²

Thermal reduction

The rapid thermal annealing was regularly used to exfoliate graphite oxide to obtain graphene in the initial stage. Once the temperature of graphite oxide increases rapidly, the oxygen-containing functional groups on the carbon plane decompose into gases (e.g. CO and CO₂). The sudden expansion of these gases creates large pressure (40 MPa at 300°C) between the stacked layers, which is enough (2.5 MPa is required) to separate two stacked GO platelets.⁴³ Moreover, the decomposition of oxygen-containing groups at elevated temperature not only realizes the exfoliation of graphite oxide but also achieves the reduction to graphene. Even though thermal annealing to obtain graphene is highly effective, it also has drawbacks such as huge energy consumption and critical temperature control (e.g. heating time and increasing speed of temperature). Another limitation is that thermal reduction is not applicable for the GO coated substrates with a low melting-point such as polymers.

2.2.2 Fabrication of graphene fibres

Graphene fibre, as a fibrous material made of individual units of graphene and its derivatives, was first fabricated via wet spinning from graphene oxide liquid crystals by Gao and Xu in 2011.⁴⁴ From then on, graphene fibres have been largely applied into fields of smart electronic fibrous devices and textiles due to their extreme mechanical and electrical properties. Figure 2-6a shows the evolution of carbonaceous fibre (carbon filaments, carbon fibres, CNT fibres and graphene fibres).⁴⁵ Figure 2-6b summarizes the increasing annual publications and citations since 2011. The growing interest in graphene fibres has led research to high-performance and hierarchical structure for multiple functions. The significant research outcomes of graphene fibres in mechanical properties, electrical and thermal conductivity are exhibited in Figure 2-6c.⁴⁶

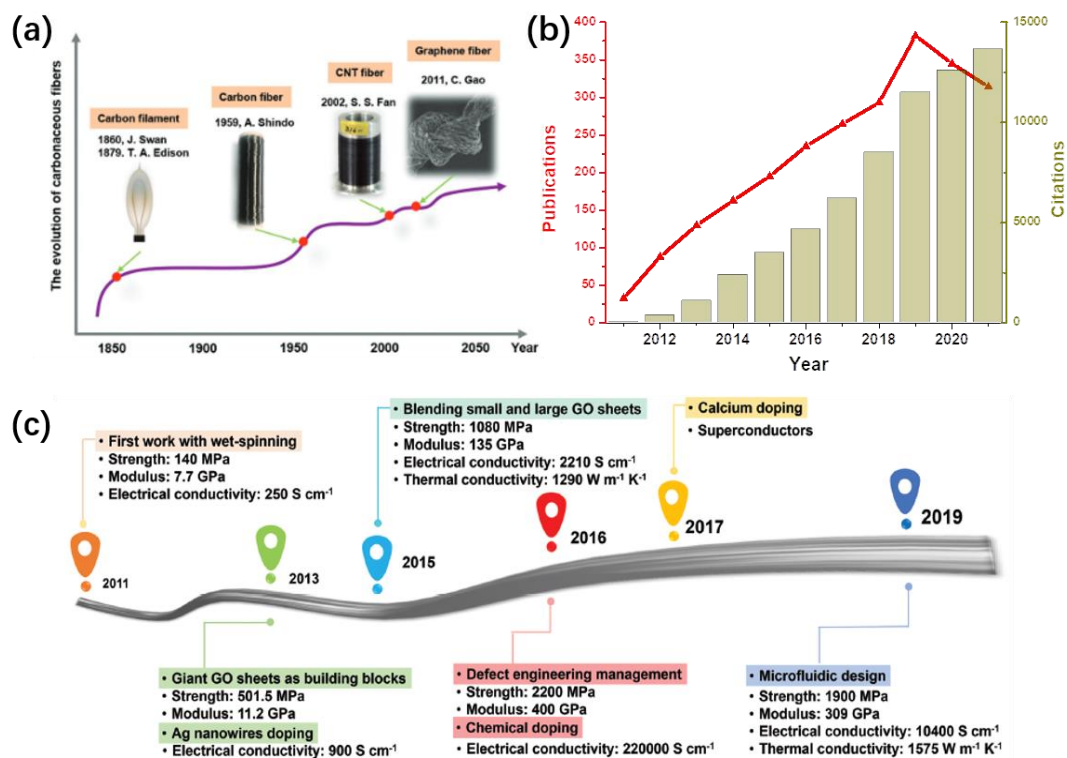


Figure 2-6. Development of graphene fibres. a) the evolution of carbonaceous fibres.⁴⁵ b) The annual publication and citation reports from Web of Science. c) Significant outcomes of graphene fibres since 2011.⁴⁶

2.2.2.1 Fabrication methods of GF

Wet-spinning method

The wet-spinning process of graphene oxide fibres (GOF) is based on the phase transformation from ordered fluids to ordered solids, which includes GO sheets alignment in spinning channel, solvent exchange in the coagulation bath and post-drafting between spinning rollers. As shown in Figure 2-7, there are three steps comprised in the phase transformation process as followed:^{24, 46}

- **Step 1:** The uniaxial shear flow in the spinning pipe induces the unidirectional alignment of GO sheets and homogenizes orientational orderings of GO sheets.
- **Step 2:** The solvents exchanging between GO dopes and coagulation bath generates the phase transformation from fluids GO to gel-state GO. The solvated GO interconnects to each other to form the gel fibres.

- **Step 3:** The GO fibres are dried after removed from coagulation bath, leading to shrinkage of GOF and formation of typical wrinkled surface.

The SEM images in Figure 2-7 exhibits the wrinkled surface and orientational orderings in the cross-section of the GOF, as well as the good weavability to construct a fabric.^{44,}

47

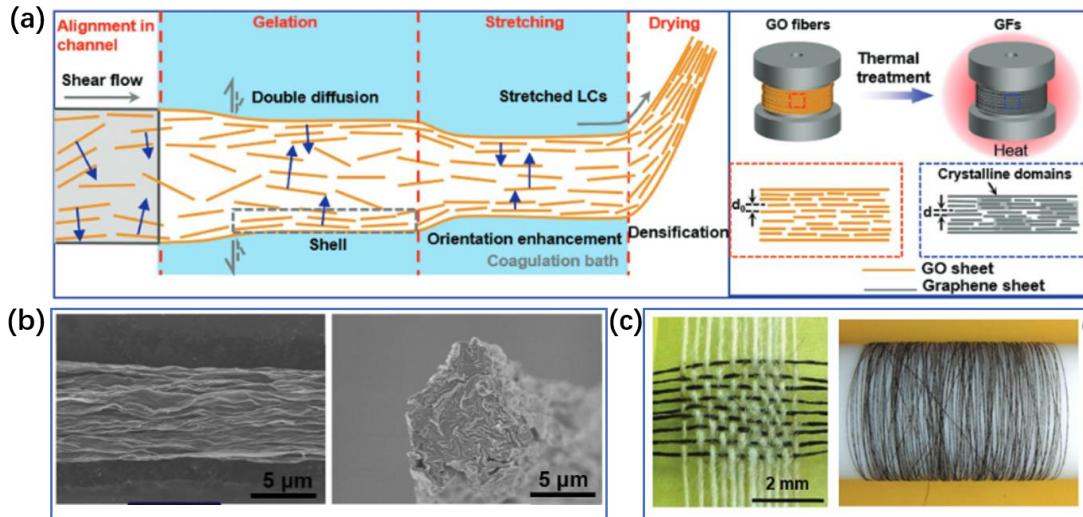


Figure 2-7. Wet-spinning fabrication of GF. a) The schematic of the evolution of GOF during wet spinning.⁴⁶ b) The SEM images of the surface and cross-section of a GF⁴⁷. c) A GF-based fabric with good weavability.⁴⁴

Some crucial factors need to be controlled to fabricate the high-quality continuous GOF, which are the quality of GO dope, the choices of spinning nozzles, coagulation baths and post treatment.⁴⁸ The performances of the obtained GOF are influenced by:

- **Spinning GO dopes:** The deaeration, filtration and centrifugation of GO dispersion are important to achieve high-performance GOF. For example, the continuous fabrication of gel fibres will be interrupted if the air in the GO dopes is not completely removed. The uniform size distribution of GO sheets is desirable, which is realised by adjusting the centrifugation speed.
- **Spinning nozzle:** The size of spinning nozzle for wet spinning is normally between 60 and 250 μm. The selection of spinning nozzle is depended on the concentration of GO, a smaller diameter and compact microstructure of GOF are formed by using a finer spinning nozzle.

- **Coagulation bath:** The solvent exchanging process between GO dopes and agents in bath promotes the curing of the gel fibres. The salt solutions (e.g. CaCl_2) and organic baths (e.g., acetone and ethyl acetate) are regularly selected for coagulation bath solvents. The metal ions (such as Ca^{2+}) in coagulation bath generates a cross-linking network between adjacent GO sheets for the enhancement of solidification of GOF.
- **Post treatment:** The post-stretching treatment before the GOF is completely dry is beneficial to straighten and flatten the wrinkled GO sheets.

The achieved GOF is hydrophilic and non-conductive due to the hydrophilic functional groups and defects in GO sheets. In order to increase the conductivity of GOF, additional reduced process is always accompanied to reduce GOF to GF. The reduction methods have been presented in Chapter 2.2.1.3.

Other methods

Unlike the constructions of cross-linking network between adjacent GO sheets in the coagulation bath, the drying-spinning approach to fabricate continuous GF is widely applied by directly extruding GO from a dry-spun spinneret and shaping GO into fibres without coagulations baths, which results in a poor mechanical strength of the dry-spun GF due to the existence of core-shell structures. To enhance the mechanical strength for the formation of self-standing GO fibrous dopes, a higher concentration of GO dopes (normally larger than 8 mg/ml) is required to form the viscoelastic gel-like GO fibres with high elastic modulus.⁴⁹ Figure 2-8 shows the fabrication of GOF by rolling and stretching of graphene nanoscroll belts, and drawing and twisting of continuous GO belts respectively.^{22, 50} The obtained GF with twisted structure exhibits high toughness and favourable flexibility.

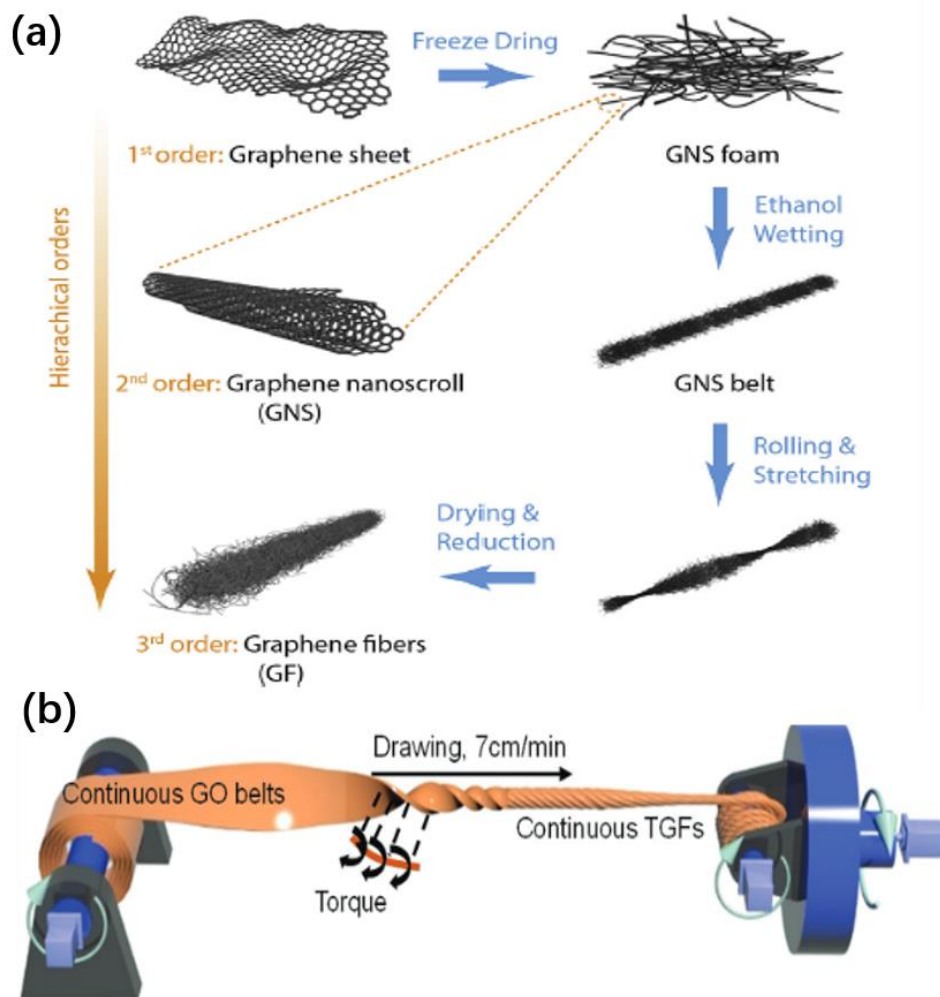


Figure 2-8. Dry-spinning fabrication of GOF. a) Rolling and stretching of graphene nanoscroll belts to obtain GF.²² b) Drawing and twisting of continuous GO belts to obtain continuous GF.⁵⁰

The chemical vapour deposition (CVD) method was frequently applied in growing single-layered or few-layered graphene films. This simple and rational approach has been extended to self-assemble porous and flexible GF from CVD-grown films.⁵¹ The as-prepared GF exhibits high conductivity and uniform pore distribution even without further reduction or purification. Recently, Choi et al. introduced an innovative design to deposit the CVD-grown shell on the surface of rGO fibres to fabricate a multifunctional rGO-CVD-graphene core-shell fibre, which shows outstanding electrical conductivity (137 S/cm) and failure strain (21%).⁵²

2.2.2.2 Properties of GF

Mechanical properties

Axial orientation & Radial alignment: The orientation and alignment of graphene sheets in the axial and radial directions are crucial for the mechanical strength and conductivity of the GF. The flow control of GO, selection of coagulation bath and post-stretching in the wet-spinning process can optimize the axial orientation of graphene sheets. Generally, a contracted spinning channel and strong post-stretching treatment will limit the expansion of the GO fluids and achieve the regular alignment of graphene in GF.⁵³ Figure 2-9a exhibits the structural analysis of graphene sheets from the macroscale to an atomic scale after a post-stretching treatment to GF, which show an improved orientation degree (up to 81%) and enhanced tensile strength (2.2 GPa).⁵⁴ The distortion of the GO sheets during the chemical assembly will generate the disorders of GO sheets alignment in the radial direction. To eliminate the disorders of radial alignment, Xin et al. selected a unique flat channel to perfectly match the GO sheets and the inner wall of the channel (Figure 2-9b), which optimised the orientation degree and improve the GF's tensile strength.⁵³

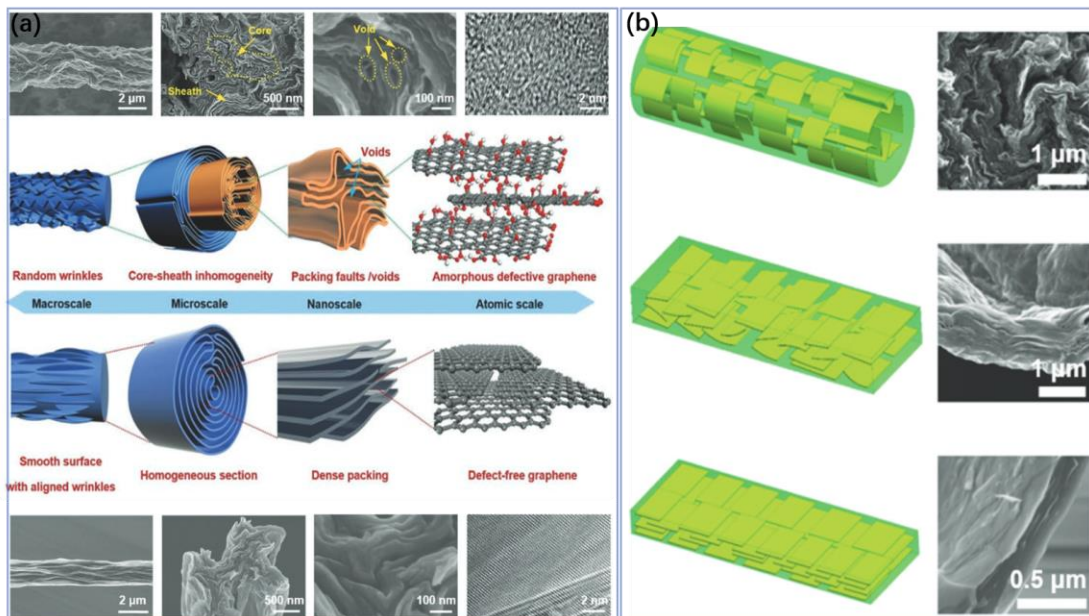


Figure 2-9. Sheet axial orientation and radial alignment of GF. a) The structure analysis of axial orientation with and without defect management.⁵⁴ b) Illustration of sheet alignments and their corresponding cross-sectional structure of GF by SEM.⁵³

Interlayer interactions: Hydrogen bonds, coordinative cross-linking and Van der Waals interactions are the three leading interactions which exist in the interlayers of GOF and GF.⁴⁷ Before reduction, the as-spun GOF contains abundant hydrogen bonds between the oxygen-containing groups which dominantly determine its mechanical strength. After chemical or thermal reduction, the GOF is converted into reduced GOF by removing the oxygen-containing functional groups, while the coordinative cross-linking and Van der Waals interactions dominate in the mechanical strength of GF at this stage. The cross-linking and Van der Waals interactions between adjacent graphene sheets can be enhanced by the introduction of Ca^{2+} and polymers guests.⁵⁵

Crystallite size: The high-temperature carbonisation will generate crystallite graphite domains in the graphene-based substrates. However, the small crystallite domain sizes bring about abundant scattering centres and grain boundaries, which will reduce the transport properties and mechanical modulus respectively. To increase the crystallite domain sizes of GF, Xu et al. used the giant GO sheets to fabricate GF. The larger-sized GO sheets enable the graphitisation temperature to increase from 1300 to 3000°C. The highly graphitised GF shows an increased mechanical strength and modulus.⁵⁴

Electrical properties

The mobility of an ideal graphene can reach as high as $200000 \text{ cm}^2 \text{ V}^{-1} \text{ s}^{-1}$. Even though the orientation and alignment adjustments of graphene sheets can optimize the electron transports in the GF, while there are still large performance gaps in electron transport between neat GF and ideal graphene. The deteriorated transporting properties arise from the structural defects (e.g., oxygen-containing groups and lattice vacancies), which form the electron-scatter centre and hinder the electrons transporting straightly along the axial direction. The high-temperature graphitisation treatment eliminates the residual functional groups and lattice defects, which also has negative influence in blocking the transport of electrons between graphene interlayers.⁵⁶ To improve the electrical ability of GF, Gao and his co-workers doped silver nanowires into GO, the

obtained silver-doped GF exhibited an improved electrical conductivity of 9×10^4 S/m.⁵⁷ Table 2-1 summarizes the performance of previously reported GF by various derivative methods from wet spinning, which includes various doping methods and thermal treatments at different temperatures. It is obvious that the high-temperature graphitisation improves the electrical conductivity of GF, however, this requires accurate temperature control and high energy consumption. The theory of thermal treatment has been introduced in Chapter 2.2.1.3. The purpose of nanometal doping is to improve the electrical conductivity of GF under a lower temperature treatment, while the nanometal will have a negative effect on the GO alignment and decrease the mechanical properties of GF.

Table 2-1. The performance of GFs associated with their preparation methods.

Study	Method	Treatment temperature (k)	Strength (MPa)	Electrical conductivity (S/m)
Xu et al (2011) ⁴⁴	Neat wet spinning	353 in HI	140	2.5×10^4
Cong et al (2012) ²⁰	Neat wet spinning	353 in HI	182	3.5×10^3
Dong et al (2012) ⁵⁸	Hydrothermal	1073 in vacuum	420	1.0×10^3
Xu et al (2013) ⁵⁷	Ag doping	363 in HI or VC	360	9.1×10^4
Xu et al (2013) ⁵⁹	Giant GO sheets	353 in HI	501.5	4.1×10^4
Liu et al (2016) ⁶⁰	K doping	3273 in Ar	N/A	2.24×10^7
Ma et al (2018) ⁶¹	Interface reinforcement	1473 in Ar	724	6.6×10^4
Li et al (2020) ²⁶	Plasticisation spinning	3073 In Ar	3400	1.19×10^6

2.2.3 Fabrication of graphene-TiO₂ composites

It is well-known that water pollution problems have become increasing severe all over the world. Organic pollutant is regarded as one of the most common pollutants in water, which take up over 50% of whole water pollutants and have huge negative influences on water contamination. Human activities are the main reasons for the water contamination, which create plenty of industrial, agricultural and domestic wastes. Industry related with pigments, plastics, synthetic rubber, synthetic fibres, pesticide and pharmaceuticals are the main target of organic pollutants creations.⁶² These hazardous

pollutants in water are harmful to both human and aquatic life which could breed diseases and threaten the ecosystem.

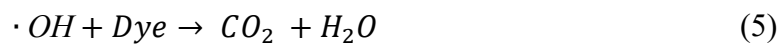
To solve the water contamination, photocatalysis technology was first applied for the serious situation in the late 1960s. Compared with other methods for water treatments such as adsorption, membranes, chemical oxidation and biological treatment, photocatalytic treatment has the superiority in efficient, simple and environmentally-friendly processes without secondary pollutants created.⁶³ Among the various semiconductor photocatalysts, TiO₂ has proved to be the most reliable and broadly used photocatalysts because of its chemical and biological inertness, low cost, non-toxicity and long-term stability.⁶⁴ However, the flash recombination rate of electron-hole pairs and low adsorption in the visible range of the solar spectrum restrict the performance of TiO₂ photocatalysts. There are still more efforts to take for improving the photocatalytic activity of TiO₂.

Recently, in order to overcome the disadvantages of pure TiO₂ photocatalytic performance, TiO₂-graphene composites are prepared and functioned in the water contamination treatment. However, the synthesis process of graphene-TiO₂ composites is complicated. The overall photocatalytic performance has not been improved too much since the TiO₂ particles do not spread homogeneously in the graphene-TiO₂ composites. Moreover, it is hard to synthesize well-dispersed graphene-TiO₂ composites, hence, the composites cannot be settled in polluted water homogeneously, which will affect the overall performance of photocatalytic activity. As a result, graphene-TiO₂ composite should be modified into a satisfied shape to enhance its photocatalytic performance for water contamination treatment.

2.2.3.1 Photocatalytic activity of pristine TiO₂

Theory and mechanism

The greatest function of heterogeneous photocatalysts is to provide certain potential for converting photon energy into chemical energy. When a certain semiconductor (i.e. TiO₂) is irradiated by a photon existing in visible or ultra-violet (UV) light, if the energy of the photon is corresponding to the band gap energy of TiO₂, electrons will be excited from the valence band (VB) into the conduction band (CB). During this process, the electron-hole pairs are generated which are responsible for the photocatalytic activity. The mechanism and equation of photocatalytic process are followed as: when TiO₂ catalyst particle is irradiated by UV radiation, electrons are promoted from the VB to CB and the electron-hole pair is generated in the meantime (equation 1). In most cases, hydroxyl radical ($\cdot OH$) are generated easily under the reaction by h_{VB}^+ and surface bound of H₂O, while superoxide radical anion of oxygen ($\cdot O_2^-$) are produced by the reaction of e_{CB}^- (equation 2 and 3). These two reactions ensure the chance to stop the recombination of the electron and hole excited in the first step. The generated $\cdot OH$ and $\cdot O_2^-$ are able to react with the organic contaminations (e.g. dyes) to generate the corresponding oxidation and reduction products, resulting in the photodegradation of organic dyes (equations 4-6).⁶⁵



Where e_{CB}^- and h_{VB}^+ are the electrons in the CB and the electron vacancy in the VB respectively.

Limitations in TiO₂

Although TiO₂ provides reliable photocatalytic ability among various semiconductor photocatalysts, the flash recombination of photo-generated electrons and holes still restricts its performance. The recombination time for the photo-generated electron-hole pairs is in the magnitudes of 10⁻⁹ s, whereas the chemical reaction time of TiO₂ is in the

range of 10^{-8} to 10^{-3} s.^{65, 66} As a result, the electron and hole always recombine before they could take effect in the chemical reaction. Another limitation which affects the solar photoconversion efficiency of TiO_2 is the low absorbance of visible light. The anatase and rutile are the two common phases in TiO_2 with corresponding band gaps of 3.2 eV and 3.0 eV respectively, which means the wavelength of excited irradiation should be below 380 nm (UV-light). Unfortunately, such low-wavelength sunlight only makes up only 5% of the total solar spectrum.⁶⁷ Therefore, making full advantages of solar light energy and hindering the rapid recombination of photogenerated electron-hole pairs will largely contribute to the enhancement of the photocatalytic performance of TiO_2 .

2.2.3.2 Photocatalytic activity of graphene- TiO_2 composites

Based on the limitations of TiO_2 , several treatments have been developed to enhance its photocatalytic performance. In 2003, Kimberly et al. put forward a method using a mixed-phase TiO_2 , within which the morphology of nanoclusters contains small rutile crystallites interwoven with anatase crystallites. As a result, the transition points between these two phases ensure a rapid electron transfer from rutile to anatase, leading to an enhancement of its photocatalytic performance.⁶⁸ In 2014, Tang et al. introduced a method that created a $\text{TiO}_2\text{-Fe}_2\text{O}_3$ nanocomposite to enhance the charge separation and photocatalytic activity. A co-catalysts Fe_2O_3 nanoparticle was deposited on the surface of TiO_2 due to its stability, earth-abundant and matched band position with TiO_2 . This bi-functional surface catalyst could catalyse the two-electron reduction of dioxygen and render the transfer of electrons from parent photocatalyst to oxygen more efficiently, resulting in enhancing the photocatalytic performance of parent TiO_2 photocatalyst.⁶⁹

However, the most effective ways to enhance the performance of TiO_2 is to ally with other superior materials. Graphene has superior properties in fast electron transporting, large specific surface area, more transparency and high adsorption capacity, which is believed to be the key supporters.^{21, 70} The incorporation of graphene onto TiO_2

photocatalysts offers the opportunity to enhance the photocatalytic properties in the following aspects: 1) enhanced adsorption of contaminants, 2) rapid charge transportation and separation, and 3) extended light adsorption range.

Synthesis of graphene-TiO₂ composite

The combination of graphene and TiO₂ nanoparticles has been studied deeply for the enhancement of photocatalytic activity. Generally, the synthesis of graphene-TiO₂ composites can be divided into an in-situ growth and reduction process. The direct interaction between graphene and TiO₂ nanoparticles has a negative effect on restacking and aggregation of exfoliated graphene sheets. Hence, Zhang et al. introduced a sol-gel method to synthesize graphene-TiO₂ with raw materials of tetrabutyl titanate and GO. The reduction process was achieved by using sodium borohydride.⁷¹ In Zhou's paper, an one-pot solvothermal reaction was used to prepare graphene/TiO₂ composite with the same raw materials. But the reduction of GO into graphene and formation of TiO₂ nanoparticles on the graphene surface took place simultaneously.⁷² Reduction of GO under solvothermal conditions was proved to be more effective in decreasing oxygen and defect levels compared with employment of other strong reductants. There are also some other methods for the synthesis of graphene/TiO₂ nanocomposites, such as hydrothermal route,⁷³ electrospinning,⁷⁴ in-situ growth⁷⁵ and microwave-assisted methods.⁷⁶

Photocatalytic performance

The graphene content in the composite has significant effects on the photocatalytic performance of the graphene-TiO₂ nanocomposites. Excessive graphene content in the composite gives the tendency of collision between holes and electrons, which accelerates the recombination of photogenerated electron-hole pairs. Furthermore, the over-loaded graphene exhibits intense light adsorption. This causes the light-harvesting competition between graphene and TiO₂, and finally reduces the photocatalytic performance. Table 2-2 summarizes the photocatalytic activity enhancement of graphene-TiO₂ composites. It shows that the structure of graphene-TiO₂ composites and

contents of graphene in composites have influences on the photocatalytic efficiency. The graphene content increase is not always linear with the photocatalytic enhancement. Especially in graphene-rich composites, the enhance in photocatalytic ability becomes unobvious or even decreased. The appropriate amount of graphene provides an alternative path for electrons transportation which improves the photocatalytic activity by prolonging the lifetime of electron/hole pairs, while the excess GO will cause blockage between TiO₂ and sunlight. However, the mechanisms are yet to be clarified.

Table 2-2. Photocatalytic performance of graphene-based TiO₂ composite materials

Type	Structure	Graphene content	Evaluation	Illumination	Enhancement (UV/Vis)
Graphene/ TiO ₂ ⁷⁴	1-D rice-shaped TiO ₂ mesostructures with single crystallinity	0.75 wt%	DP of MO	UV or Vis; 125W Hg lamp	1.5/2.0
Graphene/ TiO ₂ ⁷⁷	--	1.0 wt%	DP of MP	UV or Vis; 500W Xe arc lamp	1.46/2.41
Graphene/ TiO ₂ ⁷⁸	Graphene-wrapped anatase TiO ₂ composites	2.0 wt%	K (MB degradation)	Vis: >420; 450W Xe lamp	--/12.9
Graphene/ TiO ₂ ⁷¹	--	5 wt%	H ₂ evolution rate	UV/Vis	1.9/1.9
Graphene/ TiO ₂ ⁷⁹	TiO ₂ nanocrystals coated on graphene	10 wt%	K (RhB degradation)	UV	4/--
Graphene/ TiO ₂ ⁷⁹	Be dispersed in water	75 wt%	DP of MP	UV; 4 UV lamps (6W each)	1.4/--
GO/P25 ₂₅	--	10 wt%	DP of MB	UV or Vis	8.52/7.15
Graphene/ P25 ²³	P25 nanoparticle loaded on graphene nanosheet	1.0 wt%	DP of MB	UV; 100W Hg lamp or Vis: >400	1.21/1.18
Graphene/ P25 ⁸⁰	--	5 wt%	DP of MB	UV: 365 or Vis: >400	1.44/2.36
Graphene/ P25 ⁸¹	P25 spread on the graphene sheet	20 wt%	H ₂ evolution rate	UV/Vis; 200W Xe arc lamp	10.9/10.9

Note: DP = degradation percentage; K = apparent rate constant; RhB = rhodamine B; MO = methyl orange; MB = methyl blue.

2.2.4 Summary

In this section, we have introduced various fabrication methods and properties of graphene-based materials including graphene oxide, graphene fibre and graphene/TiO₂ composites. The modified hummers' method to synthesize GO has been widely studied and developed by many researchers, however, the techniques to fabricate GO sheets with adjustable layers and sizes still leave vacancies. The important parameters in wet spinning of GF are spinning GO dopes, spinning nozzle and coagulation bath, which determine the performance of as-prepared GF. There are challenges in the GO sheets alignments and hierarchical surface structure modification to boost the mechanical strength and flexibility of GF. Even though functional nanoparticles such as TiO₂ have been widely integrated with graphene to construct functional graphene/TiO₂ composites, especially for applications in photodegradation, the photodegradation efficiency still desiderates to be enhanced.

2.3 Functionalised graphene-based textiles fabrication

The extraordinary properties of graphene-based materials in mechanical strength, thermal and electrical transporting, adsorbing affinity and photocatalytic degradation enable them to play important roles in next-generation smart electronic fibrous devices and textiles.^{26, 46} Here, I introduce several deposition-based and textile-based techniques to simply assemble the high-performance graphene-based materials into functionalised textiles for their optimised applications in environmental remediation and wearable electronics.

2.3.1 Deposition-based techniques

Graphene oxide as a possible intermediate for the chemical synthesis of functionalised graphene, can be easily dispersed into water or other organic solvent, which exhibits different but valuable properties compared with graphene. The hydrophilic functional

groups such as hydroxyl groups and carboxyl groups in graphene oxide give it possibility to be dispersed in solvent and coated into various fabrics to fabricate sensors with various applications.

Dip coating

Dip coating could be seen as one of the most common, conventional and easy-handled ways to fabricate graphene-based textiles and sensors. Firstly, dipping fabric into a certain concentration of GO at room temperature and then drying the fabric with higher temperature (60-90°C). For a better adsorption and coating quality of GO, this process could be repeated for 3 or 4 cycles. The coating mechanism is due to the Van der Waals forces between exfoliated GO and fabric fibre surface. Mohammad et al. reported a GO-coated cotton fabrics *via* dip coating method with the electrical resistivity ranging from 10^3 to 10^6 K Ω cm⁻¹.⁸² Sun et al. reported a reduced GO films by dip coating techniques with optical transmittance as high as 81% and sheet resistance of 60 K Ω sq⁻¹.

1.83

Screen-printing

Screen-printing are considered as the most efficient, low-cost and large-scale production technologies in textile dyeing and finishing. One of the advantages using screen-printing is the tunable penetration depth on textile substrates, which could be favourable for e-textile systems as limited contact of active components with human skin. The other advantage is the pattern being repeatedly positioned at the same location over human body during screen-printing process, which improves accuracy of sensing and effective use of active materials.⁸⁴

During screen-printing process, the negative charges on GO will contribute to the formation of a stable GO dispersion in water and provide its interaction with hydroxyl groups on cellulose-based fabric surface. The cross-linking and strong bonding between GO and fibre substrate ensure the good electrical properties in flexible electronics. Qu et al. reported a screen-printing of GO patterns onto viscose nonwovens with tunable

penetration depth and electrical conductivity and schematic diagram of the fabrication process shown in Figure 2-10. The printed nonwovens show lower sheet resistances ranging from 1.2 to 6.8 $\text{K}\Omega \text{sq}^{-1}$ at a comparable loading.⁸⁵

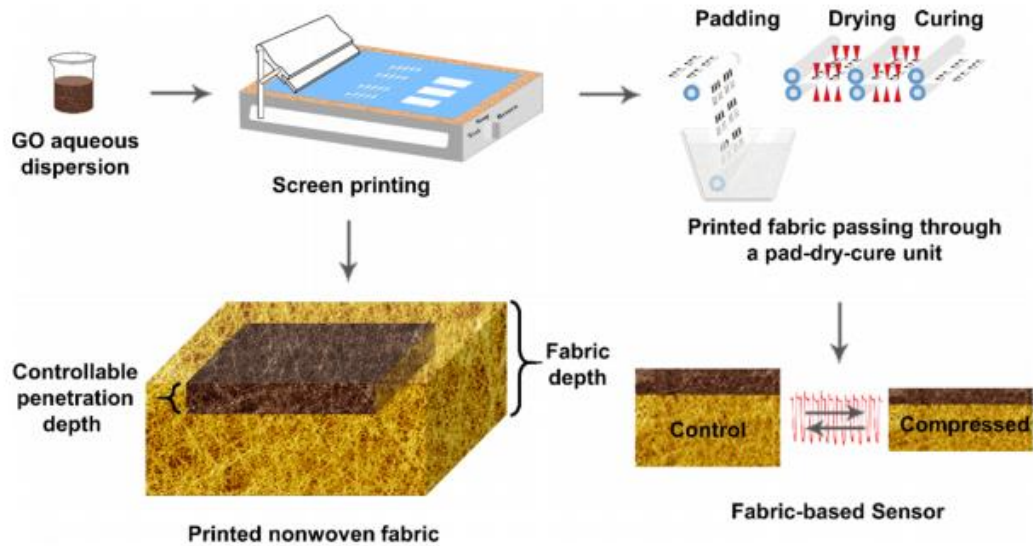


Figure 2-10. Schematic diagram of the tunable penetration screen-printing fabrication.

85

Inkjet-printing

Inkjet printing is considered as a promising technique to fabricate flexible electronics with extraordinary electronic, optical and mechanical properties. For e-textile fabrication, inkjet printing technique have several advantages compared with conventional techniques such as the ability to deposit controlled quantities of materials at precise location when weaving of conductive yarn and a reduction in material wastes. Nazmul et al. reported an inkjet-printed graphene-based conductive patterns for wearable e-textile applications and the schematic diagram is shown in Figure 2-11.⁸⁶ There is an organic nanoparticle-based surface pre-treatment onto textile before inkjet printing to enable all inkjet-printed graphene e-textiles. The organic nanoparticles function as a hydrophobic breathable coating on textiles. Under this method, the sheet resistance could be reduced from 1.09×10^6 to $2.14 \times 10^3 \Omega \text{sq}^{-1}$ compared with untreated textiles.

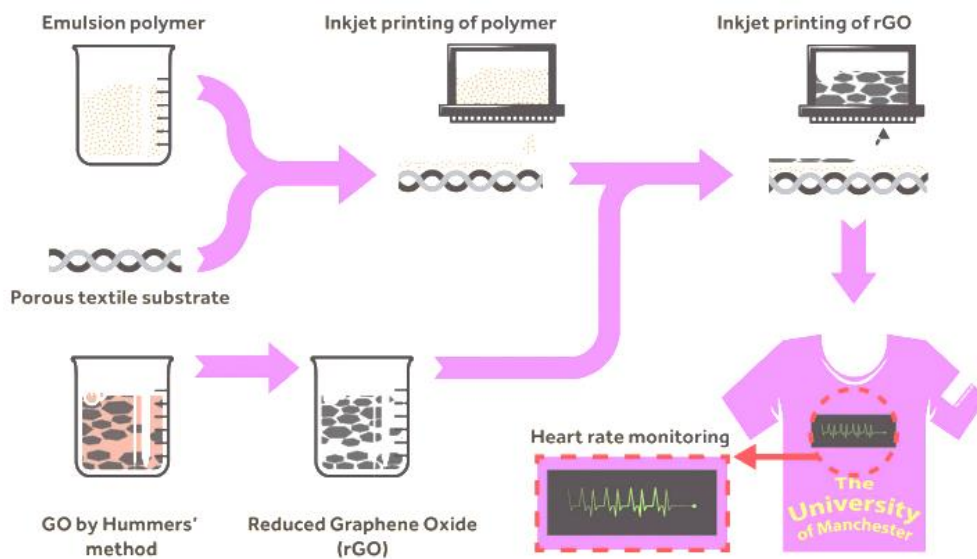


Figure 2-11. Schematic diagram of the all inkjet-printed graphene e-textile manufacturing process.⁸⁶

Pad-dyeing

Pad dyeing is an efficient, convenient and low-cost fabrication method for the mass production of graphene-based flexible textiles. It applies high pressure between spinning rollers to squeeze the GO sheets both on the surface and into the inner fabrics. Sequential heating process keeps the cross-linking of the fibre surface and GO sheets. Xu et al. reported a moisture-resilient strain sensor with GO-pad-dyed wool fabric (Figure 2-12). The strain sensor has a linear electromechanical response (relative resistance change of 65% accompanied by elongation up to 22%) and maintains stable performance after 5000 stretching-releasing cycles. Meanwhile, the sheet resistance of rGO/wool-knitted fabric could reach $12.3 \text{ K}\Omega \text{ sq}^{-1}$.⁵

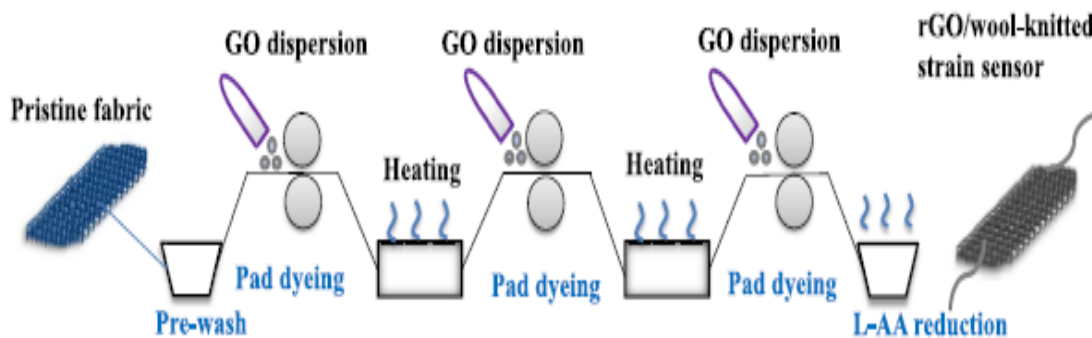


Figure 2-12. Schematic diagram of the fabrication of pad-dyed graphene-based strain sensor.⁵

Electroless deposition

Conductive textiles also can be achieved by depositing a thin layer of metals (e.g., Cu, Ag or Ni) onto the textile surface by electrochemical deposition or electroless deposition (ELD). ELD is more attractive because it is simply equipped and massively productive under ambient conditions.⁸⁷ The key to form strong bonding between metal and textile surface is to construct a copolymer layer on the textile surface. After deposition of metal, graphene can be deposited on the top layer of textiles to enhance its electrical performance. Zheng et al. fabricated a scalable graphene-metallic textile composite electrode with remarkable energy density (6.1 mWh cm^{-3}) and power density (1400 mW cm^{-3}) by ELD (Figure 2-13).⁹ The conductive yarns and textiles fabricated *via* ELD are ideal energy-storage devices for next-generation flexible and portable electronics.

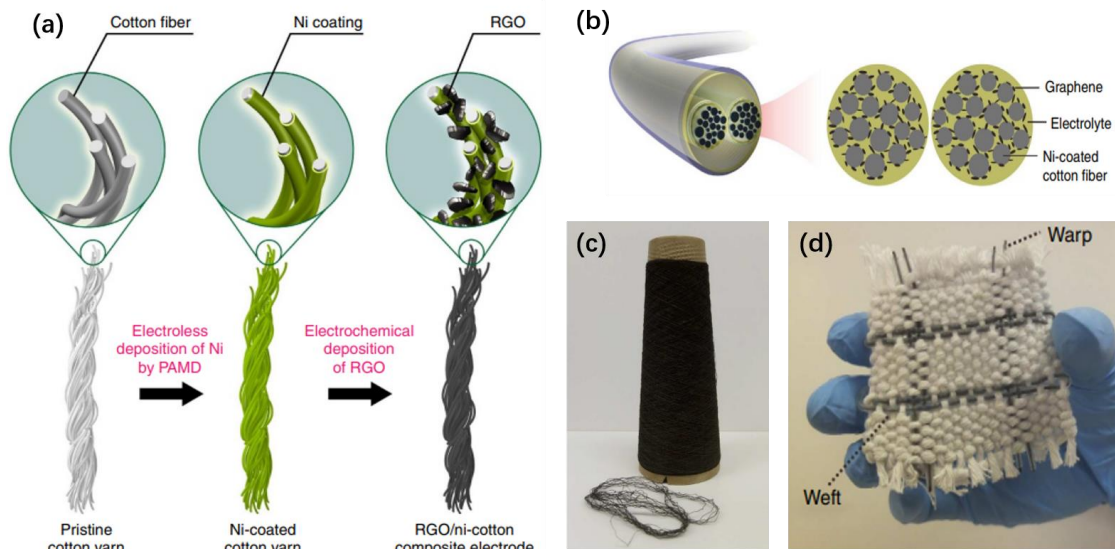


Figure 2-13. Fabrication of graphene-metallic textiles by ELD.⁹ a) Schematic illustration of fabrication. b) Illustration of structure of the functionalised yarns. c) Image of functionalised yarns. d) Woven fabric made of functionalised yarns.

2.3.2 Textile-based techniques

The graphene-deposited or graphene-coated yarns and fabrics can be directly constructed into wearable devices without any further assemblies. For example, the graphene-functionalised knitted wool fabrics fabricated by Xu et al. were able to function as strain sensors due to the contact-separation movements of conductive yarns by applying forces.⁵ However, in most circumstances, the functionalised yarns and fabrics need to be assembled into flexible electronics *via* textile-based techniques such as embroidery,⁸⁸ weaving,⁸⁹ knitting⁹⁰ and spinning³ methods. These simple, scalable and efficient technologies enable the flexible electronics to work in highly effective, accurate and stable manners.

Embroidery

Conductive yarns are able to be seamlessly integrated into fabric by stitches through a computerised embroidery machine. The most attractive advantages of machine embroidering are the freedom of circuit design and ease of fabrication. Liu et al.

designed a high-performance strain sensor by embroidery technique, where flexible Lycra yarn were served as warp yarns (in X direction) and conductive copper deposited viscose yarn were served as warp yarns (in Y direction as shown in Figure 2-14c).² The integrated fabric sensor shows remarkable sensitivity to strain in Y direction. However, the needle yarn is subjected to high tension during the high-speed embroidering, which potentially peels off the conductive coating layers or even break the needle yarn.

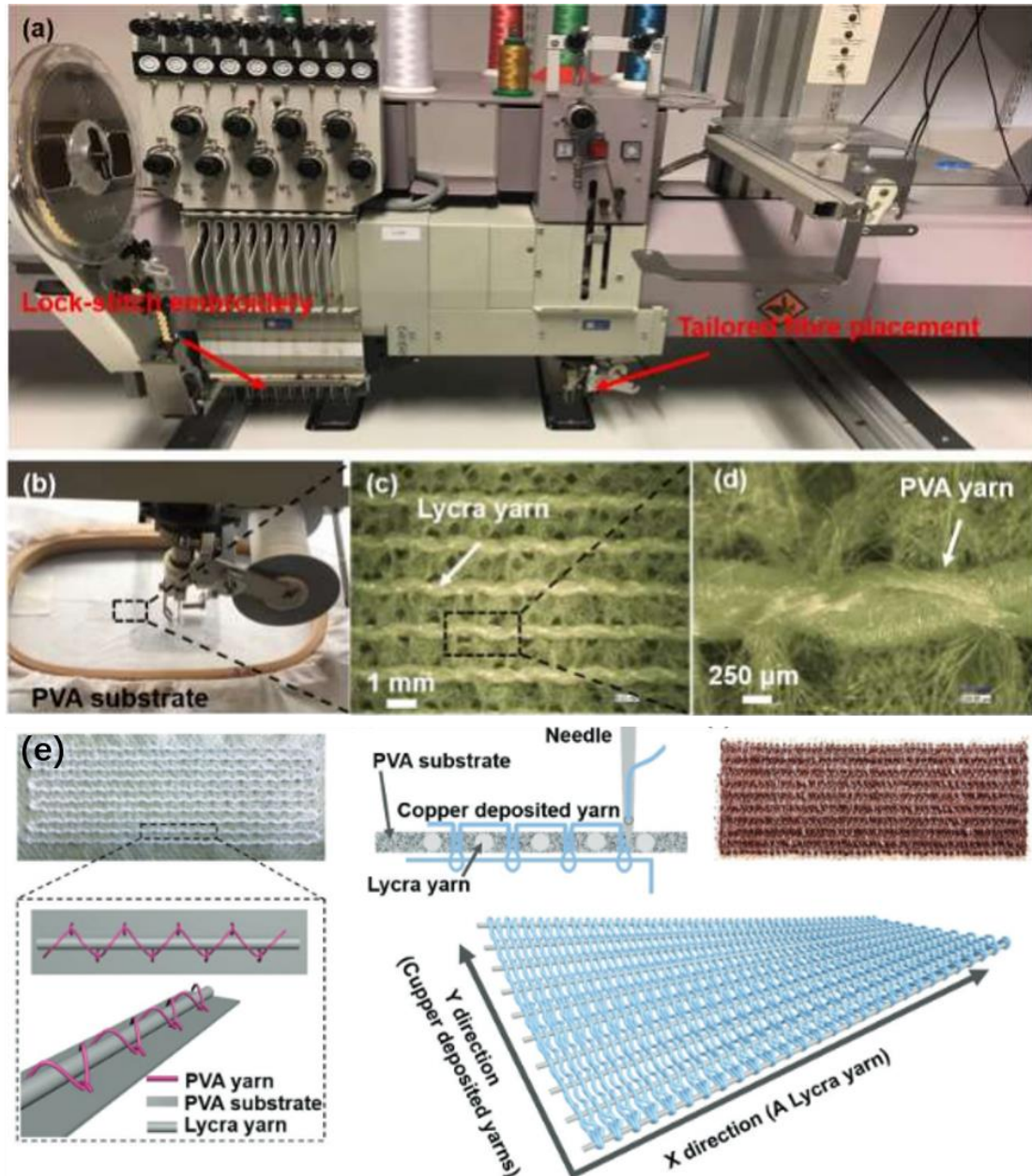


Figure 2-14. An embroidery-fabricated strain sensor². a) Embroidery machine. b-d) Close up of yarn tracks of embroidered fabrics. e) Schematic illustration of the structures and compositions of embroidered e-textiles.

Weaving

The woven fabric is interlaced by two perpendicular yarns in warp and weft directions. Plain-woven structure is the most basic structure aligned by a criss-cross pattern, which shows highly stable and condensed texture. By taking advantage of these properties, the plain-woven fabrics can be easily designed into e-textiles sensitive to stain⁹¹ and pressure,⁹² or energy-harvesting devices due to the abundant contacting zones between warp and weft yarns. Figure 2-15 shows the fabrication of plain-woven magnetoelectrical clothing generator by a weaving loom for energy harvesting.⁶ The formed woven fabric comprised of plentiful magnetic yarns generate energy when the arms (the fabric is sewing around the arms) are swing. However, one of the limitations of the plain-woven fabric is the poor stretchability due to the interlaced structures and intertwined yarns. To overcome this disadvantage, more stretchable yarns should be involved in the construction of fabrics.



Figure 2-15. A plain-woven magnetic fabric for energy harvesting.⁶ a) The preparation of a plain-woven magnetic fabric and schematic illustration of a magnetoelectrical clothing. b) Plain-woven structure of the magnetic fabric. c) Images of weaving loom and magnetic fabrics.

Spinning

Spinning is a conventional textile technology for the productions of threads and yarns, which is a fundamental process in textile fabrication. Various functional yarns can be produced by integrating filaments with diverse features. Zhu et al. discovered a functional yarn with ultraelastic and sensitive to strain by wrapping the conductive Ni-

or Cu- deposited filaments on the elastic polyurethane (PU) core as shown in Figure 2-16.³ The as-prepared metal-deposited ultraelastic yarns exhibit high conductivity ($0.2 \Omega \text{ cm}^{-1}$) and ultralight weight (1.5 mg cm^{-1}), which are applicable of being integrated into smart gloves to control movements of robotic hand through human-machine interfaces (HMIs).

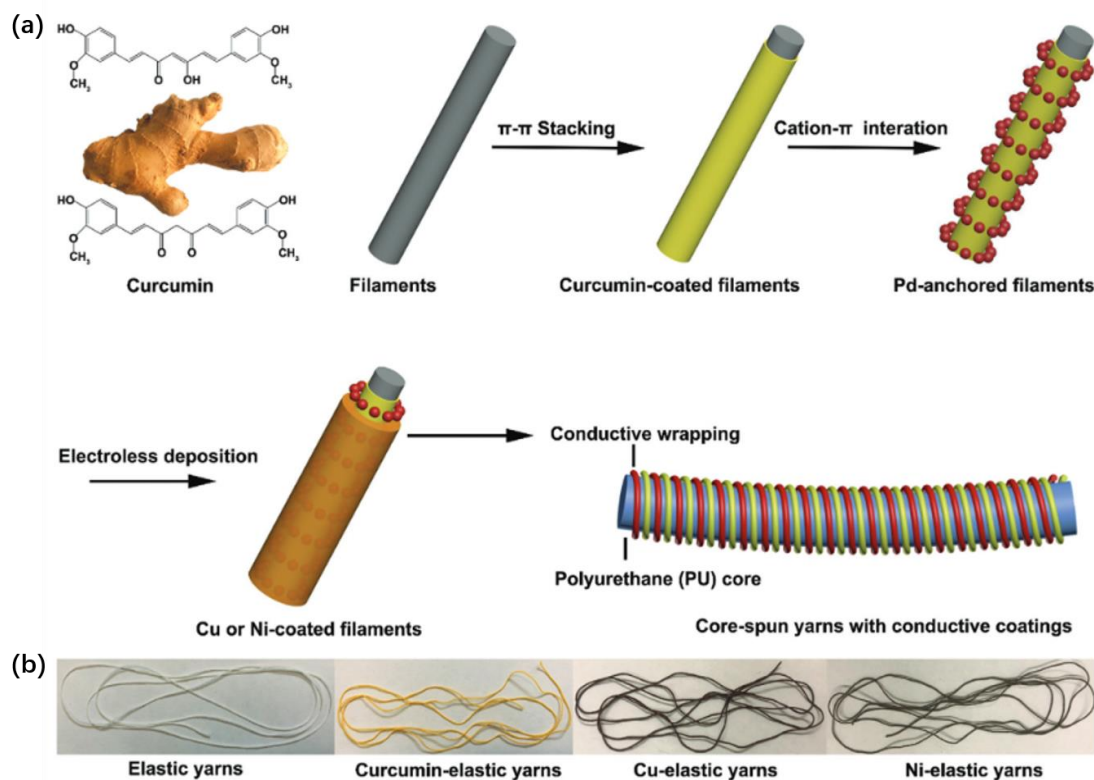


Figure 2-16. Fabrication of ultraelastic yarns via wrapping conductive filaments on the elastic core.³ a) Schematic illustration of the fabrication process. b) Observations of elastic yarns in each different state.

2.3.3 Summary

In this chapter, I summarised various techniques to integrate graphene-based materials into textile to assemble functionalised graphene-based textiles. The functionalisation techniques are highly efficient, low-cost and easy-handled, which are feasible for the scalable productions. However, the shortcomings of deposition-based techniques are the unstable bonding between conductive materials and substrates. The conductive

materials coated on substrates tend to be washed off or dissolved in solution if they are subject to cyclic washing or chronic soaking respectively. Moreover, the coating layers on the surface are possible to be damaged during the weaving or knitting fabrication. The porosity and uneven structure of the functionalised fabrics may have negative influences in their overall performances such as stability and durability. By realising the drawbacks of current functionalised wearable textile fabrication techniques, it is desirable to find out fibres or yarns with intrinsic flexibility and conductivity, along with the feasibility in the fabrication of wearable textiles with firm and even structure, to develop durable, washable and reliable wearable electronics.

2.4 Applications in environmental remediation and wearable electronics

The fabrication and properties of graphene-based materials have been introduced and summarised in Chapter 2.2. In Chapter 2.3, the technologies to assemble functionalised graphene-based textiles were mentioned. Herein, we will summarize the various applications of functional graphene-based materials, which are primarily for environmental remediation (e.g., waste textile management and wastewater treatment) and state-to-the-art wearable electronics (e.g., humidity sensor and strain sensors).

2.4.1 Waste textiles management

The development of fast fashion industry creates overproductions of garments. It was reported that about 150 billion garments are produced by the fashion industry each year, 30% of which are never sold out and over 50% of which have been disposed in a single year.⁹³ The total number of produced textile wastes is approximately 92 million tons annually, most of which (85%) end up by disposal (landfilling or incineration) and only 15% of which are recycled.⁹⁴ The increasing productions of textile wastes bring about lots of environmental concerns such as wasting of resources and water contaminations.

Thus, the management of textile wastes, especially recycling and reutilizing them in a more efficient way is of great importance for environmental remediation.

Reuse

The reuse of textiles is accomplished through donating, reselling and swapping them to new owners, which plays a significant role in diminishing the burden on waste management.⁹⁵ By prolonging the garments life, the waste textiles are delayed to enter the waste stream system, which is beneficial to avoid the potential further recycling and save the costs. The largest challenges for reuse of garment waste are the deficiency of public environmental awareness in reusing the products and inconvenient channels for garments donation. The recent booming development of e-business provides reliable platforms for clothing exchange and promotes the trades of secondhand clothing, which facilitates the sustainable consumption of textiles.⁹⁶

Recycle

Recycling the textiles is highly essential for those garments which are not suitable to wear anymore. According to the compositions and qualities of original products, the recycling process can be subcategorised into 'downcycling' and 'upcycling'. Downcycling can avoid dissipations of new raw materials and resources by reprocessing the waste materials into raw material with a much lower value than original materials. On the contrary, upcycling is a recovery process by transforming waste material into a new product with a higher value or quality in contrast to original materials, such as turning an aged curtain into a new garment.⁹⁷

The recycling steps of textile waste includes sorting, separation and processing, which are achieved through mechanical recycling, chemical recycling and thermal recycling technologies. Mechanical recycling is to tear the textile wastes into small pieces such as ripped yarns and fibres which are then processed into textile applications and other applications (e.g., filtration material, carpet underlay and nonwoven products).⁹⁸ Chemical recycling is typically applied to synthetic fibres and blending fibres by

separating, degrading and then repolymerizing the waste fibres into new fibres. Sun et al. introduced a chemical recycling method by separating fibre/polymer blended fabrics with chemical dissolution and reprocessing fibres regeneration with melt spinning and wet spinning (Figure 2-17). This green chemistry strategy solved the critical problem in separation of natural and synthetic fibres from waste textiles and regeneration of waste fibres and textile.¹⁴

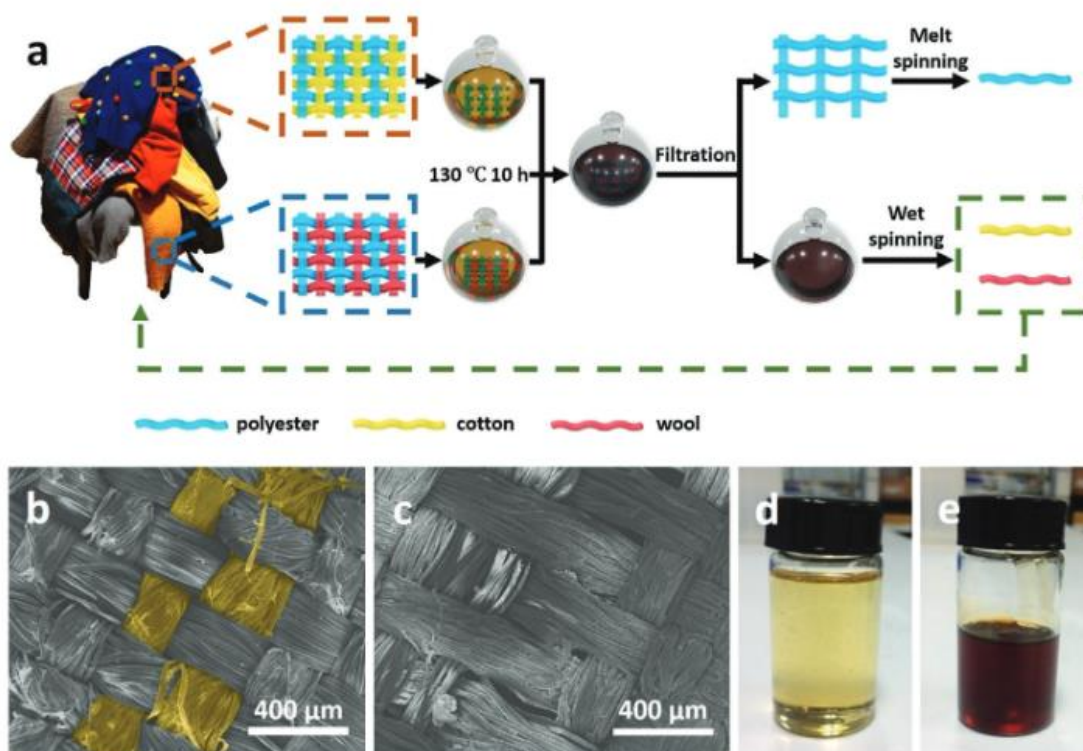


Figure 2-17. Chemical recycling of waste textile by separation of natural polymers from blended fabrics.¹⁴ a) Schematic illustration of separation and regeneration of cotton/polyester blended fabric. b) SEM image of cotton/polyester blended fabric before dissolution. c) SEM image of the remaining polyester fabric after dissolution. d) Dissolving ionic liquid. e) Cellulose and wool keratin dissolved in ionic liquid.

Disposal

Disposal of unwanted textiles is not the desirable waste management. However, there is still necessary to dispose of those obsolescent textiles which are not suitable for reutilizing and recycling anymore. Landfilling as a common and safe way, has problems in decomposing the synthetic textile wastes. For most of textile wastes, incineration can

be easily achieved due to the ignitability of textiles and will generate available thermal energy. However, the process of incineration will bring about other environmental risks such as carbon dioxide emissions.⁹⁹

2.4.2 Wastewater treatment

Water pollution has become an increasing concern and major priority for the society and public. Many human activities will lead to water contaminations such as industrial wastes, pesticides, mining activities, chemical fertilizers and etc. The textile industry is estimated to be responsible for approximately 20% of global clean water pollution arising from dyeing and finishing production.¹³ Especially the rapid development of fast fashion market, which not only brings about a great deal of textile wastes but also accelerates the water contamination by organic dyestuffs.¹⁰⁰ Here, we focus on the treatments for wastewater arising from organic dyestuffs in textile industry.

Physical adsorption

Different from ion exchange, solvent extraction, electro-chemical treatment and advanced oxidation processes which remove dye molecules with potential by-products generated, adsorption is more attractive due to its easy operation and lack of generation of residuals.¹⁰¹ The remarkable high specific surface area of GO makes it a reliable adsorbent to physically adsorb dye molecules. The functional groups in GO such as hydroxyl, carbonyl, carboxylic and epoxide groups can be easily interacted with dye molecules through electrostatic interaction and π - π stacking, which generates the adsorbing behaviour.¹⁰² The adsorption capacities of methylene blue (MB) by various GO-based adsorbents are summarised in Table 2-3. It shows that pure GO has large adsorption capacity towards MB, and this capacity could be enhanced if other nanoparticles are combined and participate in the adsorbing activity.

Table 2-3. Adsorption capacities of MB by various GO-based adsorbents.

Adsorbents	Adsorption capacity (mg.g ⁻¹)	References
------------	---	------------

GO	144.92	103
GO/CA	181.81	103
Graphene	153.85	104
Carbon nanotubes	46.20	105
Modified activated carbon	232.5	106
PT-GO bio-adsorbent	256.58	107
Carbon nanotubes with tannins	105	108
PDA-kaolin with rGO	39.66	109
PVA/CMC hydrogel-GO	172.14	110

Photocatalysis

Photocatalytic technology is widely used in degradation of dyestuffs in wastewater by converting the solar energy into chemical energy. The photocatalytic mechanism and performance of Graphene/TiO₂ composites have been introduced in Chapter 2.2.3. However, the mass of photocatalysts, dyestuff volume and concentration, as well as illumination intensity are also important parameters to evaluate the degradation efficiency. We summarised the overall degradation intensity of various TiO₂-based composites by considering all these parameters in Table 2-4. It shows that the overall degradation intensity (ODI) is improved if a pre-adsorption process is added. However, the overall degradation efficiency is still quite low because of the moderate photocatalytic and adsorbing capacities of photocatalysts as shown in Table 2-2 and Table 2-3 respectively. Especially for their adsorbing abilities, which are always ignored for the contamination's degradation enhancement.

Table 2-4. Comparisons of degradation intensity for TiO₂-based composites

PHT	PHT mass (g)	MB volume (L)	MB concentr ation (mg/L)	Illumination intensity (kW)	Complete degradation time (h)	ODI (mg/h kw g)
TiO ₂ /5%GO nanofiber ¹¹	0.1	0.1	30	0.5	0.83	72.29
Bi ₂ WO ₆ /TiO ₂ polyester fabric ¹⁵	0.2	0.05	10	0.5	2.5	2
Graphene/ TiO ₂ fibre ¹⁷	0.4	0.1	30	1	2	3.75

Ag ₂ O-TiO ₂ ¹¹²	0.1	0.1	160	0.16	6	166.67
Ni/Cr-TiO ₂ ¹¹³	0.1	0.05	5	Sunlight (0.6)	1.5	2.78
rGO-TiO ₂ (with 0.5h adsorption) ¹¹⁴	0.23	0.04	10	0.15	2	5.8
TiO ₂ nanoparticle (with 1h adsorption) ¹¹⁵	0.1	0.6	10	0.006	3	333.33

Note: PHT stands for photocatalysts, ODI represents overall degradation intensity.

2.4.3 Humidity sensor

Humidity sensors have been used for the detection of environmental parameters for the past decades, such as agriculture, industry and smart home system. Recently, the development of wearable electronic technology has extended the applications of humidity sensor to human body and health related detection, such as respiratory behaviours, skin moisture, speech recognition and diaper monitoring.¹¹⁶ The monitoring of humidity-related data resource in human body has huge significances in constructions of a full-body human health detections for the preventions of illness.

Classifications and working mechanism

Humidity sensors can be classified into various types according to different humidity sensing signal transmissions, such as resistance, capacitive and impeditive.¹¹⁷ The resistance-type humidity sensor with direct-current working mode is widely studied due to the simple constructive structure and processing circuit. The resistance of the humidity sensor changes as the surrounding relative humidity alters. The construction of impeditive-based humidity sensor is always similar to the resistive-type humidity sensor, while its signal detection requires to be assisted by an Inductance, Capacitance and Resistance (LCR) meter.¹¹⁸

The capacitive humidity sensors are always constructed with a sandwiched-structure, with a humidity sensitive layer, non-conductive substrate and two electrodes in two

ends. The measurement of capacitance-based humidity sensor can be represented by:

$$C = \frac{\epsilon_m S}{4\pi k d}$$

Where ϵ_m and d represent the permittivity and thickness of the dielectric material respectively, S represents the area of electrodes and k means the electrostatic force constant.¹¹⁹ As for the capacitive-based humidity sensors, the dielectric permittivity of selected material varies in the process of water adsorption and desorption. For example, the permittivity of polymers ranges from 2 to 5, while this value for water molecules reaches 80 roughly, which indicates the sensor's permittivity increases during the water adsorption.¹²⁰

Humidity sensing materials

The humidity sensing materials as the core component determine the sensing performance of humidity sensors. The ideal humidity sensing materials for the applications in wearable electronics should be sensitive to water molecular, good flexibility, a quick water adsorption and desorption properties, which could be summarised into the three main types below:

- **Carbonaceous materials:** The carbonaceous materials have widely been used in humidity sensors for their varieties of types and excellent sensitivity due to the large surface area and abundant oxygen-related groups, such as graphene, GO, CNT and graphitic carbon nitride. Most of them are able to be directly fabricated into fibre- or fabric-based wearable humidity electronics with remarkable flexibility.¹²¹
- **Other two-dimensional (2D) materials:** The other 2D materials excluding graphene-based material have also been studied for humidity sensor, such as WS₂, TiSi₂, MoS₂ and Mxene (Ti₃C₂T_x), which have better dispersibility and conductivity.¹²²
- **Polymer materials:** Most of polymers are hydrophilic and easy to be designed into flexible humidity sensor, such as Poly (vinyl alcohol) (PVA), which can adsorb water even under high-humidity environment (above 60%).¹²³ However, polymer

materials are always integrated with conductive materials to be integrated as a humidity sensor, such as PVA/KOH, PVA/Mxene and polydopamine (PDA)/GO.

- **Semiconductors:** The unique nature of conduction for semiconductors is seen to be an advantage for the applications in humidity sensors. The semiconductor is more likely to be an insulator under lower humidity because the low-amount water molecules are unable to move freely. The increases of humidity level generate the network of hydrogen-bonded water molecules onto substrate materials, which accelerates the transformation of H_2O to H_3O^+ , resulting in the free movement of proton and enhancement of semiconductor's conductivity.¹²⁴

Performance and applications

The performances of the flexible humidity sensors are primarily determined by the sensing range and response time, which are summarised in the Table 2-5. It shows that the textile-based humidity sensors have a larger sensing range, however, their response speeds are relatively slow which will influence the detecting accuracy in the practical application.

Table 2-5. Properties of wearable humidity sensors

Sensing materials	Substrate types	Sensing mechanism	Sensing range (%)	Response time (s)
Mxene/Silver nanowire ¹²⁵	Textile-based	Resistive	0-80	5
CNT/PVA filament ¹²⁶	Textile-based	Resistive	60-100	40
PANI/Spandex yarn ¹²⁷	Textile-based	Resistive	20-100	116
Cu/Cleancool yarn ¹²⁰	Textile-based	Capacitive	6-97	3.5
MoS ₂ coated fiber ¹²⁸	fibre-based	Optical	20-80	0.066
Carbon/PDMS ¹²⁹	PDMS	Impeditive	54-95	0.29
GO ¹³⁰	PDMS	Capacitive	20-90	N/A
PVA/KOH ¹³¹	Film-based	Resistive	10.89-81	0.4
rGO/Cellulose ¹³²	Film-based	Capacitive	10-70	100
rGO/PDDA ¹³³	Film-based	Resistive	11-97	108-147
Paper/Polyester ¹³⁴	Paper	Resistive	41-91	472
GO/rGO ¹³⁵	Paper	Bending curvature	24-86	15

Wearable humidity sensors are widely applied in the monitoring of human activities, health and respiration, which are:

- **Speech recognition:** The recognition of speech has always been realised by flexible pressure sensors, which requires the pressure sensors to be firmly attached to the throat and leads to discomfort. The flexible humidity sensor has achieved the speech recognition in a non-contact way as shown in Figure 2-18a. Various words (such as 'Hi', 'beautiful' and 'sensor') can be recognised according to the unique electrical signals.¹³⁶
- **Skin moisture detection:** The moisture content of human skin is a vital physiological parameter to evaluate human health conditions. Figure 2-18b exhibits the monitoring of skin moisture by a flexible humidity sensor, which shows the variations of facial water content at different measuring time in a single day.¹³¹
- **Respiratory monitoring:** Respiratory behaviours (e.g., rates, depth and rhythm) provide the vital information of human health. The exhaled air of human breath contains humidity as high as 90%, which can be easily detected by a humidity sensor in a facemask (Figure 2-18c).¹³⁷
- **Diaper monitoring:** Another practical application of humidity sensor is to detect the diaper conditions of infants and dementia patients. The humidity sensors should be flexible, disposable and environment-friendly.^{121, 134, 138}

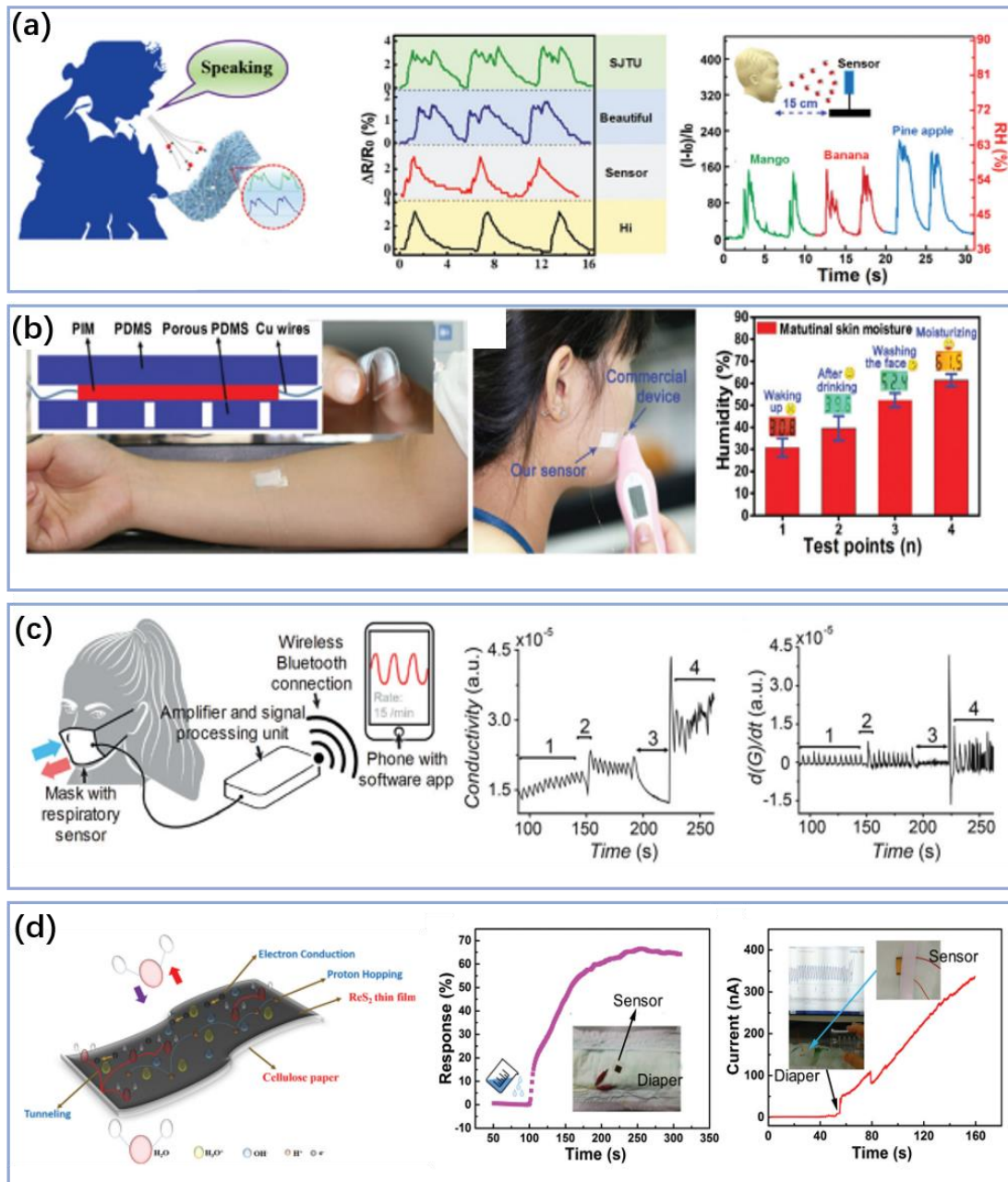


Figure 2-18. Applications of flexible humidity sensors. a) Speech recognition.¹³⁶ b) Skin humidity detection.¹³¹ c) Respiration monitoring.¹³⁷ d) Baby diapers.^{121, 134, 138}

2.4.4 Strain sensor

Recently, wearable strain sensors have been attracting increasing interests due to their potentials in human motion detection, health monitoring, future entertainments and human-machine interfaces.¹³⁹ These wearable devices are able to immediately convert

the mechanical signals into electrical signals which can be directly displayed and recognised. The superior wearable strain sensors with decent flexibility, lightweight, comfort and high accuracy, which overcome the narrow sensing range and non-flexibility of conventional rigid strain sensor, paving a new route for next-generation wearable electronics.¹⁴⁰

Classifications and working mechanism

There are various types of wearable strain sensor (e.g., resistive, capacitive, piezoelectric, triboelectric and optical) depending on the sensing mechanism. The piezoelectric-based and triboelectric-based strain sensors face challenges in poor static and dynamic sensing reliability.¹⁴¹ Even though optical-based strain sensors have superiority in sensing range and durability, their poor sensitivity (especially for the detection of small motions) hinders their applications.¹⁴² In general, the resistive and capacitive strain sensors are more favourable for their uncomplicated fabrications, decent flexibility and reliable sensing performance.¹⁴³

The sensing mechanism for a resistive strain sensor is the proportional changes of resistance of the sensors with corresponding applied strain. When the strain sensor is under strain deformation, the connected conducting materials will disconnect or slip out from each other, leading to the reduction of contact area between materials and a change in resistance. The resistance change can be resulted from the changes in the geometry of the conductive material, such as the area (A) and length (L). Moreover, the piezoresistive behaviour can possibly change the resistivity (ρ) of the conductive material, resulting in the resistance change as shown in the equation below:^{144, 145}

$$R = \frac{\rho L}{A}$$

Different from resistive strain sensor, the capacitive strain sensors are constructed with a sandwich structure, where two electrodes are separated by a dielectric. The value of the capacitance (C) depends on the overlapping area between the two electrodes (A),

the thickness of dielectric layer (d) and the permittivity of dielectric materials (ϵ_m) as shown in the equation below:¹⁴⁶

$$C = \frac{\epsilon_m \epsilon_0 A}{d}$$

Where ϵ_0 is the permittivity of free space. When the capacitive strain sensor is under stretched state, the capacitive area remains the same while the thickness of dielectric layer is decreased, leading to an increase in capacitance.

Elastomer-encapsulated and encapsulation-free strain sensors

The sensing performances of wearable strain sensors are determined by various parameters such as sensing range, durability, response time, sensitivity and linearity. Sensitivity as a fundamental characteristic for strain sensor to determine how tiny motions can be detected, is characterised by the resistance/capacitance change during stretching and recovery process.^{12, 145} The sensitivity of a resistance-based strain sensor is always determined by gauge factor (GF') as shown in the equation below:

$$GF' = \frac{\Delta R/R_0}{\epsilon}$$

Where R_0 is the initial resistance of strain sensor without stretching, ΔR is resistance change during stretching and ϵ is the strain deformation. The sensitivity of a capacitive strain sensor is similar by measuring the change of capacitance (C) instead of resistance (R).

To increase the sensitivity and reliability of strain sensor, the conductive materials are always encapsulated by elastomers (e.g., PDMS and Ecoflex). The encapsulated elastomers provide high elasticity to strain sensor and protect the conductive materials from damages at large-strain level. The thickness of encapsulated layer has significance to the electromechanical and wearable performances of strain sensors. The thin encapsulations increase the wearing comfort and breathability while bring about poor stretchability. By increasing the encapsulation thickness, the robustness of sensor is improved while bringing about inconsistent compliance between encapsulation and sensing elements.¹⁴⁷ The other advantage of an encapsulation layer is that it can stick

on the skin and support the conformal fit of flexible strain sensor to the surfaces of humans or machines.

Even though the thickness of encapsulations can be thinner to relieve the wearing uncomfotability, the negative effects of encapsulations on trapping air and sweat vapour generated from human metabolites are impossible to be completely eliminated.¹⁴⁸ The encapsulation-free strain sensors can be regarded as authentic wearables for their entire-textile-based structures, which are achieved by constructing the conductive fibres or yarns into fabric strain sensors *via* textile technologies (e.g., knitting, weaving, embroidery, braiding and spinning). The challenges in fabrication of an encapsulation-free strain sensor are to find out the sensing fibres or yarns with decent flexibility, robustness and conductivity. Deposition or coating of conductive nanomaterials onto fibres as feasible techniques for achieving flexible and conductive substrates, is suffering from infirm bonding between depositions and substrates.^{2,3} The utilisations of high-performance fibres with intrinsic flexibility and conductivity (such as GF and CNT) are more and more favourable.¹

Performance and applications

Sensitivity, stretchability and durability are the main characteristics to evaluate encapsulation-free strain sensors, which are determined by the gauge factor (GF'), sensing range and cycling stability respectively as summarised in the Table 2-6. It shows that there are some enhancements in sensitivity, sensing range or cycling stability. However, due to the intrinsic disadvantages of coating-produced conductive yarns and fabrics, the washability of the current encapsulation-free fabric strain sensor is still poor and needs to be improved.

Table 2-6. Performances of reported encapsulation-free fabric strain sensors

Sensing materials	Sensor structure	GF'	Sensing range (%)	cycling stability	Washability
Cu-deposited yarn ²	Embroidery	49.5	200	5000	Poor
rGO/CNT-coated fabric ¹⁴⁹	Woven	6	12	100000	N/A
Graphene-dyed	Knitting	2	40	500	Poor

fabric ⁵					
Ni-deposited yarn ³	Wrapping yarn	N/A	1100	5000	Poor
Mxene-coated fabric ¹⁵⁰	Nonwoven	3405	83	1000	N/A
rGO-coated fabric ¹⁵¹	Knitting	18.5	30	120	Poor
Carbonised silk fabric ¹⁵²	Woven	9.6	500	6000	Poor
rGO-coated silk fabric ¹⁵³	knitting	124.5	10	1000	N/A
Ag-coated fabric ¹⁵⁴	Embroidery	0.1	100	2500	N/A

Flexible strain sensors can be widely applied into various practical scenarios by converting strain-induced deformation into electrical signals. By analyzing these visible electrical signals, some information of human body motions and vital signs are reachable. Moreover, strain sensors are capable of indicating and forewarning human health *via* human-machine interaction.

- **Motion detecting:** The most fundamental and important application of wearable strain sensor is to detect human motions by attaching skin-mountable wearable strain sensors to different body regions. Figure 2-19a exhibits a man equipped with strain sensors on the skin surface of cheek, throat, chest, elbows, fingers and knee. By detecting the surface movements, various electrical signals can be visibly recognised such as chewing, water drinking, speaking, arm swing, walking and running.² The exhibited electrical curves are highly consistent with corresponding body motions, which is the greatest advantage of strain sensor in sensing motions.
- **Health indicators:** The respiration signals can be easily collected by attaching the strain sensors to human chest. These signals are analysed through a convolutional neural network (CNN) and classified into 3 levels (Figure 2-19b), which represents different states of breathing while sleeping (normal breath, tachypnea and tachypnea with cough). The emergency warning system will start alarming once the sleeper is in abnormal breathing state.⁴
- **Human-machine interaction:** The development of wearable electronics into human-machine interaction highly depend on the extremely high accuracy and performance of stain sensors. The motion sensing sleeve integrated with four

wearable strain sensors in Figure 2-19c has a remarkable sensitivity ($GF' > 9000$) and linear response ($R^2 > 0.98$), which enables it to detect tiny muscle motions of the arms. By using the neural network training, these small movements are studied and analysed, which will give supports to the disables who need hands mobility.¹⁵⁵ The human-machine interaction assisted by wearable strain sensors can also be applied in future entertainment, such as virtual reality and augmented reality (right part in Figure 2-19c).¹⁵⁶

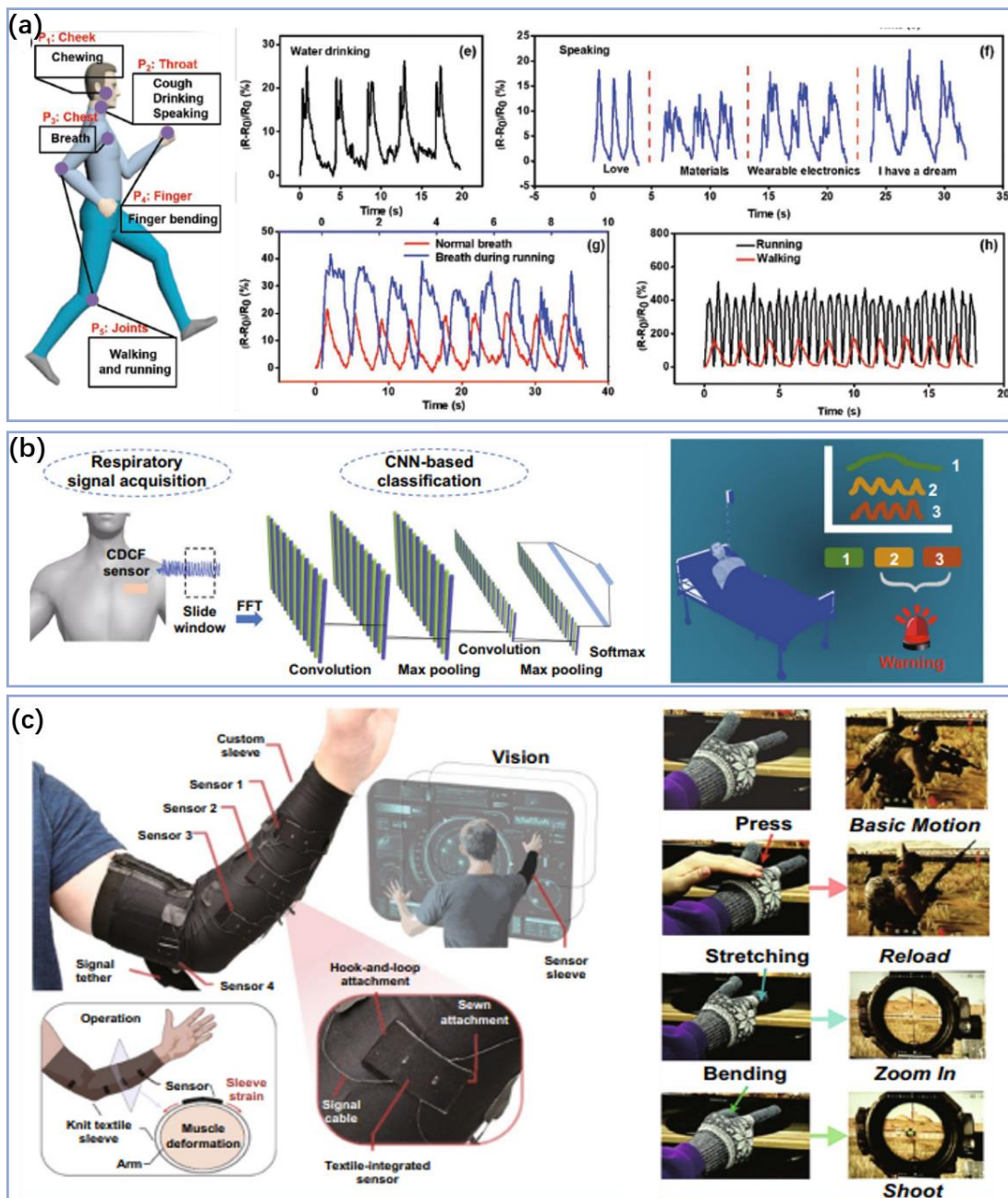


Figure 2-19. Applications of flexible strain sensors. a) Motions sensing.² b) Health

indicator.⁴ c). Human-machine interfaces.^{155, 156}

2.4.5 Summary

In this section, we have introduced the applications of graphene-based materials in environmental remediation such as waste textiles management and wastewater treatment, as well as wearable electronics such as humidity sensors and strain sensors. The downcycling and upcycling management give the opportunities for waste textiles to be transferred into high-value raw materials or high-performance new products respectively. However, the chemical dissolution and separation process of natural fibres and synthetic fibres will possibly cause secondary pollutions. The functional graphene-based materials related to wastewater treatment are always fabricated with an enhanced photocatalytic performance, there are lack of systematic studies on the enhancement of adsorbing capacities of graphene/TiO₂ composites to optimize the contamination degradation efficiency. A great deal of attractive and smart applications of wearable electronics have been highlighted, most of which focus on the optimisms of their sensitivity and sensing range. However, many core elements for wearables have been ignored such as breathability, washability, wettability and sensing-reliability.

2.5 Summary and research gaps

In this review, recent advances of graphene, GO, GF and graphene/TiO₂ composites have been summarised in Chapter 2.2. Graphene has been widely used as co-catalyst to enhance the photocatalytic performance of nascent TiO₂ nanoparticles. Table 2-2 shows that the structure of graphene-TiO₂ composites and contents of graphene in composites influence the photocatalytic efficiency. However, the overall degradation efficiency is still unsatisfactory. Table 2-4 summarizes the optimised overall degradation efficiency by adopting pre-adsorption prior to photocatalytic degradation. From the summarisation, it is desirable to take full advantage of night-time adsorption of

dyestuffs to optimize the overall degradation efficiency of graphene/TiO₂ composites. On the other hand, the overproduced textile wastes as environmental concerns mostly end up by landfilling or incineration, which bring about lots of environmental concerns such as wasting of resources and water contaminations. Thus, the management of textile wastes, especially recycling and reutilizing them in a more efficient way is of great importance for environmental remediation.

The applications of GO and GF in wearable electronics has also been attractive recently. Figure 2-18 exhibits the fascinating applications of wearable humidity sensors in the monitoring of human activities, health and respiration. Table 2-5 summarizes the properties and substrates of the state-of-the-art wearable humidity sensor, typically for sensing range and response speed. It indicates that only a few researches investigate on pure fabric-based humidity sensors due to their low response speed. Textile materials will retain water molecules inside the fibre/fabric even humidity is removed, resulting in longer recovery time for the humidity sensing. There are limitations in designing and fabricating fabric-based humidity sensor with rapid response and recovery speed.

Although graphene and GO have been widely used as surface coating materials to fabricate fabric-based flexible electronics with improved breathability, they inevitably tend to be washed off from substrates after cyclic washing and chronic wettings due to the infirm bonding between depositions and substrates. The most desirable approach is to fabricate GFs with intrinsic flexibility, strength and conductivity for the assembly of washable and wettable flexible electronics. Currently, considerable modifications have been reported to flatten the wrinkled and random GO sheets or generate hierarchical surface structure during the solidification of GFs in coagulation bath, the modified GF shows enhancements in tensile strength while its flexibility still desiderates to be boosted due to the weak stacking density of GO. Taking a typical research of Li et al. for examples, the mechanical strength of GF produced by plasticisation spinning in his research reach as high as 3.4 GPa, while its tensile strain is only 5% (Table 2-1). The inferior flexibility of GF has been considered as a challenge to restrict its applications

in fabric wearable electronics. Moreover, many researches put efforts to optimize sensitivity, stretchability and linearity of wearable strain sensors, while sensing reliability as a crucial parameter in real applications is largely ignored. Hence, it is urgent to fabricate high-performance GFs and assemble wearable strain sensors with higher sensing accuracy.

Chapter 3

Waste textile reutilisation via a scalable dyeing technology: A strategy to enhance dyestuffs degradation efficiency

This chapter focuses on completing the first and second objective addressed in Chapter 1.3. The research work has been accepted by Advanced Fiber Materials.

Authors: Heng Zhai, Zekun Liu, Lulu Xu, Ting Liu, Yangyang Fan, Lu Jin, Ruihan Dong, Yangpeiqi Yi, Yi Li

Journal: Advanced Fiber Materials (DOI: 10.1007/s42765-022-00192-1)

Statement of own contributions in joint authorship: Conceptualisation, H.Z., Y.L.; Methodology, H.Z. and L.X.; Materials preparation, H.Z. and Z.L.; Characterisation, H.Z. and Y.F.; Formal Analysis, H.Z. and T.L.; Data Curation, H.Z., R.D., Y.Y. and L.J.; Original draft preparation, H.Z.; Manuscript revision, H.Z.; Supervision, Y.L.

Abstract

The rapid expansion of fast fashion industry brings out environmental concerns such as dyestuffs-related water pollutions and waste textiles. Conventional wastewater-disposal strategies emphasize the optimisation of photocatalytic activity to improve pollutant degradation efficiency, while the adsorptivity, recyclability and sustainability of photocatalysts are always ignored. The overproduced textiles are still in urgent of being recycled and reutilised in eco-friendly approaches. In this work, a scalable dyeing technology is employed to achieve green and sustainable reutilisation of waste textiles. The functionalised TiO₂/reduced graphene oxide wool fabrics show excellent sustainability, remarkable adsorbing capacity and enhanced photocatalytic performance. By taking advantages of these properties, we develop an integrated strategy of night-time adsorption and day-time photodegradation which could significantly optimize the

dyestuffs degradation efficiency. The concept about waste textiles reutilisation and waste water treatment in this work provides practical potentials in the efficient and sustainable environmental remediation.

Keywords: waste textile reutilisation, wastewater treatment, adsorption, photocatalysis

3.1 Introduction

Nowadays, water pollution has been paid much attention due to the crisis of water resources. The textile industry is estimated to be responsible for approximately 20% of global clean water pollution arising from dyeing and finishing production.¹³ Especially the rapid development of fast fashion market, which leads to increasing overproduction and overconsumption of textiles, accelerating the water contamination by organic dyestuffs.¹⁰⁰ To address the water pollution concerns, the conversion of solar energy to degrade pollutants in water has been considered as one of the most efficient and effective solutions. Photocatalysts such as TiO₂ nanoparticles are widely employed due to their high catalytic stability, cost-effective property and moderate demands for ambient condition.¹⁵ However, the fast recombination rate of photogenerated electron-hole (e^-/h^+) pairs and weak adsorbing affinity of nanoparticles towards target contaminants restrict the photocatalytic performance of TiO₂, and affect the overall degradation efficiency.^{16, 17} Moreover, the particle-based TiO₂ photocatalysts tend to sink down into the water, which reduces their recyclability and sustainability in the practical applications.

Recent studies put more emphasis on optimizing the pollutant degradation efficiency of TiO₂ by improving its photocatalytic performance. This was achieved through various doping strategies, including metallic doping, non-metallic doping and noble-metal loading.¹⁸ Among these materials, carbonaceous materials such as carbon nanotube and graphene are more favourable owing to their superior properties in

transporting electrons, good optical transmittance, large specific surface and strong adsorption capacity.^{19, 70, 157} The integration of graphene into TiO₂ improves the photocatalytic performance of TiO₂ by increasing utilisation rates of solar energy and prolonging lifetime of electron-hole pairs.¹⁵⁸ However, the photocatalysts would no longer photodegrade contaminations without the participation of illuminations, such as in the heavy cloudy days or even at night. It is highly desirable to fabricate recyclable and sustainable photocatalysts with massive adsorption towards pollutants at night and enhanced photocatalytic performance to optimize the overall degradation efficiency.

On the other hand, the fast fashion industry generates approximately 92 million tons of textile wastes annually around the world, most of which end up in landfills or incinerations.¹⁴ Even though reuse and recycle of waste textiles as environmentally-friendly solutions have been put forward, there are only a small amount of intact textiles can be reused in the conventional ways through donating, swapping and reselling.¹⁵⁹ For those obsolescent garments which are not suitable to wear, their fabrics and fibres can be separated and recycled into new products by chemical dissolution and remanufacture.¹⁶⁰ The challenges in separations of blending fibres such as cotton/polymer blend and wool/polymers blend and potential secondary pollution in chemical dissolution of synthetic fibres hinder the effective and sustainable recycles of waste garments. To date, it still leaves a vacancy to reutilize waste textiles in a green manner.

Herein, we propose a scalable dyeing technology to synchronously realize the sustainable reutilisation of waste textiles and efficient degradation of dyestuffs in waste water. The TiO₂/reduced graphene oxide (rGO) functionalised fabrics originated from waste wool fabrics exhibit splendid adsorbing ability and enhanced photocatalytic performance. The maximum adsorbing capacity towards methylene blue (MB) is 427.35 mg/g, which is analysed by Langmuir adsorption isotherms. The complete photodegradation of MB (100 mL, 10mg/L) is within 60 minutes under 150W Xenon lamp. Notably, by integrating night-time adsorption prior to photodegradation, the

overall photodegradation could be shortened to 30 minutes. The strong bonds between TiO₂/ rGO composites and fabric substrates ensure the functionalised fabrics to stably and sustainably photodegrade dyestuffs in aqueous.

3.2 Experimental section

3.2.1 Preparation of GO dispersion and TiO₂/GO composite dispersion

TiO₂ nanoparticles were purchased from Sigma-Aldrich (average particle size of 80 nm). Graphene oxide dispersion was prepared from expandable graphite flakes (from Sigma-Aldrich with particle size larger than 300 μm) by a modified Hummers method which has been introduced in my previous work.^{1, 161} 0.5g expandable graphite was heated in the microwave oven at the power of 750 W for 30 seconds to form expanded graphite. Then expanded graphite, H₂SO₄ (100 mL, 98wt%) and KMnO₄ (5g) were mixed and stirred for 24 h. The mixture was slowly diluted with 100 mL deionised water in ice bath and followed by H₂O₂ (10 mL 35wt%). HCl (100 mL 10wt%) was then added to the mixture. Finally, graphene oxide was obtained after centrifuged for the preparation of TiO₂/GO composites dispersion with various mass ratio of GO, such as TiO₂/5%GO, TiO₂/10%GO, TiO₂/15%GO and TiO₂/20%GO dispersion which means there were 5%, 10%, 15% and 20% GO in terms of mass ratio in the dispersion respectively.

3.2.2 Pad dyeing of wool fabric

Before pad-dyeing process, the pristine wool fabric substrate was pre-washed in deionised water and dried in oven. The TiO₂/GO composite dispersion was transferred into the bath of pad-dyeing machine. Each pristine wool fabric was padded 3 cycles in the machine and dried in the oven at 60°C after each cycle. In order to ensure the GO/TiO₂ composite firmly and stably coated on the fabric surface, the coated wool

fabrics were immersed in the L-ascorbic acid (L-AA) solvent in water bath at 80°C for 24 h. The L-AA acid treatment induced the reduction of the graphene oxide on the surface. Finally, we achieved the functionalised fabrics.

3.2.3 Dark adsorption Test

Dark adsorption experiment was carried out in dark environment and room temperature (20°C) by immersing TiO₂/rGO coated wool fabrics into 100 mL MB solutions with different concentrations ranging from 5 to 20 mg/L. The adsorption equilibrium was reached when the concentration of MB solutions keep stable. The adsorption capacity was calculated using the following equation:

$$q_e = \left(\frac{C_0 - C_e}{m} \right) \times V \quad (1)$$

where C_0 and C_e represent the initial and equilibrium concentrations of MB (mg/L) respectively, m stands for the mass of TiO₂/rGO composites (g) and V is the volume of the solution (L).

3.2.4 Photocatalytic degradation measurements

All the photocatalytic experiments were carried out under a 150 W Xenon lamp (PLS-SXE300, Perfectlight Co., Ltd). TiO₂/rGO functionalised fabrics were immersed into 100 mL MB solution with an initial concentration of 10 mg/L. The irradiation was given out immediately once photocatalysts were settled down to avoid any dark adsorptions. The vertical distance between the solution plane level and lamp was fixed at 10 cm (Figure S5). For comparison, photocatalytic degradation of MB in the presence of pure TiO₂ coated wool fabrics were also studied under the same conditions. The concentration of MB was recorded at same interval time and analysed by using M550 UV/Visible Spectrophotometer. The degradation rates were calculated by equation below:

$$\eta(\%) = 1 - \left(\frac{A}{A_0}\right) \times 100\% \quad (2)$$

where A_0 and A are the initial and remaining concentration of MB.

3.2.5 Characterisation of the TiO₂/rGO coated wool fabric

The surface morphology and crystal structure were characterised by Zeiss Ultra 55 Scanning Electron Microscope (SEM) and FEI Tecnai T20 Transmission Electron Microscope (TEM). The elemental analysis and mapping of TiO₂/rGO Coated fabric were analysed from energy-dispersive X-ray spectrometer (EDX) by FEI Quanta 250. The Raman spectra of the TiO₂/GO and TiO₂/rGO coated fabrics were carried out using Horiba Raman spectrometer with 633 nm excitation wavelength. The X-ray diffraction (XRD) patterns were recorded on an XRD5 spectrometer (Type PANalytical X'Pert Pro) at operating voltage of 40 kV and current at 40 mA using Cu K α irradiation. The Fourier transform infrared (FTIR) spectra were recorded by Bruker Hyperion 3000 IR Microscope. X-ray photoelectron spectroscopy (XPS) was measured by ESCALAB 250 Xi. Photoluminescence (PL) emission spectra was obtained from LabRam HR Evolution with 325 nm edge filter.

3.3 Results and discussions

3.3.1 Preparation of functionalised fabrics

Figure 3-1 shows the basic concept of how the waste textiles are reutilised into the wastewater treatment. The fast fashion industries take responsibility for the large amounts of waste textiles and dyestuffs-related wastewater. Herein, these overproduced textiles could be transferred into TiO₂/rGO functionalised fabrics with abundant adsorption and enhanced photocatalytic property through pad dyeing technology. The

dyestuff molecules in textile wastewater are massively adsorbed on the surface of functionalised fabrics and photodegraded in a green approach.

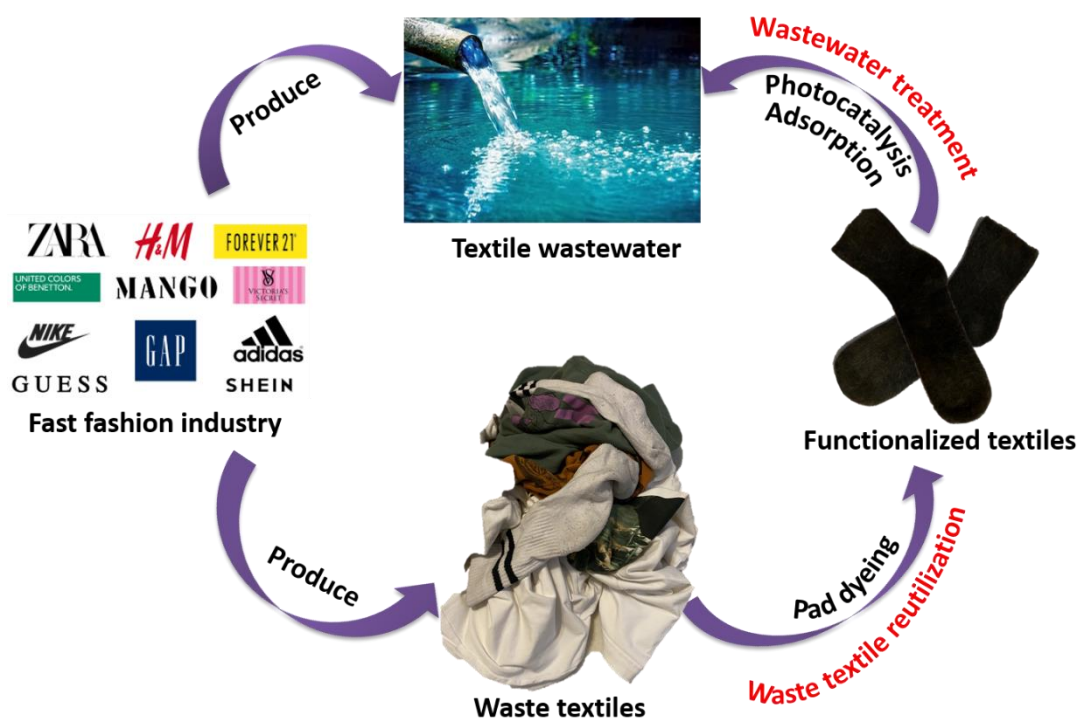


Figure 3-1. Concept of waste textiles reutilisation and wastewater treatment.

The reutilisation of waste fabrics is illustrated in Figure 3-2a, which exhibits the fabrication of TiO_2/rGO functionalised fabrics from pieces of wool fabrics by pad dyeing technology. The graphene oxide (GO) was synthesised from expandable graphite according to our previous papers.^{5, 161, 162} We introduce the pad dyeing approach, which provides considerable force from two spinning compression rollers, to assist the TiO_2/rGO nanoparticles firmly and stably coated on the surface of fabrics. Finally, we achieved the functionalised fabrics coated by $\text{TiO}_2/5\% \text{rGO}$, $\text{TiO}_2/10\% \text{rGO}$, $\text{TiO}_2/15\% \text{rGO}$, $\text{TiO}_2/20\% \text{rGO}$ and pure TiO_2 nanoparticles. They are defined as FF-5%rGO, FF-10%rGO, FF-15%rGO, FF-20%rGO and FF- TiO_2 respectively. The fabrications of GO and TiO_2/rGO functionalised fabric (FF-rGO) are explained in experimental section. The images of pristine wool fabrics after pad dyeing and L-AA reduction are shown in Figure S3-1. The tensile stress of FF-rGO has increased compared with pristine wool fabrics, which can be attributed the binding forces between rGO sheets on the fabric surface (Figure S3-2). The element distributions of Ti, C, N

and O in FF-rGO were captured by EDX mapping (Figure 3-2b and Figure S3-3), where the elements are evenly distributed. The atom percentage of Ti decreases from 19.02% to 13.16% and O decreases from 38.95% to 24.59%, indicating more TiO₂ nanoparticles in FF-5%rGO than those in FF-20%rGO (Figure 2c). Such results demonstrate the actual contents of TiO₂/rGO composite on the fabric surface were well in accordance with experimental expectation.

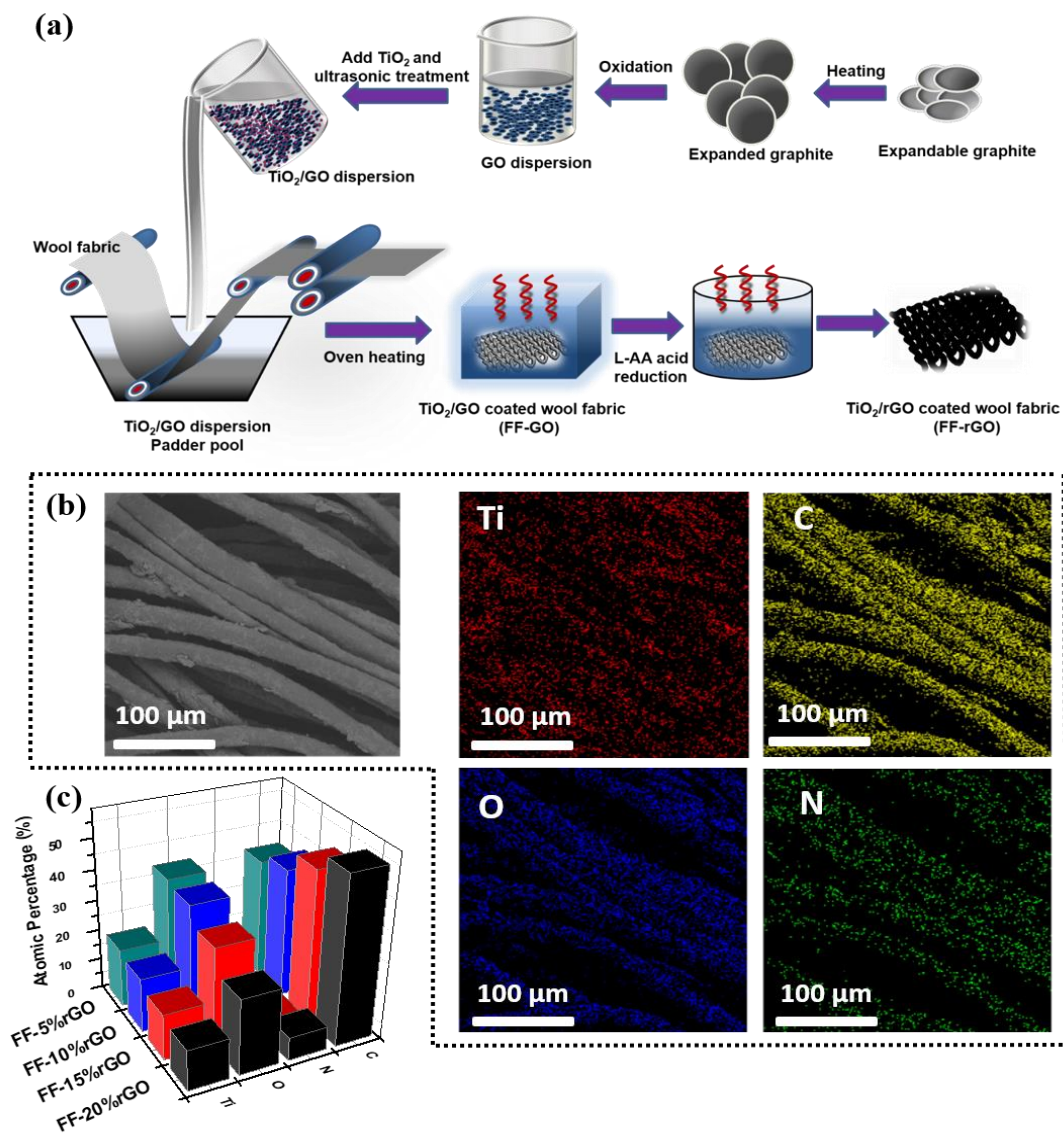


Figure 3-2. a) Schematic illustration of the fabrication of FF-rGO. b) EDX mapping images of FF-20%rGO. c) The surface elements in various FF-rGO.

3.3.2 Characterisations

Before pad dyeing, pristine wool fibre shows obvious overlapping scale structure (Figure 3-3a). After dyeing and reduction of GO, it can be apparently observed that TiO₂/15% rGO particles have been homogenously and densely coated on the wool fibre surface (Figure 3-3b). The high-magnification SEM image reveals TiO₂ nanoparticles are wrapped by rGO sheets on the fibre surface. TEM image in Figure S3-4a confirms the coexistence of TiO₂ and rGO, with TiO₂ wrapped by transparent, layered rGO sheets. High-resolution TEM image further indicates the diameter of TiO₂ nanoparticles is around 50 nm which belongs to anatase TiO₂(Figure S3-4b).¹⁶³ The diffraction peaks in the XRD patterns in Figure 3-3c can be marked as (101), (004), (200), (105), (211), (204), (215) crystal planes of TiO₂ (JCPDS NO.21-1272), which are corresponding to anatase phase.¹⁶⁴ The crystallite size was calculated by the Scherrer equation (result listed in Table S3-1). According to the analysis, the intensity of diffraction peaks decreases when incorporating rGO into TiO₂, indicating the formation of a finer crystallite size. The finest grain size of TiO₂ is 15.84 nm from FF-15%rGO, which suggests 15% rGO is more favourable to modify TiO₂ with finer crystallite size.

Figure 3-3d exhibits the Raman spectra of FF-GO, FF-15%GO and FF-15%rGO. The peaks at 156 (E_g), 399 (B_{1g}), 513 (A_{1g}) and 639 (E_g) cm⁻¹ are ascribed to the anatase phase of TiO₂. The characteristic D and G band at 1350 and 1595 cm⁻¹ were also observed, which indicates the incorporation of GO and rGO into wool fabrics. The D band corresponds to the defects and disordered carbons while the G band contributes to ordered sp²-bonded carbon.⁷³ The intensity ratio of D and G band, recorded as I_D/I_G , was employed to measure the disorder and defects, which is the main characteristic to influence electrical conductivity.¹⁶⁵ The I_D/I_G values of FF-GO, FF-15%GO and FF-15%rGO were calculated into 0.932, 0.948 and 1.017 respectively. Such results indicate the incorporation of TiO₂ nanoparticles slightly reduce the GO on the fabric surface, while largely reduce the GO into rGO when chemical reduction method was applied. The electrical conductivity of rGO increased throughout the reduction, which would

facilitate electron transferring from TiO₂ to rGO and hinder the recombination of electron-hole pairs.

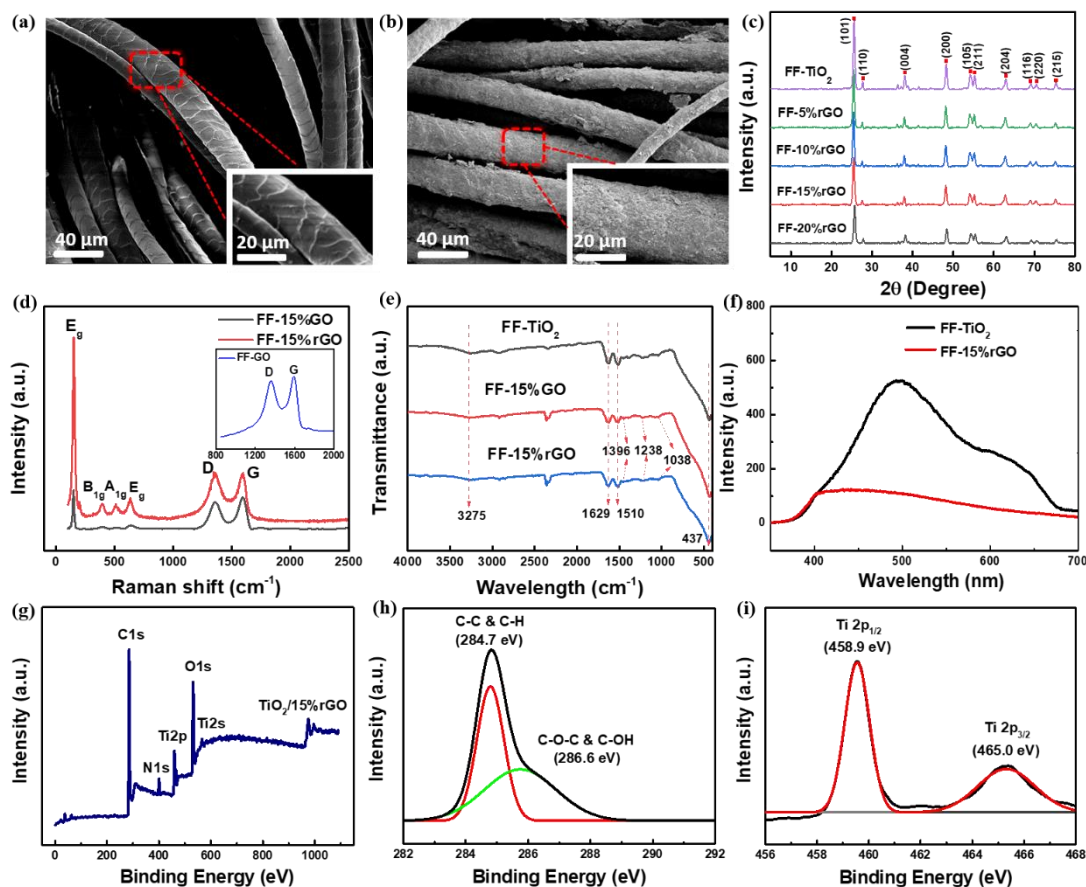


Figure 3-3. Characterisations of FF-rGO. a) SEM image of pristine wool fibres. b) SEM image of FF-15%rGO. c) XRD patterns of FF-rGO. d) Raman spectra of FF-GO, FF-15%GO and FF-15%rGO. e) FTIR spectra of FF-TiO₂, FF-15%GO and FF-15%rGO. f) PL spectra of FF-TiO₂ and FF-15%rGO. g) XPS spectra of FF-15%rGO. h) Peak deconvolution of C (1s). i) Peak deconvolution of Ti (2p).

By analysing the FTIR spectrum of FF- TiO₂, FF-15%GO and FF-15% rGO, we observed peaks around 3300 cm⁻¹ which are corresponding to O-H stretching vibration of hydroxyl groups in all functionalised fabrics (Figure 3-3e). The hydroxyl groups are beneficial to accept photo-induced holes and convert into ·OH radicals which significantly contributes to photocatalytic enhancement.¹⁶⁶ The presence of peak at 1629 cm⁻¹ is assigned to O-H distorting vibration and skeletal C=C vibration in GO and rGO, which is corresponded to sp² character. Similar characters were observed for

bands at 1238 and 1038 cm^{-1} , which are attributed to C-OH stretching vibration and C-O stretching vibration in the epoxy group respectively.²³ The peaks at 1396 and 400-700 cm^{-1} suggest the presence of both Ti-O and Ti-O-Ti, indicating the formation of chemical interactions between functional groups in rGO and surface hydroxyl groups of TiO_2 nanoparticles.²⁵

Photoluminescence (PL) Spectra is widely employed to investigate the behaviours of photoinduced e^-/h^+ pairs, including trapping, immigration and transfer of charge carries.⁷² PL phenomenon occurs due to the emitted photons, which is from the exceeded energy when the recombination of charge carrier takes place under irradiation. The weakened PL signal observed in FF-15%rGO in Figure 3-3f indicates that photoelectrons were either trapped by defect sites (e.g., oxygen vacancies) or immigrating from TiO_2 surface to rGO sheets prior to their recombination with holes.¹⁶⁷ Under both circumstances, the recombination behaviour of photoinduced e^-/h^+ pairs will be effectively blocked and the lifetime of charge carries will be promoted, accounting for an enhanced photocatalytic activity in FF-15%rGO.

We further investigated the chemical nature of modified wool fabrics through XPS, which confirms the existence of C, N, O and Ti compositions in FF-15%rGO (Figure 3-3g). The high resolution of C 1s XPS spectra (Figure 3-3h) suggests the existence of C-C bond (284.7 eV) and C-O-C of epoxy group (286.6 eV). The absence of C=O (carboxyl group) indicates GO in the composite has been reduced, which is in accordance with Raman results. The peaks located at 458.9 and 465.0 eV are related to Ti $2p_{1/2}$ and Ti $2p_{3/2}$ spin-orbital splitting photoelectrons from C-Ti bond (Figure 3-3i), suggesting chemical bond between TiO_2 and rGO has been well formed.¹⁶⁸

3.3.3 Adsorbing capacity of FF-rGO

The dark adsorption test was employed to measure the adsorbing capability of FF-rGO without irradiations. The adsorption of pollutant such as MB is mostly based on physical interactions as shown in the theoretical schematic illustration (Figure 3-4a). Electrostatic interaction as well as π - π stacking between MB molecular and functional groups in rGO play important roles in the generation of adsorbing behaviour.¹⁰² The adsorption isotherm of various FF-rGO was studied to quantitatively investigate the amount of MB molecular left in solution when the adsorption process reaches equilibrium. MB molecules are more favourably adsorbed by the FF-rGO in high-concentration MB solutions instead of FF-TiO₂ as shown in Figure 3-4b. Especially for FF-15%rGO, whose equilibrating adsorbing capacity reaches 145.68 mg/g ($R^2=0.99$) at an initial MB concentration of 20 mg/L and is much larger than that of FF-TiO₂ (71.15 mg/g, $R^2=0.97$). The adsorbing ability increases with higher contents of rGO incorporated in FF-rGO from 5% to 15%. However, less MB molecules were adsorbed even more rGO was incorporated (20%), which could be explained by the lower exposure of functional groups in FF-20%rGO caused by overlapping behaviour of exceeded rGO sheets.

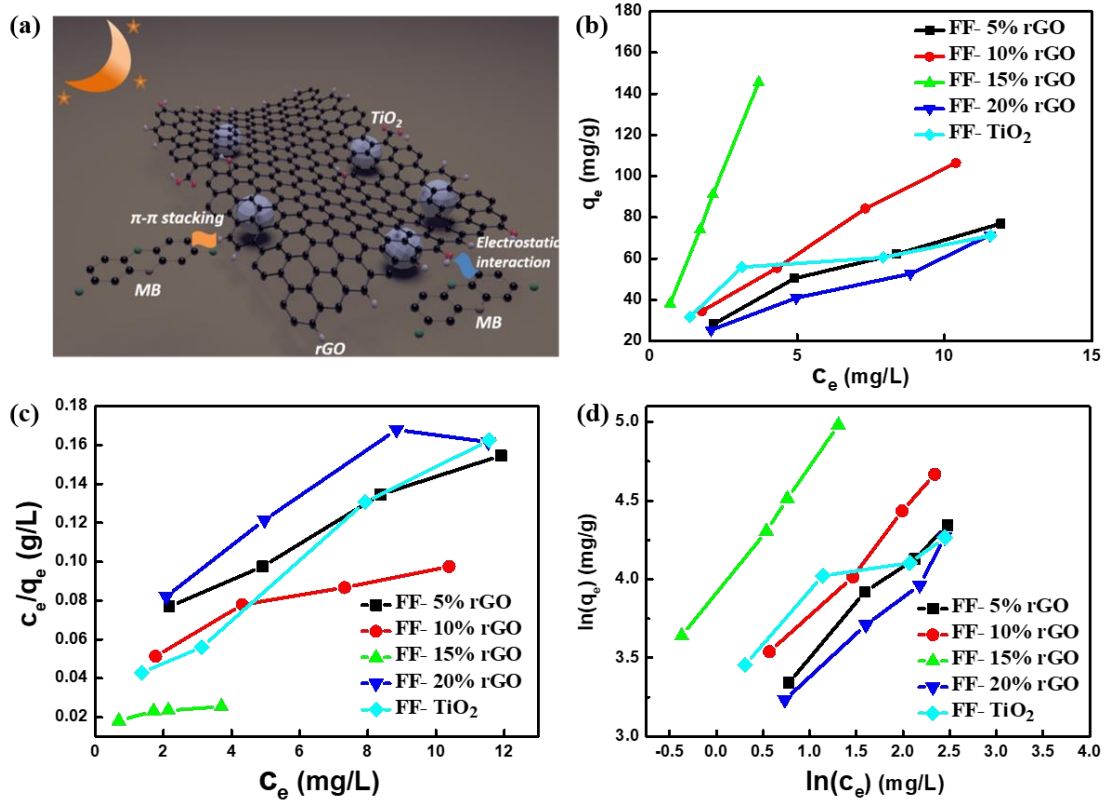


Figure 3-4. a) Schematic diagram of interactions between MB molecular and rGO sheets. b) Adsorption isotherms of MB adsorbed by FF-TiO₂ and FF-rGO under room temperature (20°C). c) Adsorption isotherms of MB analysed by Langmuir model. d) Adsorption isotherms of MB analysed by Freundlich model.

Several mathematical models have been implemented to describe the equilibrium of adsorption. The Langmuir model and Freundlich model are most frequently and widely spread among them. When applying the Langmuir model, there is a hypothesis that the uptake of dyes only occurs on a homogenous surface by monolayer adsorption.¹⁶⁹ The equation shows as:

$$\frac{C_e}{q_e} = \frac{C_e}{q_{max}} + \frac{1}{q_{max}K_L} \quad (3)$$

Where q_{max} (mg/g) is the maximum adsorbing capacity corresponding to complete monolayer coverage, K_L (L/g) is a constant related to adsorption capacity and energy of adsorption. The results from Langmuir model in Figure 3-4c show that the maximum adsorption for FF-15%rGO predicts to be 427.35 mg/g. The higher correction

coefficients of R^2 ($R^2=0.957$) suggests the excellent fitting of experimental data by Langmuir model, while FF-TiO₂ only obtains maximum adsorption with 80.76 mg/g ($R^2=0.978$). The dramatic improved maximum adsorbing capability indicates the great significance of 15%rGO incorporated in FF-rGO in adsorption enhancement of dyes, which is also confirmed by the comparative table of recent reports about adsorbing capacities of various adsorbents to MB (Table S3-2). While the Freundlich model assumes that the adsorption takes places on a heterogeneous surface.¹⁷⁰ The equation is represented by:

$$\ln q_e = \ln k_f + \frac{1}{n} \ln c_e \quad (4)$$

Where k_f (L/g) and n are the Freundlich constants, representing adsorption capacity and adsorption intensity respectively. The calculated values from Freundlich model in Figure 3-4d show an improved adsorption capacity of FF-15%rGO ($k_f=1.37$ L/g, $R^2=0.998$). The values of n are all between 1 and 10, indicating MB molecules are favourable adsorbed both on FF-TiO₂ and FF-rGO. The lower R^2 of FF-TiO₂ in Freundlich model ($R^2=0.811$) than that in Langmuir model ($R^2=0.978$) suggests the adsorption activity of FF-TiO₂ take place most likely on a homogenous surface. On the contrary, FF-20%rGO exhibits totally opposite results with a lower R^2 ($R^2=0.821$) in Langmuir model and higher R^2 ($R^2=0.969$) in Freundlich model, as represented in Table S3. Such results suggest more rGO sheets were wrapped on the fabrics to form heterogeneous surface and these extra rGO sheets make negative effects to the adsorption of MB.

3.3.4 Enhanced photocatalytic performance of FF-rGO

The photocatalytic performance of FF-rGO was evaluated by degrading MB solution under a 150 W Xenon lamp as shown in Figure S3-5. For comparison, FF-TiO₂ was evaluated under the same condition to discover the influences of rGO to the overall photocatalytic activity. The curves of MB degradation against time with different

functionalised fabrics indicate the photocatalytic degradation performance has been improved when the fabrics were incorporated with rGO (Figure 3-5a). More specifically, more than 80% of MB was removed after 30 min's photocatalysis and 95% of MB was removed after 60 min's photocatalysis in terms of FF-15%rGO, while these degradation rates decline to 50% for 30 min's photocatalysis and 80% for 60 min's photocatalysis respectively in terms of FF-TiO₂. The photocatalytic efficiency has almost doubled due to the presence of rGO in TiO₂/15%rGO composite. Although when increasing rGO content to 20%, the photocatalytic efficiency of FF-20%rGO was slightly decreased compared with that of FF-15%rGO. This is mostly because the extra rGO sheets brought about blockage between the light and TiO₂ nanoparticles, resulting in luminous energy loss in the transporting process. Figure 3-5b presents the UV-Vis adsorption spectra of MB aqueous during photodegradation for FF-15%rGO. The continuous decrease of characteristic peak at 664 nm indicates the photodegradation was in progress. The sharp decrease of MB characteristic peak in the first 30 min suggests the degradation rate was fast at the beginning due to the abundant MB in the aqueous. The colour of MB changed from blue to colourless demonstrates the chromophore of MB was removed and the benzene rings were cracked down during the photodegradation process(Figure 3-5b).¹⁷¹

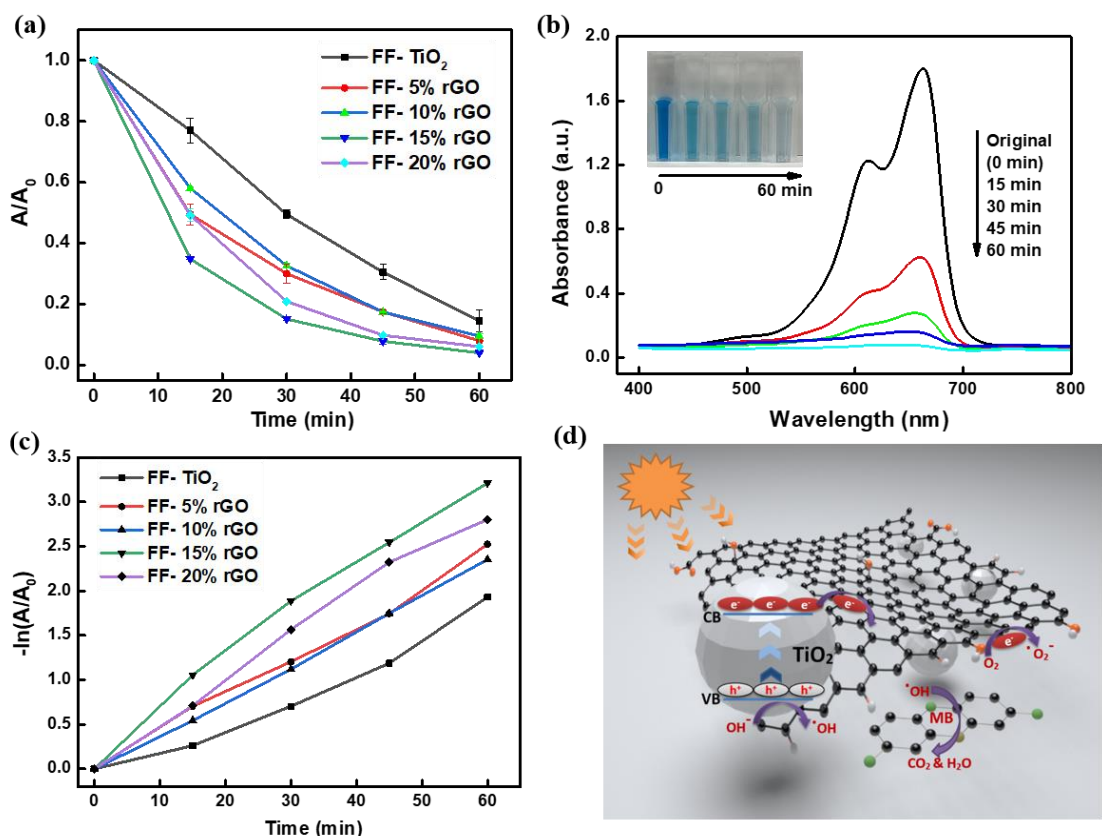


Figure 3-5. a) The photocatalytic degradation of MB over different fabrics. b) The adsorption spectra of MB photodegraded by FF-15%rGO. c) Kinetic linear simulation curves for photodegradation of MB over different fabrics. d). Schematic diagram showing electron transporting path during photodegradation of MB.

In order to have better understandings of photocatalytic efficiency regarding to the above photocatalysis. The photocatalytic degradation kinetics was investigated by pseudo-first-order kinetics,¹⁷² represented as:

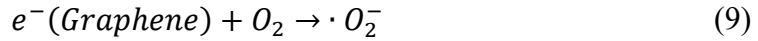
$$\ln \frac{A}{A_0} = kt \quad (5)$$

Where k is the photocatalytic reaction apparent rate constant and t is the irradiation time. The slopes of curves in Figure 3-5c were calculated as 0.0319, 0.0406, 0.0394, 0.0528 and 0.0481 for FF- TiO_2 , FF-5%rGO, FF-10%rGO, FF-15%rGO and FF-20%rGO respectively. The k values of FF-rGO are much higher than that of FF- TiO_2 , which further proves the introduction of rGO has significant effects for the photocatalytic enhancement.

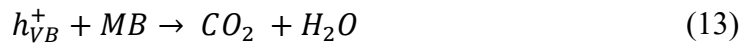
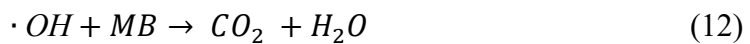
The improved photocatalysis was beneficial from the incorporation of rGO which extends the lifetimes of separated electron-hole pairs by providing alternative paths for electron transportation. During the photocatalysis, MB was mainly degraded by photoinduced holes (h_{VB}^+), hydroxyl radical ($\cdot OH$) and superoxide radical ($\cdot O_2^-$) derived from TiO_2 photocatalysts under irradiation.¹⁷³ The schematic mechanism of photodegradation process of MB by FF-rGO is illustrated in Figure 3-5d. Electrons (e^-) were firstly promoted from the valence band (VB) to conduction band (CB) of TiO_2 under light irradiation, leaving holes (h_{VB}^+) with positive charges in the VB. The photoinduced electrons could immediately react with oxygen (O_2) to create superoxide radical ($\cdot O_2^-$), which is presented by:



Alternatively, by the presence of rGO sheets, electrons could also transport from CB of TiO_2 to rGO sheets which inhibits the recombination of electron-hole pairs and prolongs the effective lifetimes of separated carries. The electron transport between TiO_2 and rGO can be presented by:



The production of $\cdot O_2^-$ would contribute to generate $\cdot OH$. The h_{VB}^+ and $\cdot OH$ played primary and secondary roles during the photodegradation of MB respectively. The inhibition of recombination between electron-hole in the previous process also extended the lifetime of h_{VB}^+ , enabling their reactions with H_2O to generate more $\cdot OH$ which could directly oxidize MB. The reaction process can be illustrated by:



3.3.5 Integration of night-time adsorption and day-time photodegradation

Under the scenario of practical application, most of traditional photocatalysts are typically designed to functionalise in the daytime when sufficient light irradiations are supported. The FF-rGO introduced here not only enhances the photocatalytic performance under light irradiation, it is also possessed of abundant adsorption with pollutants even without irradiation participated, especially in the nighttime when the functionalised fabrics could take full advantage of. The collaboration of day-time photodegradation and night-time adsorption optimizes the degradation efficiency of pollutants. Figure 3-6a shows the adsorption and degradation process of MB by FF-TiO₂ and FF-rGO during six-hour dark adsorption and one-hour photocatalysis. After six hours' adsorption, the MB concentration in solution with FF-TiO₂ didn't show any declines which suggests FF-TiO₂ was not capable of adsorbing MB molecules in such short time, while the significant declines of MB concentration in solution with FF-rGO indicates the rapid adsorbability of FF-rGO. The following one-hour photodegradation results show great improvement of total degradation efficiency by FF-rGO. Figure 3-6b presents the UV-Vis adsorption spectra of MB aqueous during the adsorption and photocatalysis for FF-15%rGO. The sharp decline of MB concentration after 15 minutes' photocatalysis demonstrates large amounts of MB molecules were aggregated and adsorbed on the photocatalysts surface before photodegradation, and instantly photodegraded once the irradiation was generated.

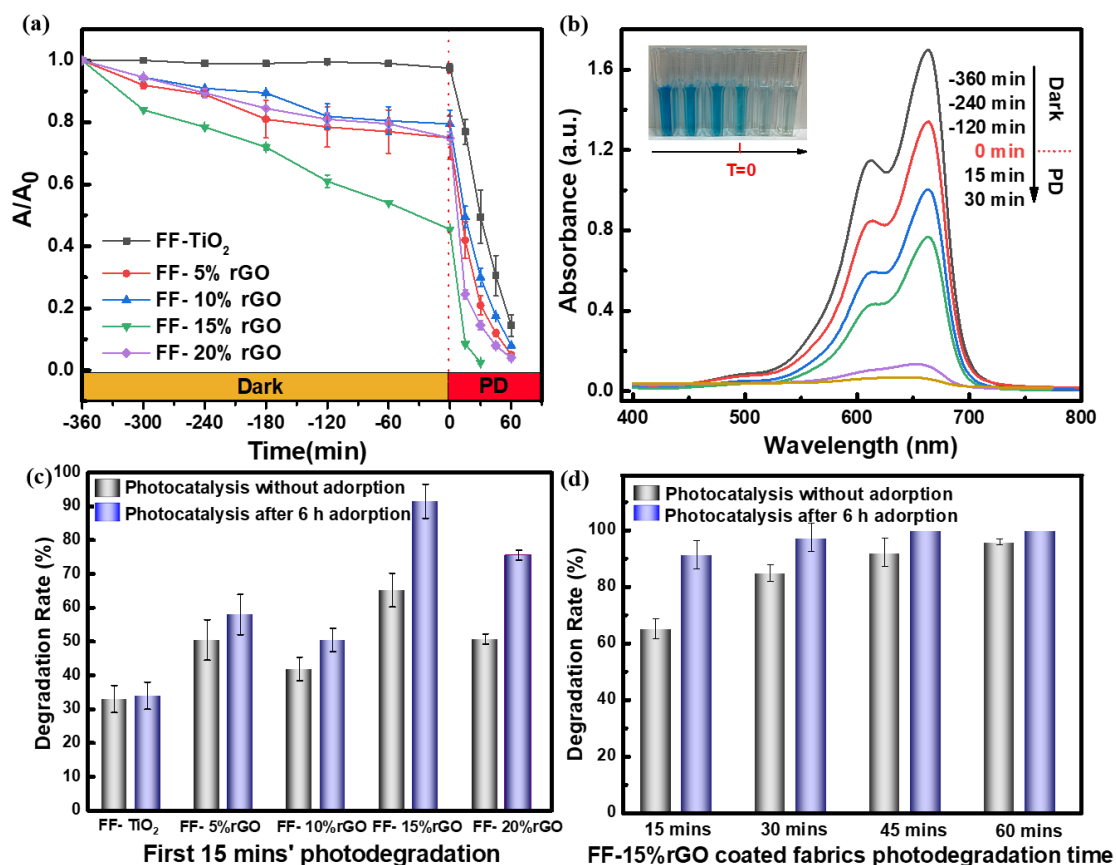


Figure 3-6. a) The integration of dark adsorption and photodegradation (PD) of MB over different fabrics. b) The adsorption spectra of MB by FF-15%rGO throughout dark adsorption and photodegradation. c) The comparisons of degradation rates within and without 6 hours' adsorption after the first 15 minutes' photodegradation of MB by different fabrics. d) The comparisons of degradation rates within and without 6 hours' adsorption by FF-15%rGO.

The comparisons of photocatalytic performance within and without six-hour pre-adsorption are shown in Figure 3-6c and Figure 3-6d respectively. At the first 15 minutes' photodegradation, there is a significant increase of degradation rate for FF-rGO within six-hour pre-adsorption (Figure 3-6c). Typically for FF-15%rGO and FF-20%rGO, which increases 26.3% and 24.7% respectively. The continuous photodegradation performance of FF-15%rGO shows 98% of MB has been photodegraded within 30 minutes if six-hour pre-adsorption was performed, while 60 minutes was taken to photodegrade such level of MB if no extra pre-adsorption activity was carried out (Figure 3-6d). Table S3-4 summarizes the photodegradation efficiency

of TiO₂-based materials, which indicates the remarkable degradation intensity of FF-15%rGO and significant enhancement in overall degradation intensity if extra pre-adsorption was participated. We have also analysed the adsorbing and photocatalytic activity of FF-rGO against another organic pollutant (Rhodamine B (RhB)) in water under the same condition. The similar adsorption and photodegradation performance of FF-rGO both in MB and RhB aqueous indicates that TiO₂/rGO coated wool fabrics can be applied into water purification affected by various dyestuffs (Figure S3-6).

3.3.6 Sustainability of FF-rGO

The stability and durability of the adsorption and photodegradation performance of FF-15%rGO was evaluated as shown in Figure 3-7a. The adsorption efficiency changes from 55% for the 1st cycle to 46% for the 4th cycle, and overall degradation efficiency changes from 98% for the 1st cycle to 92% for the 4th cycle. The overall performance does not obviously deteriorate after four cycles, revealing the outstanding sustainability of FF-15%rGO.

By considering the adsorption and photocatalytic activities always take place under water, FF-rGO requires more stability of photocatalysts on wool fabrics. We immersed FF-15%rGO into deionised water under ultrasonic treatment for 20 mins for each wash cycle. The wash test indicates that photocatalytic performance of FF-15%rGO only slightly reduced after 3 times washing cycles (Figure 3-7b). The 30-day soaking test proves that photocatalysts (TiO₂/rGO nanoparticles) could be more stably coated on wool fabric surface under water compared with non-rGO incorporated photocatalysts (Figure 3-7c). Such reliable stability in water is beneficial from the presence of strong bonds between rGO and TiO₂ nanoparticles, which has been confirmed in FTIR (Figure 3-3e) and XPS (Figure 3-3g) analysis.

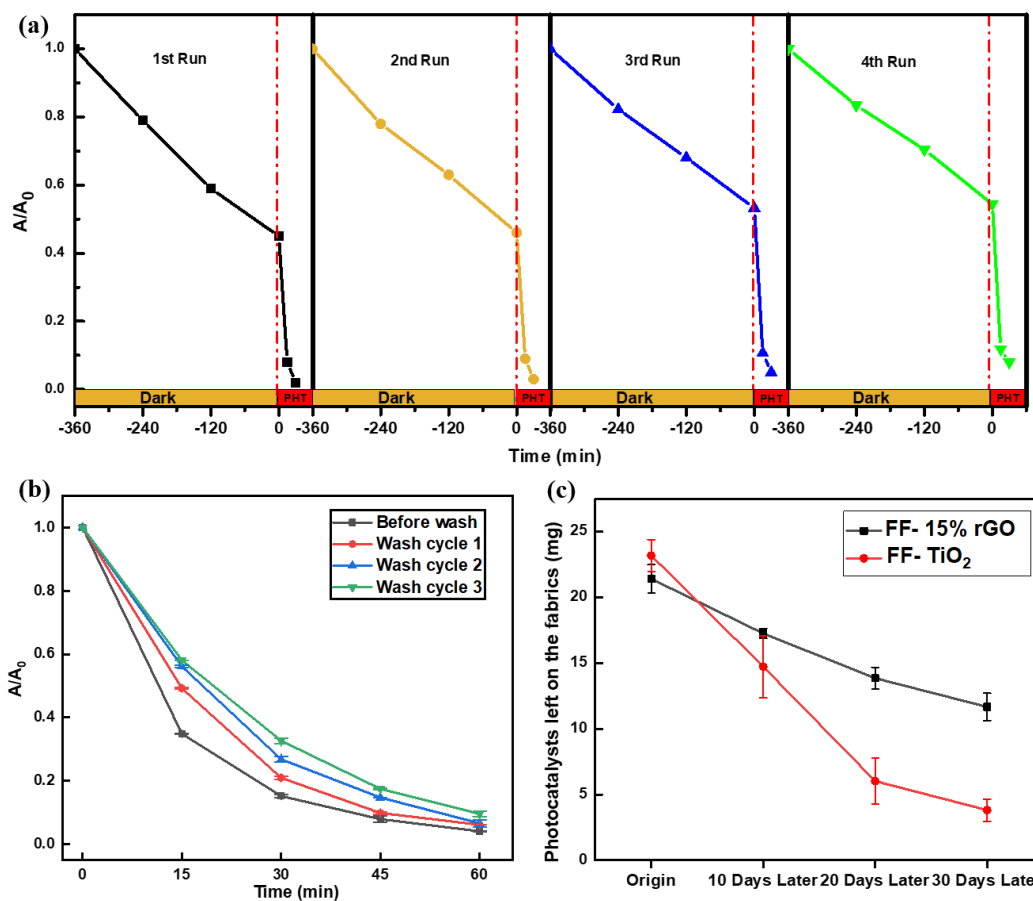


Figure 3-7. Sustainability of FF-rGO. a) Recyclability of continuous dark adsorption and photodegradation of MB by FF-15%rGO. b) Wash test of FF-15%rGO. c) Stability of photocatalysts on FF-15%rGO.

3.3.7 Applications in degradation of large-amount dyestuffs contaminations

We carried out experiment to identify the waste textile reutilisation and its practical application in degradation of large-amount dyestuffs contaminations. Figure 3-8a shows the wasted socks were pad dyed by $TiO_2/15\%rGO$ to achieve the optimised adsorbing and photocatalytic capacities. The functionalised sock was immersed in a tank with 4 L MB solution (10 mg/L) for 120 h (continuous alternation of 12 hours' night-time adsorption and 12 hours' day-time photocatalysis). More than 93% of MB in solution was removed after 120-hour continuous adsorption and photodegradation

(Figure 3-8b). The dark grey area and light grey area in Figure 3-8c represents the contribution of adsorption and photocatalysis to the overall degradation of dyestuff respectively. The colour change of MB solution in Figure 3-8d and Figure S3-7 suggests the adsorbing and degrading progress. It indicates that the integrated system of night-time adsorption and day-time photocatalysis optimizes the overall degradation of dyestuffs and have great significance to the wastewater treatment.

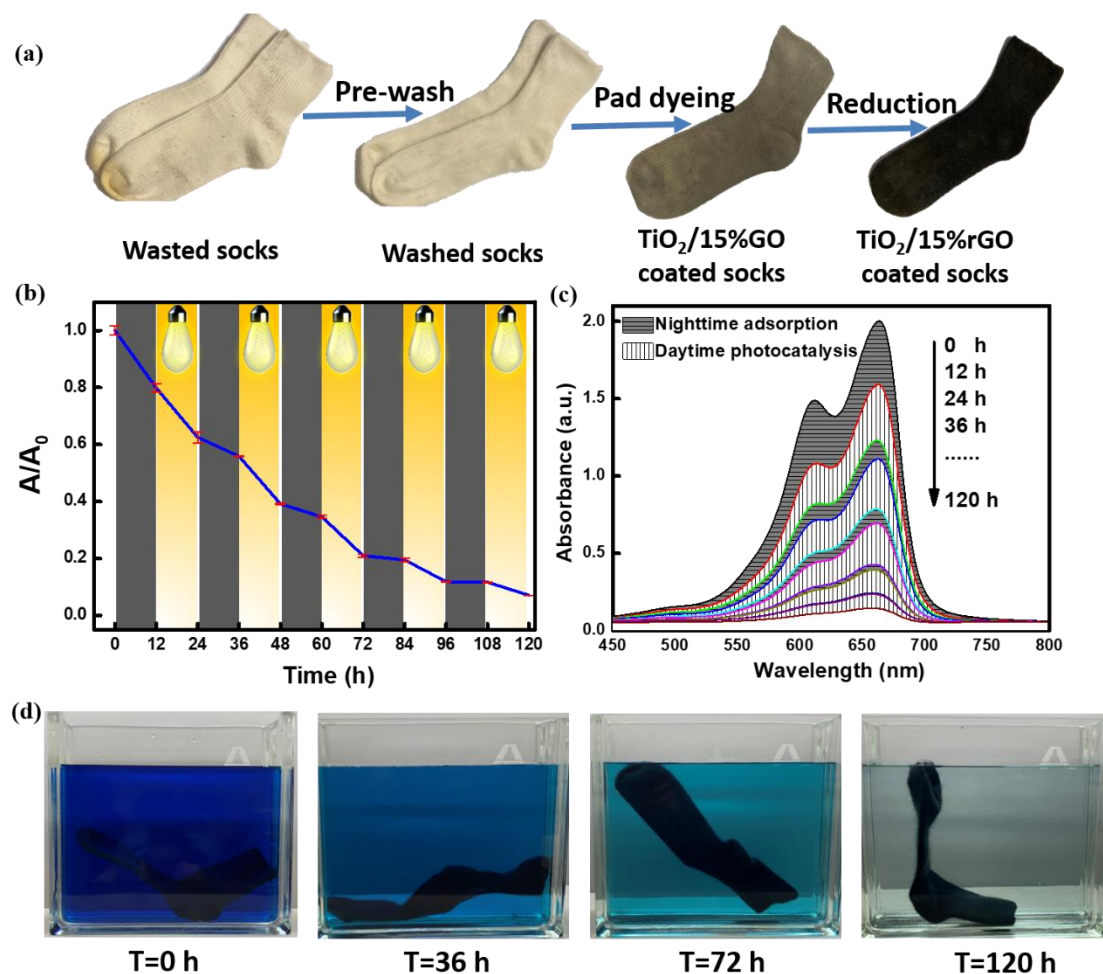


Figure 3-8. Wasted socks reutilisation in degradation of large-amount dyestuffs contaminations. a) Pad dye wasted socks into TiO₂/15%rGO functionalised socks. b) The adsorption and photodegradation of 4 L MB (10 mg/L) by functionalised sock over 120 hours, 12-hour nighttime adsorption and 12-hour daytime photodegradation for each day. c) The corresponding adsorption spectra of MB. d) The colour change of MB solutions at 0 h, 36 h, 72 h and 120 h.

3.4 Conclusions

In summary, we have introduced a concept to reutilize waste textiles in a green and sustainable manner through pad dyeing technology. The TiO₂/rGO functionalised fabrics exhibit decent sustainability, improved adsorbing and photocatalytic performance, displaying great potentials to solve the concerns of overproduced textiles and water contaminations arising from fast fashion industry. The FF-15%rGO presents the best adsorbing and photocatalytic performance, with maximum adsorbing capacity of 427.35 mg/g for MB and complete photodegradation of MB (100 mL, 10 mg/L) within 60 minutes. Particularly, we integrated pre-adsorption and photodegradation as a combined system, which significantly shortened the photodegradation process to 30 minutes. Such collaborative system takes full advantages of night-time adsorption and prominently improves the overall degradation efficiency in the practical applications, paving a new route for environmental remediation.

3.5 Supplementary information



Figure S3-1. Images of 5×5 cm wool fabric before and after treatment. a) Pristine 5×5 cm wool fabric. b) FF-20%GO after pad-dyeing process. c) FF-20%rGO after L-ascorbic acid (L-AA) reduction.

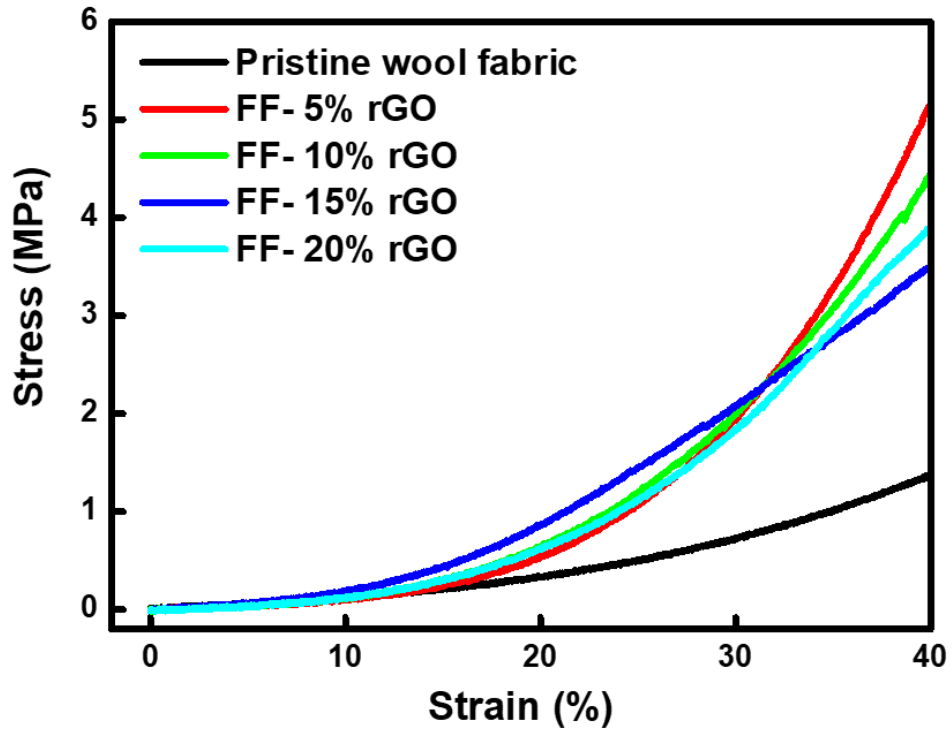


Figure S3-2. Comparison of mechanical properties of pristine and FF-rGO. The test was under x -axis direction of the wool fabrics. It indicates an improvement of mechanical property after pad-dyeing and L-AA acid reduction process of wool fabrics.

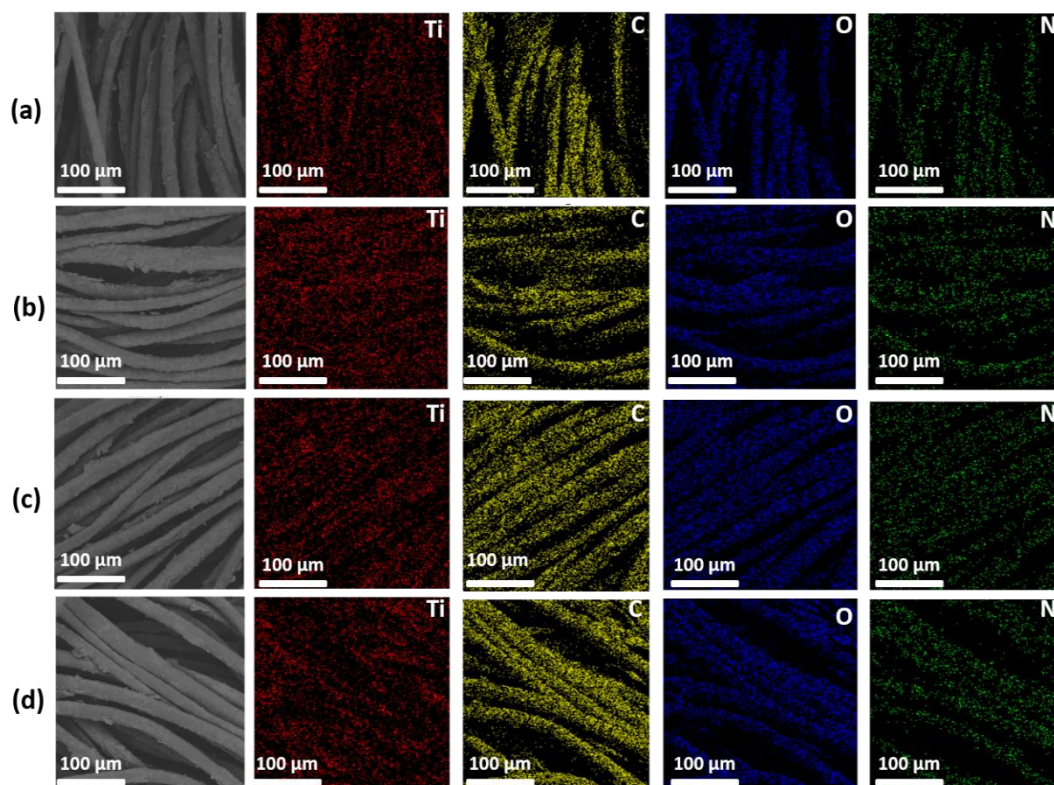


Figure S3-3. EDX mapping images of FF-rGO and element distribution of Ti, C, N and O. a) FF-5%rGO. b) FF-10%rGO. c) FF-15%rGO. d) FF-20%rGO.

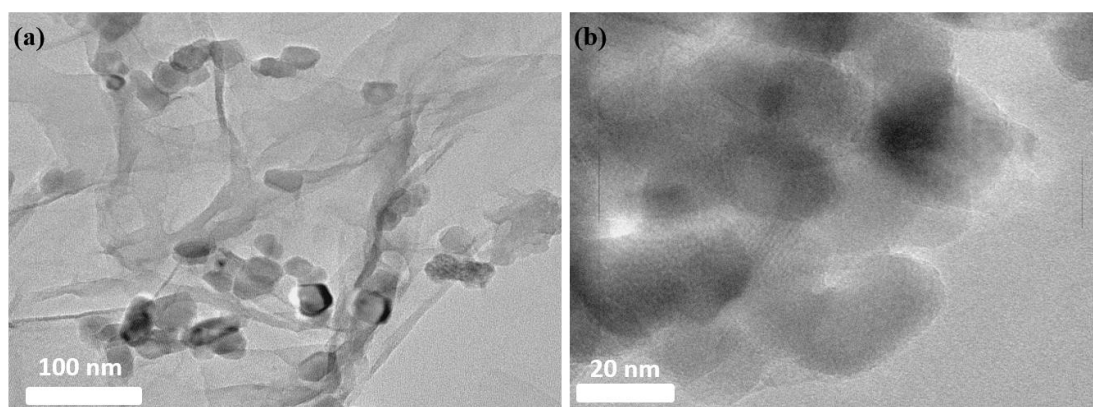


Figure S3-4. a) TEM image of FF-15%rGO. b) TEM image of FF-15%rGO with higher resolution.



Figure S3-5. Illustration of photocatalytic degradation measurements.

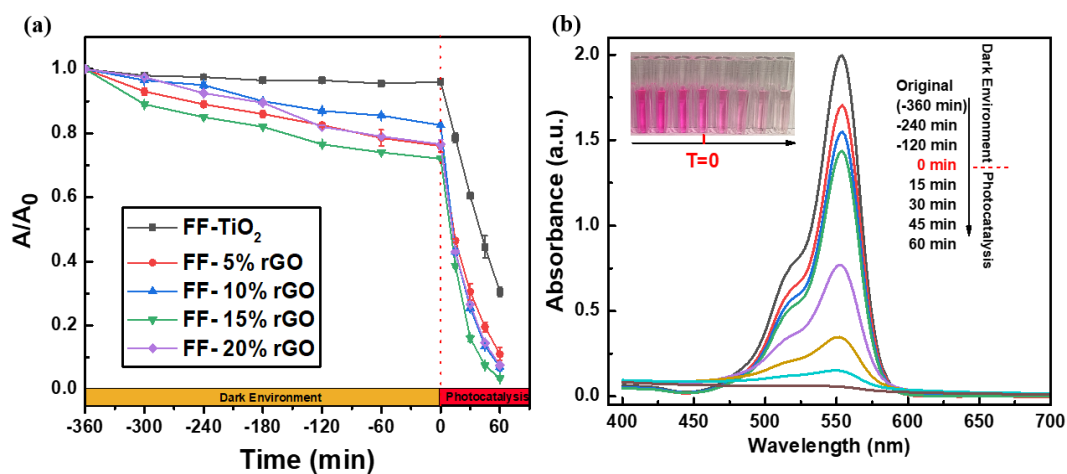


Figure S3-6. Adsorption and photodegradation results of Rhodamine B (RhB). a) Adsorption and photodegradation results during six hour's adsorption and one hour's photocatalysis. b) UV-Vis adsorption spectra of RhB aqueous.

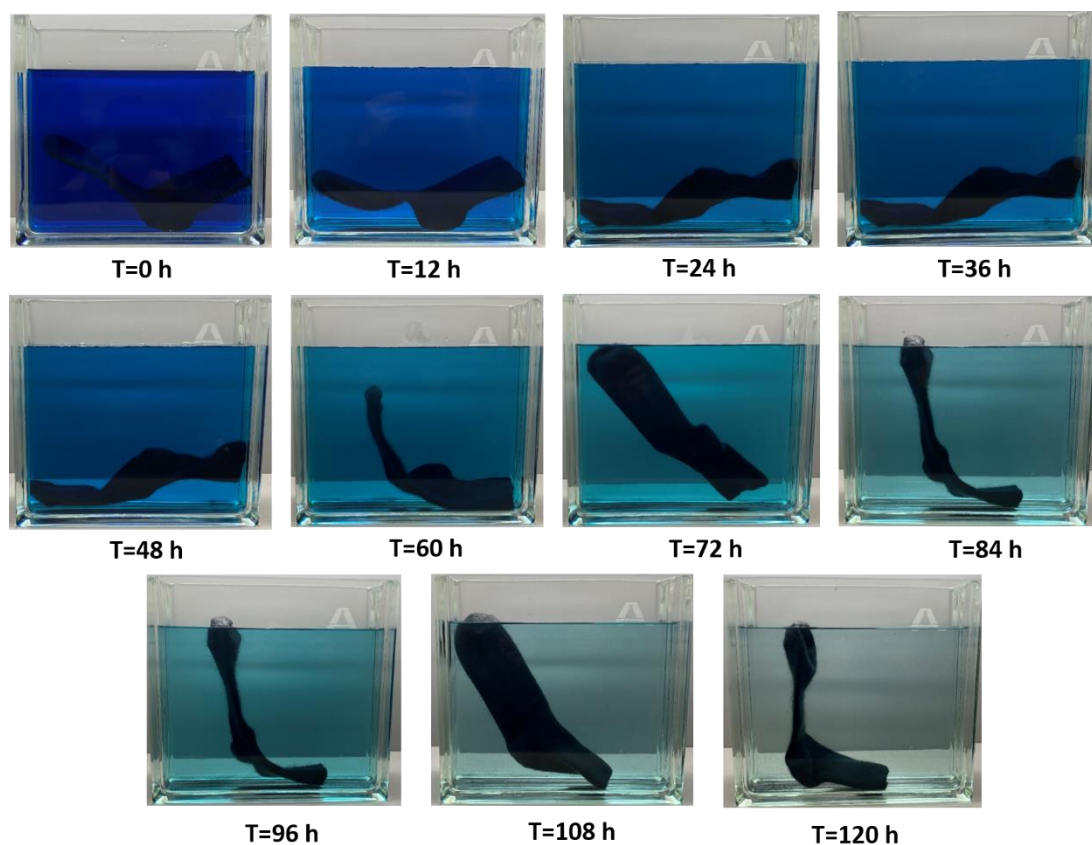


Figure S3-7. The colour change of MB solutions over 120 h.

Table S3-1. Grain size and FWHM of FF-rGO

Fabrics	Full width at half maximum (FWHM)	Grain size/nm
FF-TiO ₂	0.4678	17.23
FF-5%rGO	0.4815	16.74
FF-10%rGO	0.4614	17.46
FF-15%rGO	0.5088	15.84
FF-20%rGO	0.4958	16.26

Table S3-2. Adsorption capacities of various adsorbents to MB

Adsorbents	Adsorption capacity (mg.g ⁻¹)	References
GO	144.92	103
GO/CA	181.81	103
Graphene	153.85	104
Carbon nanotubes	46.20	105
Modified activated carbon	232.5	106

PT-GO bio-adsorbent	256.58	107
Carbon nanotubes with tannins	105	108
PDA-kaolin with rGO	39.66	109
PVA/CMC hydrogel-GO	172.14	110
TiO₂/15%rGO coated wool fabrics (FF-15%rGO)	427.35	This work

Table S3-3. Analysis of adsorption activity based on Langmuir and Freundlich model

		FF- TiO ₂	FF-5%rGO	FF-10%rGO	FF-15%rGO	FF-20%rGO
Langmuir	q_{max} (mg/g)	80.76	121.07	198.02	427.35	111.61
	K_L (L/g)	0.519	0.139	0.104	0.138	0.125
	R^2	0.978	0.979	0.861	0.957	0.821
Freundlich	k_f (L/g)	1.239	1.073	1.145	1.372	1.029
	n	2.917	1.727	1.559	1.243	1.749
	R^2	0.811	0.981	0.988	0.998	0.969

Table S3-4. Comparisons of degradation intensity for TiO₂-based composites

Photocatalyst	Phtocata- lyst mass (g)	MB volume (L)	MB concentrat ion (mg/L)	Illumination intensity (kW)	Complete degradatio n time (h)	Overall degradatio n intensity (mg/h kw g)	Ref
TiO ₂ /5%GO nanofiber	0.1	0.1	30	0.5	0.83	72.29	111
Bi ₂ WO ₆ /TiO ₂ polyester fabric	0.2	0.05	10	0.5	2.5	2	15
Graphene/ TiO ₂ fiber	0.4	0.1	30	1	2	3.75	17
Ag ₂ O-TiO ₂	0.1	0.1	160	0.16	6	166.67	112
Ni/Cr-TiO ₂	0.1	0.05	5	Sunlight (0.6)	1.5	2.78	113
rGO-TiO ₂	0.23	0.04	10	0.15	2	5.8	114

(with 0.5 h adsorption)							
TiO ₂ nanoparticle	0.1	0.6	10	0.006	3	333.33	115
(with 1h adsorption)							
FF-15%rGO	0.023	0.1	10	0.15	1	289.86	This work
FF-15%rGO (with 6 h adsorption)	0.023	0.1	10	0.15	0.5	579.72	This work

Chapter 4

Coolmax/Graphene-Oxide Functionalised Textile Humidity Sensor with Ultrafast Response for Human Activities Monitoring

This chapter focuses on completing the third objective addressed in Chapter 1.3. The research work has been published in Chemical Engineering Journal.

Authors: Lulu Xu, Heng Zhai, Xiao Chen, Yulong Liu, Miao Wang, Zhangchi Liu, Muhammad Umar, Chengyu Ji, Zhongda Chen, Lu Jin, Zekun Liu, Yi Li and Terry T. Ye

Journal: Chemical Engineering Journal (DOI: 10.1016/j.ecj.2021.128639)

Statement of own contributions in joint authorship: L.X. and H.Z. have contributed equally to this manuscript as first author. L.X. focused on the main research idea development, data acquisition and draft manuscript preparation. H.Z. focused on the methodology, material fabrication, characterisation and revision. Specifically, Conceptualisation, L.X., H.Z., Y.L. and T.Y.; Methodology, L.X., H.Z. and Z.C.; Materials preparation, L.X., H.Z. and Z.L.; Characterisation, L.X., H.Z. and C.J.; Formal Analysis, L.X., H.Z. and X.C.; Data Curation, L.X., H.Z. and L.J.; Original draft preparation, L.X.; Manuscript revision, H.Z.; Supervision, Y.L. and T.Y.

Abstract

Among different fibrous e-textile sensors, humidity sensor has a particular significance in respiration monitoring, water presence alert, and skin contact/non-contact indication. These applications not only demand sensors to have fast response and recovery speed, robustness to attrition and friction, the sensors' responses also need to be unimodal, i.e.,

only sensitive to humidity and insensitive to other impacts, such as temperature variation, folding and stretching of the fabric. Previously reported e-textile humidity sensors, when being used as a quick humidity indicator, suffered from slow response/recovery time, interference from multimodal sensitivities, or devices are non-fabric based and cannot be seamlessly integrated with apparels. In this paper, we have studied textile-based humidity sensors constructed from different natural and synthetic fibres (cotton, wool and Coolmax) and discovered that the graphene-oxide (GO) functionalised Coolmax humidity sensor (GO-Coolmax) exhibits ultrafast response/recovery time (less than 0.6 s). The sensor is also insensitive to external pressure and temperature changes, i.e., the resistance variations caused by these impacts are within 10%, much smaller than that from humidity variations (above 80%). We have also demonstrated the use of the sensor as a humidity indicator/alert in various wearable applications through prototyping and experiments.

Keywords: graphene oxide, Coolmax fibre, humidity sensor, e-textile

4.1 Introduction

Fibre-based e-textiles with sensing functionalities have gained great attentions in wearable electronics and intelligent robots industries.¹⁷⁴ E-textile devices, which can be seamlessly built into apparels by weaving, knitting, braiding, and embroidery processes, will provide aesthetic and comfortable methods for medical sign monitoring, sports and body movement tracking, as well as other wearable applications that need long-term, real-time and non-intrusive sensing and logging capabilities. Among various kinds of sensing devices, humidity sensor has a particular significance in e-textile research. They are widely used in many crucial scenarios, including human respiration monitoring,¹⁷⁵ skin hydration monitoring,¹³¹ contact/non-contact touch,¹⁷⁶ water presence (e.g., urine detection for diapers^{177, 178}), as well as wound treatment and healing.¹⁷⁹

Humidity sensors are usually constructed by conductive electrodes and humidity sensitive materials, which can interact with water molecules. The interaction causes electrical properties, such as resistance or capacitance, or both, to vary under different humidity or water content levels. Different materials have been investigated for humidity sensing in the past, i.e., semiconductor materials,¹²⁸ perovskites,¹⁸⁰ and polymers¹⁸¹ as humidity sensitive substrates; graphene,^{130, 176, 182} and carbon nanotubes¹⁸³ as humidity sensitive electrodes. Meanwhile, extensive research have been conducted for the optimisation of sensor's structure to enhance their water adsorption and desorption capabilities, e.g., microfluidic design,¹⁸⁴ fibrous Murray,¹⁸⁵ and 3D porous nano-channels.^{131, 186} These efforts present significant progresses toward higher sensors sensitivity, rapid response and recovery speed, enhanced stability and better reliability. It is worthwhile to mention that these sensors are mostly constructed from non-textile materials and they cannot be seamlessly integrated with fabric or apparel.

In addition to the requirements of sensing capabilities, textile-based sensors, as to be integrated with apparels, also demand materials to be soft, breathable, flexible and comfortable. Furthermore, textile-based sensors are to be deployed in human's daily wearable conditions. Sensors should be sensitive to the humidity level, and resilient to other variables, such as temperature, pressure, folding and stretching of fabric. To date, several approaches have been conducted to construct textile-based capacitive,¹¹⁹ resistive¹⁸⁰ or impeditive¹⁸⁷ humidity sensors. Zhou et al. developed a fibre-based resistive humidity sensor using single-walled carbon nanotubes with a Poly (vinyl alcohol) (PVA) matrix, which exhibited high sensitivity and high strength.¹⁸⁸ Guo et al. presented a stretchable resistive humidity sensor by polyaniline composite fibre.¹²⁷ Liu et al. proposed a resistive humidity sensor based on super-hydrophobic silk fabric with silver nanowires.¹²⁵ Graphene-based 2D materials with large surface area have been explored for humidity sensing as well. For example, reduced graphene oxide (rGO) has been studied as sensitive electrodes to fabricate the capacitive humidity sensor.^{177, 189}

Graphene oxide (GO), a semi-conductive material rich in oxygen-related functional groups (e.g., epoxy, hydroxyl and carboxyl groups), was used to construct a sensitive layer on textiles for humidity sensing.^{130, 190}

Although these approaches represent significant progress in the feasibility study of e-textiles as humidity sensors, there are major challenges yet to overcome. For instance, compared with film-based humidity sensors, textile-based sensor needs much more time to respond,¹²⁵ stabilize and recover,^{123, 127, 188} which prohibits its applications in real-time monitoring, where a typical less than 1s reaction time is required. Also, for long term wearing applications, the sensing materials need to be robust from attrition and friction caused by body movements.

In this paper, we have explored different fibre materials coated with graphene oxide and compared their response and recovery time to be used as humidity sensors. Three different fibres are selected, namely, cotton, wool and Coolmax. Coolmax is the brand name for a series of polyester fabrics developed by Dupont Textiles. Fibres were functionalised with GO solution through the pad-dyeing process, which forms a robust layer of GO coating on fibres. The GO layer formed on the fibre surface is very adhesive and will not easily degrade under washing cycles or with constant pressure. This proposed pad-dyeing process is simple, cost-effective, and feasible for large-scale manufacturing. We also study the morphological structures and chemical components of these fibres and explored the mechanism that underlines the performance differences as humidity sensors. We found that Coolmax fibre, functionalised with GO (GO-Coolmax), exhibits good resistive humidity sensing capabilities with ultrafast response and recovery time within 0.6 s. It also works well when being immersed with water for water presence sensing. Moreover, it is pretty resilient to pressure and temperature variations, i.e., the external pressure (range from 0 to 2 MPa) and temperature variation (under room temperature range from 20 to 40 °C) only cause resistance changes within 10%, as compared to over 80% of resistance changes caused by humidity variation (from 45% to 80%). We further demonstrate several potential applications for this GO-

Coolmax humidity sensor, i.e., 1) as a respiration sensor to monitor human breathing activities, 2) as a perspiration sensor to monitor the athletes' sport activities, 3) as a water presence sensor for baby diaper wet-alert and 4) as a finger touch sensor to be used as a fabric keypad.

4.2 Experimental section

4.2.1 Preparation of the graphene dispersion

Expandable graphite flakes (particle size larger than 300 μm) were supplied by Sigma-Aldrich. The GO dispersion was prepared according to a modified Hummers method.¹⁹¹ It was further stirred and washed in deionised water to remove the residual acid to adjust the pH value around 7. Then it was diluted with deionised water until reaching the concentration of 2 mg/mL. The morphology and structure of single-GO sheets are shown in Figure S4-1 (Supporting Information).

4.2.2 Preparation of GO-fibres and sensors

Three types of fibres (cotton, wool and Coolmax) were used for GO functionalisation. Before pad-dyeing with GO, fibres were pre-washed by deionised water for several times. Then fibres were functionalised by GO in a pad-dyeing machine with lowest pressure and speed. The fibers were padded and dried with 3 cycles (Figure 4-1a). The functional fibres referred as GO-fibres in general, or GO-cotton, GO-wool and GO-Coolmax respectively in the remaining part of this paper.

Using a manual weaving machine, GO-fibres were inter-woven with nickel conductive fibres to form an inter-digitated pattern (Figure 4-1b and Figure S4-2). The nickel inter-digitated array serves as electrodes and the GO-fibres serve as humidity sensitive materials. The resistance changes of inter-digitated pattern can be measured when being

exposed to various humidity levels. The other two GO-functionalised fibres (GO-cotton and GO-wool) go through similar processes and have similar structures to form humidity sensors.

4.2.3 Characterisation of the GO-fibres and sensors

The morphology images of the fibres were captured using the scanning electron microscope (SEM) (Ultra 55). To determine the composition of GO flakes, a Renishaw Raman spectrum (514 nm wavelength with 1.5 cm^{-1} spectral resolution) was used. Moreover, the chemical groups of pristine and GO-functionalised fibres were analysed using an X-ray photoelectron spectroscopy (XPS) system (K-Alpha). The tensile strength of fibres was measured by the Intron tester (3344) according to the standard of ASTM C1557-20. The contact angle of sensors was characterised by the DRUSS (DSA 100) drop shape analysis system with each droplet of $2\ \mu\text{L}$. The water transportation property of sensor was evaluated by the MMT (Moisture Management Tester, SDL Atlas) machine. The water transportation results were shown in Table S4-1 (Supporting Information). The water molecules retention (regain) of the fiber was determined with the method recommended by DIN 54351. Specifically, regain was calculated by the following formula: $\text{Regain} = (\text{weight of conditioned sensor} - \text{weight of dried sensor}) / \text{weight of dried sensor}$. Where the weight of conditioned sensor was the measured after the sample is conditioned in a standard environment of 65% RH at $20\text{ }^\circ\text{C}$ for 48 hours, and the weight of dried sensor was measured after the sample dried in an oven at 105°C for 4 hours. The evaporation property was tested by dropping 40 mg of water droplets on fabric and calculated the percentage of evaporated water after 5 minutes. The resistance changes were recorded by the measuring instrument (Keithley 2000). The sensors resistance-humidity property was tested in a conditioning cabinet (Datacolor CONDITIONER). The chamber can set a specific humidity and temperature. The humidity was controlled automatically by the constant air circulation throughout chamber with an accuracy of $\pm 2\%$ RH. The testing procedure of sensor was based on

ISO 139 Textile Testing Standard. The Brunauer–Emmett–Teller (BET) special surface area (SSA) of fibres was conducted with temperature of 50°C and 6 h adsorption. The pressure impact of the sensor was measured under the Instron tester, with load pressures set to 2 MPa. Before characterisation, sensors were conditioned in the standard condition (20°C and 65 % RH) for 24 hours.

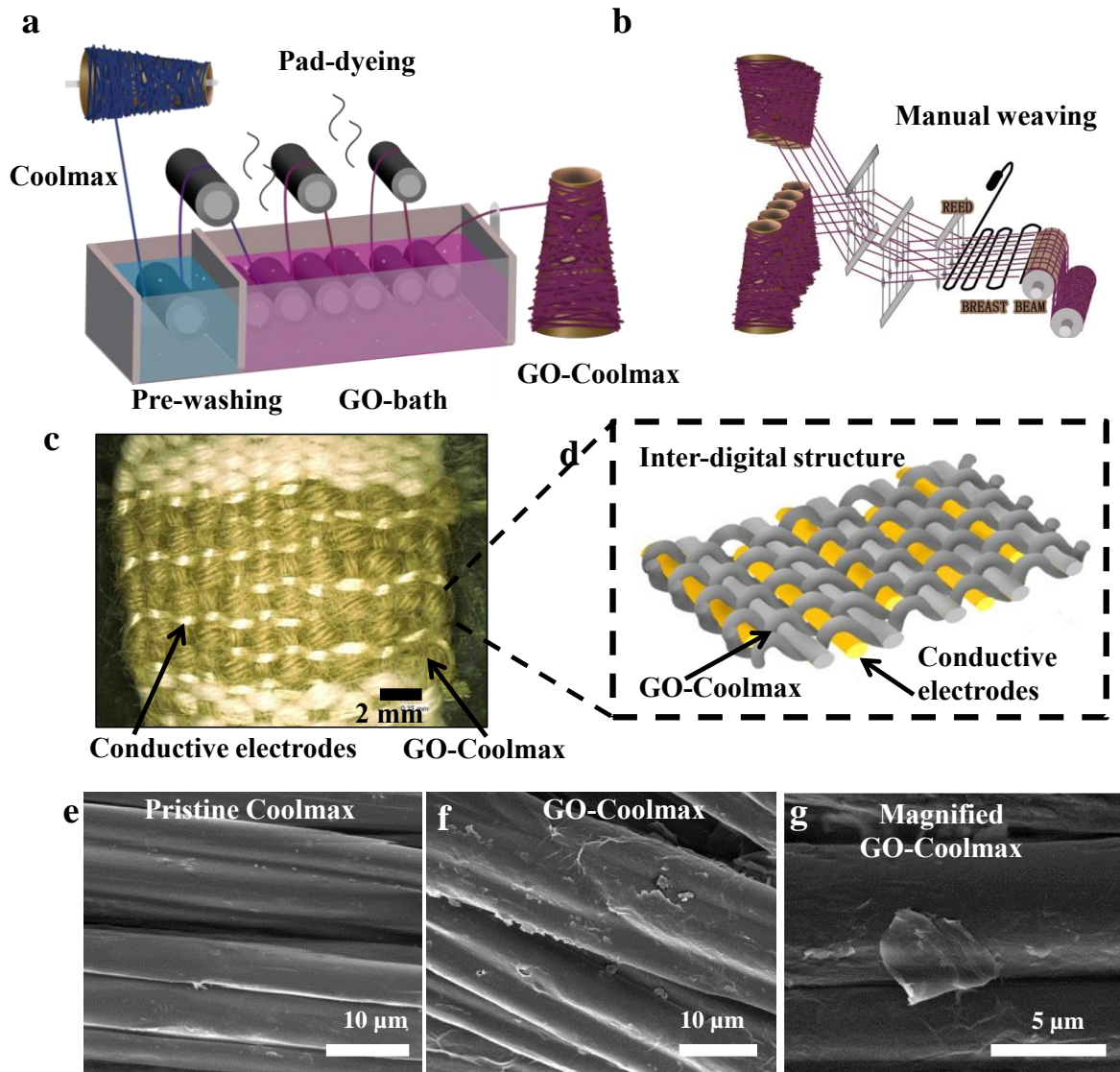


Figure 4-1. a) The process of GO-functionalisation on fibres and b) the weave process of GO-fibre with conductive electrodes. c) Optical image of woven sensor with d) inter-digital structure. SEM images of pristine Coolmax and GO-Coolmax: e) pristine Coolmax, f) GO-Coolmax, and g) magnified GO-Coolmax.

4.3 Results and discussions

4.3.1 Analysis of GO functionalisation

SEM images of pristine (non-functionalised) and GO-functionalised Coolmax fibres are shown in Figure 4-1e-g. The other two fibres are shown in Figure S4-3 (Supporting Information). It can be seen that the graphene-flakes are uniformly stacked and aligned with fibres, forming a homogeneously graphene coating on the fibres surface. There are only a few dangling GO flakes on the fibre surface due to defects in coating. The effectiveness of coating can be explained, i.e., the hydrophilicity properties of graphene oxide allow them to be dispersed in water at the molecular level and adhere onto the Coolmax fibers.¹⁹² Moreover, the pressure from mangle rollers during pad-dyeing enhances GO adhesion on the fibres' surface.⁵

The Raman spectrum has been widely used to study the functionalisation of the graphene materials.¹⁹³ The Raman spectra (Figure 4-2a) of GO-fibres shows two prominent graphene peaks at 1345 (D peak) and 1590 cm^{-1} (G peak) respectively.¹⁹⁴ These results indicate that these fibres are successfully coated with GO on their surfaces.

The effectiveness of GO coating was further verified by the X-ray photoelectron spectroscopy (XPS) analysis of pristine and GO-functionalised fibres. The pristine cotton, wool and Coolmax fibres consist of cellulose,¹⁹⁵ protein and polyester respectively, which are composed of carbon and oxygen chemical compound groups (Figure 4-3d-f). After GO functionalisation, oxygen/carbon ratio increases significantly as shown by the wide scan XPS spectrum in Figure 4-2b. High resolution XPS pictures (Figure 4-2c-e) show three main types of carbon bonds: C-C (~ 284.8 eV), C-O (~ 287 eV), and C=O (~ 288.5 eV) respectively; the C-O peak increases and C-C decreases after GO treatment. It is worth noting that the content of oxygen group of Coolmax increases dramatically from 30.84% to 63.54% after GO coating (Supporting Information, Table S4-2), which could be attributed to the trench and groove

morphological structures on the Coolmax fibre surface that help stacking more GO on its surface. The XPS results indicate that three fibres are successfully coated with GO nano-flakes after pad-dyeing process, and provide an abundant amount of oxidised carbon groups on the fibre surface to response with water molecules.

The tensile strength of fibres after GO-functionalisation is also studied. The tensile strength plays an important role during fibres manufacturing process and determines the quality and life-time of the sensor. The tensile strength comparison between the pristine and GO-functionalised fibres is illustrated in Figure 4-2f. The pad-dyeing process has almost no effect in the stress test of three fibres. Moreover, it can be seen that, GO-Coolmax fibers exhibit a much better stretchability than GO-cotton and GO-wool fibres, indicating that the GO-Coolmax fibres are more durable during the manufacturing process and wearing activities.

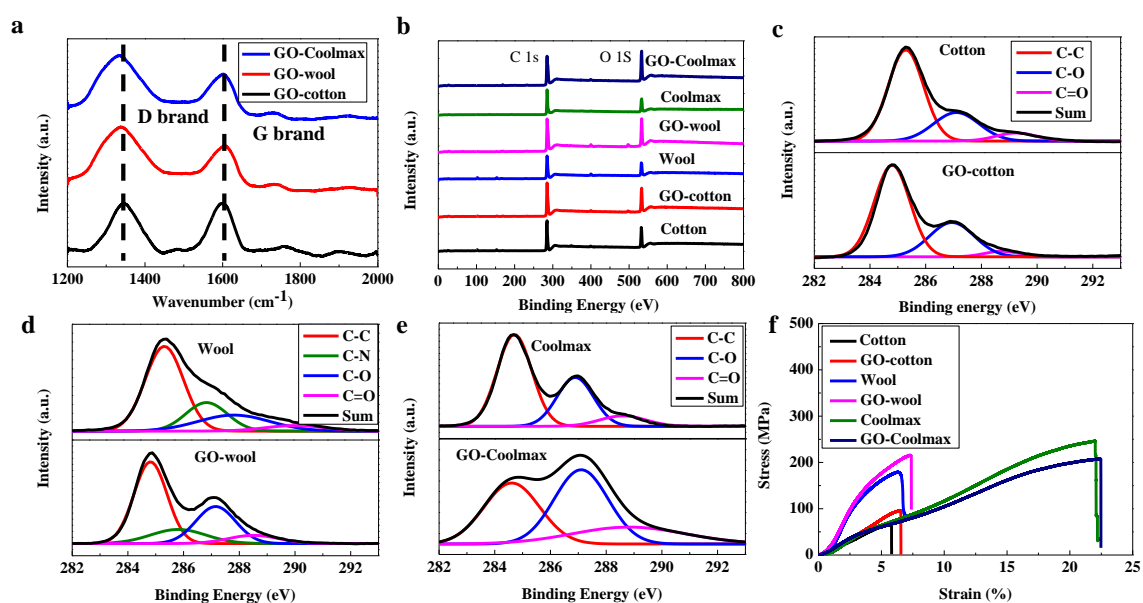


Figure 4-2. Characterisation of GO-functionalised fibres. a) Raman spectra of GO-fibres. b) Wide-scan XPS spectra of pristine and GO-fibres. High resolution C (1s) XPS spectrum of pristine and GO-fibres: c) cotton, d) wool, and e) Coolmax. f) Typical stress-strain test of the pristine and GO-fibres.

4.3.2 Analysis and comparison of GO-Fibres as humidity sensors

Morphological microstructure of GO-fibres

To understand the water adsorption, transportation and evaporation properties associated with fibres micro-structures, the surface and cross-section morphologies of three fibres are investigated respectively and illustrated in Figure 4-3. It can be seen that 1) the cotton fibre (Figure 4-3a) has a flat surface with oval-shaped and wall-structured cross-section, there is also a lumen structure inside of fibre; 2) The wool fibre (Figure 4-3b) has irregular scales on the surface and a circular cross-section. 3) Coolmax fibre (Figure 4-3c) has trenches and grooves on its surface. Three fibres' special surface areas (SSA) have been investigated and the results are shown in Table S4-3. It can be seen that the GO-Coolmax has the largest SSA of $1.15 \text{ m}^2/\text{g}$ as compared to GO-cotton ($1.10 \text{ m}^2/\text{g}$) and GO-wool ($0.69 \text{ m}^2/\text{g}$). The lumen structure of the cotton fibre and the trenches and grooves structure of Coolmax fibre all contribute to the enlarged surface area.¹⁹⁶ The different morphological micro-structures and chemical components will determine the water adsorption, transportation and evaporation properties of fibres and fabrics.¹⁸⁵ Later experiments show that these differences will further contribute to the different response and recovery time of the humidity sensors.

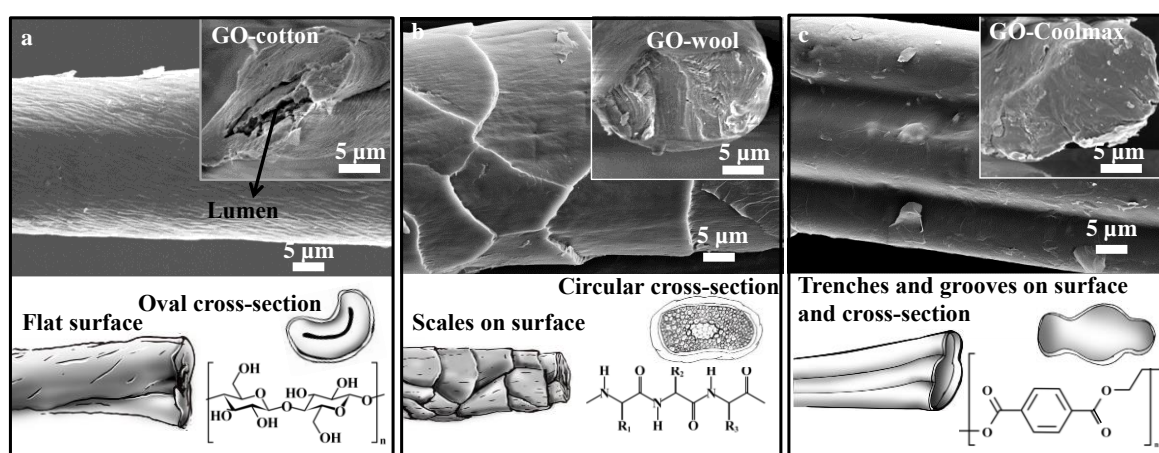


Figure 4-3. Morphological structures (SEM and schematic images) and chemical components of three fibres: a) GO-cotton, b) GO-wool, and c) GO-Coolmax.

Water adsorption, transportation and evaporation properties of sensors

The GO-cotton fibres, GO-wool fibres and GO-Coolmax fibres are woven with conductive fibres into inter-digital patterns to construct three humidity sensor prototypes. To investigate the water adsorption capabilities of these sensors, water droplets (2 μL) are dropped on these sensors. The contact angle (CA) on each sensor surface is shown in Figure 4-4a. The GO-wool ($\sim 124^\circ$) and GO-Coolmax ($\sim 129^\circ$) sensors are hydrophobic, and have higher CA than GO-cotton ($\sim 98.4^\circ$), indicating that GO-wool and GO-Coolmax sensors adsorb less water than GO-cotton sensor in a moist environment. It is worth noting that, GO-wool and GO-Coolmax sensors display hydrophobic properties to water because of the pristine fibres (without GO functionalisation) have aggregation of covalent bonds (nonpolar side chains) that repels liquid water.¹⁹⁷ The dynamic CA in 120 s indicates that the GO-Coolmax sensor (CA from 124° to 38°) has a better water wicking property than the GO-cotton sensor (CA from 98.4° to 71.8°). The excellent wicking property of the sensor helps water penetrate into the gap and pore of the fabric, resulting in a quick equilibrium in water sensing. In comparison, the GO-wool sensor repels water droplet in 120 s that would cause a slow sensing (response and recovery) time for water.

Evaporation capabilities of three sensors are studied. As depicted in Figure 4-4b, GO-Coolmax (11.2%) has higher evaporation rate than GO-cotton (4.57%) and GO-wool (2.26%). This could be attributed to trenches and grooves on Coolmax fibres surface that enhance water transportation and evaporation.¹⁹⁸ In order to further investigate the amount of water presented in sensor, the regain properties of fabrics are further studied. As shown in Figure 4-4c, GO-Coolmax sensor retains less water in fibre and fabric (0.37%) as compared to GO-cotton (4.74%) and GO-wool (8.37%) sensors.

After experimental investigation, three sensors water adsorption, transportation and evaporation properties are summarised in Figure 4-4d-f. Compared to GO-cotton and GO-wool, the GO-Coolmax sensor has a much quicker water wicking and evaporation properties that would benefit its humidity sensing performance.

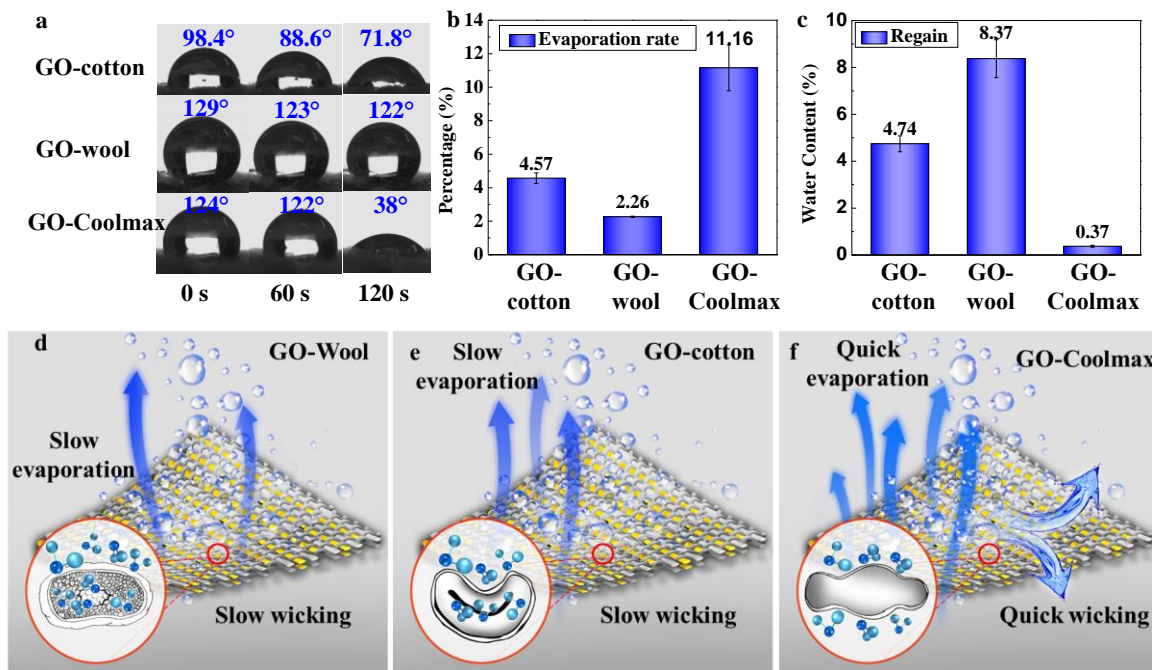


Figure 4-4. Water transportation, evaporation and wicking properties of three GO-functionalised sensors. a) Contact angle of sensors. b) Evaporation rate of sensors. c) Regain (water content) of sensors. Water adsorption, transportation and evaporation of d) GO-wool, e) GO-cotton and f) GO-Coolmax.

Humidity sensing performance and working mechanism of three sensors

In order to investigate the performance of three sensors, the sensors are quickly moved in and out of a humidity chamber and the relative humidity (RH) levels are altered between 45% (room ambient) to 80% (inside humidity chamber) back and forth repetitively. The real-time resistance responses are illustrated in Figure 4-5a, showing that all sensors are sensitive to RH changes, i.e., resistance decreases in the moist chamber and rises when being put back to room environment. It can be seen that 1) the sensor's resistance is over 120 M Ω in ambient environment, and decreases sharply when being exposed to higher moisture. The resistance changes were recorded continuously by the measuring instrument (Keithley 2000); 2) the GO-Coolmax sensor shows much better performances (quick response, fast equilibrium and rapid recovery) than GO-cotton and GO-wool sensors; 3) when being exposed to different humidity levels, the GO-Coolmax sensor shows ultrafast response and recovery time within 0.6

s (Figure 4-5b).

The GO-fibres have abundant oxygen-related functional groups (e.g., epoxy, hydroxyl and carboxyl groups), which adsorb water molecules under moist environment. However, under extremely low humidity conditions, there is less aggregation of water molecules which makes them chemically adsorbed on oxygenated groups and vacancies on the GO surface via strong double hydrogen, thus, they are unable to escape from the bonding to become free-moving water molecules. In this situation, the sensor is nearly insulating. When humidity increases, more water molecules are physically adsorbed on the GO surface, which can form water molecules layers. The water layers accelerate the transfer of H_2O to H_3O^+ ($H_2O + H_3O^+ = H_3O^+ + H_2O$) according to the ion transfer mechanism of Grotthuss.¹⁹⁹ Thus, the free movement of proton causes a decrease in the resistance of sensors as the humidity increases.

The rapid response time of GO-Coolmax humidity sensor is mainly attributed to water adsorption, transportation and evaporation properties of fibres. Specifically, GO-Coolmax fibres retain less water inside fibres, thus the sensor can reach the sensing equilibrium quickly. Also, GO-Coolmax sensor has excellent water evaporation capabilities that result in a quick recovery time when the humidity level decreases. On the contrary, the GO-cotton and GO-wool sensors have poor evaporation rate and retain much more water inside fibres and fabric, resulting in longer response and recovery time.

4.3.3 GO-Coolmax performance characterisation

As the GO-Coolmax sensor has ultrafast response time for humidity sensing, we further quantitatively characterize its performance from different aspects.

Humidity sensing response and recovery time

The GO-Coolmax maintains its quick response and recovery time at different RH levels, as shown in Figure 4-5c. Sensor reacts rapidly when the RH level switches between room ambient (RH 45%) to 60%, 70%, 80% and 90% respectively. Although the resistance settles at different values ($\sim 65\text{ M}\Omega$, $\sim 20\text{ M}\Omega$, $\sim 10\text{ M}\Omega$ and $\sim 8\text{ M}\Omega$ for 60%, 70%, 80% and 90% of RH respectively), the response and recovery time is almost the same.

We further quantify the sensing performance of the GO-Coolmax humidity sensor. Figure 4-5d illustrates the resistance variations as the RH level changes. Specifically, the resistance decreases with the increase of RH levels, which varies from $\sim 65\text{ M}\Omega$ at RH level of 60% to $\sim 6\text{ M}\Omega$ at RH level of 100%. The GO-Coolmax sensor also exhibits good repeatability, as shown in Figure 4-5e, a repeated cycle of RH level variation between 45% and 65% is applied, and the resistance values of the GO-Coolmax sensor vary accordingly and repetitively. All these results suggest that the GO-Coolmax has ultra-fast response and recovery time to humidity changes, which is superior to the textile-based humidity sensors reported by other researchers (see Table S4-4).

It is also noticed that while the GO-Coolmax humidity sensor has a fast response and recovery time as the humidity level changes. It is not a good gauge to measure the exact humidity levels. If we only need to use the GO-Coolmax as a humidity variation indicator rather than a gauge of measurement, we don't need to wait for the resistance to fully settle down, instead, a predefined resistance threshold can be used to indicate the variations of the humidity, and a circuit can quickly sense this variation. In this manner, the response/recovery time can be even faster and can be achieved in the range of 0.1 to 0.2 s. We will demonstrate this usage in our applications.

Water presence (wetness) sensing capabilities

The GO-Coolmax sensor not only can sense the humidity variations, it can also be used as an indicator for water presence or wetness alert. It detects water presence and can

recovery efficiently after water dries out (Supporting Information, Figure S4-4). To quantitatively analyse the water-presence sensing performance of the GO-Coolmax sensor, we gradually increase the water amount dropped on the sensor from 3 mg to 40 mg, until the GO-fibers are totally immersed with water. In this process, the sensor resistance decreases from $\sim 230\text{ K}\Omega$ to $\sim 20\text{ K}\Omega$ (Figure 4-5f). It is also noticed that the resistance starts to decrease slower when water amount is above 30 mg, indicating that the sensor researches water saturation.

To further analyse the dynamic water-presence sensing performance of the GO-Coolmax sensor, we use the Moisture Management Tester (MMT)²⁰⁰ to pumping water in 20 s, track the water content value of fabric surfaces (inner and outer surfaces) and record resistance changes of sensor in 120 s. As shown in Figure 4-5g, the sensor's resistance changes immediately when the water is dropped on the inner surface of the sensor, and it decreases with the increase of water content on the sensor's both surfaces. After 20 s, without further water dropping, the sensor's resistance value keeps stable. These results indicate that the GO-Coolmax sensor can detect the water content dynamically.

Resiliency to Other Modal of Impacts

As discussed earlier, a wearable humidity sensor, while being sensitive to humidity variations, should be resilient to other modal of ambient or body impacts. The GO-Coolmax sensor's resiliency to temperature and pressure variations is further studied. We keep the RH level stable at 80% while set the chamber temperature at 20°C, 30°C and 40°C respectively. The sensor's resistance variation is illustrated in Figure 4-5h. While higher temperature (40°C) correlates to larger resistance variations as compared to lower temperature (20°C), but the response and recovery time is almost unchanged. The result indicates that the humidity sensor can work well under different ambient temperatures. The sensor's resiliency to external pressure impacts is also tested, as shown in Figure 4-5i. With an increasing external pressure applied from 0 to 2 MPa, the sensor's resistance shows no obvious changes. These results suggested that the

sensor is resilient to other modal of ambient and body activity impacts. All these attributes will enable the GO-Coolmax to be used as a good humidity sensor in wearable applications.

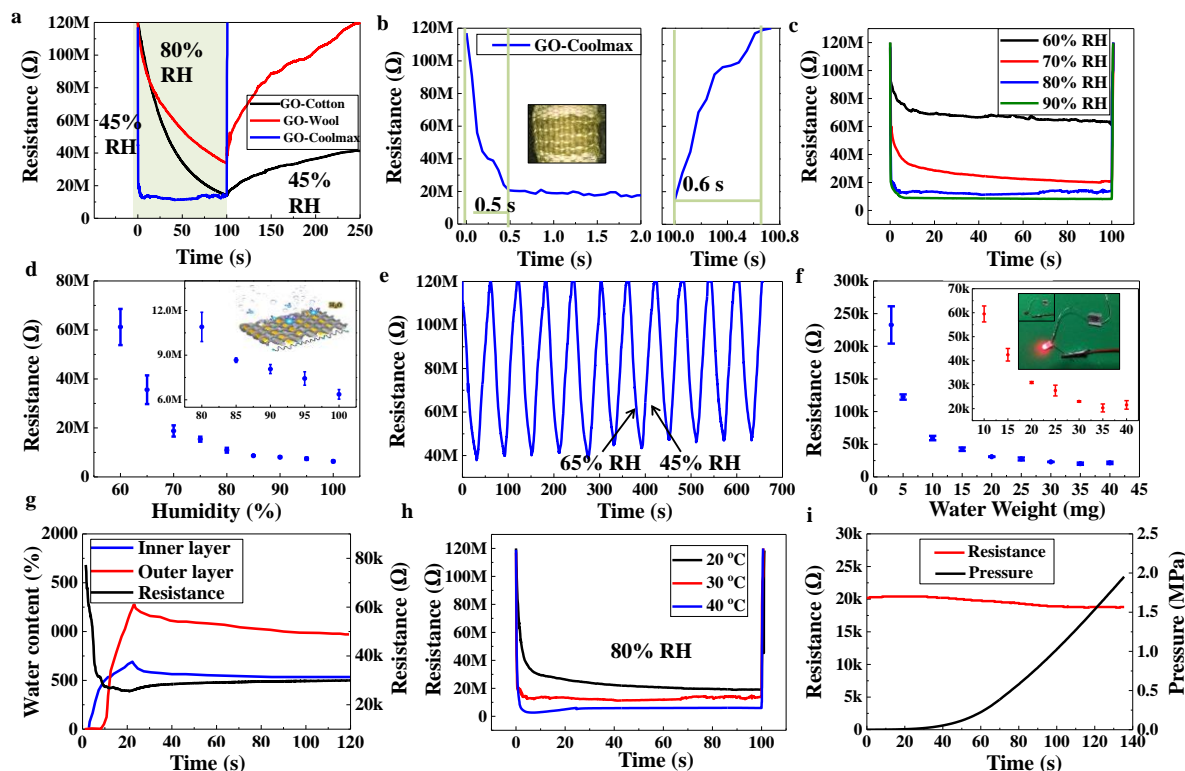


Figure 4-5. Characterisation of humidity sensing performance. a) Resistance changes of three sensors with humidity changing from 45% to 80%. b) Response and recovery time of the GO-Coolmax sensor. c) Rapid humidity sensing performance of the GO-Coolmax sensor in different humidity levels. d) Resistance at different humidity levels of the GO-Coolmax sensor. e) Repeatability test of the GO-Coolmax sensor. f) Resistance changes of the GO-Coolmax sensor under different water amounts (to immersion). g) Dynamic resistance changes of the GO-Coolmax sensor when water presence on the inner surface. h) Resistance changes of the GO-Coolmax sensor at different temperature of 20°C, 30°C and 40°C (RH from 45% to 80%). i) Resistance changes when applying external pressure on the sensor.

Coating Adhesion

The wash durability is an important property for wearable sensors. The sensor is

immersed into the distilled water (400 mL) with detergent (4 mL) for 30 minutes to assess wash durability. The washing results are shown in Figure S4-5a. It can be seen that the sensing capability does not deteriorate after being washed up to 10 cycles, as the sensor's resistance still drops sharply as the humidity increases. It also brings to our attention that the resistance under 80% of RH increases from $\sim 17 \text{ M}\Omega$ to $\sim 23 \text{ M}\Omega$ after 10 cycles of washing. The increase of resistance is probably caused by the peeling off the dangling GO after the washing cycles. Nevertheless, the rapid response and recovery sensing capability is still maintained (Figure S4-5b).

To further investigate the GO coating's adhesion under deformation, the wetted GO-Coolmax was compressed for 1000 cycles. The resistance changes are recorded and shown in Figure S4-6. It can be seen that the sensor's resistance varies between $25 \text{ K}\Omega$ to $28 \text{ K}\Omega$ during these cyclic deformations. This result confirms that the GO coatings are very adhesive on fibres surface and will not easily degrade under constant mechanical deformation.

4.3.4 Applications

We have designed several applications that utilize the proposed GO-Coolmax humidity sensor. The sensor's advantages, i.e., fast response and recovery time, repeatability, sensibility to both vapour and liquid water, have been demonstrated through these applications.

Human respiration sensor embedded in a facial mask

The GO-Coolmax sensor is woven into the fabric layer inside a facial mask. Human respiration activities produce airflow with humidity and can be detected by the sensor. It can be seen from Figure 4-6a that the resistance increases during the inhalation stages and decreases during the exhalation stages. More specifically, deep breath creates more vapour in the airflow than the normal breathing. This inhalation and exhalation

differences can also be distinguished from the resistance variations of the sensor, as illustrated in Figure 4-6a. Smaller resistance variation corresponds to normal breathing in the beginning, and it is then followed by large variations, which are caused by deep breathing. We also compare these results with a commercial humidity test machine (Bio-Pac), the results from GO-Coolmax sensor are well consistent with the results from Bio-Pac, shown in Figure 4-6a.

Perspiration sensor for human sport activities monitoring

We further integrate the GO-Coolmax sensor into a sportswear to monitoring the perspiration of human body during work-out activities. We measure the resistance changes of the sensor when human is running at different speeds (Figure 4-6b). It can be seen that the resistance decreases as the perspiration increases. During the time from 0~120 s, the sensor resistance decreases rapidly as the vapour from perspiration increases and changes into liquid sweats gradually. During the time from 120~600 s, with the running speed of 7 km/h, the sensor is almost immersed with liquid sweats and its resistance decreases to ~30 K Ω . After 600 s, the resistance changes slowly as the runner slows down to rest. We also use an APP, called Software S-smart²⁰¹ (Figure S4-7) to correlate the human's body activity with the perspiration activity. Based on body movements, S-smart can estimate the amount of perspiration, simulate the moisture processes in the clothing, as well as their dynamic interactions with ambient environments. The resistance changes from the GO-Coolmax sensor correlate well with results from the S-smart APP.

To make this GO-Coolmax sensor more wearing-friendly, we also design an embroidered NFC system to collect the sensing information from the humidity sensor. The NFC system consists of an embroidered coil antenna, which can harvest EM energy from the NFC reader (in this case, a smartphone) as well as exchange information through magnetic coupling. The harvested energy can be acquired from the DC output of the NFC NTAG chip and further power-up the MCU. The MCU can collect the sensor information from the embedded A/D converter. Figure 4-6c illustrates the schematic

and prototypes of this NFC system. Through this NFC data-collection system, the humidity sensing information can be wirelessly retrieved by a smartphone reading from a distance around 5 cm. The whole sensing system does not need battery to operate, because the energy is harvested from the smartphone, coupled through the embroidered coil antenna. Further information can be found from our previous report,²⁰² and also summarised in Supporting Information, Figure S4-8.

Water presence alert (diaper wetness alert)

Diaper wetness alert is a very practical and useful application in many occasions. The wearable GO-Coolmax humidity sensor can be used as a real-time alert of water presence. Traditional wetness alert mostly uses Ohmic-contact methods, or other solid-state sensors to detect the presence of water, which is not reliable, and in many cases, not comfortable to be integrated with diapers. The GO-Coolmax sensor is made of Coolmax fibres that are soft, flexible, robust and comfortable for wearing. We have integrated the sensor into a baby diaper. As shown in Figure 4-6d, the sensor resistance decreases dramatically when the diaper is wet with urine. Similar to previous perspiration monitoring prototype, the sensor can be also connected to a NFC system with an embroidered coil antenna. The wetness alert signal can be received by a nearby NFC reader or a smartphone.

Woven fabric touchpad (keypad)

Fabric-based woven keypad has many applications in wearable electronics. Traditional keypad utilizes pressure sensor, or mechanical switch to sense the finger touching activities. However, these mechanisms are not practical for fabric-based keypad when being integrated onto human apparels, because the fabric folding, stretching and twisting will falsely activate the keypad sensors (either pressure-based or mechanical switch based).

Humidity sensor, with fast response and recovery time, will be the ideal solution to this problem. As the glands on human's fingers produce constant evaporation of water

molecules,¹⁸⁷ when the fingers are approaching the humidity sensors, or touching the humidity sensors, the sensor can convert the approaching/touching activities into resistance variations.

Our proposed GO-Coolmax humidity sensor has a fast response and recovery time (less than 0.15 s if used as a humidity variation indicator). When being integrated into fabric layers, a woven touchpad or keypad can be constructed. Figure 4-6e shows the resistance changes of the sensor used as a touchpad. As the finger approaches, the resistivity of the sensor at the corresponding location (key) drops abruptly. As the finger leaves the sensor, the resistance also recovers sharply. Figure 4-6e also demonstrates that the touching/un-touching sensing is stable and repeatable, i.e., the resistance returns to its original value after each touching cycle. The response and recovery time is less than 0.15 s (Figure 4-6f), thus the sensor is fast enough to catch the finger movements.

Furthermore, because the GO-Coolmax sensor is resilient to pressure and temperature variations from the ambient, the touchpad only responds to touches from human's finger. If people wear gloves, or use an object to touch the touchpad, the sensor will have no responses (Supporting Information in the Movie S4-1). This resiliency to external pressure and ambient temperature effectively prevent the sensors from false activation when being used as a wearable touchpad or keypad on human body.

16 GO-Coolmax fabric sensors were woven into a 4x4 matrix to construct a 4x4 keypad, as illustrated Figure 4-6g. The sensors are connected to a FPGA and the resistance variation of the sensor under each key can be sensed by the FPGA circuit and light up a LED. Detailed design schematic is shown in Figure S4-9. When human's finger touches one key, its corresponding LED will light up accordingly, as shown in Figure 4-6h.

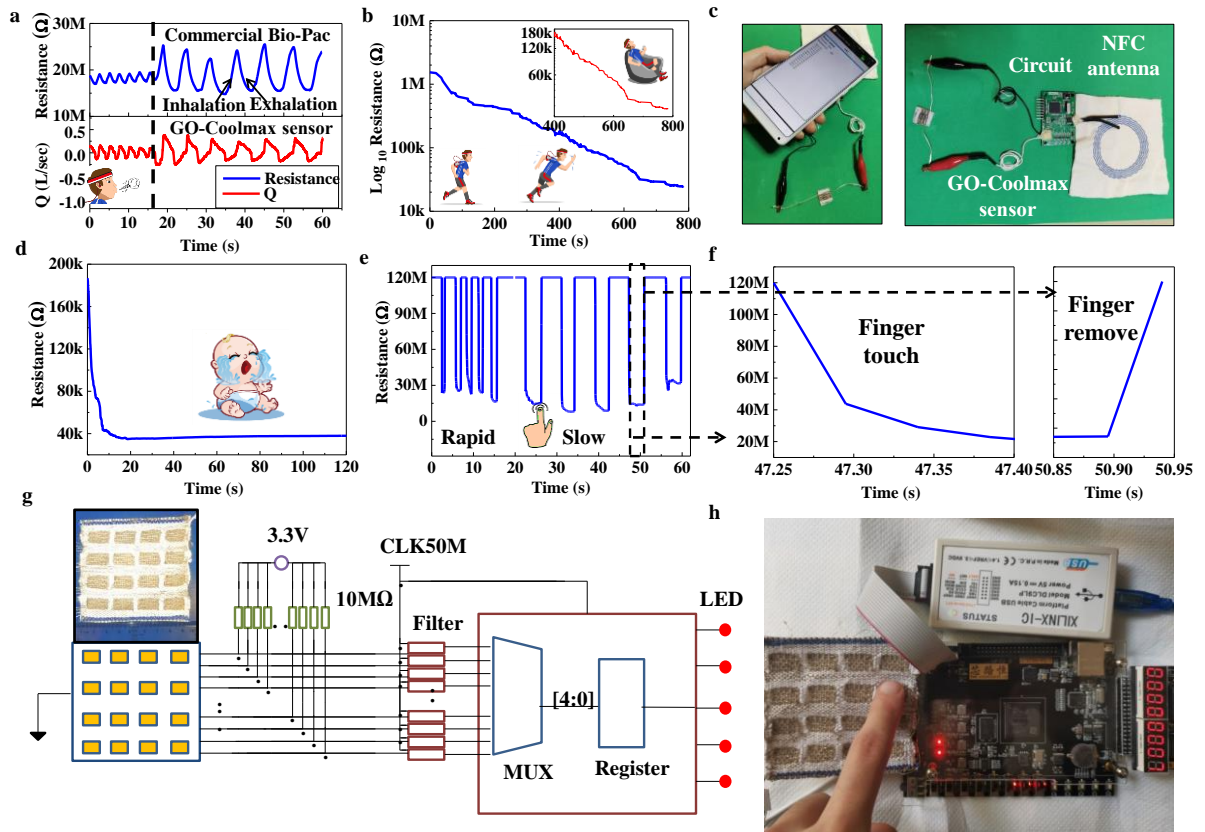


Figure 4-6. Applications of GO-Coolmax sensor for vapour and liquid water sensing. a) Human respiration monitoring (The blue line and red line are results from the commercial Bio-pac and GO-Coolmax sensor respectively. Normal breath between 0~18 s, followed by deep breath). b) The perspiration of human in sport activities (slow running between 0~120 s, quick running between 120~600 s and slow down between 600~800 s). c) The humidity sensor connected with a textile NFC antenna for wireless charging and sensing. d) Diaper wetness alert. e) A keypad for finger touch sensing. f) Rapid response and recovery when finger approaches and leaves. g) The image and circuit diagram of the GO-Coolmax fabric keypad. h) Demonstration of fabric keypad when key is touched (LED lights up).

4.4 Conclusions

In this paper, GO-functionalisation techniques had been applied to different natural and synthetic fibres (cotton, wool and Coolmax). Their morphologies, micro-structures, as

well as water adsorption, transportation and evaporation properties had been studied. We found that GO functionalised Coolmax fibres (GO-Coolmax) can be used as an excellent humidity sensor with ultrafast response and recovery time (less than 0.15 seconds of sharp changes of sensor's resistance). The superior sensing capabilities can be attributed to the special micro-structure that results in its quick reaction, fast wicking and evaporation of water molecules. Moreover, the sensor is resilient to temperature and body pressure impacts. These properties make the GO-Coolmax sensor an ideal candidate to be integrated with apparels/clothes in many wearable applications. Finally, several prototypes of applications have been demonstrated, that include a respiration sensor built inside a facial mask, a perspiration sensor integrated with a sweater for sports activity monitoring, a diaper wetness alert, and a woven fabric touchpad. These prototypes have proved that this proposed GO-Coolmax sensor can be applied in many e-textile applications.

4.5 Supplementary information

The single-layer GO is obtained by spin coating and its morphology is further investigated under SEM. Before measurement, the GO dispersion is re-prepared with a concentration of 100 $\mu\text{g/ml}$. Then, drop the GO into a silicon slice for spin coating. The GO sheets are well-distributed into a single layer on the silicon after spin coating process. The single-layer GO morphology is shown in Figure S4-1a. Assisted by ImageJ software, the size of each single GO sheet can be measured. As shown in Figure S4-1b, the average size of GO sheets is 25.5 μm , and most of those sizes are range from 7.5 to 22.5 μm .

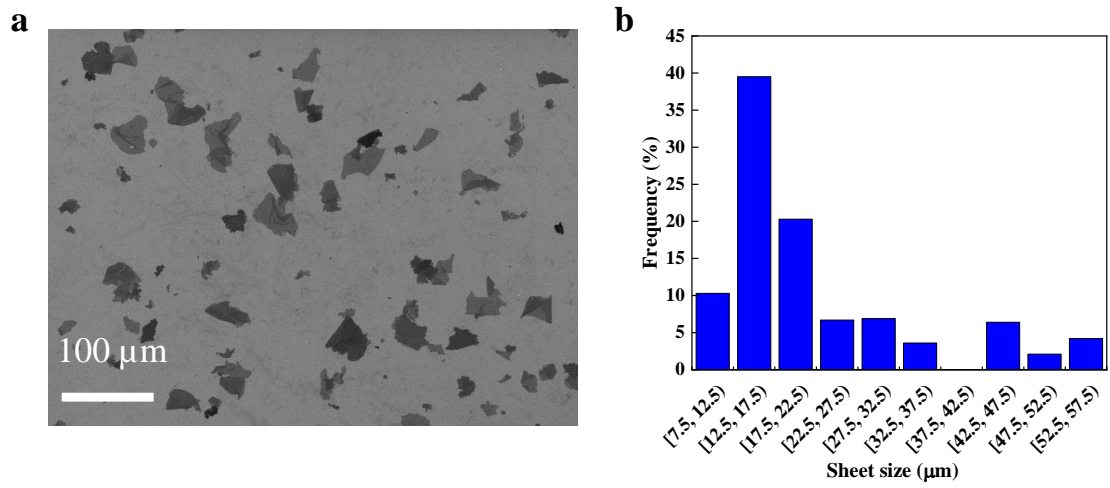


Figure S4-1. a) SEM image of single-layer GO. b) The sheet size distribution.

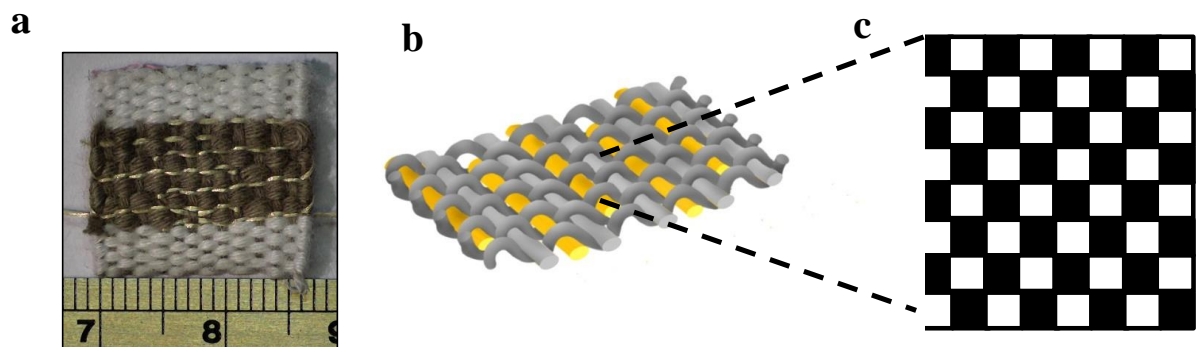


Figure S4-2. a) Optical image of the sensor. b and c) The plain-weave structure of sensor.

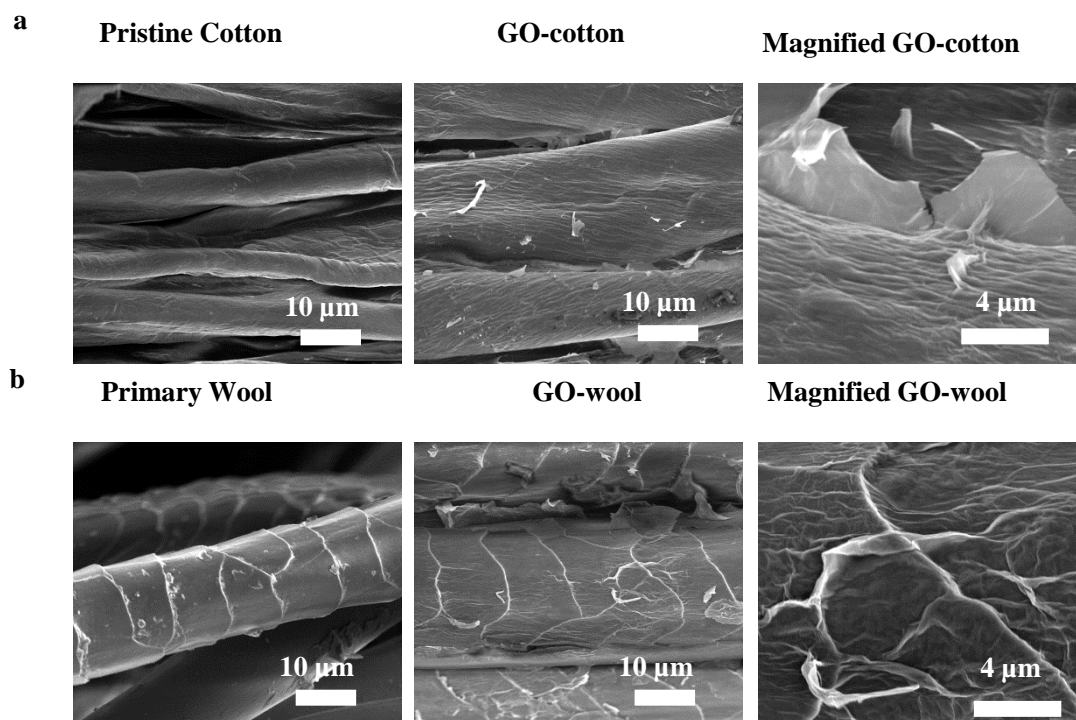


Figure S4-3. SEM images of pristine and GO fibres: a) Cotton, b) Wool.

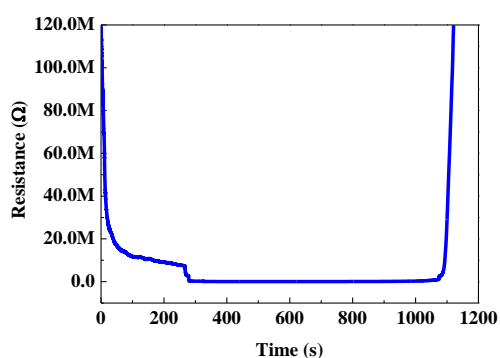


Figure S4-4. Resistance changes of GO-Coolmax sensor in water evaporation and drying process. This experiment was conducted along with contact angle test, by dropping 2 μL water on sensor surface. At the same time, the resistance changes were recorded from the water dropping on the fabric to the water drying out.

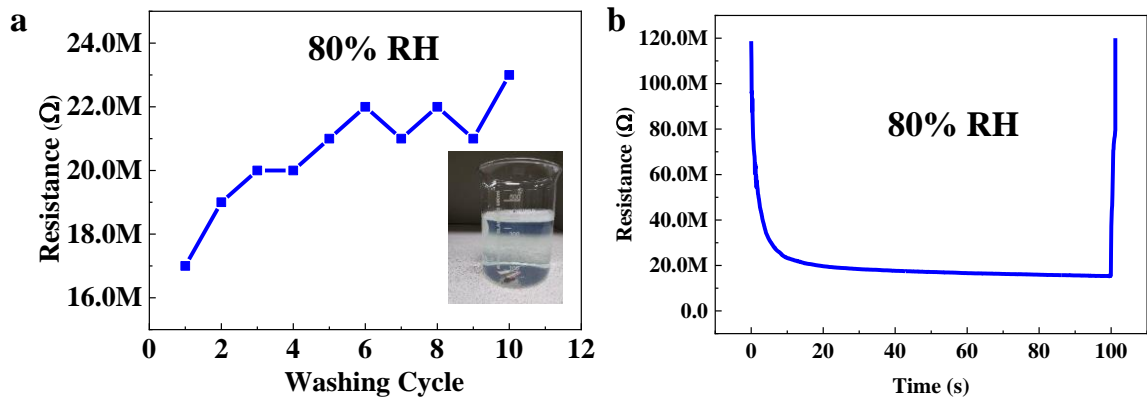


Figure S4-5. Washing cycle tests of the GO-Coolmax sensor. a) Sensor's resistance variation at RH of 80% after each cycle. b) Response and recovery time of the GO-Coolmax sensor after 10 cycles of washing.

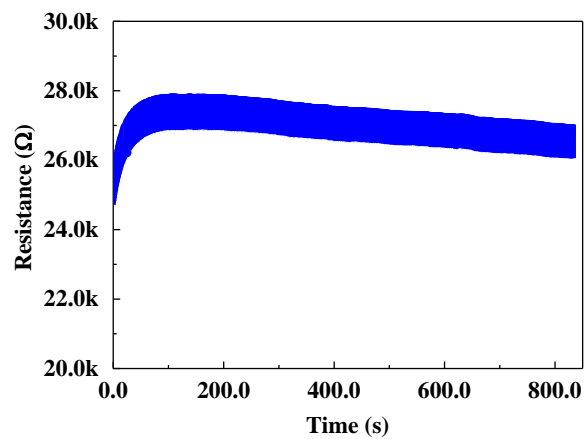


Figure S4-6. The resistance of the GO-Coolmax sensor under cyclic compression (400 N) of 1000 cycles.

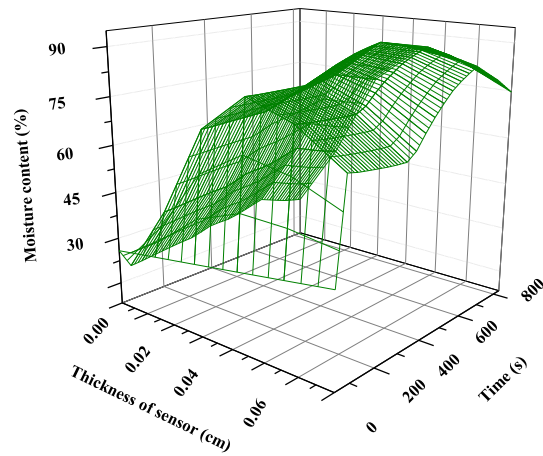


Figure S4-7. Perspiration modelled in the Software S-smart.

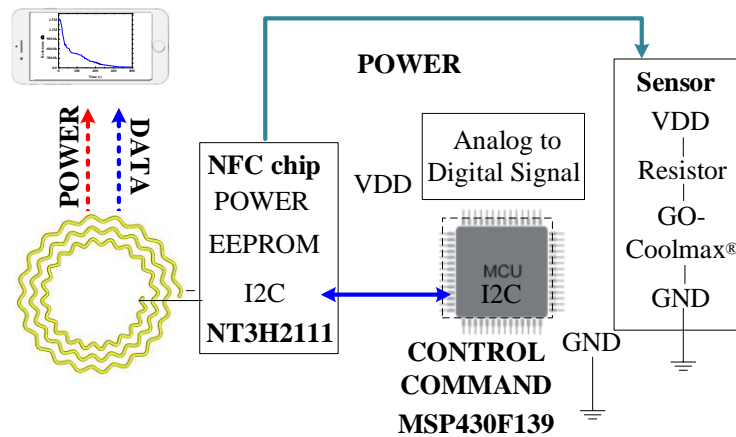


Figure S4-8. The diagram circuit of the NFC system.

The textile-based NFC antenna is embroidered with commercial conductive fibres (Liberator® 40) with the diameter of 6.2 cm, 5 turns and the interval gap of 0.15 cm. It operates at a frequency (f) of 13.56MHz, and conjugate matches with NTAG NFC chip (NT3H2111, input capacitance of 50 pF). The NFC antenna can harvest at least 6.25 mW EM energy according to our previous research,²⁰³ which is enough to drive the sensing system.

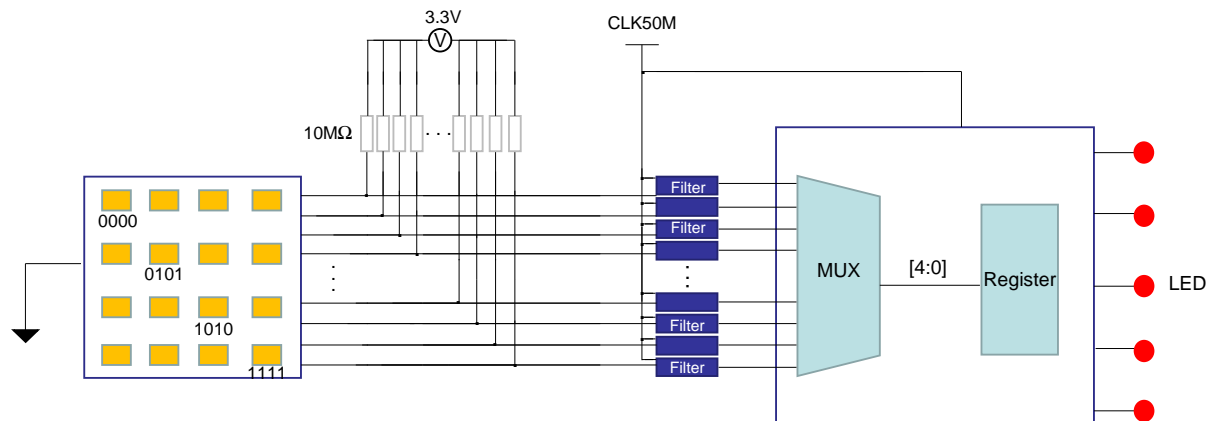


Figure S4-9. The diagram circuit of sensor to the FPGA.

The schematic diagram of the keyboard is shown in Figure S4-6, in which the 4x4 GO-Coolmax touch sensor keypads are connected to the FPGA controller. Each of the keypad sensors is connected to a 10 MΩ pull-up resistors to sense the resistance variations from the sensor. The keypads and controller are powered by a 3.3 V DC supply. The Filter module is used to filter the noises from the sensors. The FPGA internal clock signal is 50 M. The 16 keypads are encoded from 0000 to 1111. 5 LED lights are used as display the touch action, i.e., 4 LED lights for the 4-bits encoding, 1 for FPGA test. By pressing the keypads, the corresponding LED light will light up, as shown in Figure S4-6.

Table S4-1. Water transport results of MMT

	Top surface	Bottom surface
Wetting time (sec)	1.872	4.868
Adsorption rate	24.7786	60.2064
Max wetted radius (mm)	25	25
Spreading Speed (mm/sec)	7.0274	5.9324

Table S4-2. High resolution of XPS analysis of three main types of carbon bonds

	Cotton	GO-Cotton	Wool	GO-Wool	Coolmax	GO-Coolmax
C-C	66.52%	64.31%	55.00%	50.37%	69.16%	36.46%
C-O	26.73%	31.84%	19.39%	27.40	21.96%	43.08%
C=O	6.75%	3.85%	5.61%	7.69%	8.87%	20.46%

C-N	0	0	20.00%	14.54%	0	0
O/N-containing C	50.33%	55.49%	45%	49.63%	30.84%	63.54%

Table S4-3. Special surface area of fibres

	Cotton	GO-Cotton	Wool	GO-Wool	Coolmax	GO-Coolmax
SSA (BET) m ² /g	0.819	1.101	0.464	0.690	0.884	1.149

Table S4-4. The performance comparison from our work to others

Materials	Response time	Recovery time	Substrates	Refs
PVA/KOH polymer gel-electrolyte and flexible metal electrode	0.4 s	2.6 s	Polymer	131
PDMS and carbon electrodes	0.29 s	0.47 s	Ceramic substrate	187
Graphene/polypyrrole (PPy)	15 s	20 s	Alumina ceramic substrate	118
SWCNT/PVA	40 s	-	Cotton fabric	188
Mxene/Silver Nanowire	5 s	80 s	silk	125
GO coating	-	-	Silk fabric	190
PANI/spandex covered yarn	116 s	-	Composite yarn	127
Copper wire/cleancool yarn	3.5 s	4 s	Composite yarn	204
Coolmax/Graphene-Oxide	0.5 s	0.6 s	Fabric	This work

Chapter 5

Twisted graphene fibre based breathable, wettable and washable anti-jamming strain sensor for underwater motion sensing

This chapter focuses on completing the fourth objective addressed in Chapter 1.3. The research work has been published in Chemical Engineering Journal.

Authors: Heng Zhai, Lulu Xu, Zekun Liu, Lu Jin, Yangpeiqi Yi, Junze Zhang, Yangyang Fan, Dongxu Cheng, Jiashen Li, Xuqing Liu, Yi Li

Journal: Chemical Engineering Journal (DOI: 10.1016/j.cej.2022.135502)

Statement of own contributions in joint authorship: H.Z. has contributed to the main research idea development, methodology, material fabrication, characterisation, data acquisition, draft manuscript preparation and revision. Specifically, Conceptualisation, H.Z., L.X., Y.L.; Methodology, H.Z. and Z.C.; Materials preparation, H.Z. and Z.L.; Characterisation, H.Z. and D.C.; Formal Analysis, H.Z. and L.J.; Data Curation, H.Z. and Y.Y.; Original draft preparation, H.Z.; Manuscript revision, H.Z.; Supervision, Y.L. and X.L.

Abstract

Wearable electronics have promising applications in human-machine interfaces and Internet of Things. Recent reported wearable sensing techniques are implemented mainly by either encapsulated packaging approaches or deposition of conductive nanomaterials onto flexible textiles. However, such fabrication technologies sacrifice the physical comfort, washability and wettability which are the essential elements to wearables. In this paper, we report a continuous twisted graphene fibre with high tensile

strength (369 MPa) and remarkable breaking strain (48.5%), as well as stable electrical and mechanical performances under cyclic washing and chronic wetting. The as-prepared twisted graphene fibre is woven into a pure fabric-based breathable, wettable and washable strain sensor with outstanding sensitivity (gauge factor ~ 63) to strain while negligible sensitivity upon bend, pressure, temperature and humidity. The strain sensor displays undifferentiated high performance of sensitivity, stability and durability both in air and water, enabling its precise detection of human motions in complex external environment.

Keywords: twisted graphene fibre, wet-fusing assembly, washability, anti-jamming strain sensor, underwater sensing

5.1 Introduction

The precise real-time measurement of vital information in a living body with wearable strain sensors is indispensable for their applications in health monitoring, human-machine interfaces and soft medical robotics.²⁰⁵ Such accurate detections highly depend on the conformal fit of flexible strain sensors to the surfaces of humans or machines. However, plenty of surface movements contain the hybrid motions of bend, stretch and compression. To achieve the one-fold recognition of tensile strain, the ideal strain sensor has to overcome the challenges in eliminating various interferences and detecting tensile strain solely in complicated conditions.²⁰⁶

Recent studies emphasize optimizing the sensitivity, sensing range and stability of the strain sensor through encapsulating sensing substrates with elastomers (e.g., Ecoflex or PDMS).^{155, 207, 208} The encapsulating fabrication sacrifices the physical wearing comfort by trapping air and sweat vapour generated from human metabolites.^{4, 148, 209} Although encapsulation-free fabric strain sensors assembled by conductive fibres were reported with improved breathability, they inevitably respond to bend and pressure during

complex body movements.⁵ Moreover, some feasible techniques for achieving flexible and conductive substrates suffer from infirm bonding between depositions and substrates such as deposition or coating of conductive nanomaterials onto fibres.^{2, 3} Particularly after cyclic washing or chronic soaking, conductive depositions in strain sensor tend to be washed off from substrates, resulting in deteriorated sensitivity and reliability. It is desirable to fabricate fibres with intrinsic flexibility and conductivity, along with the feasibility in the fabrication of fabric-based strain sensors, to develop a breathable, wettable and washable anti-jamming strain sensor.

Graphene fibre (GF), a macroscopic one-dimensional carbonaceous fibre with superior mechanical and electrical performance fabricated by the wet spinning of graphene oxide (GO) liquid crystals, exhibits great potentials in the manufacture of high-performance strain sensors.^{46, 47} However, on account of the unfavourable crystalline structures of GO, it still has been challenging in preparation of robust and ultra-flexible GFs to achieve the feasible assembly of wearable strain sensors and reliable sensing function under repetitive stretching, bending and pressing motions.²⁶ Although considerable modifications have been reported to flatten the wrinkled and random GO sheets or generate hierarchical surface structure during the solidification of GFs in coagulation bath, the modified GF shows enhancements in tensile strength while its flexibility still desiderates to be boosted due to the weak stacking density of GO.^{44, 54, 59, 210, 211} Owing to its inferior flexibility, bare of research articles have reported to integrate pure GF into fabric wearables in a textile technology.

Herein, for the first time, we report an innovative wet-fusing assembly of twisted graphene fibre (TGF) with remarkable flexibility and electrical performance. The wrinkled GO sheets in the prepared TGF were parallelised and condensed with the assistance of twisted structure, leading to a favourable crystalline structures of GO, improved tensile strength (369 MPa) and breaking strain (48.5%), along with lower resistance ($60 \Omega \text{ cm}^{-1}$) of TWF. Particularly, the robust and ultra-flexible continuous

TGFs were woven into strain sensors with outstanding sensitivity (gauge factor ~ 63) to applied tensile strain, and negligible response to bend, pressure, temperature and humidity. Benefiting from the intrinsic superior properties of TGF and stable sensor structures, the anti-jamming strain sensor (BWVAJ) displays decent breathability, washability and wettability, enabling its reliable and stable detection of human motions under complex conditions.

5.2 Experimental section

5.2.1 Preparation of GO dispersion

Graphene oxide dispersion was prepared from expandable graphite flakes (from Sigma-Aldrich with particle size larger than 300 μm) by a modified Hummers' method. 0.5 g expandable graphite was heated in the microwave oven (750 W) for 30 seconds to form expanded graphite. The expanded graphite, H_2SO_4 (100 mL, 98 wt%) and KMnO_4 (5 g) were mixed and stirred for 24 h. The mixture was slowly diluted with 100 mL deionised water in ice bath and the colour turned into yellow as H_2O_2 (10 mL 35 wt%) was added to the mixture. After that, HCl (100 mL 10 wt%) was added to the mixture. The aqueous GO dispersion was obtained after centrifuged for several times. Finally, the water in aqueous GO dispersion was replaced by N, N-dimethyl formamide (DMF) via an extra five-time centrifugation and GO DMF dopes with concentration of 10 mg/ml was obtained.

5.2.2 Wet spinning of continuous TGOFs and chemical reduction

GO dope was extruded through two separated spinnerets (0.51 mm diameter) into coagulation bath consisting of ethyl acetate and acetone. Unlike previous reports of GOFs, large-diameter GOFs (100 μm) were coming out from the thick spinnerets. The

thick GOFs was in favour of keeping them in wet condition in the following steps for the wet-fusing assembly. The two GOFs were drafted by two rollers (V_1 and V_2 in Fig. 1a) with different spinning speed in order to stretch and flatten the wrinkled GO sheets. Innovatively, another spinning roller (V_3) was carried out to twist the two wet GOFs together. The two GOFs started to wet-fusing assembling into one TGOF. The TGOFs with different twist angle were achieved by changing the speed of spinning roller (V_3). The TGOFs were reduced by hydroiodic acid (HI) at 80°C for 8 hours.

5.2.3 Fabrication of BWWAJ strain sensor via hand weaving loom

The BWWAJ strain sensor was fabricated under hand weaving loom (Figure S5-5). A plain-weave sensor structure was constructed by weft TGF and elastic Lycra warp yarns. The size of effective sensing part (contain TGF) is 10 mm × 5 mm.

5.2.4 Washability Test

The washability test was under standard: ISO 105 CO9 C1&C2, by treating the sensor in the wash liquor containing 10 g/L ECE detergent, 12 g/L sodium perborate and 1.8 g/L TAED (bleach activator). To simulate the agitation and abrasion, 25 steel balls were added into wash liquor (Figure S5-12). The laundry was operated at 60°C in a rapid rotating speed for 30 minutes.

5.2.5 Characterisations

The surface morphologies of TGF and BWWAJ sensor were observed from Q250 Scanning electron microscope (SEM). The X-ray diffraction (XRD) patterns were recorded on an XRD5 spectrometer (Type PANalytical X'Pert Pro) at operating voltage of 40 kV and current at 40 mA using Cu K α irradiation. The Raman spectra were carried

out using Raman spectrometer with 633 nm excitation wavelength. Mechanical tests and electrical calibration of the sensor were performed using a universal testing machine (Instron 3344) and a multimeter (Keithley 2000) respectively. The air and water vapour permeability were tested by commercialised instruments (SDL, M021A, M216). The temperature and humidity tests were carried out in a conditioning cabinet (Datacolor CONDITINER). The underwater wireless motion monitoring system was built by a wireless multichannel signal transmission module (LinkZill, LZ-01ARC).

5.3 Results and discussions

5.3.1 Fabrication and characterisations of TGFs

Fig. 1a shows the schematic illustration to fabricate twist graphene oxide fibres (TGOF) by wet-fusing assembly. Previous reports regarding the fabrications of GF *via* wet-spinning and GF-based nonwoven fabrics by wet-fusing assembly have been introduced in Chao Gao's works.^{44, 59, 212} However, wet-fusing assembly has never been applied into fabricating TGF with remarkable tensile strength and breaking strain (Table S5-1). Briefly, a spinning roller (V_3 in Fig. 1a) was carried out to apply the compression in the two wet GO fibres, which accelerated the generation of hydrogen bonding between interfaces of the two wet GO fibres and induced the wet-fusing assembly (See details in experimental section).²¹² The flat GO sheets were condensed and twisted under the applied pressure, leading to the formation of uniform twisted structure on the fibre surface. The twisted level of TGF is tunable by altering the speed of the spinning roller. Figure 5-1b displays surface morphologies of TGFs with different twisted angle ranging from 10° to 40° (defined as TFG-10, TFG-20, TFG-30 and TFG-40, respectively). The average twisted angles in various regions of TGFs are shown in Figure S5-1. The resistance keeps decreasing as the twisted angle rises, and the resistance of TGF-40 is only $60 \Omega \text{ cm}^{-1}$ (Figure S5-2). Photographs in Figure 5-2c exhibit the splendid flexibility of TGF which could be bent into a circle (bending stiffness of $4.68 \times 10^{-3} \text{ cN}$

cm²), and stretched to 165% under Instron (Figure S5-3, Movie S5-1). The image in Figure 5-2d shows its high tensile strength by vertically suspending a 100-gram load.

The stress-strain curve indicates TGFs with larger twisted angle have higher tensile strength and breaking strain (Figure 5-1e). In particular, TGF-40 has maximum breaking stress (369 MPa) and strain (48.5%), which shows significant improvement in toughness and flexibility compared with previously reported works (Figure 5-1f).^{26, 59, 210, 213, 214, 215} The boosted mechanical properties are originated from the parallelised and condensed GO sheets during fibre drafting and twisting process respectively, which are confirmed by Raman and XRD spectra. The (002) peak shifted from (25.07°) (2 θ) in TGF-10 to 25.24° in TGF-40, indicating more compact interlayer spacing of TGF-40 (0.35 nm) than that of TGF-10 (0.36 nm) calculated from Bragg equation (Figure S5-4a). Full-width at half maximum (FWHM) value of (002) peak indicates the decreased lateral thickness (4.63 nm) of single graphitic crystallite in the TGF-40 than that in TGF-10 (5.80 nm) described by Scherrer equation (Figure S5-4b). The decreased ratio of the integrated intensity of the D and G band (I_D/I_G) in the TGFs (1.49 in TGF-40, 1.55 in TGF-10) shows fewer defects and a more aligned microstructure in the TGF-40 (Figure S5-4c).

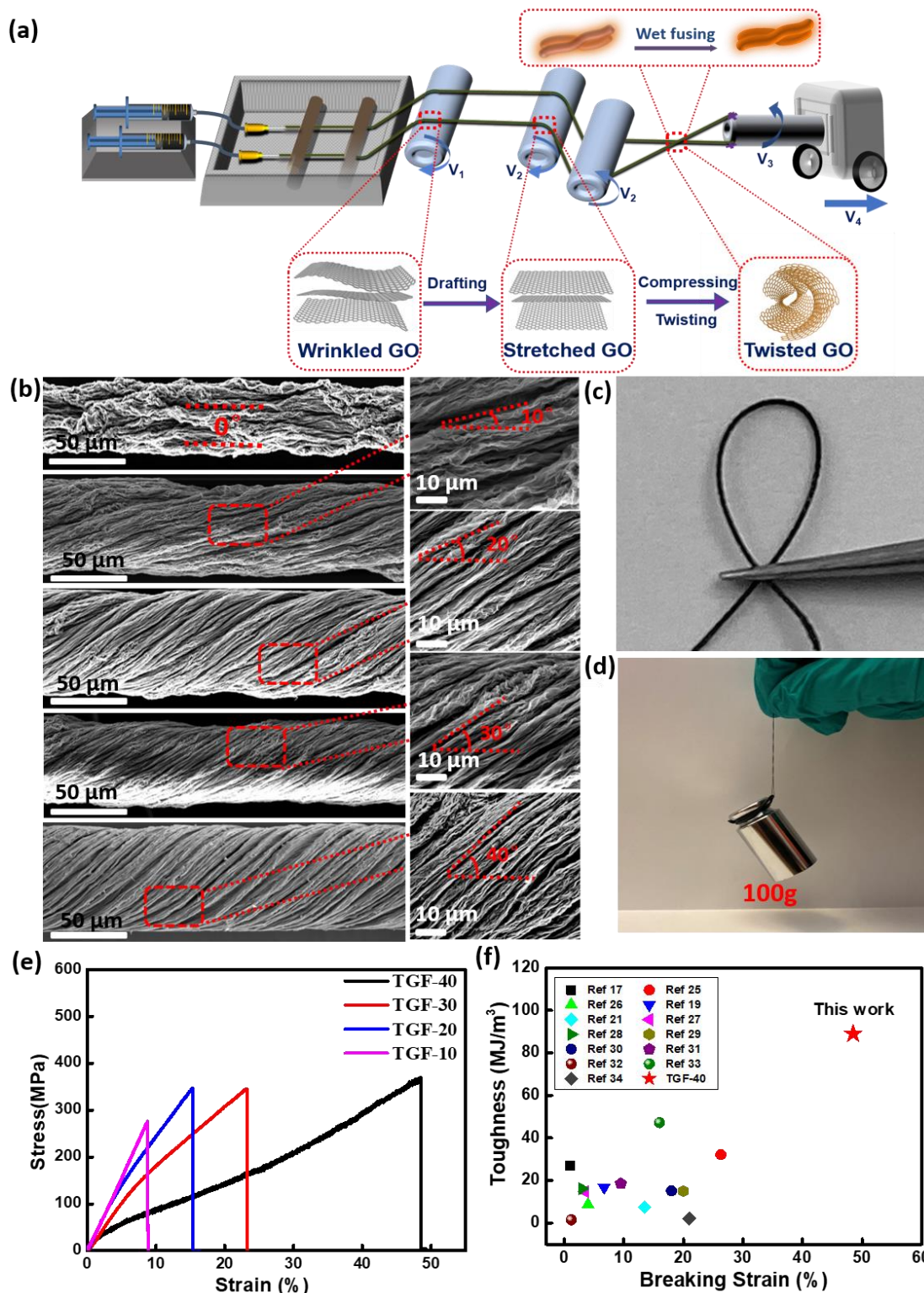


Figure 5-1. Fabrication of TGOF. a) Schematic illustration of TGOF fabrication process. The wrinkled GO sheets are stretched into flattened ones by fibre drafting process. Two wet stretched GO fibres twist together into one single TGOF by wet-fusing assembly. b) The surface morphologies of the TGFs with various twist angles from 0° to 40° . c)

Photograph of a bending TGF shows its flexibility. d) Single TGF suspends a 100g load, showing its excellent mechanical properties. e) Typical stress-strain curve of TGFs, indicating higher strength and strain TGFs are achieved by applying larger twist angles. f) Comparisons of mechanical properties of our work with previously reported graphene-based fibres. The toughness of fibre is defined by the area under the stress-strain curve. Scale bar, 50 μm (b); 10 μm (b with high resolution).

5.3.2 Fabrication, calibration and mechanism of BWVAJ sensor

By taking advantage of the superior flexibility and high strength, TGFs are capable of being woven into fabric strain sensors through conventional textile technics. Figure S5-5 shows the weaving procedure of a BWVAJ sensor under a manual weaving loom (see details in experimental section). An image of BWVAJ sensor and schematic illustration of the TGF-Lycra plane woven structure are shown in Figure 5-2a and Figure 5-2b respectively. Flexible nylon-covered Lycra fibres were served as warp yarns to generate elasticity for the fabric sensor. The single TGF-40 was served as weft yarn to create electrical signals corresponding to different external stimuli. To investigate the performance of BWVAJ sensor and its mechanism, we exposed it into various external interferences including different levels of stretch, bend, pressure, humidity and temperature.

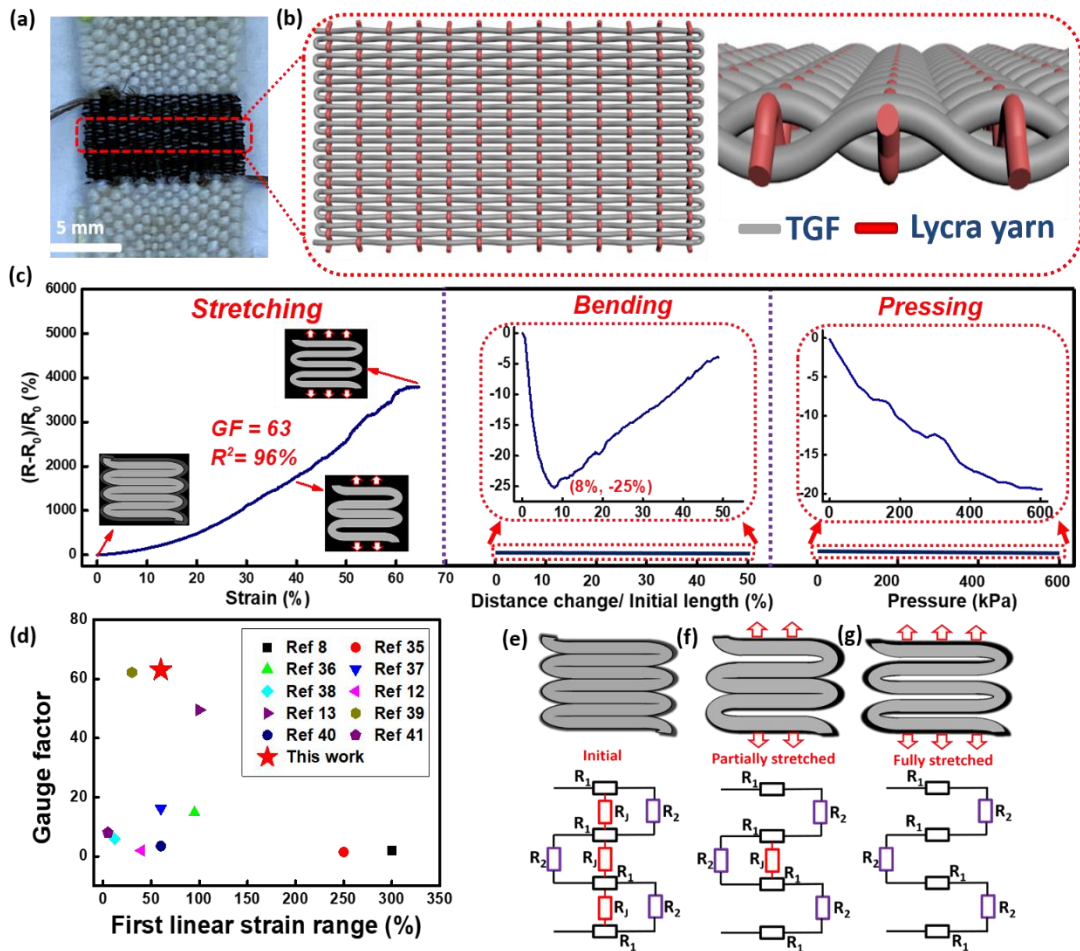


Figure 5-2. Fabrication of BWWAJ sensors and their electrical responses to external interferences. a) The image of the BWWAJ sensor, and b) Illustration of its internal plane-weave structure. The weft yarn is continuous TGF, warp yarns are elastic and nonconductive Lycra yarns. c) The sensitivity of the BWWAJ sensors under tensile strain, bend and compression, indicating the remarkable sensitivity under strain and negligible response under bending and pressing. d) Comparison of sensitivity of recent reported encapsulation-free strain sensors in terms of first linear strain range and gauge factor, which indicates the remarkable sensitivity of the BWWAJ strain sensor. e-g) The sensing networks and corresponding resistance models. Schematic illustrations show the geometry of the BWWAJ sensor in e) initial, f) partially stretched and, g) fully stretched states.

The BWWAJ sensor shows outstanding sensitivity under tensile strain (0-60%), while insignificant responses to bending, pressure, humidity and temperature (Figure 5-2c,

Figure S5-6 and Figure S5-7). When stretching the BWWAJ sensor at warp direction from 0% to 60% strain, it exhibits excellent sensitivity (gauge factor ~ 63) with high linearity ($R^2=96\%$), which is remarkable compared with unencapsulated sensors (Figure 5-2d).^{2, 5, 149, 208, 216} The bending degree is calculated by distance change/initial length of the sensor, which is demonstrated in Figure S5-8. The maximum resistance reduction (-25%) appears at bend of 8% throughout a 0-50% bending, and returns to -4% at bend of 50%. The diverse trend can be ascribed to the approaching movement of TGF under lower bending (0-8%) and separating movement of intermediate TGF under high bending (8%-50%), which has been described in our previous reports.² The sensor also displays superior insensitivity to high compression, with resistance only decreasing 20% under 600 kPa pressure. The insensitive response to pressure benefits from the non-conductive Lycra yarn which separates two layers of conductive TGF under applied pressure (cross-sectional view in Figure 5-2b). Besides, the humidity response test indicates only a low resistance increase of sensor (1.2%) by raising the relative humidity from 40% to 90% (Figure S5-6a). The minor response to humidity is attributed to the hydrophilic properties of TGF and sensor, which was confirmed by contact angle test (Figure S5-6b). The resistance of the sensor decreases 10% as the surrounding temperature increased from 20°C to 40°C (Figure S5-7). It should be noted that resistance change of the sensor can easily reach 20% with a strain of 2.7%, which exhibits the sensor is insensitive to bend, pressure, humidity and temperature compared with tensile strain. Moreover, considering the strain sensor is applied into the detection of small body movements and rarely involved in extreme conditions (high pressure, bending or temperature) simultaneously, the strain sensor is endowed with anti-jamming properties in real applications.

The flexible and robust TGF provides essential flexibility and impressive conductivity in sensor fabrication and sensing process respectively. The novel sensor structure with single TGF tightly aligning and winding in weft direction (Figure 5-2b), is equivalent to a parallel or hybrid circuit that is dependent on various stretched levels (Figure 5-2e-

g). Fig. 2e shows the initial state of sensor without stretching and the corresponding simplified circuit schematic. The initial resistance of the sensor (R) can be calculated by equation (1) below,

$$R = n \frac{R_1 R_2 + R_1 R_J + R_2 R_J}{R_2 + R_J} + R_1 \quad (1)$$

$$R' = m \frac{R_1 R_2 + R_1 R_J + R_2 R_J}{R_2 + R_J} + (n - m)(R_1 + R_2) + R_1 \quad (2)$$

Where R_1 and R_2 represent the resistances of the liner part and curved part of TGF respectively, R_J refers to the contact resistance generated by neighbouring TGF. Equation (1) can describe the total resistance of the sensor when all liner-part resistances (R_1) pack together, while the connected TGF detaches away as sufficient strain is given. The separation of TGF takes place gradually from edge to centre (Figure 5-2f), which was confirmed with SEM (Figure S5-9). Under these circumstances, the resistance of the sensor (R') increases due to the disappearance of partial parallel circuits. Equation (2) demonstrates the calculation of resistance (R') in that case, and in the extreme condition when the sensor is completely stretched with all TGF separated (Figure 5-2g). The above schematic models and equations illustrate the mechanism of the sensor in sensing stretch-induced deformation.

5.3.3 Electromechanical properties of the BWWAJ sensor

To further investigate the stability of the sensor responding to diverse mechanical stimulus, we carried out the electromechanical study on the sensor. Figure 5-3a shows the electrical response of the sensor by stretching it to various strains (10%, 20%, 30% and 40%) and holding it at such strains. The electrical output remains stable once the sensor is fixed at certain strain, indicating outstanding static stability of the sensor. The dynamic stability of the sensor responding to strain is illustrated by gradually rising the strain from 20% to 50% (Figure 5-3b). Similarly, we regulate the stretching-releasing frequency in the range between 0.05 and 0.4 Hz at strain of 30% to study the dynamic stability in terms of frequency (Figure 5-3c) and higher frequencies at 0.8 and 1.6 Hz

as shown in Figure S5-10. The repeatable electrical signals in each strain level and frequency level confirms the dynamic stability of the sensor, ensuring its reliability for strain detection under a dynamic state.

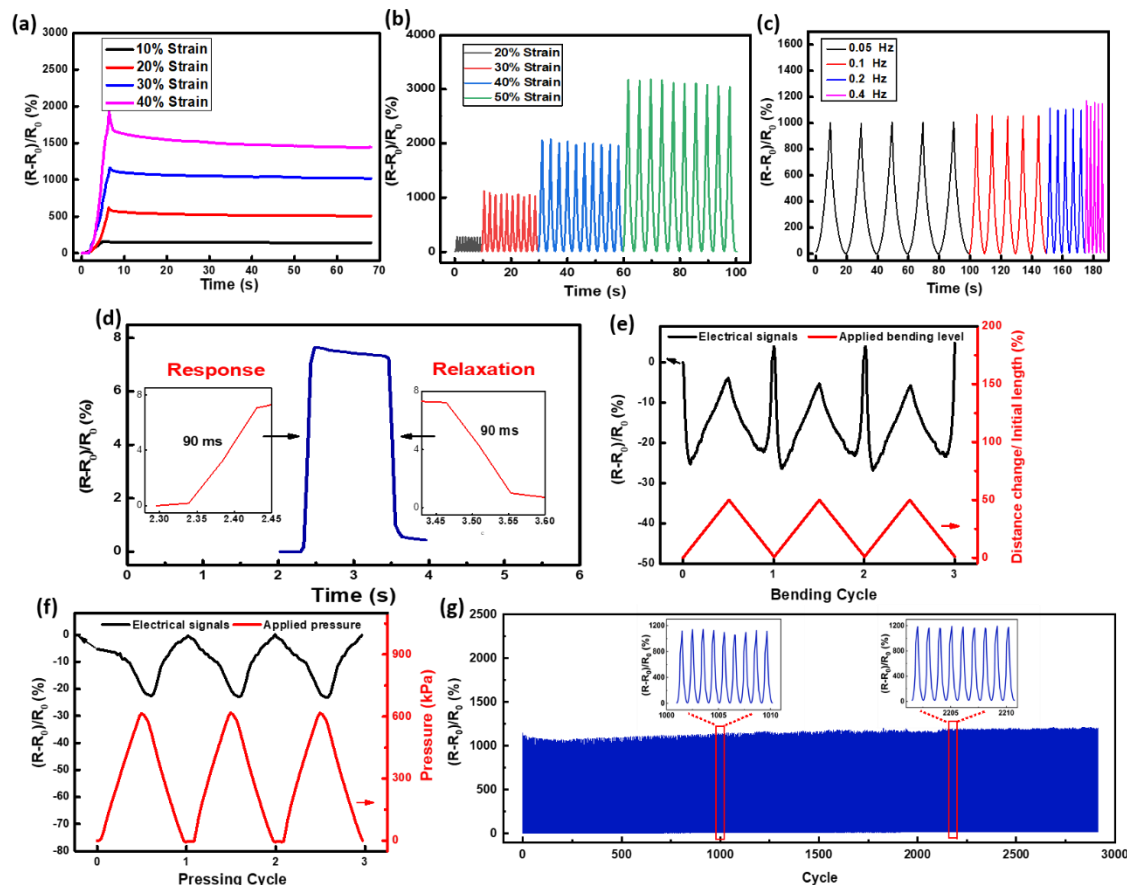


Figure 5-3. Electromechanical properties of the BWWAJ sensors. a) The relative resistance changes of the sensor with gradient stains to show the static stability. b) Dynamic stability of the sensor to various strains increased from 20% to 50%. c) Dynamic stability of the sensor to various frequencies increased from 0.05 to 0.4 Hz under strain of 30%. d) The real-time response to strain of 0.5% at a fast-stretching speed, showing the sensor has a rapid response and relaxation speed (90 ms). e) Sensor performance under repetitive 0-50% bending level, indicating the consistent insensitivity to bending. f) Sensor performance under cyclic 0-600 kPa pressure, indicating the consistent insensitivity to pressure. g) The electrical responses to repeating 3000 stretching-releasing cycles at strain of 30% and frequency of 1 Hz, showing excellent durability of the sensor.

Figure 5-3d exhibits the measurement of response and relaxation speed by rapidly stretching the sensor to a small strain (0.5%) and then releasing it. The response and relaxation time were all determined to be 90 ms, which is adequate to sense strain in many applications. The real-time electrical response to bending-relaxing cycles is shown in Figure 5-3e. The signals over consistent 3 bending cycles indicates the sensor is stably insensitive under dynamic bending conditions. We can draw an analogical conclusion to pressure by demonstration of cyclic pressing-relaxing cycles in Figure 5-3f. The constantly insensitive response of the sensor to the dynamic bending and pressing movements guarantees its anti-interference feature in complicated and practical sensing environments.

The stable durability of the sensor was determined by stretching and releasing it in the range of 0-30% strain at a frequency of 1 Hz for consecutive 3000 cycles. The electrical outputs remain steady and reproducible throughout the entire cycles with slight fluctuation (Figure 5-3g). Such reliable durability is attributed to the elastic and robust Lycra yarns, which provide durable elasticity and stable response to strain under sufficient stretching-releasing cycles at a high frequency (Figure S5-11). Furthermore, the splendid mechanical performance of TGF promotes to construct the indestructible sensing network (Figure 5-2c and Figure 5-2d). By integrating the above electromechanical features, the anti-jamming sensor is possessed of highly sensitive to strain, remarkable stability and durability, along with rapid response and relaxation.

5.3.4 Washability, breathability and wettability of the BWWAJ sensor

The recently reported wearable sensors were mostly constructed on either smart textile coated by conductive nanomaterials or encapsulated packaging approaches. Such fabrication sacrifices the physical comfort, as well as washability and wettability which are the essential elements to wearables.^{217, 218} The pure textile-based and encapsulated-free BWWAJ sensor integrated by high-performance TGF with a robust sensing

network, is considered to be authentic wearables (see taxonomy of encapsulation-free strain sensors in Table S5-2). We assessed the wash fastness of the sensor according to standard: ISO 105 CO9 C1&C2 (see details in experimental section and Figure S5-12), and calibrated it after several times of machine wash. The sensitivity of the sensor slightly decreases with incremental washing cycles (Figure 5-4a), with a reduction of gauge factor from 63 to 50 and a subtle increase of linearity from 96% to 97% after six washing cycles (Figure S5-13). The minor expected deterioration was mainly ascribed to the alkaline detergent and abrasion during the washing process, which worsen the properties of all fibres in the fabric sensor. However, the entire sensing structure remains firm and stable after all washing cycles (Figure S5-14). Noted that even the commercial garments will suffer from deteriorated performances through multiple machine washing cycles, the BWWAJ sensor is endowed with decent washability as general garments.

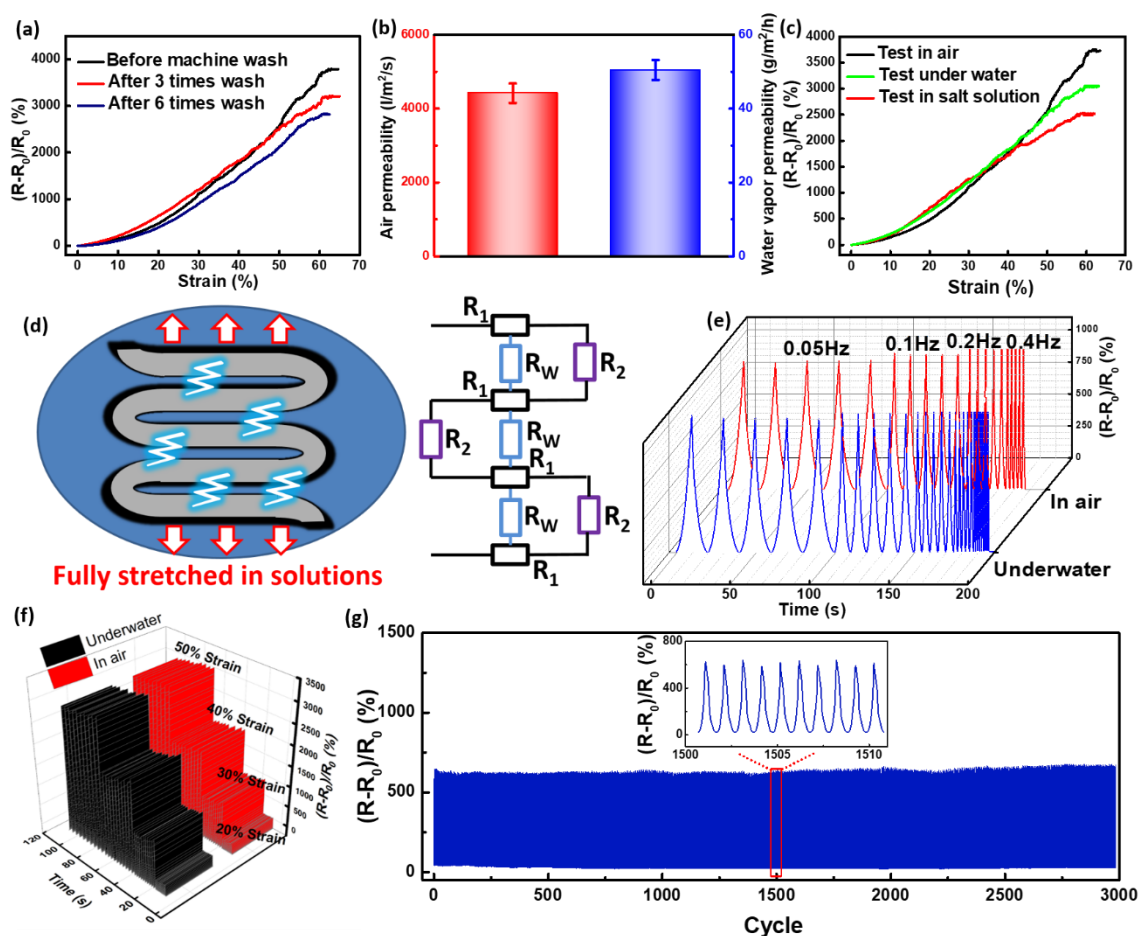


Figure 5-4. The washability, breathability and wettability of BWWAJ sensors. a)

Electrical response to strain before and after machine wash. b) The air permeability and water vapour permeability of sensor. c) Comparison of sensitivity in air, under water and under salt solutions (5% NaCl₂ solution). d) Schematic illustration shows sensor is fully stretched in solutions and its corresponding resistance models. e) & f) Comparison of the dynamic stability responding to various frequencies (e) and strain (f) in air and under water, showing the stable and reliable wettability. g) The electrical responses to a repeating 3000-cycle loadings and unloadings at strain of 20% and frequency of 1 Hz under water, indicating excellent working durability under water.

Human metabolites are always secreted out in the forms of vapour and gas, which affect the human physical comfort if they remain trapped inside the garments.^{161, 162} The air permeability (4620 l m⁻² s⁻¹) and water vapour permeability (48 g m⁻² h⁻¹) of the sensor was assessed to evaluate its breathability (Figure 5-4b). Such permeability is far above wearing standard as general garments in terms of physical comfort (Table S5-3). We further investigated the wettability of the BWWAJ sensor by calibrating its sensitivity and stability under water and salt solution (Figure S5-15), and compared its sensitivity with the response in air. Figure 5-3c indicates its sensitivity under water almost remains unchanged before fully-stretched state while declines a bit when it is entirely stretched, and more obvious reduction of sensitivity in salt solution is observed under fully-stretched state. The reduction of sensitivity is ascribed to water pathway, which generated alternative electrical pathways between adjacent TGF as shown in schematic illustration in Figure 5-4d. Equation (3) and (4) demonstrate the overall resistance of fully-stretched sensor under water (R_{SW}) and in air (R_{SA}) respectively.

$$R_{SW} = n \left(R_1 + \frac{R_2 R_W}{R_2 + R_W} \right) + R_1 \quad (3)$$

$$R_{SA} = n (R_1 + R_2) + R_1 \quad (4)$$

Where R_W represents the resistance generated from adjacent TGF and water. The dynamic stabilities of the BWWAJ sensor under various frequencies and strains in water were investigated and compared in Figure 5-4e and Figure 5-4f respectively. The stable and cyclic electrical signals of the sensor under water were almost consistent with those

in air, indicating the BWVAJ sensor can precisely and stably detect tensile strain by ignoring the effect of water. Figure 5-4g exhibits the durability of the sensor in water by repeatedly loading and unloading it at a strain of 20% and frequency of 1 Hz for 3000 cycles (Movie S5-2). After soaking in water for one week, the sensor only has a minor reduction of sensitivity (gauge factor decreases from 55 to 48 as shown in Figure S5-16). The steady and reproducible electrical outputs throughout the whole cycles guarantee its reliable durability. The outstanding and reliable wettability of the BWVAJ sensor enables it to precisely detect human motions underwater.

5.3.5 Underwater motion monitoring

The BWVAJ strain sensor is favourable to detect the human motions underwater on account of its remarkable washability and wettability. Figure 5-5a illustrates the underwater wireless motion monitoring system which was constructed by integrating the BWVAJ strain sensors and a commercial multichannel wireless signal transmission module. Typically, the four BWVAJ strain sensors were sewed onto the elbow and knee pads on human body respectively (Figure S5-17). The real-time motion signals of elbow and knee joints were acquired and displayed on the mobile interface through Bluetooth transmission. We tested the monitoring system in a swimming pool by swimming in different styles (freestyle, breaststroke and tread water), various motion signals of body parts (left arm, right arm, left leg and right leg) were captured and recorded on the mobile interface in real time (Figure 5-5b). The reproducible and rhythmic motion signals of the general swimming styles indicate the reliable motion detection of the BWVAJ sensor. We also demonstrated the motion signals of a drowning swimmer, the irregular motion signals (amplitudes and frequencies) described a potentially dangerous state of the swimmer who was urgent to be rescued.

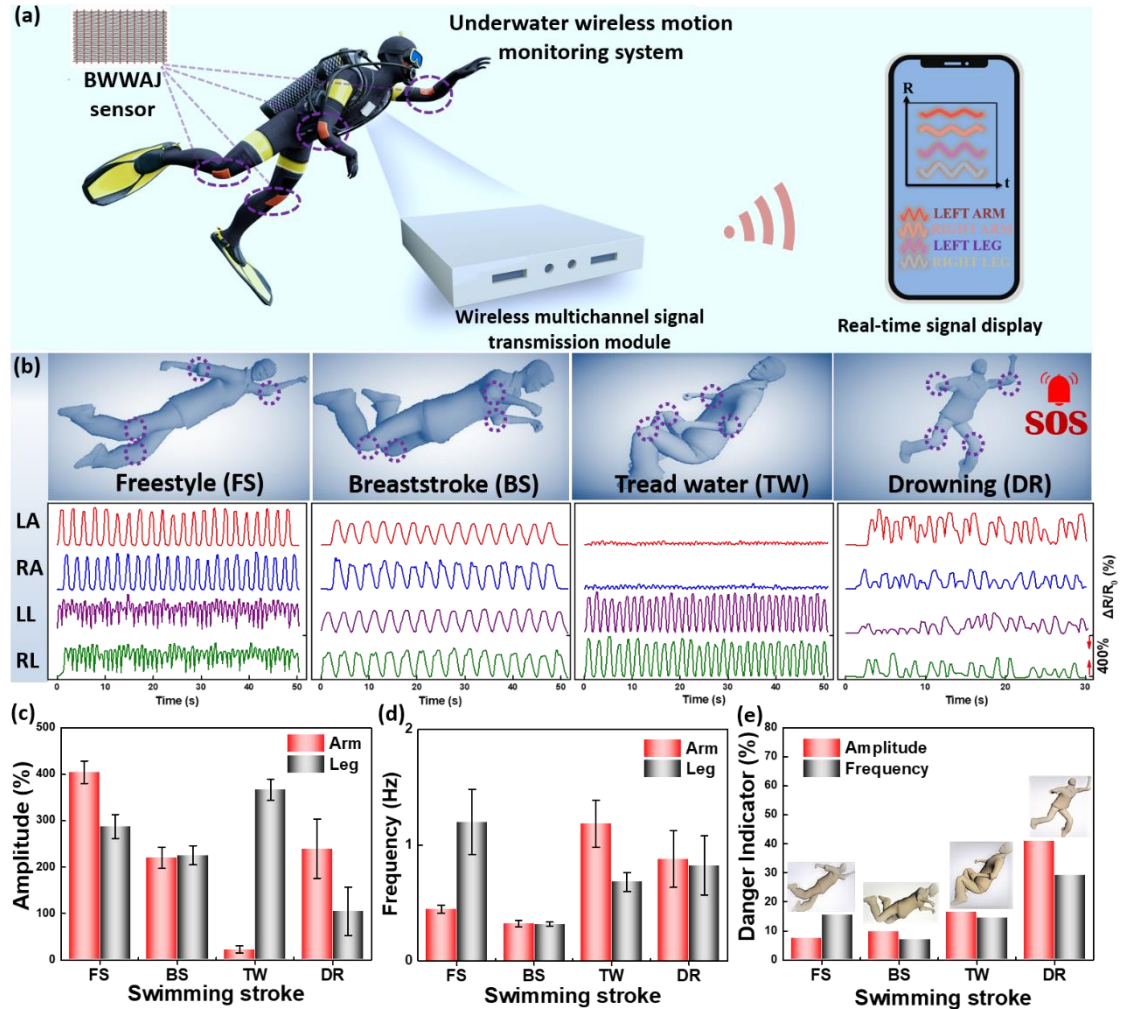


Figure 5-5. Underwater wireless motion monitoring system. a) Schematic illustration of an underwater wireless motion monitoring system. b) Electrical signals of various swimming strokes recorded by the monitoring system, LA, RA, LL and RL represents left arm, right arm, left leg and right leg respectively. c) Amplitude (average peak resistance change (%)) of arms and legs in the four swimming strokes. d) Frequency (1/average peaks interval (s)) of arms and legs in the four swimming strokes. e) Danger indicator (%) in terms of amplitude and frequency in the four swimming strokes, which was calculated from average RSD of arms and legs.

To prevent the swimmers from drowning, we investigated the motion signal characters of various swimming strokes in terms of amplitude (average peak resistance change) and frequency (1/average peaks interval). Figure 5-5c shows freestyle has the largest amplitude of arms (peak resistance change of 400%) and tread water has the largest

amplitude of legs (peak resistance change of 380%), which indicates these two swimming styles depend on active movements of arms and legs respectively. The smallest frequency of motions in the breaststroke (0.322 Hz for arms and 0.317 Hz for legs) in Figure 5-5d means slow-frequency demands for body movements in breaststroke. We employed the average relative standard deviation (RSD) of arms and legs as the danger indicator (DI) to evaluate the risks in different swimming strokes. The highest RSD of the amplitudes (28% for arms and 50% for legs in drowning) and frequencies (28% for arms and 31% for legs in drowning) describes the highly variable amplitudes and frequencies of arm swing and leg driving while in danger of drowning (Figure S5-18). Figure 5-5e illustrates the potential risks in tread water with second highest DI (16.43% for amplitude and 14.43% for frequency). The wireless motion monitoring system based on the BWWAJ strain sensors provides information about vital motion signal characters underwater to supervise swimming movements, train swimming learners and evaluate risks of drowning.

5.4 Conclusions

In summary, we have proposed a wet-fusing assembling methodology to fabricate continuous TGFs with robust and ultra-flexible properties, as well as stable electrical and mechanical performances under cyclic washing and chronic soaking. The as-prepared TGF could be directly woven into pure fabric-based breathable, washable and wetttable BWWAJ stain sensor with anti-jamming properties to bend, pressure, temperature and humidity. The BWWAJ strain sensor exhibits rapid response and relaxation, remarkable stability and durability, along with high sensitivity to tensile strain (gauge factor ~ 63). The high-performance of the TGF and novel structure of the BWWAJ sensor display feasibility in scalable fabrications of strain sensors through a cost-effective textile technology, paving a new route to assemble anti-jamming wearable electronics.

5.5 Supplementary information

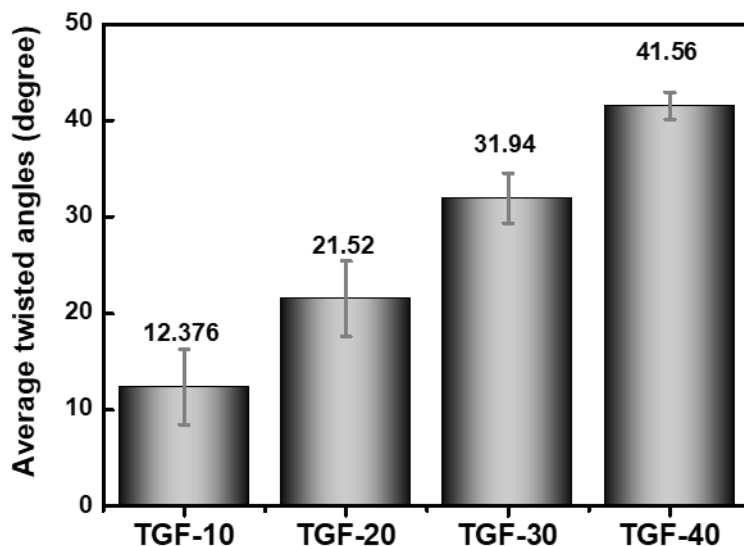


Figure S5-1. Average twisted angles in various regions of the TGFs. Five random regions were selected from each TGF to analyse the average twisted angles. The average twisted angles in the TGF-10 vary more greatly than others, which can be attributed to the smaller twisting and compressing forces during the formation of the TGF-10. The fluctuation of the small twisting force influences the twisting angles in the TGF-10 eventually.

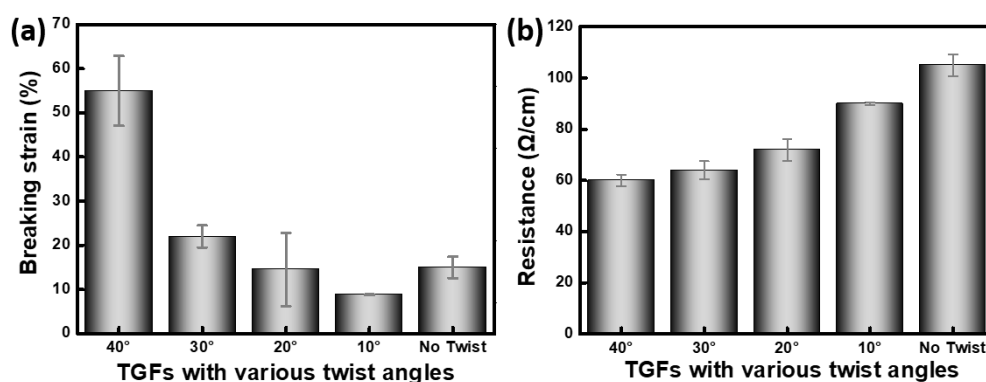


Figure S5-2. Mechanical and electrical properties of TGFs with Various twist angles. a) The breaking strain of TGFs increases with larger twist angle created on the surface (10°

to 40°), the average breaking strain of TGFs-40 can reach 55%, which is significantly improved compared with previous published works (Figure 5-1e). b) The resistance of TGFs keeps decreasing as the twist angle increases. The average resistance of TGF-40° is $60 \Omega \text{ cm}^{-1}$.

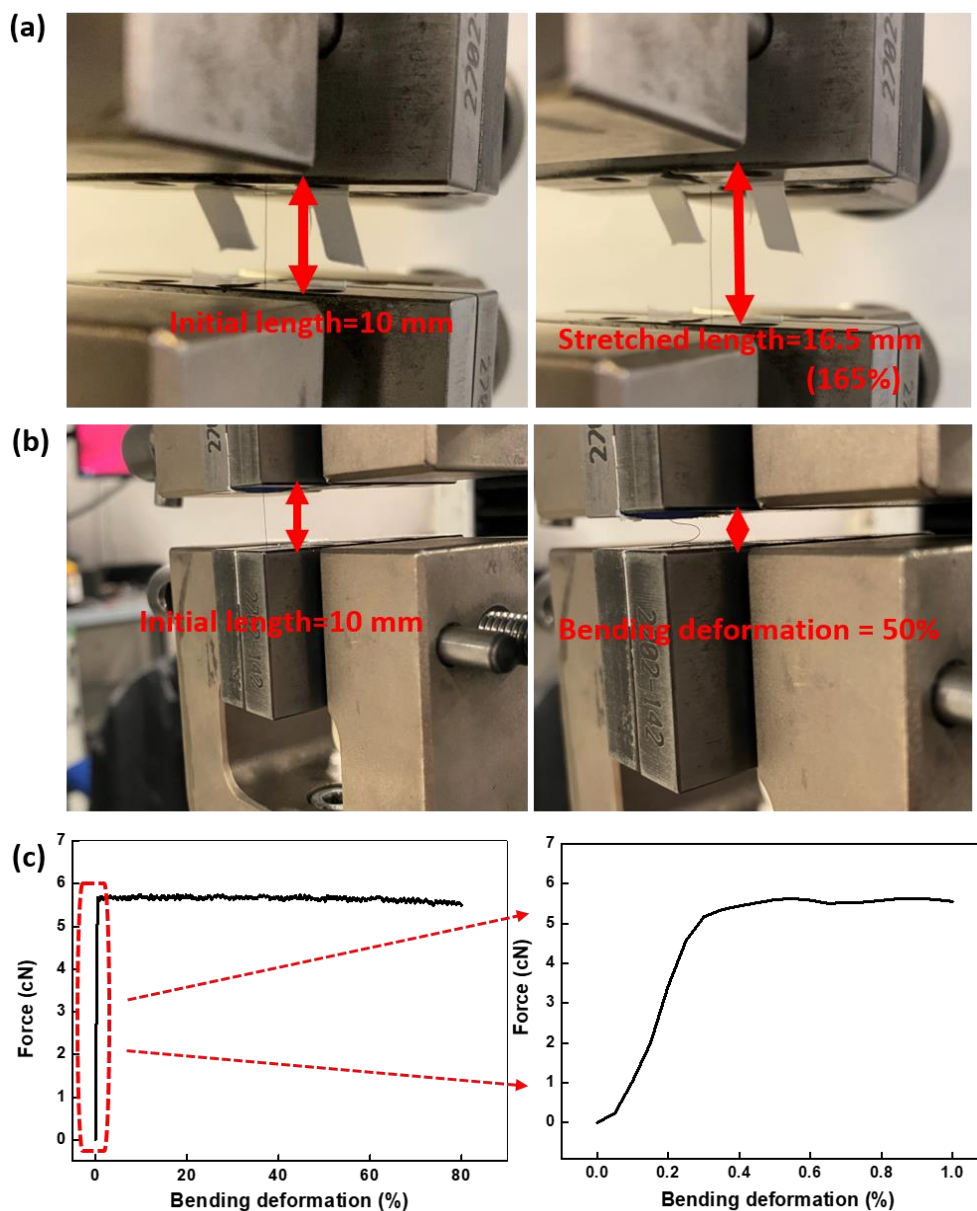


Figure S5-3. a) A typical TGF-40 could be stretched to 165% under Instron, indicating its remarkable flexibility. b) A typical TGF-40 with bending deformation (bending distance change/initial length) of 50%. c) Bending force-bending deformation curve of TGF-40, showing its maximum bending force (5.35 cN) at bending deformation of

0.35%. The bending stiffness ($R_B = 4.68 \times 10^{-3} \text{ cN cm}^2$) of TGF-40 could be calculated from the curve ($R_B = EI$, where R_B represents the bending stiffness (cN cm^2), E represents the elastic modulus (cN /cm^2), I represents the moment of inertia (cm^4)).

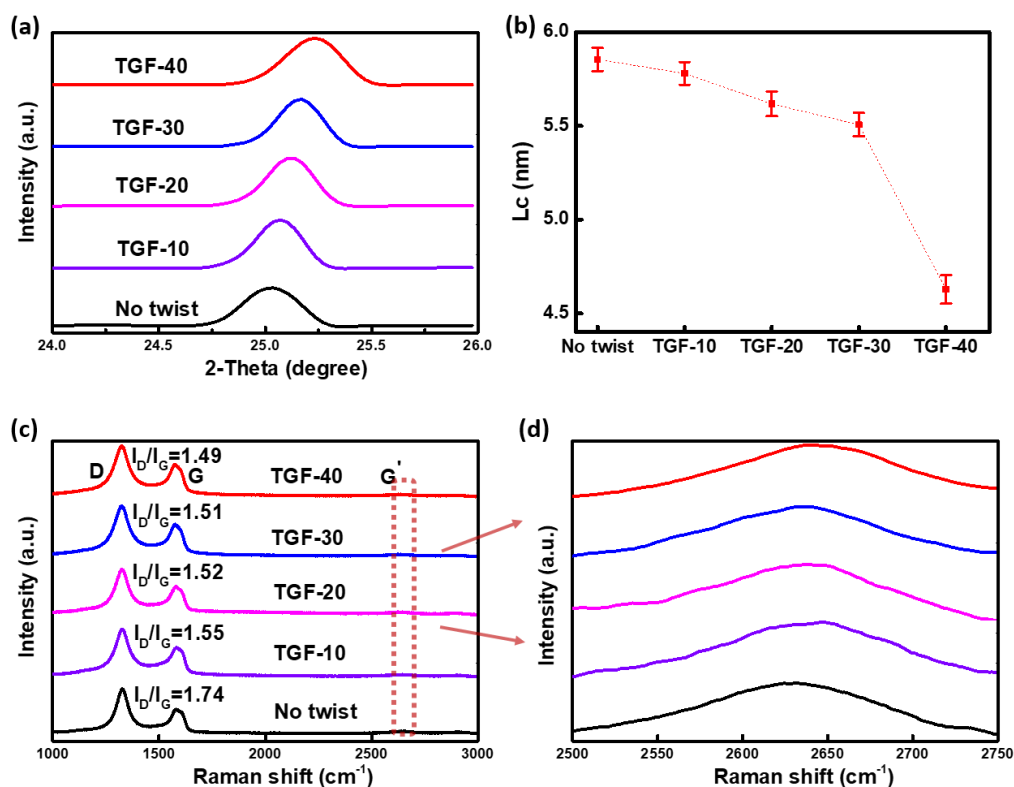


Figure S5-4. Characterisations of GF with no twist and TGFs. a) XRD spectra shows the (002) peak. b) Lateral thickness (L_c) of single graphitic crystallite. c) Raman spectra shows intensity of D, G and G' bands. d) Detailed view of G' bands in Raman spectra.



Figure S5-5. Fabrication of the BWWAJ strain sensor. a) hand weaving loom. b) hand weaving process with TGF bobbin. c) plain weave sensor structures constructed by weft TGF and elastic Lycra warp yarns.

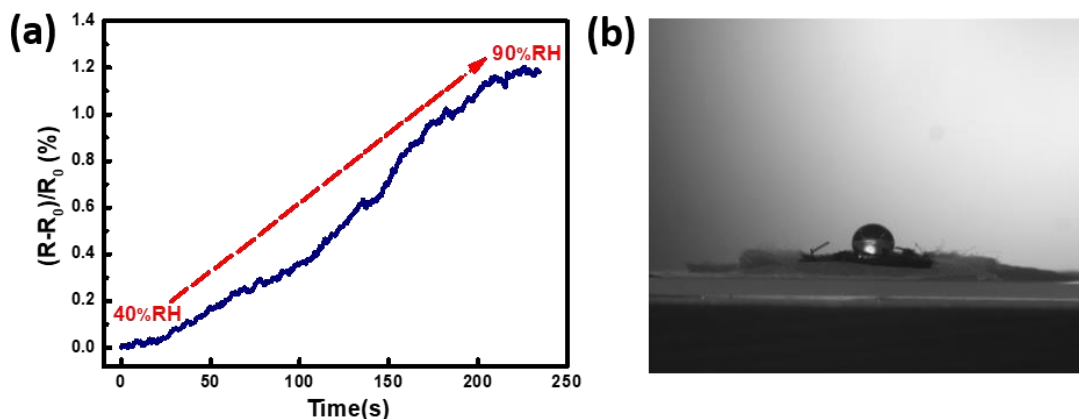


Figure S5-6. a) The electrical responses of the BWWAJ strain sensor against humidity. b) Contact angle test of the BWWAJ sensor. The figure was captured after with interval time of 30 seconds after water dropping on sensor surface. The contact angle was tested to be 145° , indicating hydrophobic property of sensor.

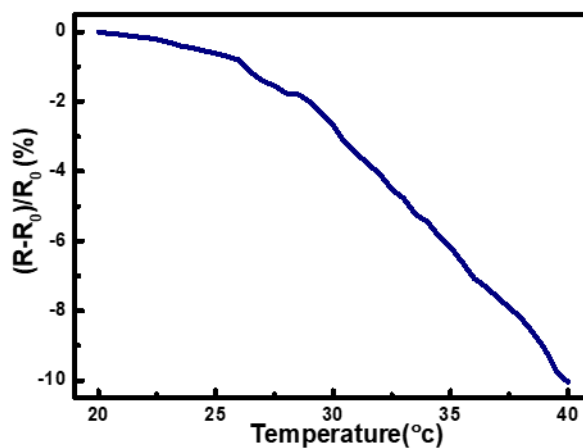


Figure S5-7. The electrical responses of the BWWAJ strain sensor against temperature (20-40 $^\circ\text{C}$).

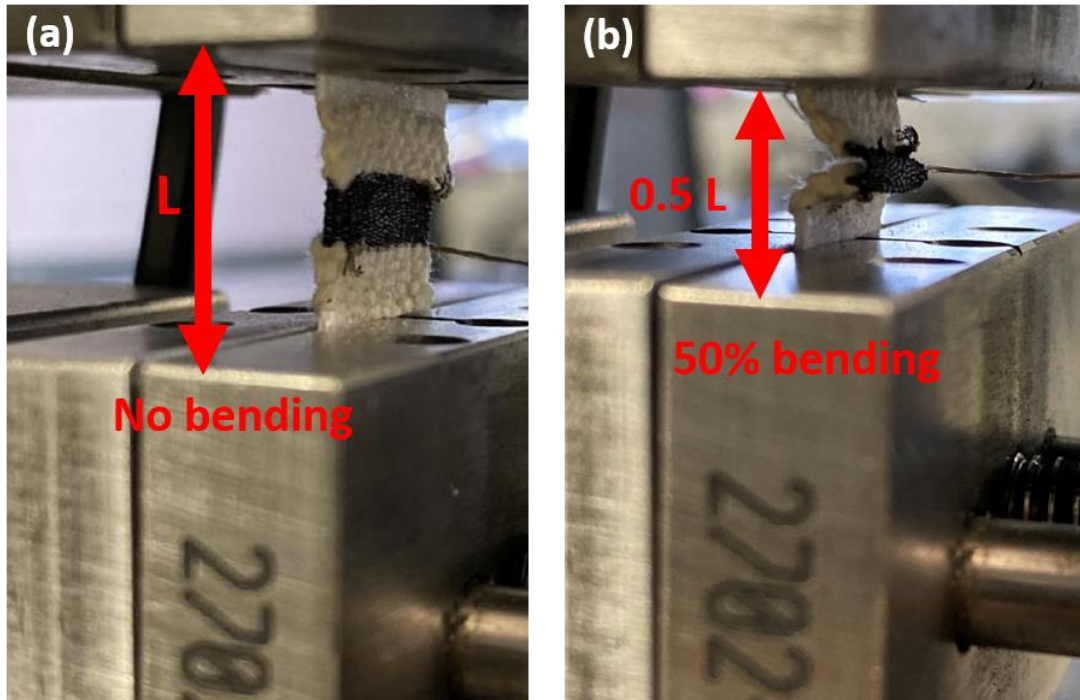


Figure S5-8. Illustration of bending test of the BWWAJ sensor. a) Sensor is flattened without any bending. b) Sensor is under 50% bending.

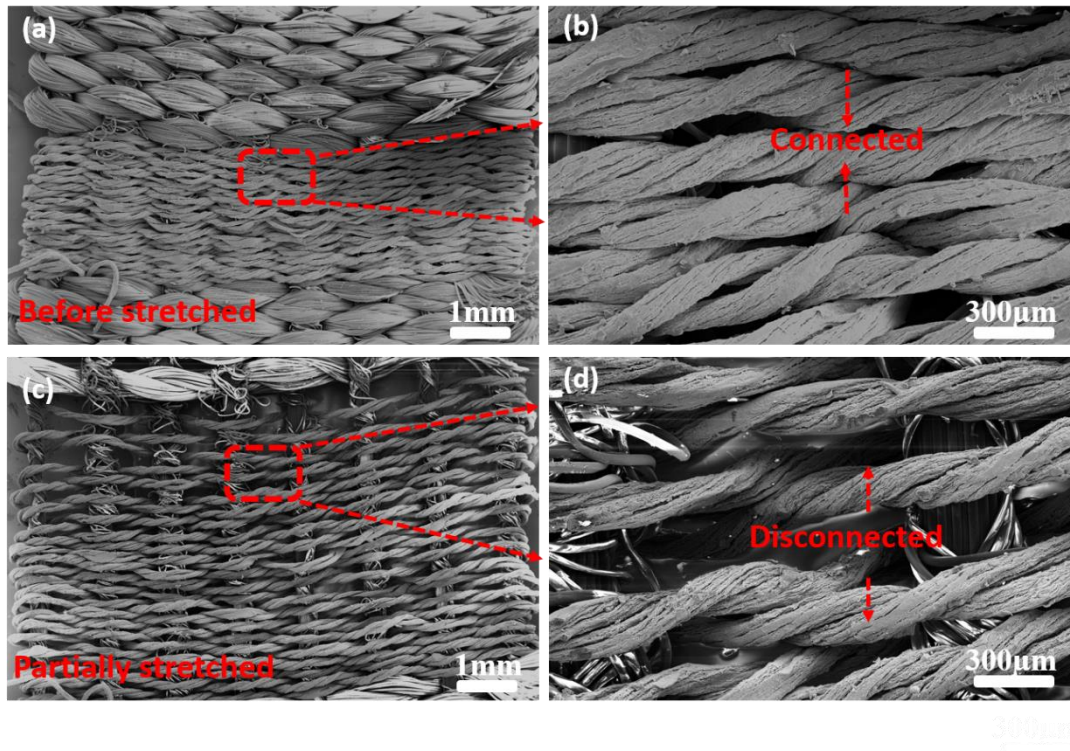


Figure S5-9. SEM images of the BWWAJ sensor before and after stretched. a & b) Sensor is at initial state, TGFs are connected to each other. c & d) Sensor is partially

stretched, TGFs starts to separating by each other.

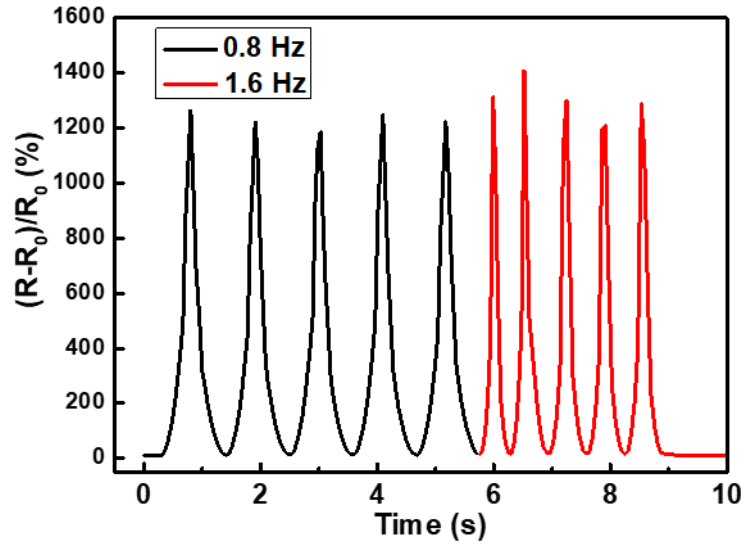


Figure S5-10. Dynamic stability of the sensor to higher frequencies of 0.8 Hz and 1.6 Hz under strain of 30%.

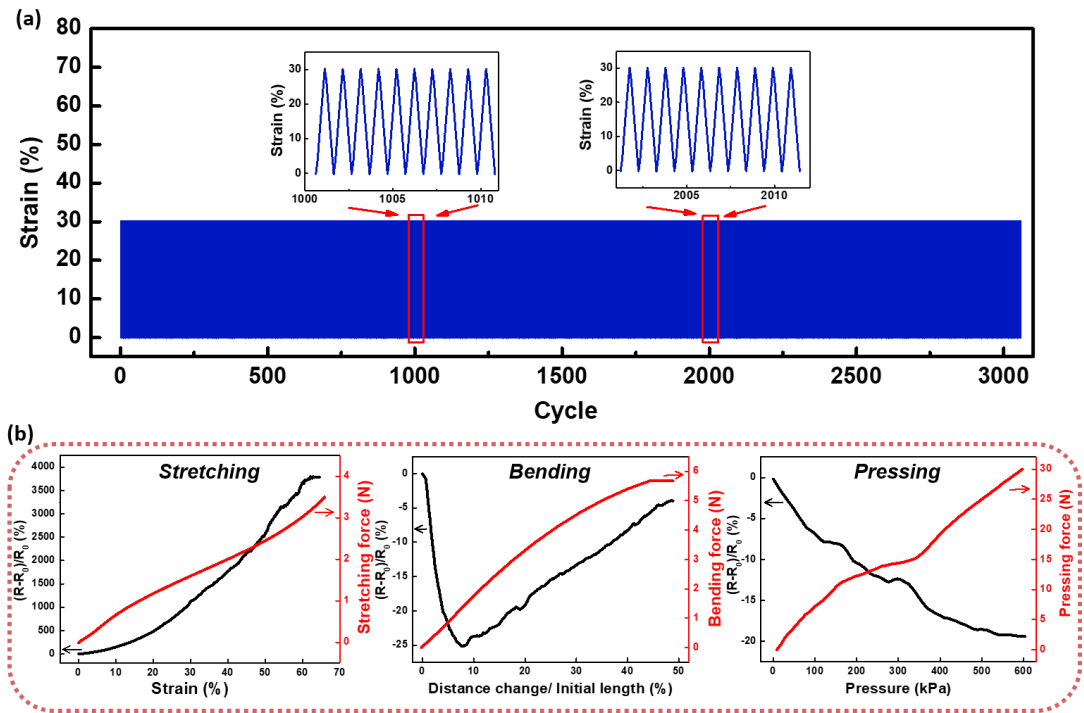


Figure S5-11. Mechanical properties of the BWWAJ sensor. a) The BWWAJ sensor under 3000-cycle loadings and unloadings at 0-30% strain at frequency of 1 Hz,

indicating the sensor has excellent mechanical durability. b) Resistance change of the BWWAJ sensor to the applied stretching, bending and pressing force.

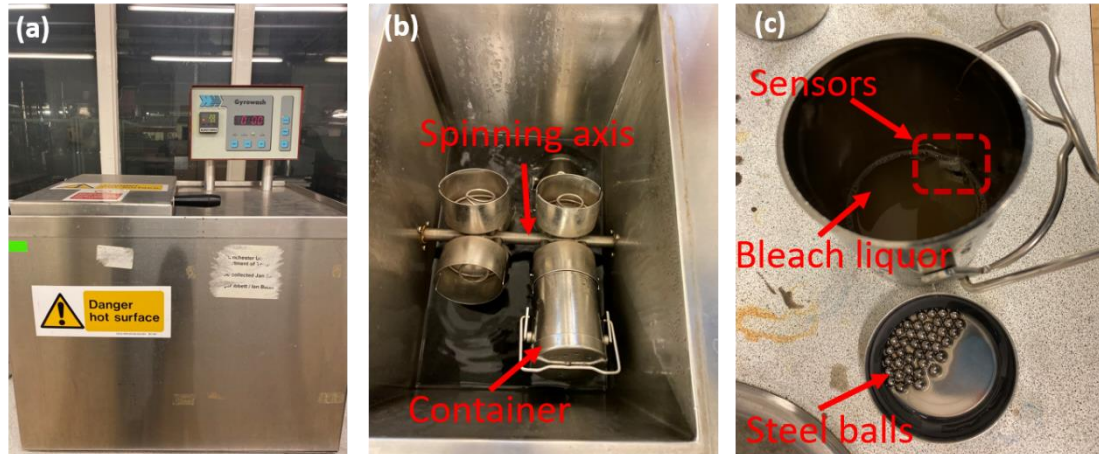


Figure S5-12. Digital images of machine wash test. a) Washing machine with adjustable washing temperature and spinning speed. b) Washing cell with the rotating container. c) Container with sensor, bleach liquor and steel balls inside.

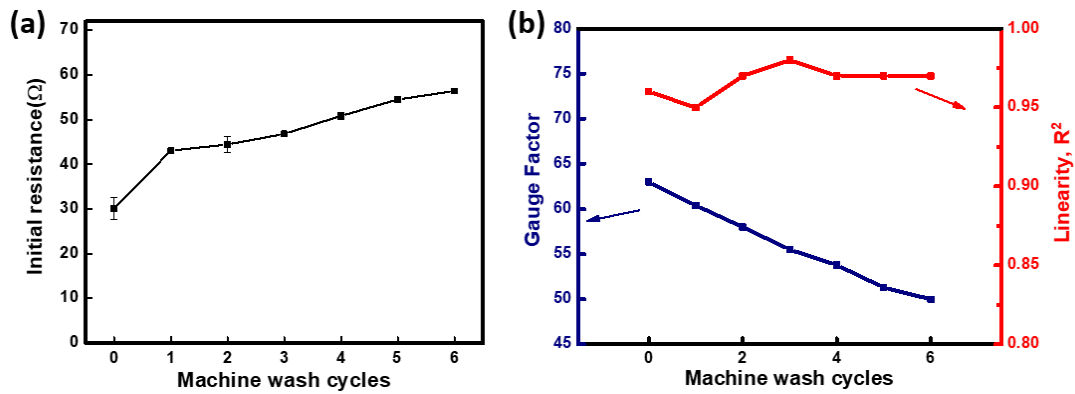


Figure S5-13. The influences of machine wash on sensor performance. a) Initial resistance change of sensor over 6 times machine wash. b) Corresponding gauge factor and linearity.

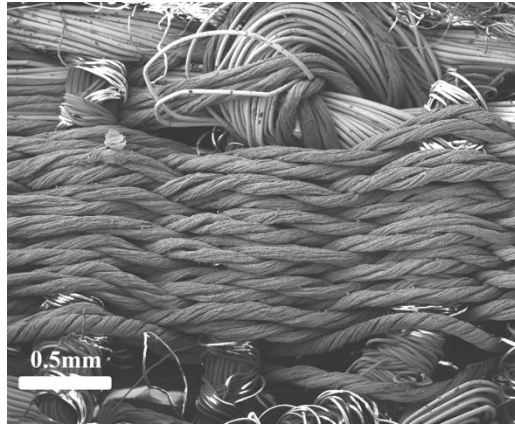


Figure S5-14. The structure of sensor remained stable after 6 times machine washing, indicating the excellent washability of sensor.

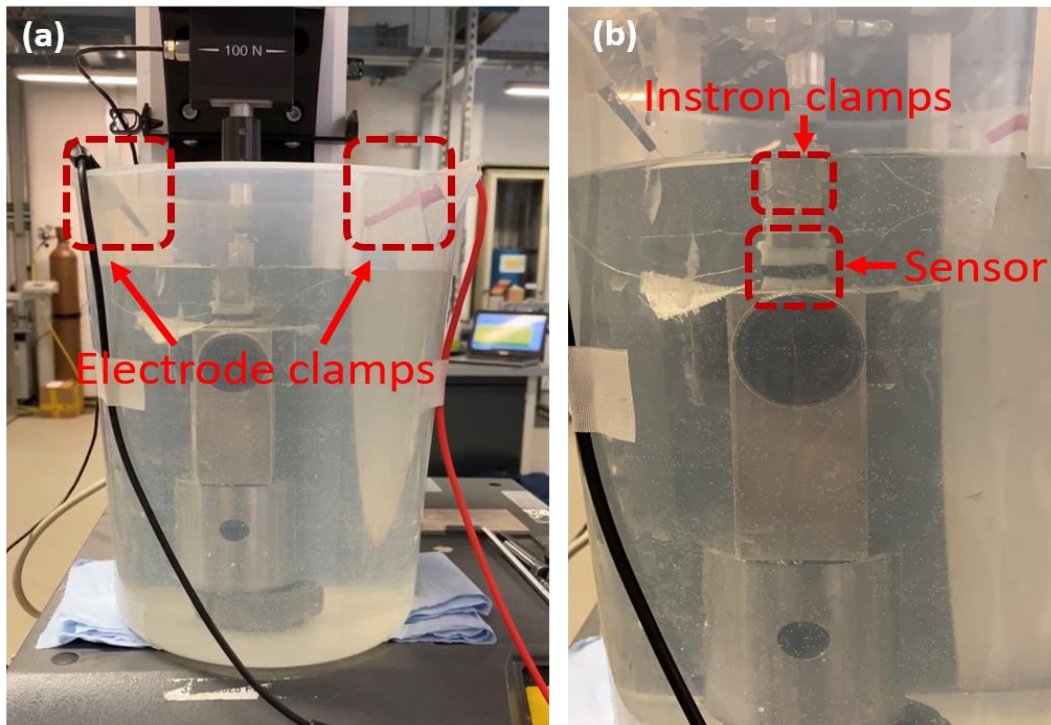


Figure S5-15. Digital images to illustrate the electromechanical experiments of sensor under wet conditions.

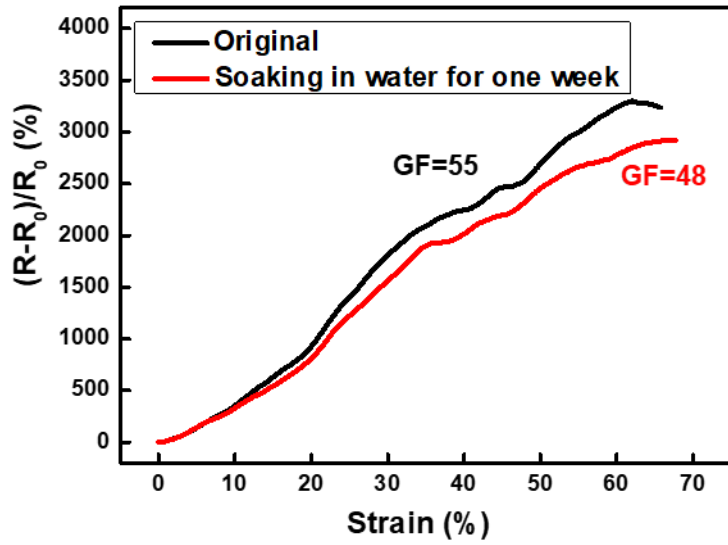


Figure S5-16. Sensitivity of the BWWAJ sensor after one week's soaking in water. It indicates the gauge factor of the sensor has a little reduction from 55 to 48.



Figure S5-17. Photographs of integrated wearable BWWAJ strain sensors on the arthrosis of athlete. a) Sewing BWWAJ strain sensors onto elbow and knee pads. b)

Integrating the BWWAJ strain sensors and wireless signal transmission module on the athlete. c) BWWAJ strain sensor under strengthened arm and bended arm. d) BWWAJ strain sensor under strengthened leg and bended leg.

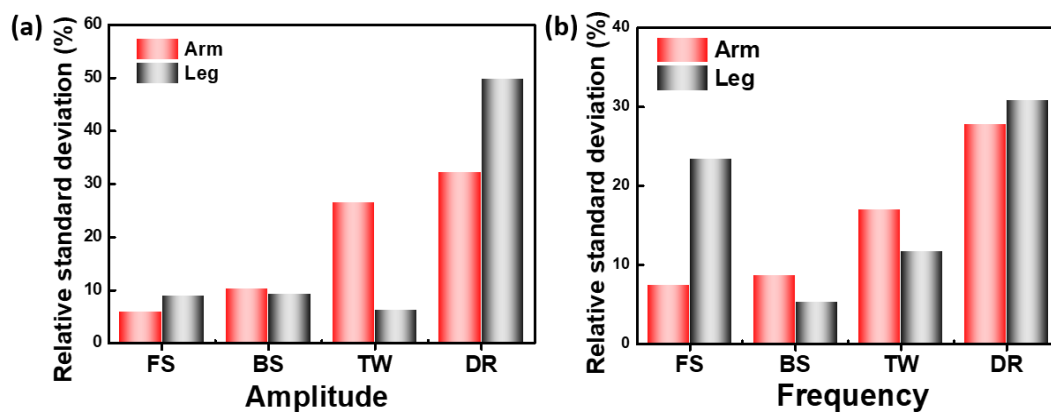


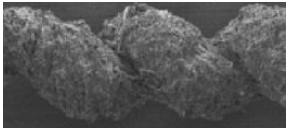



Figure S5-18. Relative standard deviation (RSD) of Amplitude (a) and Frequency (b) in the four swimming strokes. RSD = Standard deviation/Mean value, is to measure the variability of arms and legs movements under water.

Table S5-1. Comparisons of reported twisted graphene fibres

Study	Method	Surface morphology	Strength (MPa)	Breaking strain (%)
Xu and Gao 59	Rotor spinning		--	--
Cheng et al. 210	Rotating GO fibre		110	13.5
Xu and Gao 22	Rolling & stretching films		3.9	2
Yang et al. 215	Rotating axis		200	17


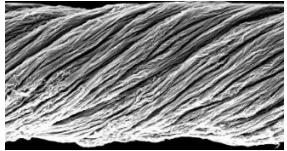
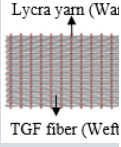

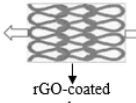
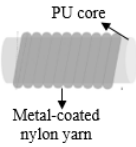
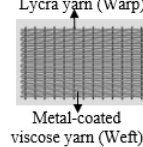
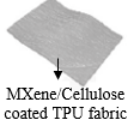
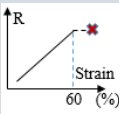
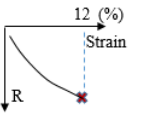
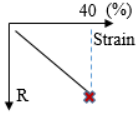
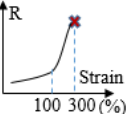
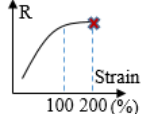
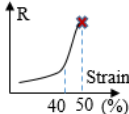
Zhang et al. 213	Dry spinning		200	27
This work	Wet assembly		369	48.5

Table S5-2. Taxonomy of encapsulation-free strain sensor

Typical strain sensor (Ref.)	Fabrics with TGF fibre (This work)	rGO/CNT coated cotton fabric 149	Graphene-dyed wool fabric 5	Metal-deposition nylon yarn 3	Fabric with metal-deposition viscose yarn 2	MXene coated TPU fabric 150	
Strain sensor design & sensitivity	Plan view						
	Sensor Structure	Woven	Woven	Knitting	Wrapping	Embroideri	Nonwove
	Strain response						
	Sensitivity (Linear GF)	63	6	2	Not given	49.5	3405
	Wearing element	Breathability	✓	×	✓	✓	✓
	Washability	✓	×	×	×	×	×
	Wettability	✓	×	×	×	×	×
Anti-jamming	Bending	✓	×	×	×	✓	×
	Pressure	✓	×	×	×	✓	×
	Temperature	✓	×	×	×	✓	×
	Humidity	✓	✓	✓	×	✓	×

This table typically concludes recent reported encapsulation-free strain sensor with

various textile structures and sensing mechanisms. The green checks in wearing element row of breathability, washability and wettability indicates there are typical experiments carried out to confirm the properties. To evaluate the washability and wettability, the fabric sensors should have stable sensitivity under cyclic machine washes according to specific standard of fastness to washing and reproducible electrical outputs under water respectively. The red cross in anti-jamming properties row indicates the fabric sensors have not been confirmed with typical anti-jamming properties to bending, pressure, temperature or humidity.

Table S5-3. Comparisons of air permeability and water vapor permeability

Fabrics (Trade name)	Structure	Air permeability ($l\ m^{-2}\ s^{-1}$)	Water vapour permeability ($g\ m^{-2}\ h^{-1}$)	Ref.
Claima F.I.T	woven	37.18	N/A	219
Epic™	woven	33.3	N/A	219
Hyper D-WR	woven	33.4	N/A	219
60/40 wool cotton	Plain weave	N/A	3130	220
100% wool	Plain weave	N/A	4330	220
100% polyester	Plain weave	N/A	6230	220
TGF-Lycra BWWAJ sensor	Plain woven	48	4620	This work

Chapter 6

A highly sensing-reliable fabric strain sensor with tunable sensitivity for motion sensing and identification

This chapter focuses on completing the fifth objective addressed in Chapter 1.3. The research work is ready to be submitted to journals.

Authors: Heng Zhai, Zekun Liu, Lulu Xu, Chen Meng, Qinghong Huang, Jiashen Li, Yangpeiqi Yi, Xuqing Liu, Yi Li

Journal: Advanced Science (target journal to be submitted)

Statement of own contributions in joint authorship: H.Z. focused on the main research idea development, data acquisition and draft manuscript preparation. Specifically, Conceptualisation, H.Z. and Y.L.; Methodology, H.Z. and L.X.; Materials preparation, H.Z. and Y.Y.; Characterisation, H.Z. and C.M.; Formal Analysis, H.Z. and Q.H.; Data Curation, H.Z.; Original draft preparation, H.Z.; Supervision, Y.L. and X.L.

Abstract

Wearable strain sensors have been recognised as the key technology in real-time motion and health detection, human-machine interaction and artificial intelligence. However, the cutting-edge wearable sensors suffer from inferior sensing reliability towards multiform mechanical stimuli and environmental interferences, leading to inadequate sensing accuracy. To address this critical issue, we propose a novel wet-fusing assembly of high-performance twisted graphene/TiO₂ fibres (TGTF) with remarkable tensile strength (515 MPa) and breaking strain (40.2%), which are capable of being directly woven into fabric sensor with tunable sensitivity. The fabric sensor shows outstanding

sensitivity to strain (Gauge factor ~ 350) and highly reliable sensing performance towards multi-direction mechanical stimuli of bend and pressure, repetitive machine-washing cycles and fickle environmental interferences such as humidity, temperature and extreme wettings. By taking advantages of the hydrophobic and photocatalytic properties of TGTF, the sensor is possessed of a novel self-cleaning capability in photodegrading surface contaminations. We demonstrate a high-accuracy motion and respiration monitoring system by integrating the sensing-reliable strain sensor with a deep learning network, showing its potentials in motion detection and identification.

Keywords: Twisted graphene/TiO₂ fibre, fabric stain sensor, sensing reliability, self-cleaning, tunable sensitivity

6.1 Introduction

Fibre-based wearable sensing devices without encapsulations have gained ever-increasing attentions in health monitoring, motion identification and interaction due to their remarkable wearing portability, conformity and comfortability.^{162, 221} They overcome the weakness of conventional encapsulated sensors with poor breathability, as well as rigid sensors with inferior flexibility. The general methods to achieve flexible fabric strain sensors with excellent conductivity are to deposit metals (i.e. Cu and Ni) or carbonaceous materials (i.e. graphene and carbon nanotubes) on textile substrates *via* dip coating, pad dyeing, chemical vapour deposition, electrochemical and electroless deposition.^{2, 3, 5} Despite sufficient modifications have been made to enhance the bonding between conductive coatings and substrates such as polymer- and plasma-assisted deposition, the conductive components still tend to be peeled off after repeated abrasion, cyclic washing and durable soaking, which deteriorate the durability and sensitivity.^{9, 222} The conductive and firm graphene fibres synthesised from graphene oxide (GO) liquid crystals by wet spinning show great potentials in the assembly of fabric strain sensors.⁴⁷ However, the challenges in efficient regulation of unfavourable

GO crystalline structures have restricted the preparations of ultra-robust and flexible graphene fibres, which are highly demanded in the sensor-fabricating and strain-sensing processes consisting of numerous physical abrasions, repetitive stretching, bending and pressing motions. Thus, it is desirable to regulate the wrinkled and random GO sheets in a flattened and aligned manner to achieve graphene fibres with boosted mechanical strength and flexibility.

Many researches put efforts to optimize sensitivity, stretchability and linearity of wearable strain sensors, while sensing reliability as a crucial parameter in real applications is always ignored.¹⁵⁵ In practice, the body movements are complex and hybrid with stretching, bending and pressing motions, which highlights the necessity in one-fold recognition of strain deformation as strain sensor.¹ On the other hand, the wearable interfaces are always exposed to harsh external environments, such as inconstant temperature, humidity and various contaminations from human metabolism (e.g., urea and lactic acid) or external matters (e.g., split milks and coffees).²²³ Moreover, the fabric sensors are indispensable to undergo multiple machine washes and chronic soaking environment.²¹⁷ The abovementioned application scenarios demonstrate the demands and significances of being a sensing-reliable strain sensor, however, state-of-the-art wearable strain sensors inevitably response to multiform mechanical stimuli or environmental interferences.

Here, we propose a highly sensing-reliable fabric strain sensor (SRTSS) with tunable sensitivity woven by high-performance twisted graphene/TiO₂ fibres (TGTF). The wet-fusing assembled TGTF with more parallelised and condensed GO sheets shows boosted mechanical strength (515 MPa) and breaking strain (40.2%). The SRTSS sensor designed with different working width exhibits tunable sensitivity and SRTSS-14 sensor (sensor width of 14 mm) has the most remarkable sensitivity (Gauge factor ~350). Particularly, the SRTSS fabric sensor is possessed of highly reliable sensing performance towards multiple machine washing, durable soaking environment

and multi-direction mechanical stimuli. By taking advantages of the hydrophobic and photocatalytic properties of TGTF, the SRTSS sensor also possesses a novel self-cleaning property by photodegradation of surface contaminations.

6.2 Experimental section

6.2.1 GO/TiO₂ dispersion preparation

Graphene oxide dispersion was synthesised from expandable graphite flakes (from Sigma-Aldrich with particle size larger than 300 μm) by a modified Hummers' method which has been reported from our previous works.¹⁶¹ The water in aqueous GO dispersion was replaced by N, N-dimethyl formamide (DMF) through extra centrifugations and GO DMF dopes were obtained. TiO₂ nanoparticles were purchased from Sigma-Aldrich (average particle size of 80 nm) and well dispersed in DMF by one-hour ultrasonic treatment. Finally, GO DMF dopes and TiO₂ DMF dispersions were mixed up to prepare GO/10%TiO₂, GO/20%TiO₂, GO/30%TiO₂ and GO/40%TiO₂ spinning dopes.

6.2.2 Wet-spinning and wet-fusing assembly of TGTF

The GO/TiO₂ spinning dopes were extruded from two single spinnerets (0.51 mm) and consolidated in coagulation bath (combination of ethyl acetate and acetone). The two wet GO/TiO₂ fibres were then drafted by the rollers ($V_2 > V_1$ as shown in Figure 6-1a) for the flattened radial alignment of wrinkled GO sheets. Two stretched GO/TiO₂ fibres in wet state were wet-fusing assembled into a single twisted fibre through the twisting and compressing force from spinning roller (V_3 in Figure 6-1a). The twisted level on the fibres could be adjusted by changing the spinning speed of V_3 . The twisted fibres were then chemically reduced by hydroiodic acid at 80°C for 8 hours and finally the TGTFs were achieved. The TGTF integrated with 10%, 20%, 30% and 40% TiO₂

nanoparticles are defined as TGTF-10, TGTF-20, TGTF-30 and TGTF-40 respectively.

6.2.3 Hand weaving of strain sensor

The strain sensor was woven to a plain-weave structure by a hand weaving loom. The elastic Lycra fibres were served as warp yarns to provide elasticity and TGTF-20 fibre was served as weft yarn for strain sensing. The effective sensing component (contain TGTF-20) of the sensors have a fixed length (3 mm) and variable width (6, 10, or 14 mm) for constructions of tunable-sensitivity strain sensor.

6.2.4 Washability test and self-cleaning test

The washability measurement was carried out under standard: ISO 105 CO9 C1&C2, which was in a washing machine containing wash liquor (ECE detergent and bleach activator) and numerous steel balls to simulate the agitation and abrasion during washing. The laundry was operated in a high speed mode at 60°C for 30 minutes as a washing cycle. The self-cleaning property of strain sensor was tested by the photodegradation of 10 mg/L methylene blue (MB), Rhodamine B (RhB) and urea respectively under a 150W Xenon lamp. The photodegradation efficiency was measured by analysing the residual dyestuffs using the M550 UV/Visible spectrophotometer. The spectrophotometric determination of urea is following the methodology published by Bojice et al.²²⁴

6.2.5 Characterisation

The morphologies of TGTF were captured and analysed by FEI Quanta 250 Scanning electron microscope (SEM). The X-ray photoelectron spectroscopy (XPS) was measured by ESCALAB 250 Xi. The X-ray diffraction (XRD) patterns were recorded

by XRD5 spectrometer (Type PANalytical X'Pert Pro) using Cu K α irradiation. The Raman spectra was recorded by Horiba Raman with 633 nm excitation wavelength. The mechanical and electrical performances were evaluated under universal testing machine (Instron 3344) and multimeter (Keithley 2000) respectively. The temperature and humidity measurements were monitored by a conditioning cabinet (Datacolor CONDITINER).

6.3 Results and discussions

6.3.1 Wet-fusing assembly of flexible TGTFs

The assembly of the twisted graphene/TiO₂ fibre (TGTF) contains three steps: 1) preparation of GO/TiO₂ dispersion, 2) wet spinning of GO/TiO₂ fibres, and 3) wet-fusing assembly of the TGTF. The first two steps have been introduced in the experimental section. Figure 6-1a shows the illustration of post-treatment of GO/TiO₂ fibres into the TGTF. The adjacent wrinkled GO layers in wet fibres were separated by the nano-sized TiO₂ particles and stretched into flattened GO sheets during the drafting process. An additional spinning roller (V₃ in Figure 6-1a) was employed to compress and twist the two wet GO/TiO₂ fibres, which induced the wet-fusing assembly of single TGTF by generating hydrogen bonding between interfaces of two wet GO/TiO₂ fibres. The flattened GO layers were condensed and twisted under the applied pressure, leading to the formation of uniform twisted structure on the TGTF surface as illustrated in Figure 6-1b. The mechanism of wet-fusing assembly of twist-structure graphene fibre has been described in our previous reports¹. The image in Figure 6-1c shows the continuous TGTF was collected on a bobbin. The splendid flexibility and tensile strength of TGTF were shown in Figure 6-1d and 6-1e respectively, where it was easily bent into a circle and suspending a 100-gram load vertically.

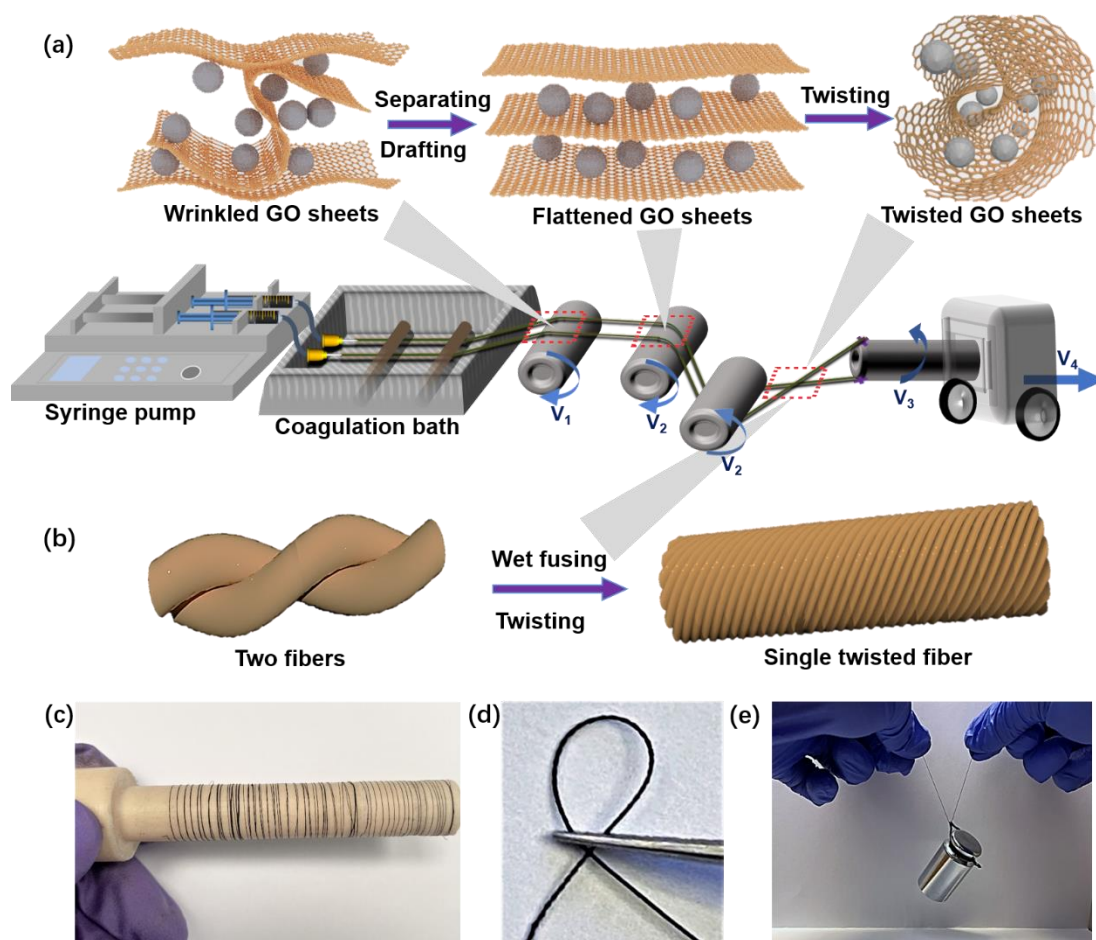


Figure 6-1. Schematic illustration of fabrication of TGOTF. a) Wet-spinning and wet-fusing assembly of TGOTF. The wrinkled GO sheets are separated by TiO_2 nanoparticles and flattened during drafting process. Two stretched wet GO/ TiO_2 fibres are twisted and assembled into one TGOTF by wet-fusing process. b) Illustration of Wet-fusing assembly of a single TGTF. c) Image shows the TGTF winds on the bobbin. d) Image of a bending TGTF shows its flexibility. e) A single TGTF vertically suspends a 100-gram load, indicating its outstanding mechanical strength.

6.3.2 Characterisation of TGTF

Our previous report proved an increasing mechanical strength and breaking strain by applying more twisted levels on the fibres¹. Herein, we produced the twisted graphene fibre without TiO_2 (TGF) and TGTF in the highest twisted level (40°). The typical

stress-strain curve in Figure 6-2a indicates an optimised mechanical strength by integrating TiO₂ nanoparticles into the fibres. The TGTF-20 exhibits the highest strength (515 MPa) and breaking strain (40.2%) in all TGTF fibres (Figure S6-1). The XRD spectrums of TGF and TGTF in Figure S6-2 show the characteristic peak of (002) for graphene and anatase (A) and rutile (R) crystal phase for TiO₂. Typically, the (002) peak shifted from 25.23° (2θ) in TGF to 25.41° in TGTF-20, indicating more compact interlayer spacing in TGTF-20 (0.34 nm) than that of TGF (0.35 nm) calculated from Bragg equation (Figure 6-2b). The changes in full-width at half maximum of (002) peak describe a large decreased lateral thickness (Lc) of single graphitic crystallite in TGTF-20 (2.21 nm) compared with that in TGF (4.68 nm) analysed by Scherrer equation (Figure 6-2c). The decreasing interlayer spacing and Lc are beneficial from more flattened and aligned GO sheets in TGTF, which are resulted from TiO₂ nanoparticles separation of curl GO and wet-fusing assembly of twisted fibres structure.

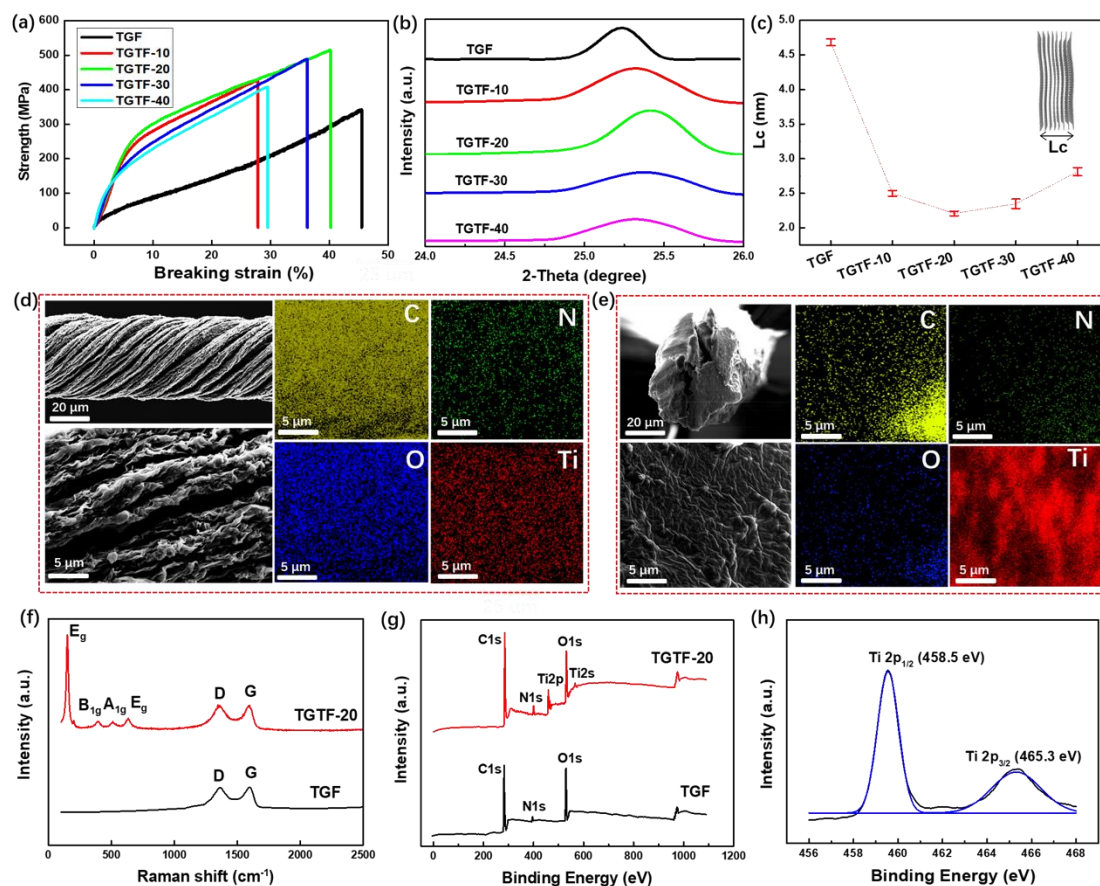


Figure 6-2. Characterisations of the TGTF. a) Stress-strain curves. b) XRD spectrum of the TGTF and TGF, showing the shifted (002) peak. c) Lateral thickness (Lc) of single

graphitic crystallite of the TGTF and TGF. d), e) Morphology and element distribution of TGTF-20 at the (d) surface, and (e) section. f) Raman spectrum of the TGTF-20 and TGF. g) Wide-scan XPS spectrum of the TGTF-20 and TGF. h) High-resolution XPS spectrum of the TGTF, showing the peak deconvolution of Ti (2p).

Figure 6-2d depicts the twisted surface morphology and element distribution of the TGTF-20, indicating the regular twisted structure and uniform distribution of TiO₂ in the fibre surface. Also, such homogenous configuration can be observed in TGTF-10, TGTF-30 and TGTF-40 (Figure S6-3a). Their corresponding weight percentage of Ti, O, N and C in each set of fibre surface are in good accordance with experimental expectation (TGTF-40 has the highest weight percentage of Ti while TGTF-10 is inverse as shown in Figure S6-3b). Figure 6-2e displays the similar evenly distributed elements in the cross section of the TGTF-20. The observation of peaks at 150 (E_g), 396 (B_{1g}), 510 (A_{1g}) and 635 (E_g) cm⁻¹ in Raman spectrum is ascribed to the anatase phase of TiO₂ in TGTF-20 (Figure 6-2f). The XPS spectrum of the TGTF-20 in Figure 6-2g further confirms the existence of Ti, O, N and C compositions. High resolution of the peaks located at 458.5 and 465.3 eV are related to the Ti 2p_{1/2} and Ti 2p_{3/2} spin-orbital splitting photoelectrons from C-Ti bond, suggesting chemical bond between TiO₂ and graphene has been well formed (Figure 6-2h).

6.3.3 Sensor fabrication, calibration and tunable sensitivity

The boosted mechanical strength and flexibility of TGTFs enable them to intactly pass through conventional textile machines and to be fabricated into wearable electronics with stable structures. Figure 6-3a displays the weaving procedure of a SRTSS sensor under the manual weaving loom, which was constructed by flexible nylon-covered Lycra fibres (warp yarns) and conductive TGTF-20 (weft yarns). Figure 6-3b illustrates the plain-weave organisation of the sensor, which guarantees a firm and sensitive structure by generating sufficient attached-and-detached segments between

neighbouring TGTF-20 during the stretching-releasing movements.

To investigate the impact of sensor width (weft direction) to the sensitivity of the SRTSS sensor, we fabricated the sensor in variable width at 6 mm (SRTSS-6), 10 mm (SRTSS-10) and 14 mm (SRTSS-14). It turns out the increase of sensor width highly promotes the sensitivity of the strain sensors. Specifically, the sensitivity or gauge factor (GF) is improved from 60 in SRTSS-6, to 150 in SRTSS-10 and 350 in SRTSS-14 at strain range from 15% to 45% (Figure 6-3c). The unique sensitivity of SRTSS-14 is almost one order of magnitude higher than most of reported encapsulation-free fabric sensor in terms of GF (Figure 6-3d).^{1, 2, 5, 149, 208, 216, 225} Such remarkable sensitivity is originated from the novel sensor structure with single flexible and conductive TGTF-20 compactly aligning and winding in weft direction (Figure 6-3b), which is equivalent to parallel circuits or hybrid circuits under different stretching levels. Figure 6-3e exhibits the simplified circuit schematics of the strain sensor in its initial and stretched state, the corresponding resistance (R and R' for initial and stretched state respectively) can be calculated by the equation (1) and (2) below, where R_1 and R_C stands for the linear- and curved-segment resistance of TGTF-20, R_J represents the contact resistance generated from neighbouring fibres due to stretching-releasing strokes.

$$R = n \left(R_1 + \frac{R_J R_C}{R_J + R_C} \right) + R_1 \quad (1)$$

$$R' = m \left(R_1 + \frac{R_J R_C}{R_J + R_C} \right) + (n - m)(R_1 + R_C) + R_1 \quad (2)$$

Equation (1) depicts the sensor resistance under the circumstance that all liner-segment fibres stick together, while they tend to detach away once sufficient stretching forces are provided as described in Equation (2). The separating movement of TGTF-20 takes place gradually from edge to centre (Figure S6-4), leading to the disappearance of sectional parallel circuits and increase of total resistance eventually. The sensitivity of SRTSS sensor is tunable by altering the sensor width as shown from the results in Figure 6-3c. Figure 6-3f shows the simplified circuit schematics for a width-increased SRTSS

sensor. Equation (3) and (4) give a similar illustration of its working mechanism in initial and stretched state, where R_2 refers to the incremental resistance in linear segment due to the additional width. The sensor resistance is decreased in its initial state (\bar{R}) and increased in stretched state (\bar{R}') in contrast to original-width sensor, resulting in a significant improvement in resistance change and sensitivity.

$$\bar{R} = n \left(\frac{2R_2R_JR_C}{2R_2 + R_J + R_C} + \frac{2R_1R_JR_C}{2R_1 + R_J + R_C} \right) + 2R_1 \quad (3)$$

$$\bar{R}' = m \left(\frac{2R_2R_JR_C}{2R_2 + R_J + R_C} + \frac{2R_1R_JR_C}{2R_1 + R_J + R_C} \right) + (n - m)(R_1 + R_C + 2R_2) + 2R_1 \quad (4)$$

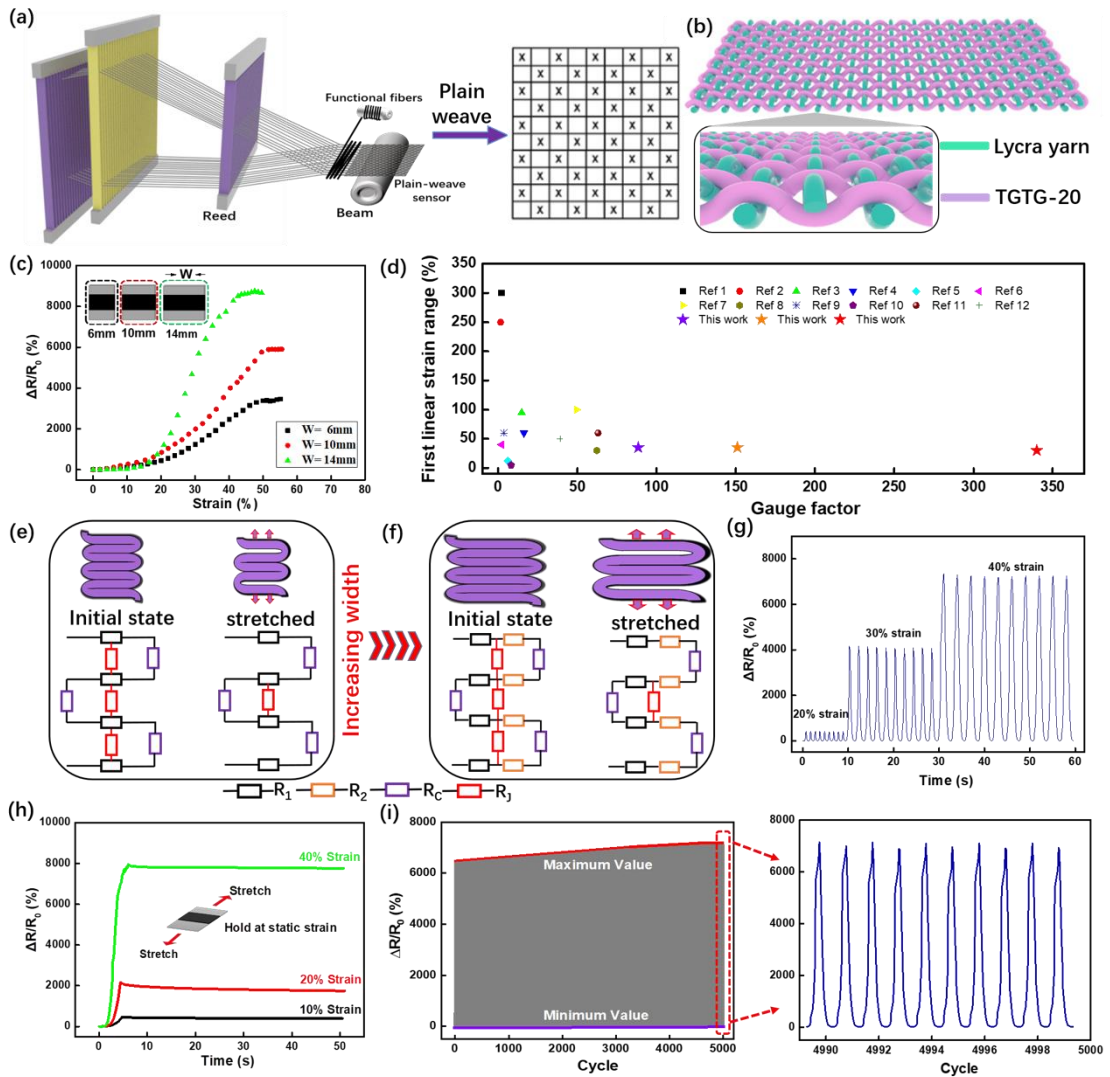


Figure 6-3. Fabrication, tunable sensitivity and sensing mechanism of strain sensor. a)

Illustration of fabrication of plain-woven fabric strain sensor under hand-weaving loom. b) Illustration of plain-woven structure with TGTF served as weft yarn and elastic Lycra served as warp yarns. c) The tunable sensitivities of strain sensors with various width (6, 10 and 14 mm). d) Comparisons between strain sensor and reported encapsulation-free fabric sensor in terms of first linear strain range and GF, showing its unique sensitivity. e), f) Electrical models in its initial state and stretched state before (e) and after (f) increasing the width of sensor. g) Dynamic stability of strain sensor to various strains at 20%, 30% and 40%. h) Static stability of strain sensor by stretching at strain of 10%, 20%, 40% and holding at such strains. i) The electrical response to repetitive 5000 stretching-releasing cycles at strain of 40% and frequency of 1 Hz.

We evaluate the stability and durability of SRTSS-14 to various mechanical stimulus by electromechanical studies. Figure 6-3g shows the dynamic stability of the sensor responding to strain by gradually rising the strain from 20% to 40%. The steady and repeatable electrical outputs in each strain level indicate it can be adapted into dynamic stretching environment. The outstanding static stability is recognised from electrical signals in Figure 6-3h, where the sensor is rapidly stretched to various strains (10%, 20% and 40%) and held at such strain. The stable durability of SRTSS-14 is determined by repeatedly stretching and releasing it in 0-40% strain at a frequency of 1 Hz for continuous 5000 cycles. The electrical signals in Figure 6-3i remain reproducible with minor increase in maximum resistance throughout the entire cyclic strokes, indicating its remarkable durability in practical applications. The reliable durability comes from the stable plain-weave structure interlaced by flexible TGTF-20 and elastic Lycra yarns, which guarantees the mechanical stability under multiple times of stretching movements (Figure S6-5). The SRTSS sensor is possessed of superior sensitive to strain, unique tunable sensitivity with various sensor width and outstanding stability and durability summarised from the electromechanical studies.

6.3.4 Sensing reliability and self-cleaning properties

Differing from mostly reported nanomaterial-coating based and elastomer-encapsulated packaged wearable strain sensors, the SRTSS sensor directly assembled by flexible, robust and conductive TGTF-20 fibres without any encapsulations exhibits remarkable wearing comfortability and sensing reliability. To evaluate the breathability of SRTSS-14 sensor, we measured its air permeability ($4373 \text{ l m}^{-2} \text{ s}^{-1}$) and water vapor permeability ($46 \text{ g m}^{-2} \text{ h}^{-1}$) as shown in Figure S6-6, which reach the general criteria compared with some commercial garments (Table S6-1).

The SRTSS-14 strain sensor shows reliable sensing performances in various hostile environments, such as different mechanical outputs, surrounding humidity and temperature, fierce machine washing and underwater working conditions. We make comparisons of the sensor responding to various mechanical outputs throughout continuing cyclic strokes, including stretching, bending and pressing (Figure 6-4a-c), where all the trends of electrical and mechanical signals keep consistent. There is a dramatic resistance change rate (8139%) under stain of 40% (Figure 6-4a). In contrast, it only reaches 25.5% under bending deformation of 80% (Figure 6-4b) and 2.3% under pressure of 200 kPa (Figure 6-4c). Besides, the sensor also shows inactive sensitivity to humidity and temperature, with resistance only decreasing 1.5% and 7.2% by rising the relative humidity from 30% to 90% and surrounding temperature from 25°C to 45°C respectively (Figure S6-7). The minor and negligible electrical responses to bending, pressure, humidity and temperature minimize the interferences generated from human activities and ensure the precise detection of strain-induced deformation.

The schematic in Figure 6-4d illustrates the sensor is washed in a wash fastness testing system containing wash liquor and steel balls to simulate the agitation and abrasion. It turns out the GF (330 for 1st run and 345 for 10th run) and linearity (98% for 1st run and 96% for 10th run) of the sensor remain stable even over multiple washes (Figure 6-4e). The particular resistance change-strain curves of a six-time and ten-time washed sensor

are highly matched, indicating the perfect sensing reliability over its entire strain range against fierce machine washing (Figure 6-4f). We further evaluate its sensing performance underwater. The curves in Figure 6-4g indicates the stable electrical response to strain underwater with only a minor deterioration in sensitivity. Such reduction is ascribed to the subtle conductivity of water molecules, which generates alternative electrical pathways between conductive fibres as illustrated in Figure 6-4h. The reproducible electrical signals throughout 1000 cycles guarantee its reliable durability for underwater strain sensing (Figure 6-4i).

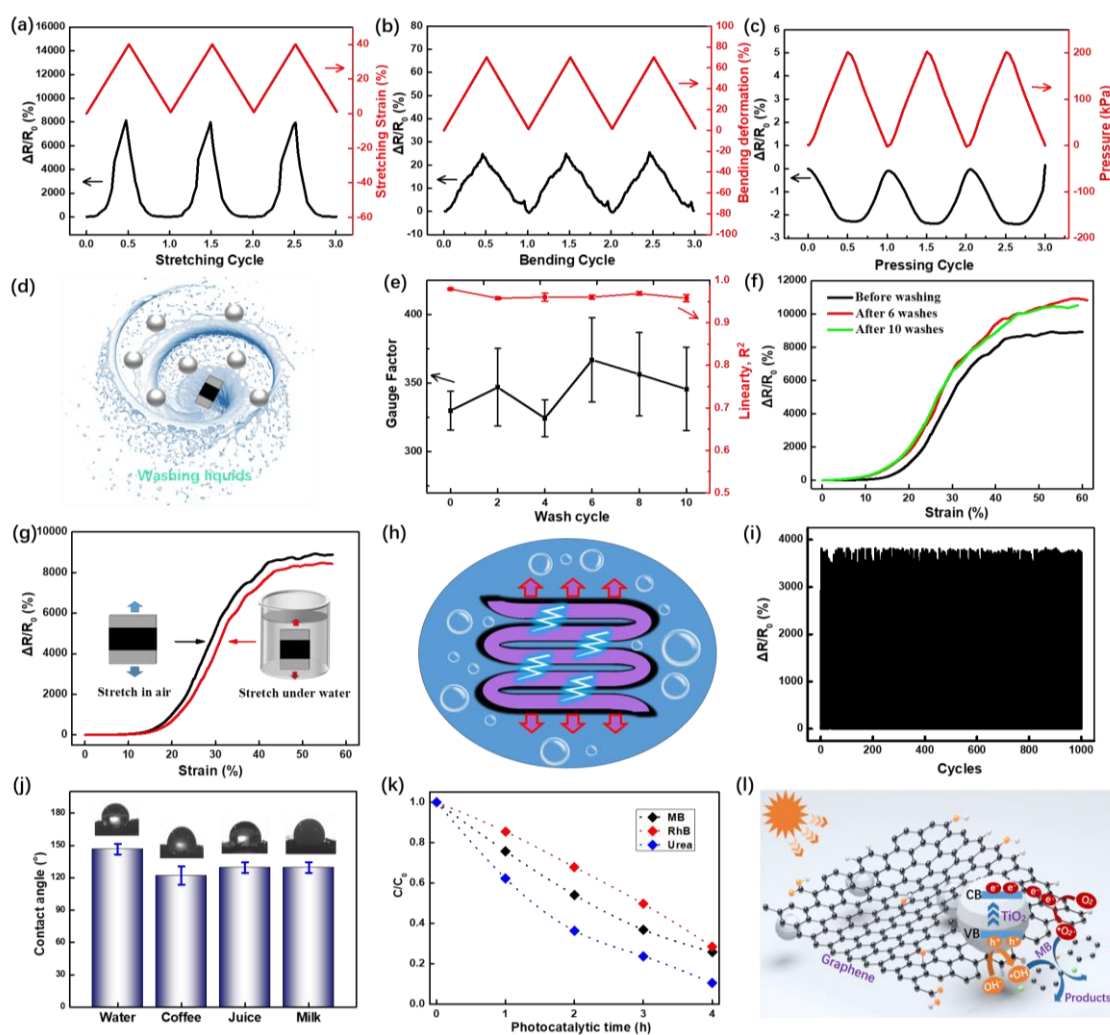


Figure 6-4. Sensing reliability and self-cleaning properties of SRTSS sensor. a-c) The comparison of SRTSS sensor performance under repetitive, a) stretching (0-40% strain), b) bending (0-80% bending deformation) and, c) pressing (0-200 kPa pressure) levels, indicating it is stably insensitive to bending and pressing motions. d) Schematic illustration of SRTSS sensor in machine-washing process. e) The sensitivity and

linearity of SRTSS-14 throughout 10 washing cycles. f) Typical electrical response against strain curve of SRTSS-14 before and after machine washing, showing its reliable washability. g) Comparison of electrical response to strain of SRTSS-14 in air and underwater, showing its reliable wettability. h) Illustration of alternative pathways generated between neighbouring conductive fibres in a stretched sensor underwater. i) Performance of SRTSS-14 under 1000-cycle stretching and releasing at strain of 30% and frequency of 1 Hz underwater. j) Contact angle test of SRTSS-14 by water, coffee, orange juice and milk. k) Photodegradation efficiency of MB, RhB and urea by SRTSS-14 sensor, showing its unique function in self-cleaning. l) Illustration of photocatalytic mechanism of SRTSS-14.

By taking advantages of the hydrophobic and photocatalytic properties of TGTF-20 fibres, the SRTSS-14 strain sensor exhibits novel self-cleaning properties. Figure 4j shows the fabric sensor is nearly superhydrophobic with a measured water contact angle of 147° . In addition, it is hydrophobic against some ordinary liquid foods such as coffee, juice and milk, the contact angle of which are 122° , 129.5° and 129.5° respectively. The food droplets can easily roll off the sensor surface to protect the sensor from liquid contaminations, which is considered as the first stage for self-cleaning process. The sensor also has unique photocatalytic function to photodegrade the contaminations on sensor surface, including urea from human metabolisms and organic dyes from faded garments. The photodegradation efficiency curves in Figure 4k indicates 90% of urea, 76% of methylene blue (MB) and 75% of Rhodamine B (RhB) have been removed respectively within 4 hours under illuminations. The UV/vis adsorbance spectrums in Figure S6-8 exhibit the decreases of characteristic peaks in urea, MB and RhB, indicating the photodegradation of contaminants over 4 hours. The remarkable photocatalytic performance is originated from graphene-wrapped-TiO₂ structure in TGTF fibres, which prolongs lifetime of photoinduced electrons and holes as illustrated in Figure 6-4l. The superior self-cleaning capability preserves the strain sensor against contaminations and stably works in harsh environments.

6.3.5 Applications in motion detection and respiration identification

Owing to the highly reliable sensitivity under various harsh environment, the SRTSS strain sensor can be applied in monitoring many body motions in real time. We firstly mount the SRTSS sensor on the skin surface with tape to detect the small human motions, such as swallowing, coughing and speaking. Figure 6-5a shows the electrical outputs during swallowing. The fluctuate signals in the peaks are in accordance with the exertion and release of swallowing strokes. The reproducible electrical signals in Figure 6-5b displays its reliable monitoring of coughing. Figure 6-5c exhibits the distinguishable patterns when speaking different words, showing its great potentials in words recognition of the dump disables and phonation rehabilitation training.

The high-performance SRTSS sensors can be integrated into a full-body wireless motion and respiration sensing network. Five SRTSS sensors are sewing on the elbow, knee and chest pads to detect the real-time motions and respiration, which are connected to a wireless transmission module to wirelessly transport signals to mobile interface. Figure 6-5d shows the corresponding electrical signals of arms, legs and respiration when running. The stable and repeatable signals indicate the reliable sensing performances of SRTSS sensors even the exerciser is profusely sweating while running. By taking advantages of its high sensitivity, the various respiration signals are also obtained with exerciser running in different speed (i.e. normal, fast and ‘danger’ speed as shown in Figure 6-5e). It can be observed that the three patterns have the similar amplitudes but distinguished frequency, which can be classified into three target classes by using a convolutional neural network (CNN). The deep learning architecture as shown in Figure S6-9, is determined to have a precise respiratory recognition performance with accuracy rate of 94.7% (Figure 6-5f). The high-accuracy identifications of exerciser’s respiration state could be directly displayed in the mobile interface, where a warning sign is raised to the extremely fast-speed runner to slow down for health management (Figure 6-5g).

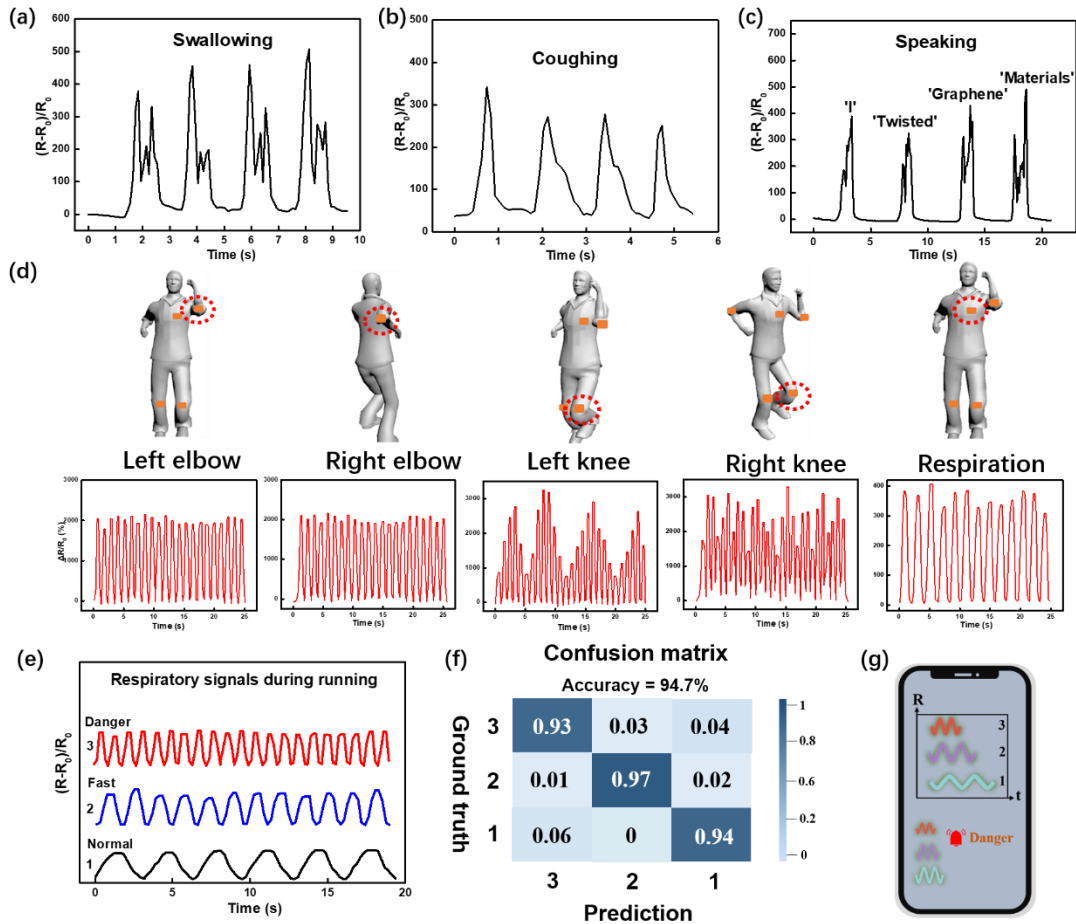


Figure 6-5. The application of SRTSS strain sensors in motion detection and identification. a) real-time detection of swallowing, b) coughing, and c) speaking. d) Full-body real-time motion detections during running assisted by a wireless transmission network, including elbows, knees and respirations. e) Typical electrical outputs of respiratory signal during running in a normal, fast and ‘danger’ speed. f) confusion matrix for the test set of the respiration monitoring and identification system, showing the high accuracy. g) Illustration showing the respiration tracking and warning in wireless interface.

6.4 Conclusions

In summary, we have reported a wet-fusing assembling approach to synthesize TGTF with improved mechanical strength and breaking strain, as well as a novel self-cleaning property. The as-prepared TGTF is directly woven into a fabric SRTSS strain sensor

showing reliable and tunable sensitivity with highest GF of 350. By taking advantages of the hydrophobic and photocatalytic properties of TGTF, along with the stable woven construction of the sensors, the SRTSS sensor is possessed of highly reliable sensing nature towards multi-direction mechanical stimuli (e.g. bend and pressure), cyclic machine-washing cycles, fickle environmental interferences (e.g. humidity, temperature and extreme wettings) and various surface contaminations. The wireless multi-channel sensing system based on high-performance SRTSS sensor are successfully constructed to detect body motion and respirations.

6.5 Supplementary information

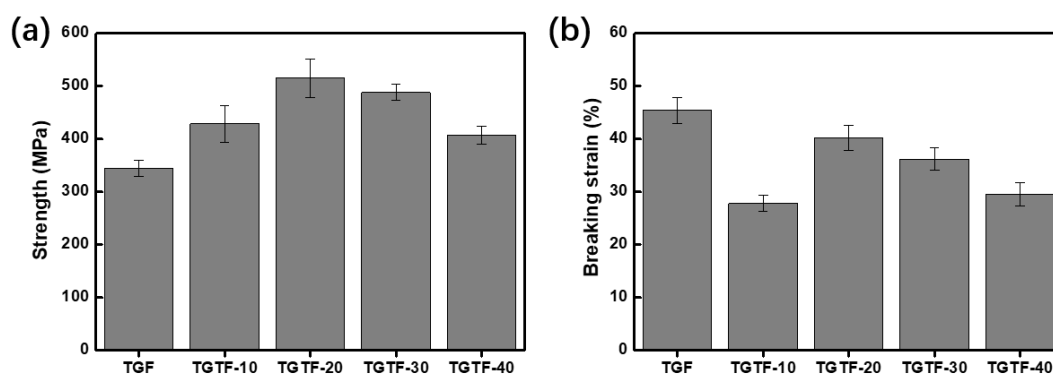


Figure S6-1. Mechanical properties of TGF and TGTF. a) Strength. b) Breaking strain.

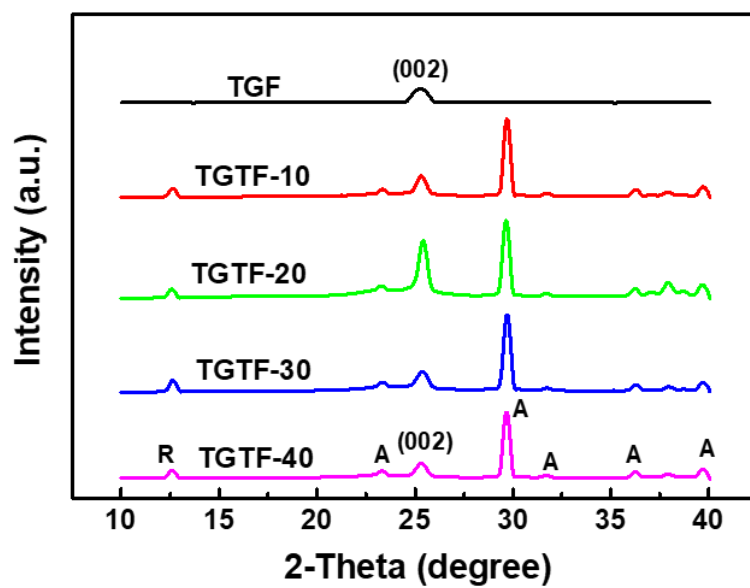


Figure S6-2. XRD spectrums of TGF and TGTF show the characteristic peak of (002) for graphene and anatase (A) and rutile (R) crystal phase for TiO₂.

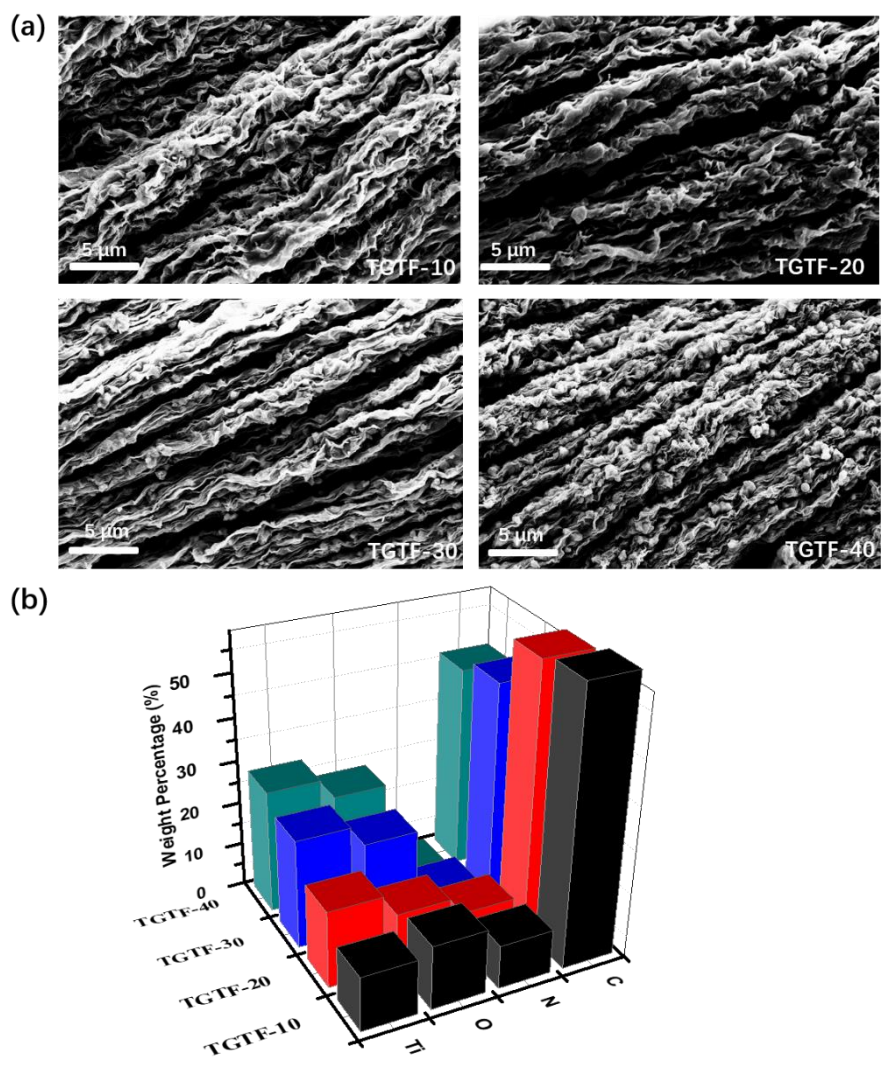


Figure S6-3. Surface morphology and element distribution. a) Twisted surface morphology of TGTF-10, TGTF-20, TGTF-30 and TGTF-40 and b) their corresponding elements distribution.

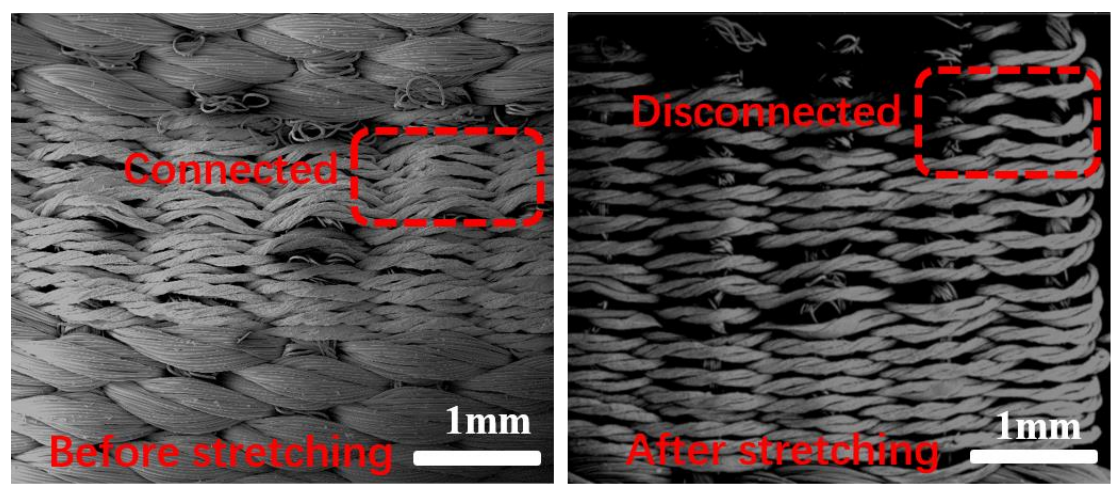


Figure S6-4. SEM images of the SRTSS-14 sensor before and after stretching, which shows the TGTF-20 fibres are connected to each other before stretched and starts to separating from the edge to centre after partially stretched.

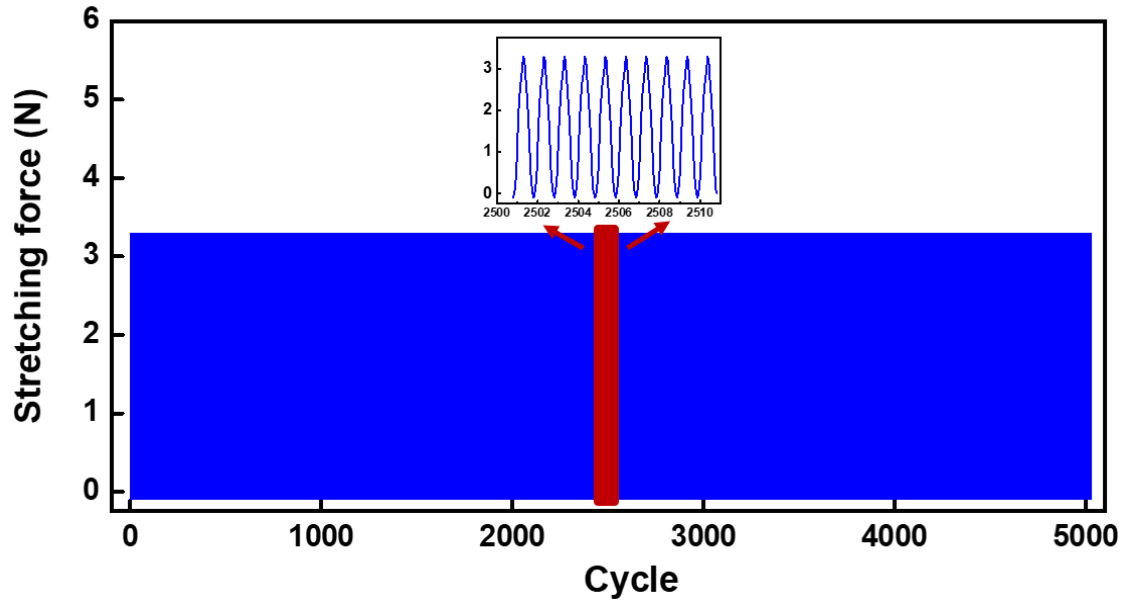


Figure S6-5. Mechanical stability of SRTSS-14 stain sensor under a continuous 5000-cycle stretching and releasing in 0-40% strain at a frequency of 1 Hz.

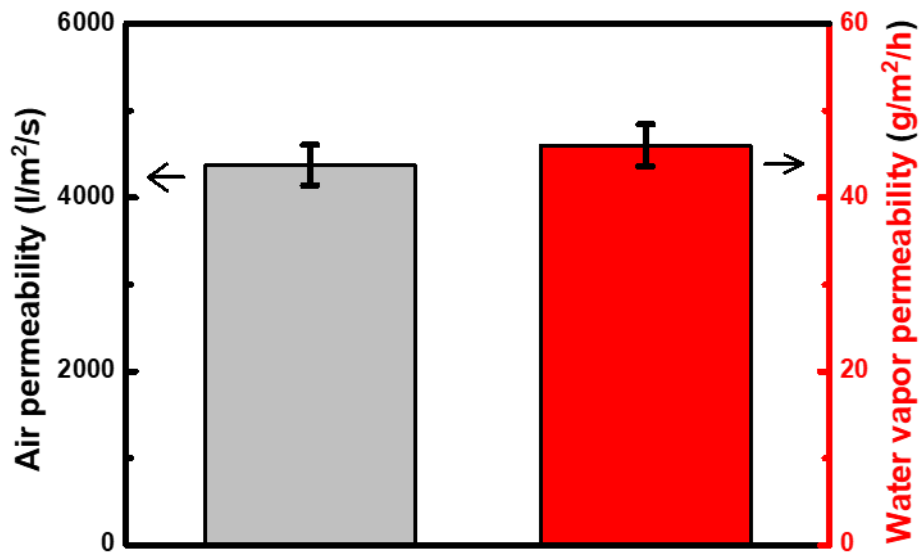


Figure S6-6. The air permeability and water vapour permeability of SRTSS-14 strain

sensor.

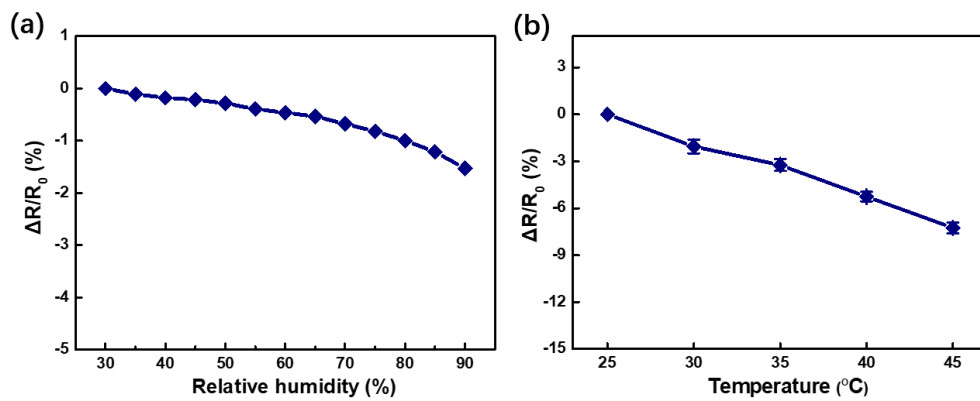


Figure S6-7. Electrical response of the SRTSS-14 to humidity and temperature. a) relative humidity of 30-90%. b) Temperature of 25-45°C.

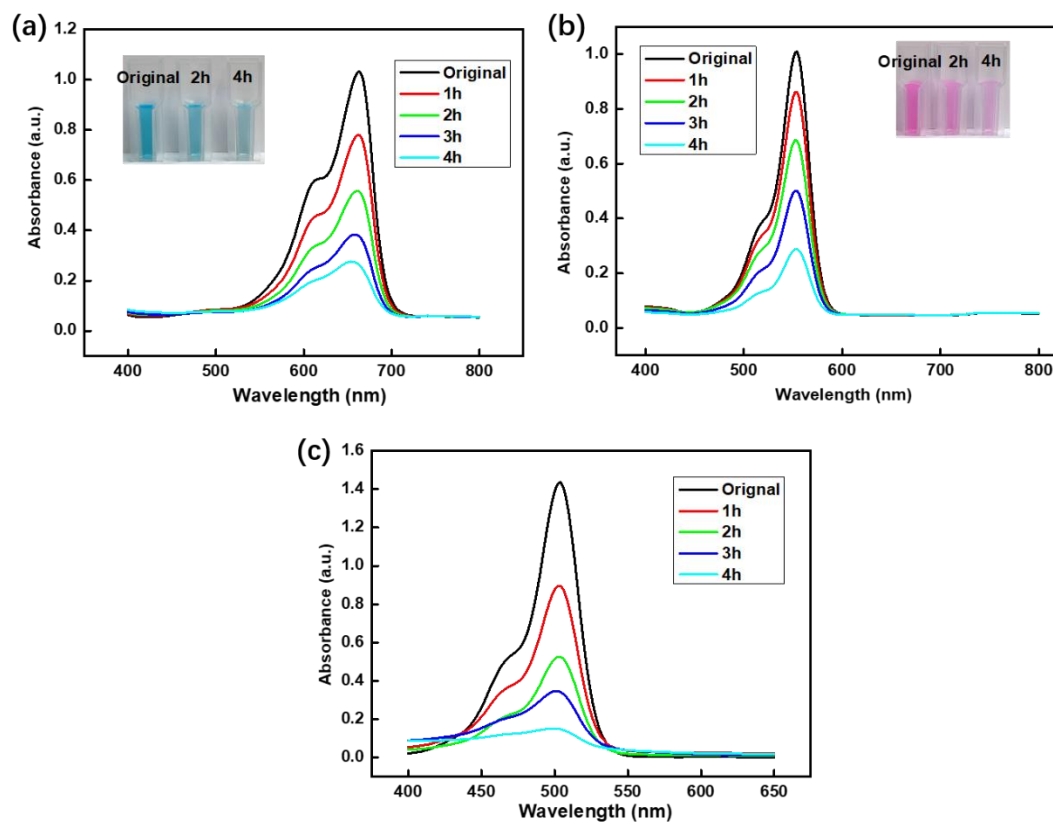


Figure S6-8. The UV/vis adsorbance spectra shows the decreases of characteristic peaks in a) MB, b) RhB and c) urea, indicating the photodegradation of contaminants over 4 hours

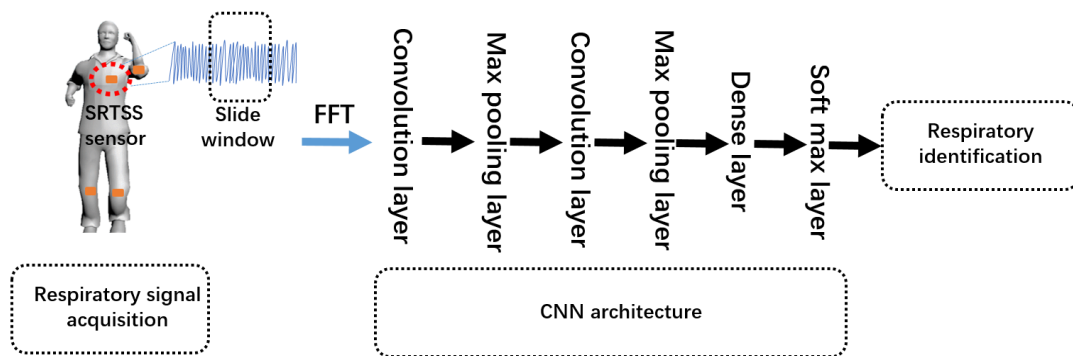


Figure S6-9. The schematic diagram of respiration monitoring and identification using SRTSS sensor with a CNN model.

Table S6-1. Comparisons of air permeability and water vapour permeability

Fabrics (Trade name)	Structure	Air permeability	Water vapour	Ref.
		($l\ m^{-2}\ s^{-1}$)	permeability ($g\ m^{-2}\ h^{-1}$)	
Claima F.I.T	woven	37.18	N/A	219
Epic™	woven	33.3	N/A	219
Hyper D-WR	woven	33.4	N/A	219
60/40 wool cotton	Plain weave	N/A	3130	220
100% wool	Plain weave	N/A	4330	220
100% polyester	Plain weave	N/A	6230	220
SRTSS-14 sensor	Plain weave	46	4373	This work

Chapter 7 Conclusions and future work

7.1 Conclusions

This research has demonstrated the development of graphene-based materials including GO, rGO and GF with the aim to improve their photocatalytic, adsorptive, conductive and mechanical properties for their applications in environmental remediation and wearable electronics. Two stages were developed for the functionalisation of graphene-based materials, from the synthesis and application of dispersion-state GO to the fabrication and application of solid-state GF.

At the first stage, the TiO₂/GO dispersions were fabricated and deposited on the surfaces of textile substrates by pad-dyeing technique. The GO was reduced into rGO by L-AA acid to increase the stability of TiO₂/GO in solution. The scanning electron microscopy, fourier transform infrared spectra and X-ray photoelectron spectroscopy proved that TiO₂/rGO composites were firmly coated on the fabrics surface and strong bonds were generated between rGO and TiO₂ nanoparticles. The TiO₂/rGO functionalised wool fabrics exhibit decent sustainability, improved adsorptive and photocatalytic performance, showing great potentials to solve the environmental concerns of overproduced textiles and water contaminations arising from fast fashion industry. By taking advantages of these properties, we developed an integrated strategy of night-time adsorption and day-time photodegradation which could significantly optimize the dyestuffs degradation efficiency. The proposed concept of waste textile reutilisation and wastewater treatment achieves the first and second research objective proposed in Chapter 1.3 respectively.

We have also studied the GO-functionalisation techniques by pad dyeing GO on different natural and synthetic fibres including cotton, wool and Coolmax to discover their micro-structures, water adsorption, transportation and evaporation properties. The GO functionalised Coolmax (GO-Coolmax) fibres exhibit good resistive humidity

sensing capabilities with ultrafast response and recovery time within 0.6 s, which is outstanding among fabric-based humidity sensors. The remarkable sensing capabilities can be attributed to the special micro-structure that results in its quick reaction, fast wicking and evaporation of water molecules. Moreover, the GO-functionalised Coolmax humidity sensor is resilient to pressure and temperature variations, i.e., the external pressure (up to 2 MPa) and temperature variation (ranges from 20 to 40°C) only influence the resistance within 10%, while over 80% of resistance changes caused by humidity variation (relative humidity ranges from 45% to 80%). The progress in fabrication of ultrafast-response GO-Coolmax fabric humidity sensor fulfils the third research objective proposed in Chapter 1.3.

At the second stage of this research, by realizing the inferior washability and wettability of GO functionalised fabrics, we fabricated a continuous TGF with stable electrical and mechanical performance under cyclic washing and chronic wetting conditions by wet-fusing assembly. The TGF shows high tensile strength (369 MPa) and remarkable breaking strain (48.5%), which could be directly woven into fabric-based breathable, washable and wettable strain sensor with anti-jamming properties to bend, pressure, temperature and humidity. The sensitivity of the sensor only slightly decreases after 6 machine washing cycles, with a reduction of gauge factor from 63 to 50. After soaking in water for one week, the sensor only has a minor reduction of sensitivity (gauge factor decreases from 55 to 48). The fabrications of high-performance TGF and breathable, wettable and washable strain sensor achieve the fourth research objectives proposed in Chapter 1.3

To achieve the fifth research objective in Chapter 1.3, TiO₂ nanoparticles were added into GO dispersion to assemble TGTF via wet-fusing methodology with self-cleaning properties. The as-prepared TGTF exhibits enhanced mechanical strength (the highest at 515 MPa), which is beneficial from more flattened and aligned GO sheets in TGTF due to TiO₂ nanoparticles separation of curl GO sheets. The SRTSS strain sensors woven with TGTF have tunable sensitivity, self-cleaning and reliable-sensing

properties, which enable them to precisely detect human motions and respirations in harsh environments. By taking advantages of the high-performance SRTSS sensors, a respiration monitoring and identification system is constructed to give warnings to the runners with respiratory risks in their exercises.

7.2 Novelties and contributions

The major novelties and research contributions of this thesis are:

- A scalable dyeing technology was proposed to synchronously realise the sustainable reutilisation of waste textiles and efficient degradation of dyestuffs in wastewater. By taking advantage of the remarkable adsorbing capacity and enhanced photocatalytic performance of the functionalised waste fabrics, an integrated strategy was developed for night-time adsorption and dye-time photodegradation which could significantly optimise the dyestuffs degradation efficiency. This work has been published in *Advanced Fibre Materials* (DOI: 10.1007/s42765-022-00192-1).
- A GO-functionalised Coolmax humidity sensor with ultrafast response and recovery time (less than 0.6s) was designed and fabricated. The proposed humidity sensor is highly resilient to pressure and temperature stimuli. This work has been published in *Chemical Engineering Journal* (DOI: 10.1016/j.cej.2021.128639).
- An innovative wet-fusing assembly of TGF with remarkable flexibility (breaking strain of 48.5%) was proposed for the first time. The robust and ultra-flexible continuous TGF was able to be woven into strain sensors with outstanding sensitivity (gauge factor ~ 63) to applied tensile strain and negligible response to bend, pressure, temperature and humidity. This work has been published in *Chemical Engineering Journal* (DOI: 10.1016/j.cej.2022.135502).
- A highly sensing-reliable fabric strain sensor with tunable sensitivity woven using high-performance TGTF was proposed. The fabric sensor is possessed of highly reliable sensing performance towards multiple machine washing, durable soaking

environment and multi-direction mechanical stimuli. By taking advantages of the hydrophobic and photocatalytic properties of TGTF, the sensor also possesses a novel self-cleaning property by photodegradation of surface contaminations. This work is now under review by Advanced Science.

7.3 Limitations

The limitations of this study are listed as follows:

- The waste textiles reutilisation in this thesis is only related to wool fabrics, other forms of waste textiles such as cotton, PET and nylon fabrics should be studied and compared in terms of overall dyestuffs degradation efficiency.
- In Chapter 3, only MB and RhB have been used for the adsorption and photodegradation tests, other organic dyes from the textile-finishing factory have not been tested yet.
- The BWVAJ sensor in Chapter 5 and SRTSS sensor in Chapter 6 shows insensitivity to deformations of bend and compression in contrast to strain deformation, however, such deformations are still detectable.

7.4 Future work

This thesis has introduced the fabrication of TiO₂/rGO functionalised fabrics and twisted TiO₂/rGO composite fibres with remarkable photocatalytic performance and conductivity, which could be applied in dyestuffs degradation and wearable electronics. However, the TiO₂/rGO materials are believed to have the bifunctions in photocatalytic degradation and sensing of organic contaminations in polluted wastewater simultaneously. This is beneficial from the excellent conductivity of graphene. The simplified mechanism is the changeable electron migration rates in TiO₂/rGO composite fibres under different photodegradation rates. Macroscopically, the changeable electron migration rates will have influences on the resistance of TiO₂/rGO

composite fibres. Assuming that intensity of light source and capability of photocatalysts remain unchanged, the change of photodegradation rates arise from the dynamic concentration of organic contaminations. Hence, there is a relationship between the resistance of TiO₂/rGO composite photocatalysts and concentration of organic contaminations. To carry out the future work, further experiments and mechanism models should be developed to prove the bi-functional performance of TiO₂/rGO composite fibres in degrading and sensing organic pollutants. Moreover, the functional composite fibres also have potentials for the applications in biosensors, such as sensing some bacteria and virus, which should be the targets for future works.

Reference

- (1) Zhai, H.; Xu, L.; Liu, Z.; Jin, L.; Yi, Y.; Zhang, J.; Fan, Y.; Cheng, D.; Li, J.; Liu, X. Twisted graphene fibre based breathable, wettable and washable anti-jamming strain sensor for underwater motion sensing. *Chemical Engineering Journal* **2022**, 135502.
- (2) Liu, Z.; Zheng, Y.; Jin, L.; Chen, K.; Zhai, H.; Huang, Q.; Chen, Z.; Yi, Y.; Umar, M.; Xu, L. Highly breathable and stretchable strain sensors with insensitive response to pressure and bending. *Advanced Functional Materials* **2021**, 31 (14), 2007622.
- (3) Zhu, C.; Li, R.; Chen, X.; Chalmers, E.; Liu, X.; Wang, Y.; Xu, B. B.; Liu, X. Ultraelastic Yarns from Curcumin-Assisted ELD toward Wearable Human–Machine Interface Textiles. *Advanced Science* **2020**, 7 (23), 2002009.
- (4) Liu, Z.; Li, Z.; Zhai, H.; Jin, L.; Chen, K.; Yi, Y.; Gao, Y.; Xu, L.; Zheng, Y.; Yao, S. A highly sensitive stretchable strain sensor based on multi-functionalized fabric for respiration monitoring and identification. *Chemical Engineering Journal* **2021**, 426, 130869.
- (5) Xu, L.; Liu, Z.; Zhai, H.; Chen, X.; Sun, R.; Lyu, S.; Fan, Y.; Yi, Y.; Chen, Z.; Jin, L. Moisture-Resilient Graphene-Dyed Wool Fabric for Strain Sensing. *ACS applied materials & interfaces* **2020**, 12 (11), 13265-13274.
- (6) Wang, R.; Du, Z.; Xia, Z.; Liu, J.; Li, P.; Wu, Z.; Yue, Y.; Xiang, Y.; Meng, J.; Liu, D. Magneto-electrical Clothing Generator for High-Performance Transduction from Biomechanical Energy to Electricity. *Advanced Functional Materials* **2022**, 32 (6), 2107682.
- (7) Liu, Z.; Zhu, T.; Wang, J.; Zheng, Z.; Li, Y.; Li, J.; Lai, Y. Functionalized Fiber-Based Strain Sensors: Pathway to Next-Generation Wearable Electronics. *Nano-Micro Letters* **2022**, 14 (1), 1-39.
- (8) Qu, H.; Skorobogatiy, M. Conductive polymer yarns for electronic textiles. In *Electronic textiles*, Elsevier, 2015; pp 21-53.
- (9) Liu, L.; Yu, Y.; Yan, C.; Li, K.; Zheng, Z. Wearable energy-dense and power-dense supercapacitor yarns enabled by scalable graphene–metallic textile composite electrodes. *Nature communications* **2015**, 6 (1), 1-9.
- (10) Atwa, Y.; Maheshwari, N.; Goldthorpe, I. A. Silver nanowire coated threads for electrically conductive textiles. *Journal of Materials Chemistry C* **2015**, 3 (16), 3908-3912.
- (11) Ko, F.; Gogotsi, Y.; Ali, A.; Naguib, N.; Ye, H.; Yang, G.; Li, C.; Willis, P. Electrospinning of continuous carbon nanotube-filled nanofiber yarns. *Advanced materials* **2003**, 15 (14), 1161-1165.
- (12) Li, W.; Zhou, Y.; Wang, Y.; Li, Y.; Jiang, L.; Ma, J.; Chen, S. Highly stretchable and sensitive SBS/graphene composite fiber for strain sensors. *Macromolecular Materials and Engineering* **2020**, 305 (3), 1900736.
- (13) Chen, X.; Memon, H. A.; Wang, Y.; Marriam, I.; Tebyetekerwa, M. Circular Economy and sustainability of the clothing and textile Industry. *Materials Circular Economy* **2021**, 3 (1), 1-9.
- (14) Sun, X.; Wang, X.; Su, F.; Tian, M.; Qu, L.; Perry, P.; Ovens, H.; Liu, X. Textile Waste Fibre Regeneration via a Green Chemistry Approach: A Molecular Strategy for Sustainable Fashion. **2021**.
- (15) Du, Z.; Cheng, C.; Tan, L.; Lan, J.; Jiang, S.; Zhao, L.; Guo, R. Enhanced photocatalytic

- activity of Bi₂WO₆/TiO₂ composite coated polyester fabric under visible light irradiation. *Applied Surface Science* **2018**, *435*, 626-634.
- (16) Li, F.-t.; Wang, Q.; Wang, X.-j.; Li, B.; Hao, Y.-j.; Liu, R.-h.; Zhao, D.-s. In-situ one-step synthesis of novel BiOCl/Bi₂₄O₃₁Cl₁₀ heterojunctions via self-combustion of ionic liquid with enhanced visible-light photocatalytic activities. *Applied Catalysis B: Environmental* **2014**, *150*, 574-584.
- (17) Zhang, Q.; Bao, N.; Wang, X.; Hu, X.; Miao, X.; Chaker, M.; Ma, D. Advanced fabrication of chemically bonded graphene/TiO₂ continuous fibers with enhanced broadband photocatalytic properties and involved mechanisms exploration. *Scientific reports* **2016**, *6* (1), 1-15.
- (18) Kowalska, E.; Remita, H.; Colbeau-Justin, C.; Hupka, J.; Belloni, J. Modification of titanium dioxide with platinum ions and clusters: application in photocatalysis. *The Journal of Physical Chemistry C* **2008**, *112* (4), 1124-1131. Tan, L. L.; Chai, S. P.; Mohamed, A. R. Synthesis and applications of graphene-based TiO₂ photocatalysts. *ChemSusChem* **2012**, *5* (10), 1868-1882.
- (19) Zhang, X.; Sun, Y.; Cui, X.; Jiang, Z. A green and facile synthesis of TiO₂/graphene nanocomposites and their photocatalytic activity for hydrogen evolution. *International Journal of Hydrogen Energy* **2012**, *37* (1), 811-815.
- (20) Cong, H.-P.; Ren, X.-C.; Wang, P.; Yu, S.-H. Wet-spinning assembly of continuous, neat and macroscopic graphene fibers. *Scientific reports* **2012**, *2* (1), 1-6.
- (21) Geim, A. K.; Novoselov, K. S. The rise of graphene. In *Nanoscience and technology: a collection of reviews from nature journals*, World Scientific, 2010; pp 11-19.
- (22) Zheng, B.; Gao, W.; Liu, Y.; Wang, R.; Li, Z.; Xu, Z.; Gao, C. Twist-spinning assembly of robust ultralight graphene fibers with hierarchical structure and multi-functions. *Carbon* **2020**, *158*, 157-162.
- (23) Zhang, H.; Lv, X.; Li, Y.; Wang, Y.; Li, J. P25-graphene composite as a high performance photocatalyst. *ACS nano* **2010**, *4* (1), 380-386.
- (24) Xu, Z.; Gao, C. Graphene in macroscopic order: liquid crystals and wet-spun fibers. *Accounts of chemical research* **2014**, *47* (4), 1267-1276.
- (25) Nguyen-Phan, T.-D.; Pham, V. H.; Shin, E. W.; Pham, H.-D.; Kim, S.; Chung, J. S.; Kim, E. J.; Hur, S. H. The role of graphene oxide content on the adsorption-enhanced photocatalysis of titanium dioxide/graphene oxide composites. *Chemical Engineering Journal* **2011**, *170* (1), 226-232.
- (26) Li, P.; Liu, Y.; Shi, S.; Xu, Z.; Ma, W.; Wang, Z.; Liu, S.; Gao, C. Highly crystalline graphene fibers with superior strength and conductivities by plasticization spinning. *Advanced Functional Materials* **2020**, *30* (52), 2006584.
- (27) Gao, W. The chemistry of graphene oxide. In *Graphene oxide*, Springer, 2015; pp 61-95.
- (28) Talyzin, A. V.; Mercier, G.; Klechikov, A.; Hedenström, M.; Johnels, D.; Wei, D.; Cotton, D.; Opitz, A.; Moons, E. Brodie vs Hummers graphite oxides for preparation of multi-layered materials. *Carbon* **2017**, *115*, 430-440.
- (29) Pendolino, F.; Armata, N. Synthesis, characterization and models of graphene oxide. In *Graphene oxide in environmental remediation process*, Springer, 2017; pp 5-21.
- (30) Pei, S.; Cheng, H.-M. The reduction of graphene oxide. *Carbon* **2012**, *50* (9), 3210-3228.
- (31) Simon, A.; Dronskowski, R.; Krebs, B.; Hettich, B. The crystal structure of Mn₂O₇.

- Angewandte Chemie International Edition in English* **1987**, 26 (2), 139-140.
- (32) Marcano, D. C.; Kosynkin, D. V.; Berlin, J. M.; Sinitskii, A.; Sun, Z.; Slesarev, A.; Alemany, L. B.; Lu, W.; Tour, J. M. Improved synthesis of graphene oxide. *ACS nano* **2010**, 4 (8), 4806-4814.
- (33) Choucair, M.; Thordarson, P.; Stride, J. A. Gram-scale production of graphene based on solvothermal synthesis and sonication. *Nature nanotechnology* **2009**, 4 (1), 30-33.
- (34) Zhang, Y.; Zhang, L.; Zhou, C. Review of chemical vapor deposition of graphene and related applications. *Accounts of chemical research* **2013**, 46 (10), 2329-2339.
- (35) Gómez-Navarro, C.; Burghard, M.; Kern, K. Elastic properties of chemically derived single graphene sheets. *Nano letters* **2008**, 8 (7), 2045-2049.
- (36) Schniepp, H. C.; Kudin, K. N.; Li, J.-L.; Prud'homme, R. K.; Car, R.; Saville, D. A.; Aksay, I. A. Bending properties of single functionalized graphene sheets probed by atomic force microscopy. *ACS nano* **2008**, 2 (12), 2577-2584.
- (37) Paredes, J.; Villar-Rodil, S.; Martínez-Alonso, A.; Tascon, J. Graphene oxide dispersions in organic solvents. *Langmuir* **2008**, 24 (19), 10560-10564.
- (38) Chua, C. K.; Pumera, M. Chemical reduction of graphene oxide: a synthetic chemistry viewpoint. *Chemical Society Reviews* **2014**, 43 (1), 291-312.
- (39) Fernández-Merino, M. J.; Guardia, L.; Paredes, J.; Villar-Rodil, S.; Solís-Fernández, P.; Martínez-Alonso, A.; Tascón, J. Vitamin C is an ideal substitute for hydrazine in the reduction of graphene oxide suspensions. *The Journal of Physical Chemistry C* **2010**, 114 (14), 6426-6432.
- (40) Gao, J.; Liu, F.; Liu, Y.; Ma, N.; Wang, Z.; Zhang, X. Environment-friendly method to produce graphene that employs vitamin C and amino acid. *Chemistry of Materials* **2010**, 22 (7), 2213-2218.
- (41) Pei, S.; Zhao, J.; Du, J.; Ren, W.; Cheng, H.-M. Direct reduction of graphene oxide films into highly conductive and flexible graphene films by hydrohalic acids. *Carbon* **2010**, 48 (15), 4466-4474.
- (42) Moon, I. K.; Lee, J.; Ruoff, R. S.; Lee, H. Reduced graphene oxide by chemical graphitization. *Nature communications* **2010**, 1 (1), 1-6.
- (43) McAllister, M. J.; Li, J.-L.; Adamson, D. H.; Schniepp, H. C.; Abdala, A. A.; Liu, J.; Herrera-Alonso, M.; Milius, D. L.; Car, R.; Prud'homme, R. K. Single sheet functionalized graphene by oxidation and thermal expansion of graphite. *Chemistry of materials* **2007**, 19 (18), 4396-4404.
- (44) Xu, Z.; Gao, C. Graphene chiral liquid crystals and macroscopic assembled fibres. *Nature communications* **2011**, 2 (1), 1-9.
- (45) Liu, K.; Zhu, F.; Liu, L.; Sun, Y.; Fan, S.; Jiang, K. Fabrication and processing of high-strength densely packed carbon nanotube yarns without solution processes. *Nanoscale* **2012**, 4 (11), 3389-3393.
- (46) Fang, B.; Chang, D.; Xu, Z.; Gao, C. A review on graphene fibers: expectations, advances, and prospects. *Advanced Materials* **2020**, 32 (5), 1902664.
- (47) Xu, Z.; Gao, C. Graphene fiber: a new trend in carbon fibers. *Materials Today* **2015**, 18 (9), 480-492.
- (48) Xu, Z.; Peng, L.; Liu, Y.; Liu, Z.; Sun, H.; Gao, W.; Gao, C. Experimental guidance to graphene macroscopic wet-spun fibers, continuous papers, and ultralightweight aerogels.

- Chemistry of Materials* **2017**, *29* (1), 319-330.
- (49) Feng, L.; Chang, Y.; Zhong, J.; Jia, D.-C. Dry Spin Graphene Oxide Fibers: Mechanical/Electrical Properties and Microstructure Evolution. *Scientific reports* **2018**, *8* (1), 1-7.
- (50) Fang, B.; Xiao, Y.; Xu, Z.; Chang, D.; Wang, B.; Gao, W.; Gao, C. Handedness-controlled and solvent-driven actuators with twisted fibers. *Materials Horizons* **2019**, *6* (6), 1207-1214.
- (51) Li, X.; Zhao, T.; Wang, K.; Yang, Y.; Wei, J.; Kang, F.; Wu, D.; Zhu, H. Directly drawing self-assembled, porous, and monolithic graphene fiber from chemical vapor deposition grown graphene film and its electrochemical properties. *Langmuir* **2011**, *27* (19), 12164-12171.
- (52) Choi, Y. S.; Yeo, C.-s.; Kim, S. J.; Lee, J.-Y.; Kim, Y.; Cho, K. R.; Ju, S.; Hong, B. H.; Park, S. Y. Multifunctional reduced graphene oxide-CVD graphene core-shell fibers. *Nanoscale* **2019**, *11* (26), 12637-12642.
- (53) Xin, G.; Zhu, W.; Deng, Y.; Cheng, J.; Zhang, L. T.; Chung, A. J.; De, S.; Lian, J. Microfluidics-enabled orientation and microstructure control of macroscopic graphene fibres. *Nature nanotechnology* **2019**, *14* (2), 168-175.
- (54) Xu, Z.; Liu, Y.; Zhao, X.; Peng, L.; Sun, H.; Xu, Y.; Ren, X.; Jin, C.; Xu, P.; Wang, M. Ultrastiff and strong graphene fibers via full-scale synergetic defect engineering. *Advanced Materials* **2016**, *28* (30), 6449-6456.
- (55) Wan, S.; Cheng, Q. Fatigue-Resistant Bioinspired Graphene-Based Nanocomposites. *Advanced Functional Materials* **2017**, *27* (43), 1703459.
- (56) Ghosh, S.; Bao, W.; Nika, D. L.; Subrina, S.; Pokatilov, E. P.; Lau, C. N.; Balandin, A. A. Dimensional crossover of thermal transport in few-layer graphene. *Nature materials* **2010**, *9* (7), 555-558.
- (57) Xu, Z.; Liu, Z.; Sun, H.; Gao, C. Highly electrically conductive Ag-doped graphene fibers as stretchable conductors. *Advanced Materials* **2013**, *25* (23), 3249-3253.
- (58) Dong, Z.; Jiang, C.; Cheng, H.; Zhao, Y.; Shi, G.; Jiang, L.; Qu, L. Facile fabrication of light, flexible and multifunctional graphene fibers. *Advanced Materials* **2012**, *24* (14), 1856-1861.
- (59) Xu, Z.; Sun, H.; Zhao, X.; Gao, C. Ultrastrong fibers assembled from giant graphene oxide sheets. *Advanced Materials* **2013**, *25* (2), 188-193.
- (60) Liu, Y.; Xu, Z.; Zhan, J.; Li, P.; Gao, C. Superb electrically conductive graphene fibers via doping strategy. *Advanced Materials* **2016**, *28* (36), 7941-7947.
- (61) Ma, T.; Gao, H. L.; Cong, H. P.; Yao, H. B.; Wu, L.; Yu, Z. Y.; Chen, S. M.; Yu, S. H. A bioinspired interface design for improving the strength and electrical conductivity of graphene-based fibers. *Advanced materials* **2018**, *30* (15), 1706435.
- (62) DeFuria, M. D.; Zeller, M.; Genna, D. T. Removal of pharmaceuticals from water via π - π stacking interactions in perfluorinated metal-organic frameworks. *Crystal Growth & Design* **2016**, *16* (6), 3530-3534.
- (63) Bahnemann, D. Photocatalytic water treatment: solar energy applications. *Solar energy* **2004**, *77* (5), 445-459.
- (64) Ajmal, A.; Majeed, I.; Malik, R. N.; Idriss, H.; Nadeem, M. A. Principles and mechanisms of photocatalytic dye degradation on TiO₂ based photocatalysts: a comparative overview. *Rsc Advances* **2014**, *4* (70), 37003-37026.
- (65) Jeni, J.; Kanmani, S. Solar nanophotocatalytic decolorisation of reactive dyes using

- titanium dioxide. *Journal of Environmental Health Science & Engineering* **2011**, 8 (1), 15-24.
- (66) Woan, K.; Pyrgiotakis, G.; Sigmund, W. Photocatalytic carbon-nanotube–TiO₂ composites. *Advanced Materials* **2009**, 21 (21), 2233-2239.
- (67) Malato, S.; Fernández-Ibáñez, P.; Maldonado, M. I.; Blanco, J.; Gernjak, W. Decontamination and disinfection of water by solar photocatalysis: recent overview and trends. *Catalysis today* **2009**, 147 (1), 1-59.
- (68) Hurum, D. C.; Agrios, A. G.; Gray, K. A.; Rajh, T.; Thurnauer, M. C. Explaining the enhanced photocatalytic activity of Degussa P25 mixed-phase TiO₂ using EPR. *The Journal of Physical Chemistry B* **2003**, 107 (19), 4545-4549.
- (69) Moniz, S. J.; Shevlin, S. A.; An, X.; Guo, Z. X.; Tang, J. Fe₂O₃–TiO₂ nanocomposites for enhanced charge separation and photocatalytic activity. *Chemistry—A European Journal* **2014**, 20 (47), 15571-15579.
- (70) Zhu, Y.; Meng, X.; Cui, H.; Jia, S.; Dong, J.; Zheng, J.; Zhao, J.; Wang, Z.; Li, L.; Zhang, L. Graphene frameworks promoted electron transport in quantum dot-sensitized solar cells. *ACS applied materials & interfaces* **2014**, 6 (16), 13833-13840.
- (71) Zhang, X.-Y.; Li, H.-P.; Cui, X.-L.; Lin, Y. Graphene/TiO₂ nanocomposites: synthesis, characterization and application in hydrogen evolution from water photocatalytic splitting. *Journal of Materials Chemistry* **2010**, 20 (14), 2801-2806.
- (72) Zhou, K.; Zhu, Y.; Yang, X.; Jiang, X.; Li, C. Preparation of graphene–TiO₂ composites with enhanced photocatalytic activity. *New Journal of Chemistry* **2011**, 35 (2), 353-359.
- (73) Shen, J.; Yan, B.; Shi, M.; Ma, H.; Li, N.; Ye, M. One step hydrothermal synthesis of TiO₂-reduced graphene oxide sheets. *Journal of Materials Chemistry* **2011**, 21 (10), 3415-3421.
- (74) Zhu, P.; Nair, A. S.; Shengjie, P.; Shengyuan, Y.; Ramakrishna, S. Facile fabrication of TiO₂–graphene composite with enhanced photovoltaic and photocatalytic properties by electrospinning. *ACS applied materials & interfaces* **2012**, 4 (2), 581-585.
- (75) Li, N.; Liu, G.; Zhen, C.; Li, F.; Zhang, L.; Cheng, H. M. Battery performance and photocatalytic activity of mesoporous anatase TiO₂ nanospheres/graphene composites by template-free self-assembly. *Advanced Functional Materials* **2011**, 21 (9), 1717-1722.
- (76) Liu, X.; Pan, L.; Lv, T.; Zhu, G.; Lu, T.; Sun, Z.; Sun, C. Microwave-assisted synthesis of TiO₂-reduced graphene oxide composites for the photocatalytic reduction of Cr (VI). *RSC advances* **2011**, 1 (7), 1245-1249.
- (77) Liu, B.; Huang, Y.; Wen, Y.; Du, L.; Zeng, W.; Shi, Y.; Zhang, F.; Zhu, G.; Xu, X.; Wang, Y. Highly dispersive {001} facets-exposed nanocrystalline TiO₂ on high quality graphene as a high performance photocatalyst. *Journal of Materials Chemistry* **2012**, 22 (15), 7484-7491.
- (78) Lee, J. S.; You, K. H.; Park, C. B. Highly photoactive, low bandgap TiO₂ nanoparticles wrapped by graphene. *Advanced Materials* **2012**, 24 (8), 1084-1088.
- (79) Liu, J.; Bai, H.; Wang, Y.; Liu, Z.; Zhang, X.; Sun, D. D. Self-assembling TiO₂ nanorods on large graphene oxide sheets at a two-phase interface and their anti-recombination in photocatalytic applications. *Advanced Functional Materials* **2010**, 20 (23), 4175-4181.
- (80) Zhang, Y.; Tang, Z.-R.; Fu, X.; Xu, Y.-J. TiO₂– graphene nanocomposites for gas-phase photocatalytic degradation of volatile aromatic pollutant: is TiO₂– graphene truly different from other TiO₂– carbon composite materials? *ACS nano* **2010**, 4 (12), 7303-7314.
- (81) Fan, W.; Lai, Q.; Zhang, Q.; Wang, Y. Nanocomposites of TiO₂ and reduced graphene oxide as efficient photocatalysts for hydrogen evolution. *The Journal of Physical Chemistry C*

2011, *115* (21), 10694-10701.

(82) Shateri-Khalilabad, M.; Yazdanshenas, M. E. Fabricating electroconductive cotton textiles using graphene. *Carbohydrate polymers* **2013**, *96* (1), 190-195.

(83) Sun, H.; Yang, J.; Zhou, Y.; Zhao, N.; Li, D. Preparation of reduced graphene oxide films by dip coating technique and their electrical conductivity. *Materials Technology* **2014**, *29* (1), 14-20.

(84) Yi, W.; Wang, Y.; Wang, G.; Tao, X. Investigation of carbon black/silicone elastomer/dimethylsilicone oil composites for flexible strain sensors. *Polymer Testing* **2012**, *31* (5), 677-684.

(85) Qu, J.; He, N.; Patil, S. V.; Wang, Y.; Banerjee, D.; Gao, W. Screen printing of graphene oxide patterns onto viscose nonwovens with tunable penetration depth and electrical conductivity. *ACS applied materials & interfaces* **2019**, *11* (16), 14944-14951.

(86) Karim, N.; Afroj, S.; Malandraki, A.; Butterworth, S.; Beach, C.; Rigout, M.; Novoselov, K. S.; Casson, A. J.; Yeates, S. G. All inkjet-printed graphene-based conductive patterns for wearable e-textile applications. *Journal of materials chemistry C* **2017**, *5* (44), 11640-11648.

(87) Paripovic, D.; Klok, H.-A. Polymer brush guided formation of thin gold and palladium/gold bimetallic films. *ACS applied materials & interfaces* **2011**, *3* (3), 910-917.

(88) Wang, Z.; Zhang, L.; Bayram, Y.; Volakis, J. L. Embroidered conductive fibers on polymer composite for conformal antennas. *IEEE Transactions on Antennas and Propagation* **2012**, *60* (9), 4141-4147.

(89) Cherenack, K.; Zysset, C.; Kinkeldei, T.; Münzenrieder, N.; Tröster, G. Woven electronic fibers with sensing and display functions for smart textiles. *Advanced materials* **2010**, *22* (45), 5178-5182.

(90) Wu, Y.; Mechael, S. S.; Chen, Y.; Carmichael, T. B. Solution deposition of conformal gold coatings on knitted fabric for e-textiles and electroluminescent clothing. *Advanced Materials Technologies* **2018**, *3* (3), 1700292.

(91) Zhang, M.; Wang, C.; Wang, H.; Jian, M.; Hao, X.; Zhang, Y. Carbonized cotton fabric for high-performance wearable strain sensors. *Advanced Functional Materials* **2017**, *27* (2), 1604795.

(92) Wu, R.; Ma, L.; Balkrishna Patil, A.; Hou, C.; Meng, Z.; Zhang, Y.; Liu, X.; Yu, W. A facile method to prepare a wearable pressure sensor based on fabric electrodes for human motion monitoring. *Textile Research Journal* **2019**, *89* (23-24), 5144-5152.

(93) Ciornea, R. Is the Transition to Bioeconomy a Sustainable Solution in Fast-fashion Industry, Considering the Overconsumption?-Premises for Future Research. *Mark. Inf. Decis. J* **2020**, *3*, 27-44.

(94) Nunes, L. J.; Godina, R.; Matias, J. C.; Catalão, J. P. Economic and environmental benefits of using textile waste for the production of thermal energy. *Journal of Cleaner Production* **2018**, *171*, 1353-1360.

(95) Damayanti, D.; Wulandari, L. A.; Bagaskoro, A.; Rianjanu, A.; Wu, H.-S. Possibility Routes for Textile Recycling Technology. *Polymers* **2021**, *13* (21), 3834.

(96) Fortuna, L. M.; Diyamandoglu, V. Disposal and acquisition trends in second-hand products. *Journal of cleaner production* **2017**, *142*, 2454-2462.

(97) Vats, S.; Rissanen, M. Parameters affecting the upcycling of waste cotton and PES/CO textiles. *Recycling* **2016**, *1* (1), 166-177.

- (98) Haule, L. V.; Carr, C.; Rigout, M. Preparation and physical properties of regenerated cellulose fibres from cotton waste garments. *Journal of cleaner production* **2016**, *112*, 4445-4451.
- (99) Sotayo, A.; Green, S.; Turvey, G. Carpet recycling: a review of recycled carpets for structural composites. *Environmental Technology & Innovation* **2015**, *3*, 97-107.
- (100) Fotostock, A. The price of fast fashion. *Nat. Clim. Chang* **2018**, *8*, 1.
- (101) Molla, A.; Li, Y.; Mandal, B.; Kang, S. G.; Hur, S. H.; Chung, J. S. Selective adsorption of organic dyes on graphene oxide: theoretical and experimental analysis. *Applied Surface Science* **2019**, *464*, 170-177.
- (102) He, Y. Q.; Zhang, N. N.; Wang, X. D. Adsorption of graphene oxide/chitosan porous materials for metal ions. *Chinese Chemical Letters* **2011**, *22* (7), 859-862.
- (103) Li, Y.; Du, Q.; Liu, T.; Sun, J.; Wang, Y.; Wu, S.; Wang, Z.; Xia, Y.; Xia, L. Methylene blue adsorption on graphene oxide/calcium alginate composites. *Carbohydrate polymers* **2013**, *95* (1), 501-507.
- (104) Liu, T.; Li, Y.; Du, Q.; Sun, J.; Jiao, Y.; Yang, G.; Wang, Z.; Xia, Y.; Zhang, W.; Wang, K. Adsorption of methylene blue from aqueous solution by graphene. *Colloids and Surfaces B: Biointerfaces* **2012**, *90*, 197-203.
- (105) Yao, Y.; Xu, F.; Chen, M.; Xu, Z.; Zhu, Z. Adsorption behavior of methylene blue on carbon nanotubes. *Bioresource technology* **2010**, *101* (9), 3040-3046.
- (106) Kuang, Y.; Zhang, X.; Zhou, S. Adsorption of methylene blue in water onto activated carbon by surfactant modification. *Water* **2020**, *12* (2), 587.
- (107) Wang, Z.; Gao, M.; Li, X.; Ning, J.; Zhou, Z.; Li, G. Efficient adsorption of methylene blue from aqueous solution by graphene oxide modified persimmon tannins. *Materials Science and Engineering: C* **2020**, *108*, 110196.
- (108) Gan, D.; Liu, M.; Huang, H.; Chen, J.; Dou, J.; Wen, Y.; Huang, Q.; Yang, Z.; Zhang, X.; Wei, Y. Facile preparation of functionalized carbon nanotubes with tannins through mussel-inspired chemistry and their application in removal of methylene blue. *Journal of Molecular Liquids* **2018**, *271*, 246-253.
- (109) He, K.; Zeng, G.; Chen, A.; Huang, Z.; Peng, M.; Huang, T.; Chen, G. Graphene hybridized polydopamine-kaolin composite as effective adsorbent for methylene blue removal. *Composites Part B: Engineering* **2019**, *161*, 141-149.
- (110) Dai, H.; Huang, Y.; Huang, H. Eco-friendly polyvinyl alcohol/carboxymethyl cellulose hydrogels reinforced with graphene oxide and bentonite for enhanced adsorption of methylene blue. *Carbohydrate polymers* **2018**, *185*, 1-11.
- (111) Zhang, L.; Zhang, Q.; Xie, H.; Guo, J.; Lyu, H.; Li, Y.; Sun, Z.; Wang, H.; Guo, Z. Electrospun titania nanofibers segregated by graphene oxide for improved visible light photocatalysis. *Applied Catalysis B: Environmental* **2017**, *201*, 470-478.
- (112) Chen, F.; Liu, Z.; Liu, Y.; Fang, P.; Dai, Y. Enhanced adsorption and photocatalytic degradation of high-concentration methylene blue on Ag₂O-modified TiO₂-based nanosheet. *Chemical engineering journal* **2013**, *221*, 283-291.
- (113) Shaban, M.; Ahmed, A. M.; Shehata, N.; Betiha, M. A.; Rabie, A. M. Ni-doped and Ni/Cr co-doped TiO₂ nanotubes for enhancement of photocatalytic degradation of methylene blue. *Journal of colloid and interface science* **2019**, *555*, 31-41.
- (114) Moztahida, M.; Lee, D. S. Photocatalytic degradation of methylene blue with

P25/graphene/polyacrylamide hydrogels: optimization using response surface methodology. *Journal of Hazardous Materials* **2020**, *400*, 123314.

(115) Azeez, F.; Al-Hetlani, E.; Arafa, M.; Abdelmonem, Y.; Nazeer, A. A.; Amin, M. O.; Madkour, M. The effect of surface charge on photocatalytic degradation of methylene blue dye using chargeable titania nanoparticles. *Scientific reports* **2018**, *8* (1), 1-9.

(116) Tai, H.; Duan, Z.; Wang, Y.; Wang, S.; Jiang, Y. based sensors for gas, humidity, and strain detections: a review. *ACS applied materials & interfaces* **2020**, *12* (28), 31037-31053. Zheng, Y.; Wang, L.; Zhao, L.; Wang, D.; Xu, H.; Wang, K.; Han, W. A flexible humidity sensor based on natural biocompatible silk fibroin films. *Advanced Materials Technologies* **2021**, *6* (1), 2001053. Hua, Q.; Sun, J.; Liu, H.; Bao, R.; Yu, R.; Zhai, J.; Pan, C.; Wang, Z. L. Skin-inspired highly stretchable and conformable matrix networks for multifunctional sensing. *Nature communications* **2018**, *9* (1), 1-11.

(117) Fei, T.; Jiang, K.; Jiang, F.; Mu, R.; Zhang, T. Humidity switching properties of sensors based on multiwalled carbon nanotubes/polyvinyl alcohol composite films. *Journal of Applied Polymer Science* **2014**, *131* (1).

(118) Lin, W.-D.; Chang, H.-M.; Wu, R.-J. Applied novel sensing material graphene/polypyrrole for humidity sensor. *Sensors and Actuators B: Chemical* **2013**, *181*, 326-331.

(119) Huang, T.-H.; Chou, J.-C.; Sun, T.-P.; Hsiung, S.-K. A device for skin moisture and environment humidity detection. *Sensors and Actuators B: Chemical* **2008**, *134* (1), 206-212.

(120) Ma, L.; Wu, R.; Patil, A.; Zhu, S.; Meng, Z.; Meng, H.; Hou, C.; Zhang, Y.; Liu, Q.; Yu, R. Full-textile wireless flexible humidity sensor for human physiological monitoring. *Advanced Functional Materials* **2019**, *29* (43), 1904549.

(121) Zhao, Q.; Yuan, Z.; Duan, Z.; Jiang, Y.; Li, X.; Li, Z.; Tai, H. An ingenious strategy for improving humidity sensing properties of multi-walled carbon nanotubes via poly-L-lysine modification. *Sensors and Actuators B: Chemical* **2019**, *289*, 182-185.

(122) Duan, Z.; Jiang, Y.; Huang, Q.; Wang, S.; Wang, Y.; Pan, H.; Zhao, Q.; Xie, G.; Du, X.; Tai, H. Paper and carbon ink enabled low-cost, eco-friendly, flexible, multifunctional pressure and humidity sensors. *Smart Materials and Structures* **2021**, *30* (5), 055012.

(123) Li, W.; Xu, F.; Sun, L.; Liu, W.; Qiu, Y. A novel flexible humidity switch material based on multi-walled carbon nanotube/polyvinyl alcohol composite yarn. *Sensors and Actuators B: Chemical* **2016**, *230*, 528-535.

(124) Agmon, N. The grotthuss mechanism. *Chemical Physics Letters* **1995**, *244* (5-6), 456-462.

(125) Liu, L. X.; Chen, W.; Zhang, H. B.; Wang, Q. W.; Guan, F.; Yu, Z. Z. Flexible and multifunctional silk textiles with biomimetic leaf-like MXene/silver nanowire nanostructures for electromagnetic interference shielding, humidity monitoring, and self-derived hydrophobicity. *Advanced Functional Materials* **2019**, *29* (44), 1905197.

(126) Zhou, G.; Byun, J.-H.; Oh, Y.; Jung, B.-M.; Cha, H.-J.; Seong, D.-G.; Um, M.-K.; Hyun, S.; Chou, T.-W. Highly sensitive wearable textile-based humidity sensor made of high-strength, single-walled carbon nanotube/poly (vinyl alcohol) filaments. *ACS applied materials & interfaces* **2017**, *9* (5), 4788-4797.

(127) Guo, Y.-N.; Gao, Z.-Y.; Wang, X.-X.; Sun, L.; Yan, X.; Yan, S.-Y.; Long, Y.-Z.; Han, W.-P. A highly stretchable humidity sensor based on spandex covered yarns and nanostructured

- polyaniline. *RSC advances* **2018**, *8* (2), 1078-1082.
- (128) Du, B.; Yang, D.; She, X.; Yuan, Y.; Mao, D.; Jiang, Y.; Lu, F. MoS₂-based all-fiber humidity sensor for monitoring human breath with fast response and recovery. *Sensors and Actuators B: Chemical* **2017**, *251*, 180-184.
- (129) Dai, J.; Zhao, H.; Lin, X.; Liu, S.; Liu, Y.; Liu, X.; Fei, T.; Zhang, T. Ultrafast response polyelectrolyte humidity sensor for respiration monitoring. *ACS applied materials & interfaces* **2019**, *11* (6), 6483-6490.
- (130) Ho, D. H.; Sun, Q.; Kim, S. Y.; Han, J. T.; Kim, D. H.; Cho, J. H. Stretchable and multimodal all graphene electronic skin. *Advanced Materials* **2016**, *28* (13), 2601-2608.
- (131) Li, T.; Li, L.; Sun, H.; Xu, Y.; Wang, X.; Luo, H.; Liu, Z.; Zhang, T. Porous ionic membrane based flexible humidity sensor and its multifunctional applications. *Advanced science* **2017**, *4* (5), 1600404.
- (132) Zhao, X.; Long, Y.; Yang, T.; Li, J.; Zhu, H. Simultaneous high sensitivity sensing of temperature and humidity with graphene woven fabrics. *ACS applied materials & interfaces* **2017**, *9* (35), 30171-30176.
- (133) Zhang, D.; Tong, J.; Xia, B. Humidity-sensing properties of chemically reduced graphene oxide/polymer nanocomposite film sensor based on layer-by-layer nano self-assembly. *Sensors and Actuators B: Chemical* **2014**, *197*, 66-72.
- (134) Duan, Z.; Jiang, Y.; Yan, M.; Wang, S.; Yuan, Z.; Zhao, Q.; Sun, P.; Xie, G.; Du, X.; Tai, H. Facile, flexible, cost-saving, and environment-friendly paper-based humidity sensor for multifunctional applications. *ACS applied materials & interfaces* **2019**, *11* (24), 21840-21849.
- (135) Han, D. D.; Zhang, Y. L.; Jiang, H. B.; Xia, H.; Feng, J.; Chen, Q. D.; Xu, H. L.; Sun, H. B. Moisture-responsive graphene paper prepared by self-controlled photoreduction. *Advanced Materials* **2015**, *27* (2), 332-338.
- (136) Lu, L.; Jiang, C.; Hu, G.; Liu, J.; Yang, B. Flexible noncontact sensing for human-machine interaction. *Advanced Materials* **2021**, *33* (16), 2100218. Mondal, S.; Kim, S. J.; Choi, C.-G. Honeycomb-like MoS₂ nanotube array-based wearable sensors for noninvasive detection of human skin moisture. *ACS Applied Materials & Interfaces* **2020**, *12* (14), 17029-17038.
- (137) Güder, F.; Ainla, A.; Redston, J.; Mosadegh, B.; Glavan, A.; Martin, T.; Whitesides, G. M. Paper-based electrical respiration sensor. *Angewandte Chemie International Edition* **2016**, *55* (19), 5727-5732.
- (138) Adepu, V.; Bokka, N.; Mattela, V.; Sahatiya, P. A highly electropositive ReS₂ based ultra-sensitive flexible humidity sensor for multifunctional applications. *New Journal of Chemistry* **2021**, *45* (13), 5855-5862.
- (139) Tan, C.; Dong, Z.; Li, Y.; Zhao, H.; Huang, X.; Zhou, Z.; Jiang, J.-W.; Long, Y.-Z.; Jiang, P.; Zhang, T.-Y. A high performance wearable strain sensor with advanced thermal management for motion monitoring. *Nature communications* **2020**, *11* (1), 1-10. Yamada, T.; Hayamizu, Y.; Yamamoto, Y.; Yomogida, Y.; Izadi-Najafabadi, A.; Futaba, D. N.; Hata, K. A stretchable carbon nanotube strain sensor for human-motion detection. *Nature nanotechnology* **2011**, *6* (5), 296-301.
- (140) Li, C.; Cong, S.; Tian, Z.; Song, Y.; Yu, L.; Lu, C.; Shao, Y.; Li, J.; Zou, G.; Rummeli, M. H. Flexible perovskite solar cell-driven photo-rechargeable lithium-ion capacitor for self-powered wearable strain sensors. *Nano Energy* **2019**, *60*, 247-256.
- (141) Leber, A.; Cholst, B.; Sandt, J.; Vogel, N.; Kolle, M. Stretchable thermoplastic elastomer

- optical fibers for sensing of extreme deformations. *Advanced Functional Materials* **2019**, *29* (5), 1802629.
- (142) Zhao, H.; O'Brien, K.; Li, S.; Shepherd, R. F. Optoelectronically innervated soft prosthetic hand via stretchable optical waveguides. *Science robotics* **2016**, *1* (1), eaai7529.
- (143) Duan, L.; D'hooge, D. R.; Cardon, L. Recent progress on flexible and stretchable piezoresistive strain sensors: From design to application. *Progress in Materials Science* **2020**, *114*, 100617.
- (144) Huang, T.; He, P.; Wang, R.; Yang, S.; Sun, J.; Xie, X.; Ding, G. Porous fibers composed of polymer nanoball decorated graphene for wearable and highly sensitive strain sensors. *Advanced Functional Materials* **2019**, *29* (45), 1903732.
- (145) Wang, Y.; Hao, J.; Huang, Z.; Zheng, G.; Dai, K.; Liu, C.; Shen, C. Flexible electrically resistive-type strain sensors based on reduced graphene oxide-decorated electrospun polymer fibrous mats for human motion monitoring. *Carbon* **2018**, *126*, 360-371.
- (146) Choi, C.; Lee, J. M.; Kim, S. H.; Kim, S. J.; Di, J.; Baughman, R. H. Twistable and stretchable sandwich structured fiber for wearable sensors and supercapacitors. *Nano letters* **2016**, *16* (12), 7677-7684.
- (147) Jang, S.; Kim, J.; Kim, D. W.; Kim, J. W.; Chun, S.; Lee, H. J.; Yi, G.-R.; Pang, C. Carbon-based, ultraelastic, hierarchically coated fiber strain sensors with crack-controllable beads. *ACS applied materials & interfaces* **2019**, *11* (16), 15079-15087. Lee, W. S.; Kim, D.; Park, B.; Joh, H.; Woo, H. K.; Hong, Y. K.; Kim, T. i.; Ha, D. H.; Oh, S. J. Multiaxial and transparent strain sensors based on synergetically reinforced and orthogonally cracked hetero-nanocrystal solids. *Advanced Functional Materials* **2019**, *29* (4), 1806714.
- (148) Zeng, W.; Shu, L.; Li, Q.; Chen, S.; Wang, F.; Tao, X. M. Fiber-based wearable electronics: a review of materials, fabrication, devices, and applications. *Advanced materials* **2014**, *26* (31), 5310-5336.
- (149) Kim, S. J.; Song, W.; Yi, Y.; Min, B. K.; Mondal, S.; An, K.-S.; Choi, C.-G. High durability and waterproofing rGO/SWCNT-fabric-based multifunctional sensors for human-motion detection. *ACS applied materials & interfaces* **2018**, *10* (4), 3921-3928.
- (150) Li, Q.; Yin, R.; Zhang, D.; Liu, H.; Chen, X.; Zheng, Y.; Guo, Z.; Liu, C.; Shen, C. Flexible conductive MXene/cellulose nanocrystal coated nonwoven fabrics for tunable wearable strain/pressure sensors. *Journal of Materials Chemistry A* **2020**, *8* (40), 21131-21141.
- (151) Cai, G.; Yang, M.; Xu, Z.; Liu, J.; Tang, B.; Wang, X. Flexible and wearable strain sensing fabrics. *Chemical Engineering Journal* **2017**, *325*, 396-403.
- (152) Wang, C.; Li, X.; Gao, E.; Jian, M.; Xia, K.; Wang, Q.; Xu, Z.; Ren, T.; Zhang, Y. Carbonized silk fabric for ultrastretchable, highly sensitive, and wearable strain sensors. *Advanced materials* **2016**, *28* (31), 6640-6648.
- (153) Wang, S.; Ning, H.; Hu, N.; Liu, Y.; Liu, F.; Zou, R.; Huang, K.; Wu, X.; Weng, S. Environmentally-friendly and multifunctional graphene-silk fabric strain sensor for human-motion detection. *Advanced materials interfaces* **2020**, *7* (1), 1901507.
- (154) Park, S.; Ahn, S.; Sun, J.; Bhatia, D.; Choi, D.; Yang, K. S.; Bae, J.; Park, J. J. Highly bendable and rotational textile structure with prestrained conductive sewing pattern for human joint monitoring. *Advanced Functional Materials* **2019**, *29* (10), 1808369.
- (155) Araromi, O. A.; Graule, M. A.; Dorsey, K. L.; Castellanos, S.; Foster, J. R.; Hsu, W.-H.; Passy, A. E.; Vlassak, J. J.; Weaver, J. C.; Walsh, C. J. Ultra-sensitive and resilient compliant

- strain gauges for soft machines. *Nature* **2020**, 587 (7833), 219-224.
- (156) Choi, S.; Yoon, K.; Lee, S.; Lee, H. J.; Lee, J.; Kim, D. W.; Kim, M. S.; Lee, T.; Pang, C. Conductive hierarchical hairy fibers for highly sensitive, stretchable, and water-resistant multimodal gesture-distinguishable sensor, VR applications. *Advanced Functional Materials* **2019**, 29 (50), 1905808.
- (157) Schneider, J.; Bahnemann, D.; Ye, J.; Puma, G. L.; Dionysiou, D. D. *Photocatalysis: fundamentals and perspectives*; Royal Society of Chemistry, 2016. Wang, Z.; Huang, B.; Dai, Y.; Liu, Y.; Zhang, X.; Qin, X.; Wang, J.; Zheng, Z.; Cheng, H. Crystal facets controlled synthesis of graphene@TiO₂ nanocomposites by a one-pot hydrothermal process. *CrystEngComm* **2012**, 14 (5), 1687-1692.
- (158) Faraldos, M.; Bahamonde, A. Environmental applications of titania-graphene photocatalysts. *Catalysis Today* **2017**, 285, 13-28. Tolosana-Moranchel, Á.; Manassero, A.; Satuf, M. L.; Alfano, O. M.; Casas, J. A.; Bahamonde, A. Influence of TiO₂-rGO optical properties on the photocatalytic activity and efficiency to photodegrade an emerging pollutant. *Applied Catalysis B: Environmental* **2019**, 246, 1-11.
- (159) Pandit, P.; Nadathur, G. T.; Jose, S. Upcycled and low-cost sustainable business for value-added textiles and fashion. In *Circular Economy in Textiles and Apparel*, Elsevier, 2019; pp 95-122.
- (160) Schmidt, A. *Gaining benefits from discarded textiles: LCA of different treatment pathways*; Nordic Council of Ministers, 2016.
- (161) Zhai, H.; Li, Y.; Fan, Y.-Y. The Effect of Graphene Oxide Sheets on the Mechanical Properties of Graphene Fibres. *Journal of Fiber Bioengineering and Informatics* **2018**, 11 (1), 49-63.
- (162) Xu, L.; Zhai, H.; Chen, X.; Liu, Y.; Wang, M.; Liu, Z.; Umar, M.; Ji, C.; Chen, Z.; Jin, L. Coolmax/graphene-oxide functionalized textile humidity sensor with ultrafast response for human activities monitoring. *Chemical Engineering Journal* **2021**, 412, 128639.
- (163) Katal, R.; Masudy-Panah, S.; Tanhaei, M.; Farahani, M. H. D. A.; Jiangyong, H. A review on the synthesis of the various types of anatase TiO₂ facets and their applications for photocatalysis. *Chemical Engineering Journal* **2020**, 384, 123384.
- (164) Zhang, L.; Li, Y.; Zhang, Q.; Wang, H. Hierarchical nanostructure of WO₃ nanorods on TiO₂ nanofibers and the enhanced visible light photocatalytic activity for degradation of organic pollutants. *CrystEngComm* **2013**, 15 (30), 5986-5993.
- (165) Gómez-Navarro, C.; Weitz, R. T.; Bittner, A. M.; Scolari, M.; Mews, A.; Burghard, M.; Kern, K. Electronic transport properties of individual chemically reduced graphene oxide sheets. *Nano letters* **2007**, 7 (11), 3499-3503.
- (166) Linsebigler, A. L.; Lu, G.; Yates Jr, J. T. Photocatalysis on TiO₂ surfaces: principles, mechanisms, and selected results. *Chemical reviews* **1995**, 95 (3), 735-758.
- (167) Wang, C.; Shao, C.; Zhang, X.; Liu, Y. SnO₂ nanostructures-TiO₂ nanofibers heterostructures: controlled fabrication and high photocatalytic properties. *Inorganic Chemistry* **2009**, 48 (15), 7261-7268.
- (168) Huang, Q.; Tian, S.; Zeng, D.; Wang, X.; Song, W.; Li, Y.; Xiao, W.; Xie, C. Enhanced photocatalytic activity of chemically bonded TiO₂/graphene composites based on the effective interfacial charge transfer through the C-Ti bond. *Acs Catalysis* **2013**, 3 (7), 1477-1485.
- (169) Langmuir, I. The adsorption of gases on plane surfaces of glass, mica and platinum.

- Journal of the American Chemical Society* **1918**, *40* (9), 1361-1403.
- (170) Freundlich, H. Über die adsorption in lösungen. *Zeitschrift für physikalische Chemie* **1907**, *57* (1), 385-470.
- (171) An, W.; Cui, W.; Liang, Y.; Hu, J.; Liu, L. Surface decoration of BiPO₄ with BiOBr nanoflakes to build heterostructure photocatalysts with enhanced photocatalytic activity. *Applied Surface Science* **2015**, *351*, 1131-1139.
- (172) Corbett, J. F. Pseudo first-order kinetics. *Journal of Chemical Education* **1972**, *49* (10), 663.
- (173) Zhang, L.; Mohamed, H. H.; Dillert, R.; Bahnemann, D. Kinetics and mechanisms of charge transfer processes in photocatalytic systems: a review. *Journal of Photochemistry and Photobiology C: Photochemistry Reviews* **2012**, *13* (4), 263-276.
- (174) Afroj, S.; Karim, N.; Wang, Z.; Tan, S.; He, P.; Holwill, M.; Ghazaryan, D.; Fernando, A.; Novoselov, K. S. Engineering Graphene Flakes for Wearable Textile Sensors via Highly Scalable and Ultrafast Yarn Dyeing Technique. *ACS Nano* **2019**, *13* (4), 3847-3857. DOI: 10.1021/acsnano.9b00319.
- (175) Kano, S.; Kim, K.; Fujii, M. Fast-Response and Flexible Nanocrystal-Based Humidity Sensor for Monitoring Human Respiration and Water Evaporation on Skin. *ACS sensors* **2017**, *2* (6), 828-833. DOI: 10.1021/acssensors.7b00199.
- (176) Wang, X.; Xiong, Z.; Liu, Z.; Zhang, T. Exfoliation at the liquid/air interface to assemble reduced graphene oxide ultrathin films for a flexible noncontact sensing device. *Adv Mater* **2015**, *27* (8), 1370-1375. DOI: 10.1002/adma.201404069.
- (177) Zhao, X.; Long, Y.; Yang, T.; Li, J.; Zhu, H. Simultaneous High Sensitivity Sensing of Temperature and Humidity with Graphene Woven Fabrics. *ACS applied materials & interfaces* **2017**, *9* (35), 30171-30176. DOI: 10.1021/acsmi.7b09184.
- (178) Zhang, D.; Zong, X.; Wu, Z.; Zhang, Y. Hierarchical self-assembled SnS₂ nanoflower/Zn₂SnO₄ hollow sphere nanohybrid for humidity-sensing applications. *ACS applied materials & interfaces* **2018**, *10* (38), 32631-32639.
- (179) McColl, D.; Cartlidge, B.; Connolly, P. Real-time monitoring of moisture levels in wound dressings in vitro: An experimental study. *International Journal of Surgery* **2007**, *5* (5), 316-322.
- (180) Weng, Z.; Qin, J.; Umar, A. A.; Wang, J.; Zhang, X.; Wang, H.; Cui, X.; Li, X.; Zheng, L.; Zhan, Y. Lead-Free Cs₂BiAgBr₆ Double Perovskite-Based Humidity Sensor with Superfast Recovery Time. *Advanced Functional Materials* **2019**, *29* (24), 1902234.
- (181) He, J.; Xiao, P.; Shi, J.; Liang, Y.; Lu, W.; Chen, Y.; Wang, W.; Théato, P.; Kuo, S.-W.; Chen, T. High Performance Humidity Fluctuation Sensor for Wearable Devices via a Bioinspired Atomic-Precise Tunable Graphene-Polymer Heterogeneous Sensing Junction. *Chemistry of Materials* **2018**, *30* (13), 4343-4354. DOI: 10.1021/acs.chemmater.8b01587.
- (182) Ahmad, H.; Rahman, M. T.; Sakeh, S. N. A.; Razak, M. Z. A.; Zulkifli, M. Z. Humidity sensor based on microfiber resonator with reduced graphene oxide. *Optik* **2016**, *127* (5), 3158-3161. DOI: 10.1016/j.ijleo.2015.11.184.
- (183) Bulusheva, L. G.; Sysoev, V. I.; Lobiak, E. V.; Fedoseeva, Y. V.; Makarova, A. A.; Dubois, M.; Flahaut, E.; Okotrub, A. V. Chlorinated holey double-walled carbon nanotubes for relative humidity sensors. *Carbon* **2019**, *148*, 413-420. DOI: 10.1016/j.carbon.2019.04.010.
- (184) Reeder, J. T.; Choi, J.; Xue, Y.; Gutruf, P.; Hanson, J.; Liu, M.; Ray, T.; Bandodkar, A. J.;

- Avila, R.; Xia, W. Waterproof, electronics-enabled, epidermal microfluidic devices for sweat collection, biomarker analysis, and thermography in aquatic settings. *Science advances* **2019**, *5* (1), eaau6356.
- (185) Wang, X.; Huang, Z.; Miao, D.; Zhao, J.; Yu, J.; Ding, B. Biomimetic Fibrous Murray Membranes with Ultrafast Water Transport and Evaporation for Smart Moisture-Wicking Fabrics. *ACS Nano* **2019**, *13* (2), 1060-1070. DOI: 10.1021/acsnano.8b08242.
- (186) Shen, D.; Xiao, M.; Zou, G.; Liu, L.; Duley, W. W.; Zhou, Y. N. Self-Powered Wearable Electronics Based on Moisture Enabled Electricity Generation. *Adv Mater* **2018**, *30* (18), e1705925. DOI: 10.1002/adma.201705925.
- (187) Dai, J.; Zhao, H.; Lin, X.; Liu, S.; Liu, Y.; Liu, X.; Fei, T.; Zhang, T. Ultrafast Response Polyelectrolyte Humidity Sensor for Respiration Monitoring. *ACS applied materials & interfaces* **2019**, *11* (6), 6483-6490. DOI: 10.1021/acsmi.8b18904.
- (188) Zhou, G.; Byun, J. H.; Oh, Y.; Jung, B. M.; Cha, H. J.; Seong, D. G.; Um, M. K.; Hyun, S.; Chou, T. W. Highly Sensitive Wearable Textile-Based Humidity Sensor Made of High-Strength, Single-Walled Carbon Nanotube/Poly(vinyl alcohol) Filaments. *ACS applied materials & interfaces* **2017**, *9* (5), 4788-4797. DOI: 10.1021/acsmi.6b12448.
- (189) Choi, S. J.; Yu, H.; Jang, J. S.; Kim, M. H.; Kim, S. J.; Jeong, H. S.; Kim, I. D. Nitrogen-Doped Single Graphene Fiber with Platinum Water Dissociation Catalyst for Wearable Humidity Sensor. *Small* **2018**, *14* (13), e1703934. DOI: 10.1002/sml.201703934.
- (190) Li, B.; Xiao, G.; Liu, F.; Qiao, Y.; Li, C. M.; Lu, Z. A flexible humidity sensor based on silk fabrics for human respiration monitoring. *Journal of Materials Chemistry C* **2018**, *6* (16), 4549-4554. DOI: 10.1039/c8tc00238j.
- (191) Hummers Jr, W. S.; Offeman, R. E. Preparation of graphitic oxide. *Journal of the american chemical society* **1958**, *80* (6), 1339-1339. Rourke, J. P.; Pandey, P. A.; Moore, J. J.; Bates, M.; Kinloch, I. A.; Young, R. J.; Wilson, N. R. The real graphene oxide revealed: stripping the oxidative debris from the graphene-like sheets. *Angewandte Chemie International Edition* **2011**, *50* (14), 3173-3177.
- (192) Tissera, N. D.; Wijesena, R. N.; Perera, J. R.; de Silva, K. N.; Amaratunge, G. A. Hydrophobic cotton textile surfaces using an amphiphilic graphene oxide (GO) coating. *Applied Surface Science* **2015**, *324*, 455-463.
- (193) Ferrari, A. C.; Meyer, J.; Scardaci, V.; Casiraghi, C.; Lazzeri, M.; Mauri, F.; Piscanec, S.; Jiang, D.; Novoselov, K.; Roth, S. Raman spectrum of graphene and graphene layers. *Physical review letters* **2006**, *97* (18), 187401.
- (194) Stankovich, S.; Dikin, D. A.; Piner, R. D.; Kohlhaas, K. A.; Kleinhammes, A.; Jia, Y.; Wu, Y.; Nguyen, S. T.; Ruoff, R. S. Synthesis of graphene-based nanosheets via chemical reduction of exfoliated graphite oxide. *carbon* **2007**, *45* (7), 1558-1565.
- (195) Zhou, J.; Cai, D.; Xu, Q.; Zhang, Y.; Fu, F.; Diao, H.; Liu, X. Excellent binding effect of l-methionine for immobilizing silver nanoparticles onto cotton fabrics to improve the antibacterial durability against washing. *RSC Advances* **2018**, *8* (43), 24458-24463. DOI: 10.1039/c8ra04401e.
- (196) Dochia, M.; Sirghie, C.; Kozłowski, R.; Roskwitalski, Z. Cotton fibres. In *Handbook of natural fibres*, Elsevier, 2012; pp 11-23. Li, D.; Ni, M. Moisture properties of coolmax fiber blended with regenerated cellulose fibers. In *2009 second international conference on information and computing science*, 2009; IEEE: Vol. 2, pp 129-131.

- (197) Kuffner, H.; Popescu, C. 8 - Wool fibres. In *Handbook of Natural Fibres*, Kozłowski, R. M. Ed.; Vol. 1; Woodhead Publishing, 2012; pp 171-195. Bertaux, E.; Le Marec, E.; Crespy, D.; Rossi, R.; Hegemann, D. Effects of siloxane plasma coating on the frictional properties of polyester and polyamide fabrics. *Surface and Coatings Technology* **2009**, *204* (1-2), 165-171.
- (198) Wang, F.; Annaheim, S.; Morrissey, M.; Rossi, R. Real evaporative cooling efficiency of one-layer tight-fitting sportswear in a hot environment. *Scandinavian Journal of Medicine & Science in Sports* **2014**, *24* (3), e129-e139.
- (199) Yi, Y.; Yu, C.; Zhai, H.; Jin, L.; Cheng, D.; Lu, Y.; Chen, Z.; Xu, L.; Li, J.; Song, Q. A free-standing humidity sensor with high sensing reliability for environmental and wearable detection. *Nano Energy* **2022**, *103*, 107780.
- (200) Hu, J.; Li, Y.; Yeung, K.-W.; Wong, A. S.; Xu, W. Moisture management tester: a method to characterize fabric liquid moisture management properties. *Textile Research Journal* **2005**, *75* (1), 57-62.
- (201) Mao, A.; Luo, J.; Li, Y.; Luo, X.; Wang, R. A multi-disciplinary strategy for computer-aided clothing thermal engineering design. *Computer-Aided Design* **2011**, *43* (12), 1854-1869.
- (202) Xu, L.; Liu, Z.; Chen, X.; Sun, R.; Hu, Z.; Zheng, Z.; Ye, T. T.; Li, Y. Deformation-Resilient Embroidered Near Field Communication Antenna and Energy Harvesters for Wearable Applications. *Advanced Intelligent Systems* **2019**, *1* (6), 1900056.
- (203) Xu, L.; Liu, Z.; Chen, X.; Sun, R.; Hu, Z.; Zheng, Z.; Ye, T. T.; Li, Y. Deformation-Resilient Embroidered NFC Antenna and Energy Harvester for Wearable Applications. *Advanced Intelligent Systems*.
- (204) Ma, L.; Wu, R.; Patil, A.; Zhu, S.; Meng, Z.; Meng, H.; Hou, C.; Zhang, Y.; Liu, Q.; Yu, R.; et al. Full-Textile Wireless Flexible Humidity Sensor for Human Physiological Monitoring. *Advanced Functional Materials* **2019**, *29* (43), 1904549. DOI: 10.1002/adfm.201904549.
- (205) Pang, C.; Lee, C.; Suh, K. Y. Recent advances in flexible sensors for wearable and implantable devices. *Journal of Applied Polymer Science* **2013**, *130* (3), 1429-1441. Zhao, X.; Zhou, Y.; Xu, J.; Chen, G.; Fang, Y.; Tat, T.; Xiao, X.; Song, Y.; Li, S.; Chen, J. Soft fibers with magnetoelasticity for wearable electronics. *Nature communications* **2021**, *12* (1), 1-11. Li, S.; Zhang, Y.; Wang, Y.; Xia, K.; Yin, Z.; Wang, H.; Zhang, M.; Liang, X.; Lu, H.; Zhu, M. Physical sensors for skin-inspired electronics. *InfoMat* **2020**, *2* (1), 184-211.
- (206) Oh, J.; Yang, J. C.; Kim, J.-O.; Park, H.; Kwon, S. Y.; Lee, S.; Sim, J. Y.; Oh, H. W.; Kim, J.; Park, S. Pressure insensitive strain sensor with facile solution-based process for tactile sensing applications. *ACS nano* **2018**, *12* (8), 7546-7553.
- (207) Yin, B.; Wen, Y.; Hong, T.; Xie, Z.; Yuan, G.; Ji, Q.; Jia, H. Highly stretchable, ultrasensitive, and wearable strain sensors based on facilely prepared reduced graphene oxide woven fabrics in an ethanol flame. *ACS applied materials & interfaces* **2017**, *9* (37), 32054-32064. Luo, J.; Gao, S.; Luo, H.; Wang, L.; Huang, X.; Guo, Z.; Lai, X.; Lin, L.; Li, R. K.; Gao, J. Superhydrophobic and breathable smart MXene-based textile for multifunctional wearable sensing electronics. *Chemical Engineering Journal* **2021**, *406*, 126898.
- (208) Qin, Z.; Sun, X.; Yu, Q.; Zhang, H.; Wu, X.; Yao, M.; Liu, W.; Yao, F.; Li, J. Carbon nanotubes/hydrophobically associated hydrogels as ultrastretchable, highly sensitive, stable strain, and pressure sensors. *ACS applied materials & interfaces* **2020**, *12* (4), 4944-4953.
- (209) Liu, Z.; Chen, K.; Fernando, A.; Gao, Y.; Li, G.; Jin, L.; Zhai, H.; Yi, Y.; Xu, L.; Zheng, Y. Permeable graphited hemp fabrics-based, wearing-comfortable pressure sensors for

monitoring human activities. *Chemical Engineering Journal* **2021**, *403*, 126191.

(210) Cheng, H.; Hu, Y.; Zhao, F.; Dong, Z.; Wang, Y.; Chen, N.; Zhang, Z.; Qu, L. Moisture-activated torsional graphene-fiber motor. *Advanced Materials* **2014**, *26* (18), 2909-2913.

(211) Wang, R.; Xu, Z.; Zhuang, J.; Liu, Z.; Peng, L.; Li, Z.; Liu, Y.; Gao, W.; Gao, C. Highly stretchable graphene fibers with ultrafast electrothermal response for low-voltage wearable heaters. *Advanced Electronic Materials* **2017**, *3* (2), 1600425. Cruz-Silva, R.; Morelos-Gomez, A.; Kim, H.-i.; Jang, H.-k.; Tristan, F.; Vega-Diaz, S.; Rajukumar, L. P.; Elías, A. L.; Perea-Lopez, N.; Suhr, J. Super-stretchable graphene oxide macroscopic fibers with outstanding knotability fabricated by dry film scrolling. *ACS nano* **2014**, *8* (6), 5959-5967.

(212) Li, Z.; Xu, Z.; Liu, Y.; Wang, R.; Gao, C. Multifunctional non-woven fabrics of interfused graphene fibres. *Nature communications* **2016**, *7* (1), 1-11.

(213) Zhang, Z.; Zhang, D.; Lin, H.; Chen, Y. Flexible fiber-shaped supercapacitors with high energy density based on self-twisted graphene fibers. *Journal of Power Sources* **2019**, *433*, 226711.

(214) Liu, F.; Dong, Y.; Shi, R.; Wang, E.; Ni, Q.; Fu, Y. Continuous graphene fibers prepared by liquid crystal spinning as strain sensors for Monitoring Vital Signs. *Materials Today Communications* **2020**, *24*, 100909. Zhang, Y.; Li, Y.; Ming, P.; Zhang, Q.; Liu, T.; Jiang, L.; Cheng, Q. Ultrastrong bioinspired graphene-based fibers via synergistic toughening. *Advanced Materials* **2016**, *28* (14), 2834-2839. Xin, G.; Yao, T.; Sun, H.; Scott, S. M.; Shao, D.; Wang, G.; Lian, J. Highly thermally conductive and mechanically strong graphene fibers. *Science* **2015**, *349* (6252), 1083-1087. Li, J.; Li, J.; Li, L.; Yu, M.; Ma, H.; Zhang, B. Flexible graphene fibers prepared by chemical reduction-induced self-assembly. *Journal of Materials Chemistry A* **2014**, *2* (18), 6359-6362. Tian, Q.; Xu, Z.; Liu, Y.; Fang, B.; Peng, L.; Xi, J.; Li, Z.; Gao, C. Dry spinning approach to continuous graphene fibers with high toughness. *Nanoscale* **2017**, *9* (34), 12335-12342. Fang, B.; Peng, L.; Xu, Z.; Gao, C. Wet-spinning of continuous montmorillonite-graphene fibers for fire-resistant lightweight conductors. *Acs Nano* **2015**, *9* (5), 5214-5222. Wang, X.; Qiu, Y.; Cao, W.; Hu, P. Highly stretchable and conductive core-sheath chemical vapor deposition graphene fibers and their applications in safe strain sensors. *Chemistry of Materials* **2015**, *27* (20), 6969-6975. Yang, Z.; Niu, Y.; Zhao, W.; Zhang, Y.; Zhang, H.; Zhang, C.; Zhang, W.; Xiang, X.; Li, Q. Nanoparticle intercalation-modulated stretchable conductive graphene fibers with combined photoelectric properties. *Carbon* **2019**, *141*, 218-225.

(215) Yang, Z.; Jia, Y.; Niu, Y.; Zhang, Y.; Zhang, C.; Li, P.; Zhu, M.; Li, Q. One-step wet-spinning assembly of twisting-structured graphene/carbon nanotube fiber supercapacitor. *Journal of Energy Chemistry* **2020**, *51*, 434-441.

(216) Sun, X.; Qin, Z.; Ye, L.; Zhang, H.; Yu, Q.; Wu, X.; Li, J.; Yao, F. Carbon nanotubes reinforced hydrogel as flexible strain sensor with high stretchability and mechanically toughness. *Chemical Engineering Journal* **2020**, *382*, 122832. Zhou, J.; Hsieh, Y.-L. Conductive polymer protonated nanocellulose aerogels for tunable and linearly responsive strain sensors. *ACS applied materials & interfaces* **2018**, *10* (33), 27902-27910. Liu, Q.; Chen, J.; Li, Y.; Shi, G. High-performance strain sensors with fish-scale-like graphene-sensing layers for full-range detection of human motions. *ACS nano* **2016**, *10* (8), 7901-7906. Yang, S.; Li, C.; Wen, N.; Xu, S.; Huang, H.; Cong, T.; Zhao, Y.; Fan, Z.; Liu, K.; Pan, L. All-fabric-based multifunctional textile sensor for detection and discrimination of humidity, temperature, and strain stimuli. *Journal of Materials Chemistry C* **2021**, *9* (39), 13789-13798. Wang, X.; Li, Q.;

- Tao, X. Sensing mechanism of a carbon nanocomposite-printed fabric as a strain sensor. *Composites Part A: Applied Science and Manufacturing* **2021**, *144*, 106350. Yang, G.; Xing, R.; Li, Y.; Ma, C.; Cheng, B.; Yan, J.; Zhuang, X. Toward high-performance multifunctional electronics: Knitted fabric-based composite with electrically conductive anisotropy and self-healing capacity. *Chemical Engineering Journal* **2021**, *426*, 131931.
- (217) Zou, Y.; Tan, P.; Shi, B.; Ouyang, H.; Jiang, D.; Liu, Z.; Li, H.; Yu, M.; Wang, C.; Qu, X. A bionic stretchable nanogenerator for underwater sensing and energy harvesting. *Nature Communications* **2019**, *10* (1), 1-10.
- (218) Gao, J.; Li, B.; Huang, X.; Wang, L.; Lin, L.; Wang, H.; Xue, H. Electrically conductive and fluorine free superhydrophobic strain sensors based on SiO₂/graphene-decorated electrospun nanofibers for human motion monitoring. *Chemical Engineering Journal* **2019**, *373*, 298-306.
- (219) McCullough, E. A.; Kwon, M.; Shim, H. A comparison of standard methods for measuring water vapour permeability of fabrics. *Measurement Science and Technology* **2003**, *14* (8), 1402.
- (220) Stoffberg, M. E.; Hunter, L.; Botha, A. The effect of fabric structural parameters and fiber type on the comfort-related properties of commercial apparel fabrics. *Journal of Natural Fibers* **2015**, *12* (6), 505-517.
- (221) Hajiaghajani, A.; Afandizadeh Zargari, A. H.; Dautta, M.; Jimenez, A.; Kurdahi, F.; Tseng, P. Textile-integrated metamaterials for near-field multibody area networks. *Nature Electronics* **2021**, *4* (11), 808-817. Liu, Z.; Li, Z.; Yi, Y.; Li, L.; Zhai, H.; Lu, Z.; Jin, L.; Lu, J. R.; Xie, S. Q.; Zheng, Z. Flexible strain sensing percolation networks towards complicated wearable microclimate and multi-direction mechanical inputs. *Nano Energy* **2022**, 107444.
- (222) Liu, Z.; Li, Z.; Zhai, H.; Jin, L.; Chen, K.; Yi, Y.; Gao, Y.; Xu, L.; Zheng, Y.; Yao, S. A highly sensitive stretchable strain sensor based on multi-functionalized fabric for respiration monitoring and identification. *Chemical Engineering Journal* **2021**, 130869.
- (223) Liu, H.; Li, Q.; Bu, Y.; Zhang, N.; Wang, C.; Pan, C.; Mi, L.; Guo, Z.; Liu, C.; Shen, C. Stretchable conductive nonwoven fabrics with self-cleaning capability for tunable wearable strain sensor. *Nano Energy* **2019**, *66*, 104143. Li, Q.; Liu, H.; Zhang, S.; Zhang, D.; Liu, X.; He, Y.; Mi, L.; Zhang, J.; Liu, C.; Shen, C. Superhydrophobic electrically conductive paper for ultrasensitive strain sensor with excellent anticorrosion and self-cleaning property. *ACS applied materials & interfaces* **2019**, *11* (24), 21904-21914.
- (224) Bojic, J.; Radovanovic, B.; Dimitrijevic, J. Spectrophotometric determination of urea in dermatologic formulations and cosmetics. *Analytical sciences* **2008**, *24* (6), 769-774.
- (225) Wu, L.; Fan, M.; Qu, M.; Yang, S.; Nie, J.; Tang, P.; Pan, L.; Wang, H.; Bin, Y. Self-healing and anti-freezing graphene-hydrogel-graphene sandwich strain sensor with ultrahigh sensitivity. *Journal of Materials Chemistry B* **2021**, *9* (13), 3088-3096.